



# **Analysis of Rock Performance under Three-Dimensional Stress to Predict Instability in Deep Boreholes**

**Arash Mirahmadizoghi**

**September 2012**

**School of Civil, Environmental and Mining Engineering**

**The University of Adelaide**

# Contents

Abstract.....	xii
Statement of Originality .....	xv
Acknowledgements .....	xvi
<b>CHAPTER 1 Introduction</b>	
1.1. Introduction .....	1
1.2. Aims of the Study .....	4
1.3. Research Method .....	6
1.4. Organisation of the Thesis.....	8
<b>CHAPTER 2 Literature review</b>	
2.1. Introduction .....	10
2.2. In situ Stresses Prior to the Introduction of the Borehole.....	10
2.3. Stress Analysis around the Borehole .....	12
2.4. Strength Analysis of Intact Rock.....	16
Coulomb criterion .....	17
Hoek-Brown criterion .....	18
2.4.1. The influence of intermediate principal stress on rock failure stress .....	21
Yield and failure .....	22
2.4.2. Frictional criteria.....	25
Drucker-Prager criterion .....	26
Modified Wiebols and Cook criterion .....	27
Modified Lade criterion .....	29
2.4.3. Hoek-Brown based criteria .....	31
Pan-Hudson criterion .....	32

Generalised Priest criterion.....	33
Simplified Priest criterion.....	34
Generalised Zhang-Zhu criterion.....	35
<b>CHAPTER 3 Stress analysis around a borehole</b>	
3.1. Introduction .....	37
3.2. Stress Analysis around a Vertical Borehole .....	40
Stresses before drilling the borehole.....	40
Stresses after drilling the borehole.....	42
Changes in the initial stress state due to the introduction of the borehole.....	44
Total induced in situ stresses .....	44
3.2.1. Numerical model of a vertical borehole .....	46
3.3. Stress Analysis around a Deviated Borehole.....	53
3.3.1. Stresses at the borehole wall due to far-field in-plane shear, $\sigma_{xy}$ and normal stresses, $\sigma_{xx}$ , $\sigma_{yy}$ and $\sigma_{zz}$ .....	55
3.3.2. Stresses at the borehole wall due to longitudinal shear stresses ( $\sigma_{xz} = \sigma_{zx}$ ) and ( $\sigma_{yz} = \sigma_{zy}$ ).....	58
3.4. Numerical Counterpart of the Generalised Kirsch Equations .....	60
3.5. A Modification to the Generalised Kirsch Equations.....	70
<b>CHAPTER 4 Rock strength analysis in three-dimensional stress</b>	
4.1. Introduction .....	76
4.2. Definition of General, Principal and Deviatoric Stress Tensors .....	77
4.3. Failure Function in Principal Stress Space .....	80
4.4. Failure functions in deviatoric stress space .....	82
4.5. Failure Criteria on Deviatoric and Meridian Planes .....	87
4.6. Failure Criteria Especially Developed For Rock Material .....	91

4.6.1. The Hoek-Brown criterion.....	92
4.6.2. The Pan-Hudson criterion.....	96
4.6.3. The Zhang-Zhu criterion.....	99
4.6.4. Generalised priest criterion.....	102
4.6.5. The Simplified Priest Criterion.....	106
4.7. Experimental Evaluations of Rock Behaviour under Three-Dimensional Stress.....	109
4.7.1. The influence of intermediate principal stress on failure stress.....	110
4.7.2. A modification to the simplified Priest criterion .....	116
4.7.3. Comparison of three-dimensional, Hoek-Brown based failure criteria.....	120
4.8. True-triaxial Experiments at the University of Adelaide .....	124
4.8.1. Experimental setup .....	124
True-triaxial apparatus.....	124
Specimen preparation .....	126
True-triaxial tests .....	127
Comparison and validation of three-dimensional failure criteria against true-triaxial data.....	128
<b>CHAPTER 5 A case study of prediction of borehole instability</b>	
5.1. Introduction .....	136
5.2. Prediction of borehole instability .....	137
5.3. Designing the drilling fluid.....	143
<b>CHAPTER 6 Conclusion</b>	
6.1. Summary and conclusions.....	147
6.2. Recommendations for future studies .....	148
References .....	<b>Error! Bookmark not defined.</b>
Appendix A The Finite Element Method.....	155

The Finite Element Method (FEM) .....	155
Mesh quality .....	157
APPENDIX B Quantitative comparison between analytical and numerical models.....	159
APPENDIX C True-triaxial data from the literature .....	164
APPENDIX D $\sigma_1$ - $\sigma_2$ plots for the selected rock types from the literature .....	174
APPENDIX E Error analysis diagrams.....	196
APPENDIX F MATLAB programs for plotting three dimensional failure surfaces in the principal stress space .....	201
Hoek-Brown Criterion .....	201
Pan-Hudson Criterion .....	204
Zhang-Zhu Criterion .....	207
Simplified Priest Criterion.....	210
Generalised Priest Criterion.....	213

# Figures

Figure 1.1 Failure ( $\sigma_f$ ) and yield ( $\sigma_y$ ) stresses for brittle materials.....	4
Figure 1.2 Demonstration of different phases in the stepwise research method adopted in this study .....	6
Figure 2.1 Coordinate system for a deviated borehole [after Fjær et al. (2008)] .....	12
Figure 2.2 Mean octahedral shear stress, $\tau_{oct}$ vs. mean octahedral normal $\sigma_{oct}$ at yield for Dunham dolomite (after Mogi (2007)) .....	24
Figure 2.3 The cross section of (a) the Coulomb, (b) the circumscribed and (c) the inscribed Drucker-Prager on the deviatoric plane .....	27
Figure 2.4 Relation between intermediate and major principal stresses at failure for eight different failure criteria for a rock mass subjected to a minor principal stress of 15 MPa, with a uniaxial compressive strength of 75 MPa, $m_i = 19$ and GSI = 90 (Priest, 2010) .....	33
Figure 3.1 Stresses on an element at a radial distance $r$ from the centre of a circular hole with radius $a$ , in polar coordinates.....	38
Figure 3.2 The model of the pre-stressed rock block into which the borehole will be drilled .....	41
Figure 3.3 Demonstrating the conditions for applying plane strain assumption for calculating longitudinal stress components around a borehole.....	43
Figure 3.4 Radial distance from the borehole centre and angular position of a given element.....	48
Figure 3.5 Comparison between numerical and analytical model for variation of induced radial ( $\sigma_{rr}$ ) and tangential ( $\sigma_{\theta\theta}$ ) stresses around the vertical borehole at $r = 0.085$ m .....	50

Figure 3.6 Comparison between numerical and analytical model for variation of induced vertical ( $\sigma_{zz}$ ) and in-plane shear ( $\sigma_{r\theta}$ ) stresses around the vertical borehole at $r = 0.085$ m .....	51
Figure 3.7 Comparison between numerical and analytical model for variation of induced stresses along the radial direction $r$ , at $\theta = 0$ , for the vertical borehole .....	52
Figure 3.8 Comparison between numerical and analytical model for variation of induced in-plane shear stress along the radial direction $r$ , at $\theta = 0$ , for a vertical borehole .....	53
Figure 3.9 General stress state in the vicinity of an inclined borehole .....	54
Figure 3.10 Corresponding stresses for (a) and (b) plain strain problem and (c) for anti-plane strain problem.....	55
Figure 3.11 Demonstrating the method adopted for calculating induced stresses around a borehole due to pure far-field shear stresses, acting on a plane perpendicular to the borehole axis .....	56
Figure 3.12 Deformations associated with anti-plane strain boundary conditions.....	60
Figure 3.13 Comparison between numerical and analytical model for variation of induced radial ( $\sigma_{rr}$ ) and tangential ( $\sigma_{\theta\theta}$ ) stresses around the inclined borehole at $r = 0.085$ m .....	64
Figure 3.14 Comparison between numerical and analytical model for variation of induced vertical ( $\sigma_{zz}$ ) and in-plane shear ( $\sigma_{r\theta}$ ) stresses around the borehole at $r = 0.085$ m.....	65
Figure 3.15 Comparison between numerical and analytical model for variation of induced longitudinal shear stresses $\sigma_{rz}$ and $\sigma_{\theta z}$ , around the inclined borehole at $r = 0.085$ m .....	66
Figure 3.16 Comparison between numerical and analytical model for variation of induced stresses along the radial direction $r$ , at $\theta = 55.166^\circ$ , for the inclined borehole .....	69
Figure 3.17 A section of a borehole at the depth of 3000 m.....	71
Figure 3.18 Changes in longitudinal shear stresses around the borehole under the proposed boundary conditions .....	73

Figure 3.19	Changes in longitudinal shear stresses under the proposed boundary conditions, along the radial direction from the borehole wall .....	74
Figure 4.1	Compressive general stresses on a block of rock .....	77
Figure 4.2	Principal stresses on a block of rock .....	78
Figure 4.3	Failure surface in the principal stress space .....	81
Figure 4.4	Hydrostatic axis and the stress vector $\sigma$ in the principal stress space .....	82
Figure 4.5	Deviatoric and $\pi$ -plane .....	83
Figure 4.6	Cartesian coordinate system on the deviatoric plane .....	84
Figure 4.7	Polar components of point $P$ on the deviatoric Plane .....	86
Figure 4.8	Symmetry properties of a failure criterion on the deviatoric plane.....	88
Figure 4.9	Meridional plane ( $\xi - \rho$ coordinates) [after Ottosen and Ristimna(2005)] .....	90
Figure 4.10	Intersection of tensile and compressive meridians with the deviatoric plane.....	91
Figure 4.11	The cross section of the Hoek-Brown failure surface on the deviatoric plane.....	93
Figure 4.12	The Hoek-Brown criterion in the principal stress space .....	95
Figure 4.13	The cross section of the Hoek-Brown criterion on the deviatoric plane .....	97
Figure 4.14	The Pan-Hudson criterion in the principal stress space .....	98
Figure 4.15	The cross section of the Zhang-Zhu criterion on the deviatoric plane .....	101
Figure 4.16	The Zhan-Zhu criterion in the Principal stress space .....	102
Figure 4.17	The cross section of the generalised Priest criterion on the deviatoric plane.....	105
Figure 4.18	The generalised priest criterion in the principal stress space .....	106
Figure 4.19	The cross section of the simplified Priest criterion on the deviatoric plane for (a) $\sigma_3 = 10$ MPa, (b) $\sigma_3 = 100$ MPa.....	108
Figure 4.20	The Simplified Priest criterion in the principal stress space, for (a) $\sigma_3 = 10$ MPa $w = 0.211$ and (b) $\sigma_3 = 100$ MPa, $w = 2.99$ .....	109
Figure 4.21	Fitting quadratic functions to true-triaxial experimental data in $\sigma_1 - \sigma_2$ domain (continues) .....	113

Figure 4.22	Non-linear correlation coefficient between the failure stress ( $\sigma_1$ ) and the intermediate principal stress ( $\sigma_2$ ) versus the least principal stress ( $\sigma_3$ ).....	115
Figure 4.23	Actual values of the weighting factor $w$ versus values of the term $\mu\eta - \sigma_3\sigma_c$ .....	119
Figure 4.24	Difference between predicted and observed failure stresses.....	121
Figure 4.25	True-triaxial apparatus of the University of Adelaide [after Schwartzkopff et al.(2010)] .....	125
Figure 4.26	Block of Kanmantoo Blue stone and preparation of cubic specimens [after Dong et al., (2011)] .....	126
Figure 4.27	(a) The V-shaped failure mode and (b) the M-shaped failure mode [after Dong et al. (2011)] .....	128
Figure 4.28	Best fit line to conventional triaxial data for determining the Hoek-Brown constant parameter $m$ .....	130
Figure 4.29	$\sigma_1$ - $\sigma_2$ plots, demonstrating that all 3D failure criteria underestimate the strength of the rock specimen .....	131
Figure 4.30	Intrusion of the HDPE plastic layer into the rock specimen [after Dong et al (2011)].....	132
Figure 4.31	Best fit line to triaxial test data on cubic specimens for determining the empirical parameter $m$ .....	133
Figure 4.32	$\sigma_1$ - $\sigma_2$ plots, demonstrating the comparison of the selected three-dimensional failure criterion.....	134
Figure 5.1	Principal in situ stresses acting on a rock element at the borehole wall, with drilling fluid .....	145
Figure A.1	The numerical error of the observed field variable (in this case $u(x)$ ) can be minimized by increasing the discretisation resolution stepwise from (a) to (c). .....	158

Figure C.1	Linear correlation coefficient calculated by the means of Pearson linear correlation coefficient for the nine sets of true-triaxial data.....	173
Figure D.1	$\sigma_1$ vs. $\sigma_2$ Plots for KTB Amphibolite for different constant values of $\sigma_3$ .....	174
Figure D.2	$\sigma_1$ vs. $\sigma_2$ Plots for Westerly Granite for different constant values of $\sigma_3$ .....	176
Figure D.3	$\sigma_1$ vs. $\sigma_2$ Plots for Dunham Dolomite for different constant values of $\sigma_3$ .....	180
Figure D.4	$\sigma_1$ vs. $\sigma_2$ Plots for Solnhofen Limestone for different constant values of $\sigma_3$ .....	184
Figure D.5	$\sigma_1$ vs. $\sigma_2$ Plots for Yamaguchi Marble for different constant values of $\sigma_3$ .....	186
Figure D.6	$\sigma_1$ vs. $\sigma_2$ Plots for Mizuho Trachyte for different constant values of $\sigma_3$ .....	187
Figure D.7	$\sigma_1$ vs. $\sigma_2$ Plots for Manazuru Andesite for different constant values of $\sigma_3$ .....	189
Figure D.8	$\sigma_1$ vs. $\sigma_2$ Plots for Inada Granite for different constant values of $\sigma_3$ .....	191
Figure D.9	$\sigma_1$ vs. $\sigma_2$ Plots for Orikabe Monzonite for different constant values of $\sigma_3$ .....	194
Figure E.1	Normal distribution of failure prediction accuracy of selected failure criteria for Orikabe Monzonite.....	196
Figure E.2	Normal distribution of failure prediction accuracy of selected failure criteria for Inada Granite .....	196
Figure E.3	Normal distribution of failure prediction accuracy of selected failure criteria for Manazuru Andesite.....	197
Figure E.4	Normal distribution of failure prediction accuracy of selected failure criteria for Mizuho Trachyte .....	197
Figure E.5	Normal distribution of failure prediction accuracy of selected failure criteria for Yamaguchi Marble.....	198
Figure E.6	Normal distribution of failure prediction accuracy of selected failure criteria for Solnhofen Limestone.....	198
Figure E.7	Normal distribution of failure prediction accuracy of selected failure criteria for Dunham Dolomite .....	199
Figure E.8	Normal distribution of failure prediction accuracy of selected failure criteria for Westerly Granite.....	199
Figure E.9	Normal distribution of failure prediction accuracy of selected failure criteria for KTB Amphibolite.....	200

## Tables

Table 3.1 Determining the angular position of the two points of stress concentration.....	68
Table 4.1 Hoek-Brown and Coulomb parameters of the rock types studied.....	110
Table 4.2 Comparison of 3D Hoek-Brown based criteria .....	122
Table 4.3 True-triaxial experimental data of Kanmantoo Bluestone, The University of Adelaide (2011) .....	127
Table 4.4 Uniaxial compressive strength of cylindrical and cubic specimens of Kanmantoo bluestone. ....	128
Table 4.5 Conventional triaxial tests for determining the Hoek-Brown constant parameter $m$ .....	129
Table 4.6 Predicted values of failure stress by the means of each selected failure criteria for $m = 16.131$ and $\sigma_c = 147$ MPa.....	131
Table 4.7 Triaxial test data on cubic rock specimens for determination the empirical parameter $m$ .....	133
Table 4.8 Predicted values of failure stress by the means of each selected failure criteria for $m = 36.6$ and $\sigma_c = 190.3$ MPa.....	134
Table 4.9 Error analysis and quantitative comparison of selected 3D failure criteria.....	135
Table 5.1 Calculation of the failure stress for Granite and Marble .....	143
Table B.1 Error analysis of the finite element model in comparison with the analytical solution, for calculating the induced stresses around the vertical borehole (for a quarter-model).....	159
Table B.2 Error analysis of the finite element model in comparison with the analytical solution (the generalised Kirsch equations), for calculating the induced stresses around a deviated borehole (for a quarter-model) .....	160

Table B.3	Error analysis of the finite element analysis based on the proposed boundary conditions in comparison with the analytical solution (the generalised Kirsch's equations), for calculating the induced stresses around a deviated borehole (for a quarter-model).....	161
Table B.4	Error analysis of the finite element model in comparison with the analytical solution (the generalised Kirsch's equations), for calculating the induced stresses along the radial distance $r$ from the wall of a deviated borehole at $\theta = 55.166^\circ$ .....	162
Table B.5	Error analysis of the finite element analysis based on the proposed boundary conditions in comparison with the analytical solution (the generalised Kirsch's equations), for calculating the induced stresses along the radial distance $r$ from the wall of a deviated borehole at $\theta = 55.166^\circ$ .....	163
Table C.1	True-triaxial data of Solnhofen Limestone, Mogi (2007).....	164
Table C.2	True-triaxial data on Dunham Dolomite, Mogi (2007).....	165
Table C.3	True-triaxial data on Yamaguchi Marble, Mogi (2007) .....	166
Table C.4	True-triaxial test data on Mizuho Trachyte (Mogi, 2007) .....	167
Table C.5	True-triaxial test data on Orikabe Monzonite (Mogi, 2007).....	168
Table C.6	True-triaxial test data on Inada Granite (Mogi, 2007).....	169
Table C.7	True-triaxial test data on Manazuru Andesite (Mogi, 2007) .....	170
Table C.8	True-triaxial test data on KTB Amphibolite (Chang and Haimson, 2000).....	171
Table C.9	True-triaxial test data on Westerly Granite (Haimson and Chang, 2000).....	172

## Abstract

Underground rock formations are always under some stress, mostly due to overburden pressure and tectonic stresses. When a borehole is drilled, the rock material surrounding the hole must carry the load which was initially supported by the excavated rock. Therefore, due to the introduction of a borehole, the pre-existing stress state in the sub-surface rock mass is redistributed and a new stress state is induced in the vicinity of the borehole. This new stress state around the borehole can be determined directly by means of *in situ* measurements, or can be estimated by applying numerical methods or closed form solutions.

In this thesis borehole stability analysis is undertaken by means of the linear elasticity theory. The introduction of a borehole into a block of rock which behaves linearly elastic, leads to stress concentration near the hole. If the rock material around the borehole is strong enough to sustain the induced stress concentration, the borehole will remain stable; otherwise rock failure will occur at the borehole wall. Therefore, a key aspect in stability evaluation of a borehole is the assessment of rock response to mechanical loading.

For borehole stability evaluation in good quality brittle rock formations, which can be considered as isotropic, homogeneous and linearly elastic, stresses around the borehole are usually calculated using a closed form formulation known as the generalised Kirsch equations. These equations are the three-dimensional version of the original form of the well known Kirsch equations for calculating stresses around a circular hole in an isotropic, linearly elastic and homogeneous material. These equations have been widely used in the petroleum and mining industries over the past few decades. However, the boundary conditions on which these equations were based have been poorly explained in the literature and therefore merit further investigation.

In this thesis, in order to eliminate the ambiguity associated with the boundary conditions assumed for deriving the analytical model for stress analysis around the borehole, finite element analysis (FEA) was carried out to create a numerical counterpart of the current analytical solution. It appeared that the assumed boundary conditions for deriving the analytical model, i.e. the generalised Kirsch equations, are incompatible in the physical sense.

A new set of boundary conditions in better compliance with the physics of the problem was introduced in order to modify the analytical model, by reducing the simplifying assumptions made to facilitate the derivation of the closed form solution.

Another key parameter in borehole stability evaluation is the strength of the rock material at the borehole wall. The rock strength is usually evaluated using a failure criterion which is a mathematical formulation that specifies a set of stress components at which failure occurs. A number of different failure criteria have been introduced in the literature to describe brittle rock failure among which the Coulomb and the Hoek-Brown criteria have been widely used in industry; however, they both have limitations. For instance, both the Coulomb and the Hoek-Brown criteria identify the rock strength only in terms of maximum and minimum principal stresses and do not account for the influence of the intermediate principal stress on failure. On the other hand, at the borehole wall where a general stress state ( $\sigma_1 > \sigma_2 > \sigma_3$ ) is encountered, a failure criterion which neglects the influence of the intermediate principal stress on failure seems to be inadequate for rock strength estimation in the borehole proximity.

Although a number of three-dimensional failure criteria have been proposed over the past decades, none of them has been universally accepted. A major limitation in studying the three-dimensional rock failure criteria is the lack of adequate true-triaxial experimental data that can be used for validation of theoretical rock failure models. A number of true-triaxial tests were carried out at the University of Adelaide and the results, along with nine sets of published true-triaxial experimental data, were utilised for comparison and validation of five selected failure criteria. These failure criteria have been developed especially for rock material and include; the Hoek-Brown, the Pan-Hudson, the Zhang-Zhu, the Generalised Priest and the Simplified Priest. A new three-dimensional failure criterion was also developed by modifying the simplified Priest criterion and was identified as a three-dimensional model which best describes the rock failure in three-dimensional stress state, compared to other selected criteria.

In this thesis, a case example is presented where the borehole instability is predicted by comparing the induced major principal stress at the borehole wall to the predicted rock failure stress. The major in situ principal stress around the borehole is calculated by means of the FEA based on the assumption of a new set of boundary conditions. The rock failure stress

under the three-dimensional stress state at the borehole wall is calculated by means of the newly proposed three-dimensional failure criterion.

## **Statement of Originality**

This work contains no material which has been accepted for the award of any other degree or diploma in any University or other tertiary institution and, to the best of my knowledge and belief no material previously published or written by any other person, except where due reference has been made in the text.

I give consent to this copy of my thesis, when deposited in the University Library, being made available for loan and photocopying, subject to the provisions of the Copyright Act 1968.

I also give permission for the digital version of my thesis to be made available on the web, via the University's digital research repository, the Library catalogue, and also through web search engines, unless permission has been granted by the University to restrict access for a period of time.

SIGNED:..... DATE:.....

## Acknowledgements

The work described in this thesis was carried out in the School of Civil, Environmental and Mining Engineering at the University of Adelaide during the period 2010 to 2012. The candidate was supervised for the first one and a half years by Professor Stephen D. Priest and Dr. Nouné S. Melkounian and, after Professor Priest retired, by Dr. Nouné S. Melkounian and Associate Professor Mark B. Jaksa. The author is indebted to Professor Stephen D. Priest for providing the opportunity for this research to be carried out and for seeing it to fruition. Much appreciation is also shown to Dr. Nouné S. Melkounian and Assoc. Prof. Mark B. Jaksa for being generous with their advice, assistance and guidance. The author is grateful for the discussions with Assoc. Prof. Hamid Sheikh and for his technical advice on finite element analysis presented in Chapter 3 of this thesis.

The author wishes to acknowledge the support of the Deep Exploration Technologies CRC for partially funding the true-triaxial test and the ABAQUS licenses used in this research. No amount of thanks would be enough to give to the technical staff in the School of Civil, Environmental and Mining Engineering at the University of Adelaide, for without their assistance and encouragement conducting the true-triaxial tests would have been impossible. In particular the author would like to give special mention to:

- Mr. David Hale, the manager of technical operations, for providing invaluable comments and advice for true-triaxial experiments.
- Mr. Adam Ryntje for preparation of rock specimens for true-triaxial tests and for his assistance in operating the true-triaxial apparatus.
- Mr. Ian Cates for supervising the laboratory instrumentation and running the data acquisition system and for his assistance in collecting the true-triaxial test data.
- Dr. Stephen Carr for his help in running ABAQUS models associated with the finite element analysis presented in Chapter 3.

I wish to express my appreciation to my mother and my wife for without their financial and mental supports conducting this research would be impossible.

# **CHAPTER 1**

## **Introduction**

	<b>Page</b>
<b>1.1. Introduction</b>	<b>1</b>
<b>1.2. Aims of the study</b>	<b>4</b>
<b>1.3. Research method</b>	<b>6</b>
<b>1.4. Organisation of the thesis</b>	<b>8</b>

## 1.1. Introduction

Borehole stability problems have been encountered for as long as wells have been drilled. Several new challenges have appeared in recent years, however, making the stability issue more difficult to handle, and also more important to solve. For example, there has been an increasing demand from the petroleum industry for more sophisticated well trajectories. Highly deviated, multilateral and horizontal wells are attractive to the petroleum industry, since a single production platform supporting a sophisticated well can drain a larger area, reducing the number of platforms required to produce a given field (Fjær et al., 2008). Stable drilling is however normally more difficult in deviated than in vertical boreholes. Other situations where borehole stability problems may be expected to occur are during infill drilling in depleted reservoirs, when drilling in tectonically active areas, and in deep and geologically complex surroundings (Zoback, 2007).

A borehole stability problem is an example of what drillers refer to as a “tight hole” or “stuck pipe” incident. There are many possible reasons for drilling rigs to become stuck, but in the majority of field cases reported, the fundamental reason is the mechanical collapse of the borehole wall (Bol et al., 1994, Gazaniol et al., 1994). Moreover, the mechanical collapse of the borehole wall is often combined with a lack of down-hole cleaning ability. Such stability problems typically amount to 5%–10% of drilling costs in exploration and production, in terms of time lost and sometimes loss of equipment. These numbers imply a worldwide cost to the petroleum industry of hundreds of millions of dollars per year (Fjær et al., 2008).

Underground formations are always under some stress, mostly due to overburden pressure and tectonic stresses. When a borehole is drilled the rock material surrounding the hole must carry the load which was initially supported by the excavated rock. Therefore, the pre-existing stress state in the sub-surface rock mass is redistributed and a new stress state is induced in the borehole proximity. This new stress state around the borehole can be determined directly by applying in situ measurements, numerical methods or closed form solutions. The introduction of a borehole into a block of rock which can be considered as linearly elastic, leads to stress concentration near the hole. If the rock material around the borehole is strong enough to

sustain the induced stress concentration the borehole will remain stable. On the other hand, if the stresses around the borehole exceed the strength of the surrounding rock, failure will eventually occur and a fractured zone will develop around the hole. If the fractured zone is too extensive either the design of the excavation must be modified or the excavation must be supported appropriately.

A key aspect in the stability evaluation of a borehole, therefore, is the assessment of the rock response to mechanical loading. Ideally a technical model should account for all factors which could affect stability, such as well pressure, temperature, time and mud chemistry; however, such a model is currently unavailable. The focus of the current study will be on the effect of rock response to mechanical loading on borehole stability

For borehole stability evaluation in good quality brittle rock formations, which can be treated as isotropic, homogeneous and linearly elastic, a two-step analysis is suggested, which consists of:

1. Calculating the stresses around the borehole using the linear elastic theory.
2. Assessing the strength of the rock material surrounding the borehole under the induced stress state due to drilling the borehole.

**Calculating stresses:** When a borehole is drilled into an ideal rock block (isotropic, linearly elastic and homogeneous) stresses around the borehole are usually calculated using a closed form formulation known as the generalised Kirsch equations. These equations are a three-dimensional version of the original form of the Kirsch equations (1898) for calculating stresses around a circular hole in an isotropic, linearly elastic and homogeneous material. The three-dimensional version of Kirsch equations can be found in a report by Fairhurst (1968). These equations have been widely used in the petroleum and mining industries over the past few decades. However, the boundary conditions on which these equations were based have been poorly explained in the literature and therefore merit further investigation.

**Assessing rock strength:** Another key parameter in borehole stability evaluation is the strength of the rock material at the borehole wall. The rock strength is usually formulated as a failure criterion, which is a mathematical formulation that specifies a set of stress components

at which failure occurs. A number of different criteria have been introduced in the literature to describe brittle rock failure, among which the Coulomb, introduced in 1773, and the Hoek-Brown (1980) criteria have been widely used in industry; however, each has some limitations. For instance, both the Coulomb and the Hoek-Brown criteria identify the rock strength only in terms of maximum and minimum principal stresses and do not account for the influence of the intermediate principal stress on failure. On the other hand, at the borehole wall where a general stress state ( $\sigma_1 > \sigma_2 > \sigma_3$ ) is encountered, a failure criterion which neglects the influence of the intermediate principal stress on failure seems to be inadequate to rock strength estimation in the borehole proximity.

Nevertheless, currently in the petroleum industry, estimation of rock strength around the borehole is mostly undertaken by applying either the Coulomb criterion, or the Drucker-Prager criterion (1952), which is a three-dimensional failure criterion and incorporates the influence of the intermediate principal stress. However, the Drucker-Prager criterion was initially developed for soil. The results of true-triaxial rock testing show that this criterion is unable to accurately predict rock strength under a three-dimensional stress state when compared with the three-dimensional criteria which have been developed especially for rock material (Colmenares and Zoback, 2002). It is desirable, therefore, to use a three-dimensional failure criterion specifically designed for rock material to predict rock strength.

Although a number of three-dimensional rock failure criteria have been proposed over the past few decades, none has been universally accepted. A major limitation for studying three-dimensional rock failure criteria is inadequate true-triaxial test data on rock specimens and as pointed out by Mogi (2007) the few published results of true-triaxial tests have been interpreted more as interesting curiosities, rather than serious challenges to the accepted Mohr-type criteria. Therefore, three-dimensional rock failure criteria require further investigation, incorporating more comprehensive true-triaxial experimentation.

After calculating the induced stresses around the borehole and predicting the failure stress using an appropriate rock failure criterion, which best describes the rock behaviour -under a three-dimensional stress state-, the possibility of the failure of the rock at the borehole wall can be estimated. It is worthwhile emphasising that in this study borehole stability analysis is

undertaken by means of the linear elasticity theory. Therefore, strength evaluation of intact brittle rock material, which can be assumed to be continuum, homogeneous, isotropic and linearly elastic (CHILE), is of interest in this study. The portion of inelastic behaviour, in stress-strain plots, before failure, is small in brittle rocks and an abrupt failure occurs shortly after the elastic limit or the yield stress,  $\sigma_y$  is reached (Fig. 1.1). Therefore, since yield and failure for brittle materials are approximately the same, it is theoretically rational to compare the value of the maximum induced stress at the borehole wall estimated by means of linear elasticity theory to the failure stress of the brittle rock material. It also merits mentioning that in the case of ductile materials since the failure stress is significantly greater than the elastic limit, linear elastic analysis is a conservative model for predicting borehole failure. Furthermore, failure progression as the accumulation of damage and non-linearly elastic behaviour of rock is beyond the scope of this study.

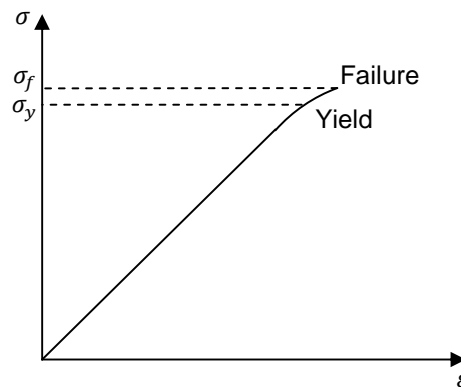


Figure 1.1 Failure ( $\sigma_f$ ) and yield ( $\sigma_y$ ) stresses for brittle materials

## 1.2. Aims of the Study

Boundary conditions based on which stresses around the borehole were formulated, in the generalised Kirsch equations, have been poorly explained in the existing literature and need to be studied in further detail. It is important to remember that some simplifying assumptions were made about the constitutive behaviour of the rock material to rationalise the application of the Kirsch equations for rock material. In other words the rock material is assumed to be a continuum, homogeneous, isotropic and linear elastic material. Even for the linear elastic

constitutive behaviour solving a general three-dimensional problem may be impossible. Therefore, boundary conditions are defined, considering the physics of the problem, in a way to facilitate the derivation of an analytical model. However, the boundary conditions assumed in the current analytical model do not seem to be in compliance with the physics of the real problem and need modifications.

On the other hand, since the rock material at the borehole wall is subjected to a three-dimensional stress state ( $\sigma_{\theta\theta} > \sigma_{zz} > \sigma_{rr}$ ), a two-dimensional failure criterion such as the Coulomb or the Hoek-Brown is inadequate for estimating rock strength in the borehole proximity. Therefore, in order to predict the rock failure at the borehole wall, three-dimensional rock failure criteria need to be given further consideration.

Aims of this thesis are outlined as follows:

- Providing a clear explanation to eliminate the ambiguity about the boundary conditions assumed for deriving the current analytical model, i.e. the generalised Kirsch equations.
- Modification of the current analytical model by introducing a new set of boundary conditions, which reflects the physics of the problem more realistically.
- Theoretically investigating a number of selected three-dimensional rock failure criteria through conceptual studies on failure theory.
- Development and introduction of a new three-dimensional rock failure criterion.
- Conducting true-triaxial experiments to validate and compare the existing and the newly proposed rock failure criteria against the true-triaxial experimental data.
- Demonstration of the linkage between techniques of the stress analysis in the borehole proximity and the strength estimation of rock material adjacent to the borehole wall through a case study, by predicting instability of a deviated borehole and calculating the minimum and maximum allowable mud weight to safely drilling the deviated borehole.

### 1.3. Research Method

In order to evaluate the stability of deep boreholes a stepwise analysis is adopted. This stepwise analysis is depicted in the flow chart in Fig. 1.2 and the aims of this research in the frame of this analysis are subsequently discussed.

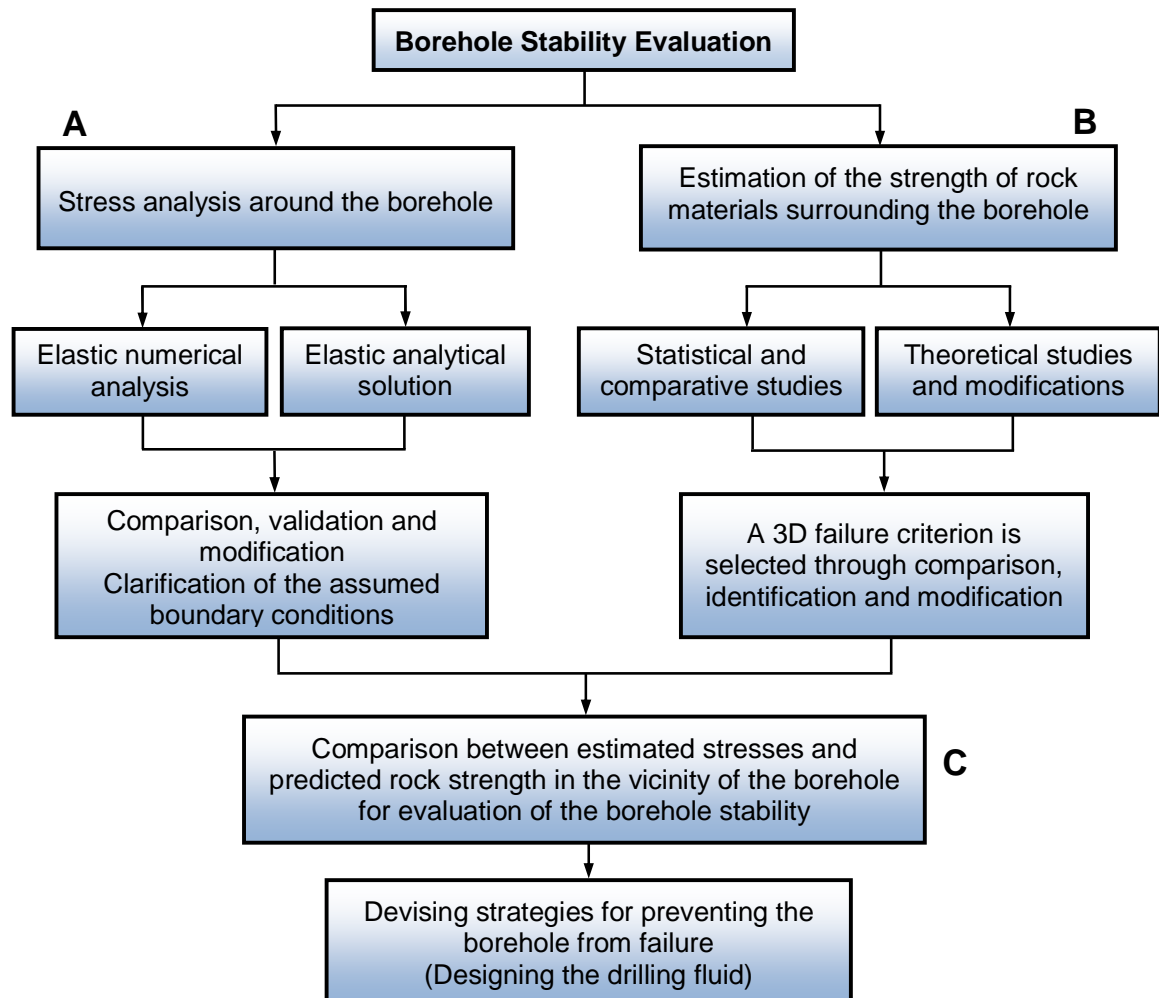


Figure 1.2 Demonstration of different phases in the stepwise research method adopted in this study

**Step A** Linear elastic stress analysis is carried out to estimate the induced stresses around the borehole by means of numerical and analytical models. Results of the numerical and analytical models are cross-evaluated to investigate the boundary conditions assumed in formulating the

generalised Kirsch equations as an elastic analytical solution. Finite element analysis is also carried out to calculate the induced stresses around the borehole based on newly proposed boundary conditions, which more accurately represent the problem in the physical sense. The current analytical solution will then be modified based on the finite element analysis, incorporating the proposed boundary conditions.

**Step B** Five failure criteria, especially developed for rock material, are selected and theoretically studied based on the fundamentals of the failure theory. A new three-dimensional failure criterion is also developed by modifying the simplified Priest criterion. True-triaxial tests are conducted and the results of the experiments along with nine sets of published true-triaxial test data are applied to validate and compare the three-dimensional rock failure criteria against the experimental data. As a result one failure criterion from among the five selected criteria is identified as the best three-dimensional model for predicting the rock failure in three-dimensional stress state.

**Step C** Following the stepwise analysis, the instability of a deviated borehole is predicted in a case study. For this purpose, the maximum in situ stress induced around the borehole is compared to the predicted failure stress of the rock material surrounding the borehole to predict the initiation of failure at the borehole wall. In addition, to maintain safe drilling of an inclined borehole and to prevent the rock material at the borehole wall from compressive and tensile (hydro fracturing) failure, the minimum and maximum allowable mud weight are determined

Examination of the influence of all factors affecting borehole stability, such as time, temperature and mud chemistry, is beyond the scope of this research. Furthermore, since the focus of this research is on borehole stability in good quality brittle rock material or rock masses, for which the elastic solution is still valid (Brady and Brown, 1993), the failure is assumed to take place when the elastic limit is reached. The progression of failure due to the accumulation of micro-cracks and also post failure behaviour of rock are beyond the scope of this thesis.

## 1.4. Organisation of the Thesis

This thesis is made up of two main sections consisting of six chapters overall, including this introduction and the conclusion in Chapter 6. The first section, presented in Chapter 3, discusses elastic stress analysis around vertical and deviated boreholes by means of analytical and numerical approaches. The second section in Chapter 4 discusses procedures for determining the failure stress of rock in the three-dimensional stress state.

The elastic analytical solution for estimating stresses around a borehole, which has been drilled in an isotropic, homogeneous and linearly elastic rock was developed in 1962 by Hiramatsu and Oka, and has been widely used in industry ever since. The applications of the existing elastic analytical solution, which is also known as the generalised Kirsch equations, are outlined in Chapter 2. Moreover, the current techniques for evaluating the strength of rock material in a three-dimensional stress state have evolved over the past few decades. In Chapter 2 the evolution and shortcomings of each of these methods are discussed.

Finite element analysis was carried out to create a numerical counterpart to the current analytical solution for stress analysis around a borehole, aiming to eliminate the ambiguity associated with the boundary conditions assumed for deriving the current analytical model. The detailed procedure of the numerical analysis and the results of the cross-evaluation of the analytical and the numerical models are presented in Chapter 3. Furthermore, a new set of boundary conditions with respect to the physics of the problem is introduced in Chapter 3. The number of simplifying assumptions is reduced and the current analytical model is modified to bring it closer to reality. The analytical and numerical models are compared quantitatively in Appendix B.

Current failure models, which have been especially developed for predicting rock failure in a three-dimensional stress state, are discussed in detail in Chapter 4. A new three-dimensional failure criterion is also proposed in Chapter 4, by modifying the simplified Priest criterion introduced by Priest (2005). In order to compare and validate the three-dimensional rock failure criteria, a number of true-triaxial tests were carried out at the University of Adelaide. Furthermore, nine sets of published true-triaxial test data are applied to evaluate the accuracy

of the newly proposed rock failure criterion, in comparison with other existing three-dimensional failure models. True-triaxial data sets used in this study are given in Appendix C. In addition, an illustrative comparison between three-dimensional rock failure criteria and the experimental data is given in Appendix D by plotting the major principal stress versus the intermediate principal stress at failure.

Chapter 5 presents a case study in which the borehole instability is predicted by comparing the induced major principal stress at the borehole wall to the predicted rock failure stress. The major in situ principal stress around the borehole is calculated by means of finite element analysis, based on the assumption of a new set of boundary conditions. The rock failure stress under a three-dimensional stress state at the borehole wall is calculated by means of the proposed three-dimensional rock failure criterion. These techniques are also applied in Chapter 5 to calculate the minimum and maximum allowable mud weight for safely drilling a deviated borehole. Chapter 6 presents conclusions and recommendations for future studies.

# **CHAPTER 2**

## **Literature review**

	<b>Page</b>
<b>2.1. Introduction</b>	<b>10</b>
<b>2.2. In situ stresses before the introduction of the borehole</b>	<b>10</b>
<b>2.3. Stress Analysis around the Borehole</b>	<b>12</b>
<b>2.4. Strength analysis of intact rock</b>	<b>16</b>

## 2.1. Introduction

Underground formations are inherently subjected to a stress field, mainly due to the weight of the overburden geo-materials and tectonic activities. Due to the introduction of a borehole to the underground formations, the pre-existing stress field is redistributed which leads to stress concentration at the borehole wall. The stability of the borehole depends upon whether the formation surrounding the borehole fails or remains stable under the new induced stress field. The answer to this question is of paramount importance for the stability evaluation of a borehole.

Considering a borehole which has been drilled in a good quality rock mass, the following information is required in order to evaluate the stability of the borehole:

- estimation or measurement of the pre-existing in situ stress field
- an accurate estimation of the induced in situ stresses in the borehole proximity
- an accurate estimation of the strength of the rock surrounding the borehole

## 2.2. In situ Stresses Prior to the Introduction of the Borehole

It is important to have an accurate estimation of the pre-existing state of stress in the subsurface formations before a borehole is drilled since the stress boundary conditions for modelling and estimating induced stresses around the borehole are determined based on the pristine state of the in situ stress field. In general, the pre-existing stress state is a function of depth; however, the manner in which the three principal stresses and their associated directions vary with depth does not always follow a predictable pattern (Amadei and Stephansson, 1997). These stresses will be influenced by topography, tectonic forces, constitutive behaviour of the rock material and by the local geological history.

At any given depth below the Earth's surface the stress state can be described by three components; a vertical component,  $\sigma_v$ , due to the weight of the over lying rock at the depth  $Z$ , equal to  $\gamma Z$ , where  $\gamma$  is the average unit weight of the rock (e.g. in  $\text{KN/m}^3$ ); and two horizontal

components such as  $\sigma_H$ , the major, and  $\sigma_h$ , the minor horizontal stresses. A key assumption here is that these stresses are principal stresses, i.e. no shear stresses exist.

Many expressions for the variations of the magnitude of the vertical and horizontal in situ stresses with depth, at specific sites or for different regions of the world, have been introduced in the literature. Examples of stress profiles and stress variations are given by Brown and Hoek (1978), Haimson and Lee (1980), Zoback and Zoback (1980), Zoback and Healy (1992), Lim and Lee (1995) and Jaeger et al. (2007). However, detailed investigation of models and expressions for estimating stress variations and stress profiles is beyond the scope of this research.

It is important to note that, to date, no rigorous methods are available for accurately predicting the in situ stresses. Furthermore, the process of estimating in situ stresses should not be considered as a substitute for their measurement (Amadei and Stephansson, 1997). Various techniques for rock stress measurement were comprehensively explained by Amadei and Stephansson (1997) such as (a) hydraulic methods including: hydraulic fracturing (Fairhurst, 1964), sleeve fracturing (Stephansson, 1983), Hydraulic Test on Pre-existing Fracture (HTPF) (Cornet, 1986); (b) relief methods including: surface relief methods, borehole relief methods and relief of large rock volumes; (c) jacking methods; (d) strain recovery methods and (e) borehole breakout methods.

It merits noting that stress in rock masses cannot be measured directly and methods for measuring in situ stresses basically consist of disturbing the rock and analysing the response of the rock associated with the disturbance. This analysis is often undertaken based on assumptions about the constitutive behaviour of rock, which relates the rock strains to applied stresses. However, it is important to remember that due to the complex nature of rocks and rock masses, constitutive modelling of rock behaviour is not usually a straightforward matter. As pointed out by Amadei and Stephansson (1997), in good to very good rock conditions, where the rock is essentially linearly elastic, homogeneous and continuous, and between well-defined geological boundaries, rock stresses can be determined with an error of  $\pm 10\% - 20\%$  for their magnitude and an error of  $\pm 10\% - 20\%$  for their orientation. On the other hand, in poor quality rocks, i.e. weathered, weak, soft and heavily fractured, the measurement of rock

stresses is extremely difficult. In such cases the success rate of stress measurements is usually low.

### 2.3. Stress Analysis around the Borehole

The stress distribution around a circular hole in an infinite plate in one-dimensional tension was published by Kirsch (1898). Kirsch equations can also be generalised to calculate stresses around vertical and deviated boreholes with anisotropic far-field stresses. The general form of the Kirsch equations can be given by calculating the induced stresses around a deviated borehole around which there exists a general stress state.

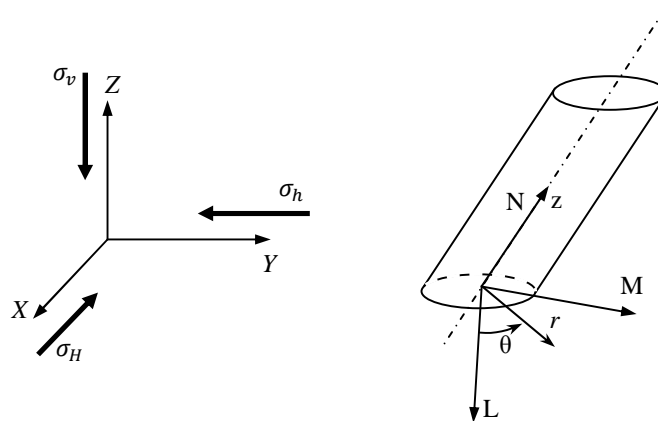


Figure 2.1 Coordinate system for a deviated borehole [after Fjær et al. (2008)]

If in situ stresses in a formation are principal stresses with respect to a defined Cartesian coordinate system, as illustrated in Fig. 2.1, the general stress state which is induced around an inclined borehole can be given by transforming the in situ principal stress components into a local Cartesian coordinate system. This local coordinate system is defined by transforming the global coordinate system in such a way that the  $Z$ -axis coincides with the axis of the inclined borehole. A transform from  $(X, Y, Z)$  to  $(L, M, N)$  can be obtained in two operations; a rotation  $\alpha$  around the  $Z$ -axis and a rotation  $\beta$  around the  $Y$ -axis, in a manner that the  $Z$ -axis coincides with the  $N$ -axis, as shown in Fig. 2.1. Such rotations can be undertaken by calculating the direction cosines between the axes in the  $X, Y, Z$  coordinates and the corresponding axes in  $L, M, N$  coordinates (Fig. 2.1) and by applying the following relationship:

$$\begin{bmatrix} L \\ M \\ N \end{bmatrix} = \begin{bmatrix} l_{XL} & l_{XM} & l_{XN} \\ l_{YL} & l_{YM} & l_{YN} \\ l_{ZL} & l_{ZM} & l_{ZN} \end{bmatrix} \begin{bmatrix} X \\ Y \\ Z \end{bmatrix} \quad (2.3.1)$$

Where direction cosines,  $l_{ij}$  in Eq.2.3.1, and consequently the rotation matrix  $[R]$ , are defined as follows:

$$[R] = \begin{bmatrix} l_{XL} & l_{XM} & l_{XN} \\ l_{YL} & l_{YM} & l_{YN} \\ l_{ZL} & l_{ZM} & l_{ZN} \end{bmatrix} = \begin{bmatrix} \cos \alpha \cos \beta & \sin \alpha \cos \beta & -\sin \beta \\ -\sin \alpha & \cos \alpha & 0 \\ \cos \alpha \sin \beta & \sin \alpha \sin \beta & \cos \beta \end{bmatrix} \quad (2.3.2)$$

Accordingly, the general stress state can be expressed by a general stress tensor which results from transforming the principal stress tensor from the global coordinate system  $(X, Y, Z)$  into the local coordinate system  $(L, M, N)$  in the following manner:

$$\begin{bmatrix} \sigma_{xx} & \sigma_{xy} & \sigma_{xz} \\ \sigma_{yx} & \sigma_{yy} & \sigma_{yz} \\ \sigma_{zx} & \sigma_{zy} & \sigma_{zz} \end{bmatrix} = [R] \begin{bmatrix} \sigma_H & 0 & 0 \\ 0 & \sigma_h & 0 \\ 0 & 0 & \sigma_v \end{bmatrix} [R]^T \quad (2.3.3)$$

Where  $[R]$  is the rotation matrix, given by Eq.2.3.2, and  $[R]^T$  is the transpose of the rotation matrix. Furthermore, components  $\sigma_H$  and  $\sigma_h$ , in Eq.2.3.3, represent in situ maximum and minimum horizontal stresses, respectively, and the component  $\sigma_v$  is the vertical stress due to the weight of the over lying geo-materials.

It is important to note that the general stress tensor in Eq. 2.3.3 represents the pristine stress state, before the introduction of the borehole. Defining a cylindrical coordinate system by measuring the angle  $\theta$  counter-clockwise from the  $L$ -axis and the radial distance  $r$  from the centre of the borehole, as illustrated in Fig. 2.1, the induced stresses around the borehole as a result of redistribution of the virgin stress field due to the influence of the borehole, can be given by the following stress tensor:

$$[\sigma_{ij}] = \begin{bmatrix} \sigma_{rr} & \sigma_{r\theta} & \sigma_{rz} \\ \sigma_{r\theta} & \sigma_{\theta\theta} & \sigma_{\theta z} \\ \sigma_{rz} & \sigma_{\theta z} & \sigma_{zz} \end{bmatrix} \quad (2.3.4)$$

For an unsupported borehole of radius  $a$ , components of the stress tensor in Eq. 2.3.4 are given by a three-dimensional version of Kirsch equations, which can also be referred to as the generalised Kirsch equations as follows:

$$\begin{aligned}
\sigma_{rr} &= \frac{\sigma_x + \sigma_y}{2} \left(1 - \frac{a^2}{r^2}\right) + \frac{\sigma_x - \sigma_y}{2} \left(1 + \frac{3a^4}{r^4} - \frac{4a^2}{r^2}\right) \cos 2\theta + \sigma_{xy} \left(1 + \frac{3a^4}{r^4} - \frac{4a^2}{r^2}\right) \sin 2\theta \\
\sigma_{\theta\theta} &= \frac{\sigma_x + \sigma_y}{2} \left(1 + \frac{a^2}{r^2}\right) - \frac{\sigma_x - \sigma_y}{2} \left(1 + \frac{3a^4}{r^4}\right) \cos 2\theta - \sigma_{xy} \left(1 + \frac{3a^4}{r^4}\right) \sin 2\theta \\
\sigma_{zz} &= \sigma_z - 2\nu(\sigma_x - \sigma_y) \left(\frac{a^2}{r^2}\right) \cos 2\theta - 4\nu\sigma_{xy} \frac{a^2}{r^2} \sin 2\theta \\
\sigma_{r\theta} &= \left(-\frac{\sigma_x - \sigma_y}{2} \sin 2\theta + \sigma_{xy} \cos 2\theta\right) \left(1 - \frac{3a^4}{r^4} + \frac{2a^2}{r^2}\right) \\
\sigma_{\theta z} &= (\sigma_{yz} \cos \theta - \sigma_{xz} \sin \theta) \left(1 + \frac{a^2}{r^2}\right) \\
\sigma_{rz} &= (\sigma_{yz} \sin \theta + \sigma_{xz} \cos \theta) \left(1 - \frac{a^2}{r^2}\right)
\end{aligned} \tag{2.3.5}$$

A detailed description of the derivation of Eqs.2.3.5 was provided by Bradley (1979), who referred to a report by Fairhurst (1968). However, as was also reported by Peska and Zoback (1995), the generalised Kirsch equations were first published by Hiramatsu and Oka (1962). It is important to note that there exists a sign error in the expression of  $\sigma_{r\theta}$  (Eqs. 2.3.5) in Bradley's paper, as was also reported by Fjær et al. (2008). This error can be observed elsewhere in the literature, for instance in the first edition of the "Petroleum Related Rock Mechanics" (Fjær et al., 1992), and several other works. However, correct expressions of these equations are given by Fairhurst (1968) and Hiramatsu and Oka (1968).

Eqs. 2.3.5 are used in linear elastic analysis of borehole stability for calculating the induced stresses around an unsupported borehole, which has been drilled into nonporous materials. Due to the superposition principle, pore pressure effects may simply be added. The borehole

influence is given by terms in  $r^{-2}$  and  $r^{-4}$ , which vanishes rapidly with increasing  $r$ . The solutions depend also on the angle  $\theta$  (Fig. 2.1) indicating that the stresses vary with position around the borehole. Generally the shear stresses are non-zero. Thus,  $\sigma_{rr}$ ,  $\sigma_{\theta\theta}$  and  $\sigma_{zz}$  are not principal stresses for arbitrary orientations of the borehole. At the borehole wall, Eqs. 2.3.5 are reduced to:

$$\sigma_{rr} = 0$$

$$\sigma_{\theta\theta} = (\sigma_x + \sigma_y) - 2(\sigma_x - \sigma_y)\cos 2\theta - 4\sigma_{xy}\sin 2\theta$$

$$\sigma_{zz} = \sigma_z - 2\nu(\sigma_x - \sigma_y)\cos 2\theta - 4\nu\sigma_{xy}\sin 2\theta$$

$$\sigma_{r\theta} = 0$$

$$\sigma_{\theta z} = 2(\sigma_{yz}\cos\theta - \sigma_{xz}\sin\theta)$$

$$\sigma_{rz} = 0 \tag{2.3.6}$$

According to Jaeger et al. (2007) and Fjær et al. (2008), Eqs. 2.3.5 were derived based on the assumption of plain strain normal to the borehole axis. However, as explained by Fairhurst (1968), the general stress problem was divided into two separate problems; a plane strain problem for calculating induced stresses around the borehole by considering only far-field normal and in-plane shear stresses and an anti-plane strain problem for estimating the influence of far-field, out-of-plane shear stresses on the induced stresses around the borehole. In the plane strain problem it is assumed that there exists no displacement along the borehole axis and all displacements or deformations occur in planes perpendicular to the axis of the borehole. On the other hand, in the anti-plane strain problem the only deformation is assumed to be a constant deformation along the borehole axis.

Although the generalised Kirsch equations, given by Eqs. 2.3.5, have been presented in several works in the literature, the boundary conditions assumed for deriving this analytical elastic solution have been poorly explained. Thus, to eliminate the existing ambiguity about the boundary conditions assumed for deriving the generalised Kirsch equations necessitates a

detailed investigation of the simplifying assumptions made in defining the associated boundary conditions.

After calculating the components of the induced stress state in the borehole proximity (Eqs. 2.3.4), in order to evaluate the stability of the borehole, it is essential to develop accurate knowledge of the strength of the rock material surrounding the borehole wall. If the rock material at the borehole wall is strong enough to tolerate the induced stresses, rock failure does not initiate; otherwise the rock will fail. The rock failure stress under a given state of stress can be predicted by means of a mathematical model, which sources its input parameters from the rock material characteristics. Since the borehole stability analysis in this study is carried out by means of linear elastic solutions, either numerically or analytically, the strength of intact rock under the three-dimensional stress state around the borehole is the focal point of interest in rock strength analysis. Intact rock refers to the non-fractured blocks which occur between structural discontinuities in a typical rock mass. Failure of intact rock can be classified as brittle which implies a sudden reduction in strength when a limiting stress level is exceeded (Hoek, 1983).

## **2.4. Strength Analysis of Intact Rock**

The maximum stress that can be sustained by rock material under a given set of conditions is usually referred to as failure stress, which can also be interpreted as a measure of rock strength. If the induced stresses in the proximity of an excavation exceed the failure stress of the rock material or rock mass, failure occurs and the excavation may not be able to fulfil the function for which it was excavated. Hence, failure stress is a key parameter in the design of underground excavations (Hoek and Brown, 1980) and needs to be estimated as accurately as possible. Therefore, the experiments for conducting studies on rock deformation and rock strength must be designed to simulate the natural conditions as closely as possible (Mogi, 1966). Moreover, numerous empirical and hypothetical models have been introduced for the estimation, or rather prediction, of rock strength. Empirical criteria have been formulated predominantly based on laboratory experiments on rock specimens under the stress conditions simulating those encountered in situ. Hypothetical failure criteria are also dependent upon

laboratory tests to source the relevant input parameters such as rock material constants which are characteristic of a particular rock type.

Conventional experiments used for the study of the mechanical characteristics of rocks are triaxial tests, in which cylindrical rock specimens are subjected to uniform lateral, confining pressure ( $\sigma_2 = \sigma_3$ ) and an axial stress  $\sigma_1$ . Conventional triaxial tests have been widely used because of the equipment simplicity and convenient specimen preparation and testing procedures. However, such tests allow to simulate a special case only where the intermediate and the minor principal stresses,  $\sigma_2$  and  $\sigma_3$ , are equal. To simulate a general stress state, for example at the borehole wall ( $\sigma_{\theta\theta} > \sigma_{zz} > \sigma_{rr}$ ), more complex equipment and sophisticated testing procedures are needed. A true-triaxial apparatus, which enables to apply three independent stresses on a prismatic or cubic rock specimen, can be employed to simulate the in situ, general stress state. However, due to equipment complexity, complicated testing procedures and difficulties in specimen preparation, a limited number of true-triaxial experiments have been conducted so far. According to Mogi (1971b) a common difficulty in true-triaxial rock testing is to achieve three different yet uniform stresses. Non-uniform stresses can introduce substantial errors into the calculations of failure stresses done according to the elasticity theory using a linear stress-strain relationship.

A model used for the prediction of rock strength is usually expressed as a failure criterion which is a mathematical formulation of the stress components governing the occurrence of failure. A number of predictive models have been introduced in the literature to describe brittle rock failure, among which the Coulomb (1773), which is a hypothetical failure model, and the Hoek-Brown (1980) which is an empirical failure model, have been widely accepted and applied by rock mechanics practitioners and scientists. The Coulomb and the Hoek-Brown criteria formulate rock failure under a special stress condition, in which the intermediate and the minor principal stresses are equal ( $\sigma_1 > \sigma_2 = \sigma_3$ ). These criteria do not take into account the influence of the intermediate principal stress,  $\sigma_2$  on rock strength as it grows beyond the minor principal stress,  $\sigma_3$ .

***Coulomb criterion***

The Coulomb criterion was introduced by Coulomb in 1773, who suggested that rock failure in compression occurs when the value of the shear stress on a hypothetical plane is sufficient to overcome the natural cohesion of the rock and also the frictional force that opposes motion along the hypothetical failure plane. The Coulomb criterion gives the shear stress at failure as:

$$\tau = c + \sigma_n \tan \varphi \quad (2.4.1)$$

Where  $\sigma_n$  is the effective normal stress acting on the shear plane, and  $c$  and  $\varphi$  are cohesion and the angle of internal friction, respectively. When the Coulomb criterion is written in terms of the principal stresses, the major principal stress at failure is given by:

$$\sigma_1 = \sigma_c + q\sigma_3 \quad (2.4.2)$$

Where  $\sigma_1$  and  $\sigma_3$  are the maximum and minimum principal stresses, respectively, and  $\sigma_c$  is the uniaxial compressive strength of intact rock and is given by the following expression:

$$\sigma_c = \frac{2c \cos \varphi}{1 - \sin \varphi} \quad (2.4.3)$$

The parameter  $q$ , in Eq. 2.4.2, is also defined as:

$$q = \frac{1 + \sin \varphi}{1 - \sin \varphi} \quad (2.4.4)$$

In the three-dimensional stress space ( $\sigma_1, \sigma_2, \sigma_3$ ), the Coulomb criterion can be represented by a failure surface which is a cone with a hexagonal cross section on a plane perpendicular to the hydrostatic axis ( $\sigma_1 = \sigma_2 = \sigma_3$ ).

***Hoek-Brown criterion***

Hoek and Brown (1980) introduced their failure criterion for evaluating rock strength as an important parameter for designing underground excavations in hard rocks. The Hoek-Brown criterion was derived based on the results from the research on the brittle failure of intact rock and on model studies of jointed rock mass behaviour. The Hoek-Brown criterion was initially

developed based on intact rock properties and then these properties were reduced by introducing factors, which were representative of the characteristics of joints in a rock mass. According to Hoek et al. (2002) the generalised Hoek-Brown criterion, which is an empirical model and is based on observed rock behaviour, is expressed in terms of principal stresses as follows:

$$\sigma_1 = \sigma_3 + \sigma_c \left( m_b \frac{\sigma_3}{\sigma_c} + s \right)^a \quad (2.4.5)$$

Parameters  $m_b$ ,  $s$  and  $a$  are rock mass constants and can be estimated from the Geological Strength Index ( $GSI$ ) as follows:

$$\begin{aligned} m_b &= m_i e^{\left( \frac{GSI-100}{28} \right)} \\ s &= e^{\left( \frac{GSI-100}{9} \right)} \quad \text{and} \quad a = 0.5 \quad \text{if } GSI > 25 \\ s &= 0 \quad \text{and} \quad a = 0.65 - \frac{GSI}{200} \quad \text{if } GSI < 25 \end{aligned} \quad (2.4.6)$$

The parameter  $m_i$  is the Hoek-Brown constant parameter  $m$  for intact rock material and depends on rock type and mineralogy. Geological Strength Index ( $GSI$ ) varies from 0 for highly fractured rocks to 100 for intact rocks. Broadly speaking,  $GSI$  depends on the degree of interlocking of the rock blocks and on the surface quality of the discontinuities in the rock mass (Hoek and Brown, 1997). Hoek et al. (2002) introduced a disturbance factor  $D$ , which indicates the amount of disturbance caused by blast damage and stress relaxation. The disturbance factor  $D$ , ranges from 0 for rock masses adjacent to machine excavated underground openings, to between 0.7 and 1.0 for open pit mine slopes, depending on the quality of blasting. Hoek et al. (2002) proposed the following revised empirical expressions for  $m_b$ ,  $s$  and  $a$ :

$$m_b = m_i e^{\left( \frac{GSI-100}{28-14D} \right)}$$

$$s = e^{\left( \frac{GSI-100}{9-3D} \right)}$$

$$a = 0.5 + \frac{e^{\left(\frac{-GSI}{15}\right)} - e^{\left(\frac{-20}{3}\right)}}{6} \quad (2.4.7)$$

Eqs. 2.4.7 have the benefit of covering the entire range of  $GSI$  values in a single group of expressions. Furthermore, from Eqs. 2.4.6 and 2.4.7 it is obvious that for intact rock, parameters  $m_b$ ,  $s$  and  $a$  are calculated as  $m_i$ , 1 and 0.5, respectively. Therefore, the generalised Hoek-Brown criterion takes the following form:

$$\sigma_1 = \sigma_3 + \sigma_c \left( m_i \frac{\sigma_3}{\sigma_c} + 1 \right)^{0.5} \quad (2.4.8)$$

Eq. 2.4.8 is the original form of the Hoek-Brown criterion, which was first introduced in 1980. The Hoek-Brown criterion is widely accepted, predominantly because it fits experimental data reasonably well and its input data can be determined simply by measuring the uniaxial compressive strength (for determining  $\sigma_c$ ), from mineralogical investigations (for determining  $m_i$ ) and structural properties of the rock i.e.  $GSI$ , (for determining parameters  $a$  and  $s$ ). It is also noteworthy that if a more accurate estimation of input parameter  $m_i$  is required, conventional triaxial tests can be conducted to measure this input parameter. In this thesis the intact-rock version of the Hoek-Brown criterion (Eq. 2.4.8) is adopted. However, adopting the generalised version would ultimately allow the borehole stability evaluation techniques discussed in this thesis to be applied for fractured rock masses when sufficient experimental data is available.

It is important to remember that both the Hoek-Brown and the Coulomb criteria incorporate only the major,  $\sigma_1$  and the minor,  $\sigma_3$  principal stresses in the rock failure model on the assumption that the intermediate principal stress,  $\sigma_2$  does not have any influence on rock strength. However, numerous studies have revealed that rock strength is substantially influenced when the intermediate principal stress grows beyond the minor principal stress.

### 2.4.1. The influence of intermediate principal stress on rock failure stress

Experiments and observations that revealed the potential effect of the intermediate principal stress,  $\sigma_2$  on brittle failure of rocks started with Böker (1915), who carried out biaxial extension tests on Carrara marble. Böker first applied an axial stress to the rock specimen and kept it constant, i.e.  $\sigma_3 = \text{constant}$ , and then raised the confining pressure, i.e.  $\sigma_1 = \sigma_2$ , until failure occurred. Von Kármán (1911) also compared the results of the biaxial extension tests and conventional triaxial compression ( $\sigma_1 > \sigma_2 = \sigma_3$ ) tests on the same rock, and it was clear that Carrara marble was stronger when  $\sigma_2$  equalled  $\sigma_1$ , at any level of  $\sigma_3$  tested. Similar results were observed and presented by Handin et al. (1967), who conducted similar conventional triaxial compression and biaxial extension tests on a limestone, a dolomite and glass. Hollow cylinder experiments by Hoskins (1969) on trachyte also showed that  $\sigma_2$  has a significant influence on rock strength. Other researchers also have conducted similar types of experiments. Mogi (1966), however, argued that their experimental procedures were not accurate enough, because of non-uniform stress distribution at the ends of the specimens in the Von Karman triaxial cell, i.e. end effects.

In 1967 Mogi measured the failure stress and the fracture angle of Dunham dolomite, Westerly granite and Solnhofen limestone in extension tests ( $\sigma_1 = \sigma_2 > \sigma_3$ ) after nearly eliminating the end effects. He compared the results from compression and extension tests and noted that the effect of  $\sigma_2$  on rock strength and fracture angle is indisputable. However, Mogi (1971a) pointed out that in order to investigate more closely the influence of the intermediate principal stress on brittle failure of rock, a high-pressure true-triaxial apparatus was needed to test hard rock specimens under three independently applied principal stresses  $\sigma_1 > \sigma_2 > \sigma_3$ .

The true-triaxial apparatus designed by Mogi (1971b) consisted of a pressure vessel that accommodated a rectangular prismatic rock sample of size 15×15×30 mm. Two sets of pistons were employed to apply intermediate,  $\sigma_2$  and major,  $\sigma_1$  principal stresses, and the minor,  $\sigma_3$  principal stress was provided by the confining pressure in the vessel to ensure a uniform distribution of  $\sigma_3$ . A minor principal stress of the magnitude of 800 MPa could be applied. In order to prevent the hydraulic fluid from intruding into the rock specimen, silicon rubber jacketing was applied to the specimen sides subjected to confining pressure. Mogi

minimised friction on the sample faces subjected to piston loading by applying lubricants such as copper sheet jacketing and Teflon or thin rubber sheets between specimen faces and pistons. Stress concentration at specimen ends was found to be greatly reduced by the high confining pressure (Mogi, 1966).

Mogi (1971b) tested a number of carbonate and silicate rocks and plotted the results in the form of  $\sigma_1$  at failure versus  $\sigma_2$  for different families of tests in which  $\sigma_3$  was kept constant. According to Mogi's experimental studies, failure strength increases steadily with the magnitude of  $\sigma_2$  until a plateau is reached following which strength tends to decline as  $\sigma_2$  approaches  $\sigma_1$ . The best-fitting curve to experimental data for any given  $\sigma_3$  is downward concave, but the strength as  $\sigma_2$  grows closer to  $\sigma_1$  remains higher than that when  $\sigma_2 = \sigma_3$ . This behaviour is also predicted by the theoretical model proposed by Wiebols and Cook (1968), which will be discussed further in Section 2.4.2.

The same results were obtained by Chang and Haimson (2000) and Haimson and Chang (2000) who studied the deformational and strength characteristics of specimens of KTB amphibolite and Westerly granite. Since Mogi's pioneering work on the design and fabrication of a true-triaxial apparatus, a series of true-triaxial testing machines have been developed to investigate the  $\sigma_2$ -dependency of the failure stress. Haimson (2006) has reviewed the research conducted over the last 100 years, characterising and formulating the influence of the intermediate principal stress,  $\sigma_2$  on brittle failure of rock. According to Haimson (2006), there is conclusive evidence that the intermediate principal stress has substantial effect on rock strength in brittle field.

Scanning electron microscopy observations of the failure process conducted by Chang and Haimson (2000) revealed that micro-cracks develop mainly parallel to the  $\sigma_2$ -direction as the intermediate stress grows beyond  $\sigma_3$ . The micromechanical processes leading to brittle fracture under true-triaxial stress conditions begin with the dilatancy onset, when the development of micro-cracks is sub-parallel to the major principal stress  $\sigma_1$ -direction. As  $\sigma_1$  increases, micro-cracks grow and localise, creating a shear-band dipping in the  $\sigma_3$ -direction. Upon brittle fracture the shear band fails, forming the eventual main fracture. Similar observations were also reported by Crawford et al. (1995) based on the results from sandstone

specimens failed under true-triaxial stress. With respect to deformation, Chang and Haimson (2000) established that for the same  $\sigma_3$  the onset of dilatancy increases significantly with the magnitude of  $\sigma_2$ , similar to observations by Mogi (1971b) in Mizuho trachyte. Thus, the intermediate principal stress appears to extend the elastic range of the stress-strain behaviour, for a given  $\sigma_3$ , and therefore to retard the onset of the failure process, suggesting a strengthening effect of  $\sigma_2$ .

### ***Yield and failure***

In engineering contexts, the terms ‘yield’ and ‘failure’ often cause confusion. In order to avoid such confusion a clear definition of both terms seems to be necessary. As defined by Priest and Hunt (2005), ‘yield’ refers to the stress state at which the rock starts to develop rapidly accelerating inelastic deformations, and ‘failure’ is the stress level at which the rock disintegrates due to the development of macroscopic fractures. Therefore, when yield is reached, the rock may still be able to carry some extra load or fulfil its engineering function. Since for brittle rocks the portion of inelastic deformation after the yield point and before the failure point is small, i.e. less than 3% of permanent deformation before failure (Heard, 1960), a specific point on the stress-strain curve that can be attributed to yield stress cannot be easily identified. However, the stress at some small permanent strain, such as 0.2%, can crudely be taken as the yield stress. On the other hand, for ductile materials, the yield point on the stress-strain curve can be determined more easily and there exists a single well-established three-dimensional criterion for yield, which originated with Von Mises (Nadai, 1950) as follows:

$$\tau_{oct} = \frac{1}{3} \sqrt{(\sigma_1 - \sigma_2)^2 + (\sigma_2 - \sigma_3)^2 + (\sigma_3 - \sigma_1)^2} = c \quad (2.4.9)$$

Eq. 2.4.9 states that the yield point is reached when the distortional energy, represented by the octahedral shear stress  $\tau_{oct}$ , is equal to a constant  $c$ , which is a constant characteristic of a particular material. However, this is not the case in brittle rock the strength of which varies considerably with confining pressure.

Mogi (1971b) measured the yield stress of three carbonate rocks, namely, Solnhofen Limestone, Dunham Dolomite and Yumaguchi Marble, and four silicate rocks such as Mizuho

trachyte, Orikabe monzonite, Inada granite and Manazuru andesite, under three-dimensional stress state. He observed that yielding appeared clearly in all carbonates and also trachyte. According to his experimental results, Mogi (1971b) concluded that the yield stress is markedly affected by  $\sigma_2$ , but scarcely affected by  $\sigma_3$ . He also pointed out that the measured yield stresses were correlated well by the following formulation:

$$\tau_{oct} = f(\sigma_1 + \sigma_2 + \sigma_3) \quad (2.4.10)$$

Plotting the octahedral shear strength,  $\tau_{oct}$  versus mean normal stress  $\left(\frac{\sigma_1 + \sigma_2 + \sigma_3}{3} = \sigma_{oct}\right)$ , Mogi (1971b) found that Eq. 2.4.10 can be satisfactory as a yield criterion for rocks (Fig. 2.2). He also pointed out that this criterion includes the Von Mises criterion as a special case with slope of the curve equal to zero. The physical interpretation of the generalised Von Mises criterion (Eq. 2.4.10) is that yielding will occur when the distortional strain energy reaches a critical value. This critical energy is not constant, but monotonically increases with the effective mean normal stress (Fig. 2.2).

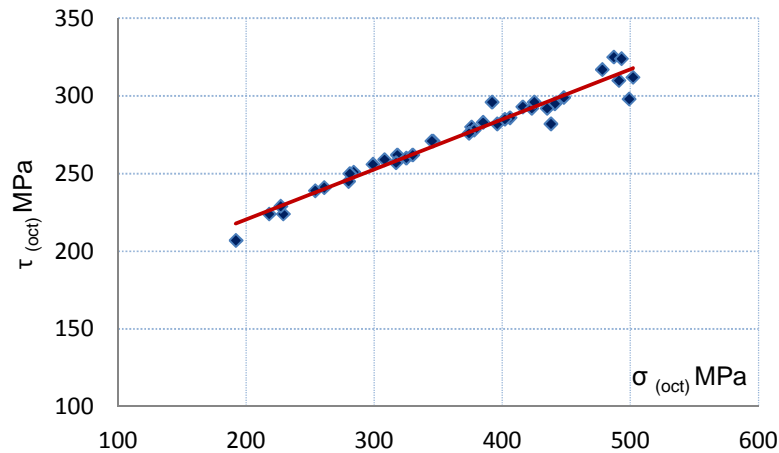


Figure 2.2 Mean octahedral shear stress,  $\tau_{oct}$  vs. mean octahedral normal  $\sigma_{oct}$  at yield for Dunham dolomite [after Mogi (2007)]

Mogi (1971b) also found that at failure the shear faulting takes place on a plane parallel to the direction of  $\sigma_2$  and therefore, there is no stress component associated with the intermediate principal stress on the failure plane. Hence, the mean normal stress contributing to failure is

not  $\sigma_{oct}$ , but its two-dimensional representation, i.e.  $\sigma_{m,2} = \frac{\sigma_1 + \sigma_3}{2}$ . Accordingly, Mogi (1971b) suggested that a failure criterion for rock can be expressed in the following form:

$$\tau_{oct} = f(\sigma_1 + \sigma_3) \quad (2.4.11)$$

Where  $f$  is a monotonically increasing function. The physical interpretation of Eq. 2.4.11 is that failure takes place when the distortional strain energy, which increases monotonically with the effective mean stress ( $\sigma_{m,2}$ ), reaches a critical value on the failure plane. Experimental studies on KTB amphibolite by Chang and Haimson (2000) and Westerly granite by Haimson and Chang (2000) also mirrored Mogi's conclusion of a general formulation for brittle 'failure' of rock.

It should be noted that 'yielding' does not occur on any definite slip plane with a definite direction, therefore, the mean stress ( $\frac{\sigma_1 + \sigma_2 + \sigma_3}{3} = \sigma_{oct}$ ) is taken as the effective mean normal stress when formulating a 'yield' criterion. Substantial evidence suggests that the intermediate principal stress,  $\sigma_2$  has a strengthening effect on rock. It can be inferred that the intermediate principal stress causes the yield stress of the rock to increase. As a result of the increase in the yield stress of rock the failure stress of rock also increases. It is important, however, to note that after the yield point is reached, the intermediate principal stress does not influence the rock failure. Therefore, rock failure criteria, which neglect the influence of  $\sigma_2$ , do not appropriately reflect the mechanical behaviour of rock under a general stress state. Several theoretical and empirical three-dimensional failure criteria, which incorporate  $\sigma_2$  in the rock failure formulation, have been introduced over the past few decades. In the following section for a number of selected three-dimensional failure criteria detailed discussions are presented.

### 2.4.2. Frictional criteria

Theoretical or hypothetical criteria are also referred to as 'frictional criteria' after Priest (2010) who commented that these criteria source their input parameters from one or more of the parameters of uniaxial compressive strength, cohesion ( $c$ ) and the coefficient, or the angle, of

internal friction ( $\varphi$ ). Some frictional failure criteria, which have been more commonly used in the petroleum and mining studies, are briefly explained below.

### ***Drucker-Prager criterion***

Drucker and Prager (1952) proposed a mean-stress-dependent failure criterion, combining the Coulomb and the Von Mises criteria. Drucker and Prager suggested their criteria as:

$$J_2^{1/2} = A + BJ_1 \quad (2.4.12)$$

Parameters  $A$  and  $B$  are rock constants and by defining  $\sigma_1$ ,  $\sigma_2$  and  $\sigma_3$  as major, intermediate and minor principal stresses, respectively, the mean principal stress,  $J_1$  is given by:

$$J_1 = \frac{\sigma_1 + \sigma_2 + \sigma_3}{3} = \sigma_{oct} \quad (2.4.13)$$

The mean shear stress  $J_2$  at failure is given by:

$$J_2 = \frac{(\sigma_1 - \sigma_2)^2 + (\sigma_2 - \sigma_3)^2 + (\sigma_3 - \sigma_1)^2}{6} \quad (2.4.14)$$

A physical interpretation of the Drucker-Prager criterion is that failure occurs when the octahedral shear stress ( $\tau_{oct} = \sqrt{3/2} J_2^{1/2}$ ) exceeds a certain value that depends on the octahedral normal stress,  $\sigma_{oct}$ . Parameters  $A$  and  $B$  can be estimated from the Coulomb shear strength parameters cohesion,  $c$  and the angle of internal friction  $\varphi$ . The following values for the parameters  $A$  and  $B$  represent an inscribed cone to the Coulomb failure surface in the principal stress space ( $\sigma_1, \sigma_2, \sigma_3$ ):

$$A_i = \frac{6c \cos \varphi}{\sqrt{3}(3 + \sin \varphi)} \quad \text{and} \quad B_i = \frac{2 \sin \varphi}{\sqrt{3}(3 + \sin \varphi)} \quad (2.4.15)$$

The circumscribed Drucker-Prager can be derived by defining  $A$  and  $B$  as:

$$A_c = \frac{6c \cos \varphi}{\sqrt{3}(3 - \sin \varphi)} \quad \text{and} \quad B_c = \frac{2 \sin \varphi}{\sqrt{3}(3 - \sin \varphi)} \quad (2.4.16)$$

The cross section of the inscribed and circumscribed Drucker-Prager and the cross section of the Coulomb criterion on the deviatoric plane are presented in Fig. 2.3. A deviatoric plane is a plane perpendicular to the hydrostatic axis in the principal stress space ( $\sigma_1, \sigma_2, \sigma_3$ ). Detailed explanations on the principal stress space and the deviatoric plane and associated concepts are given in Chapter 4.

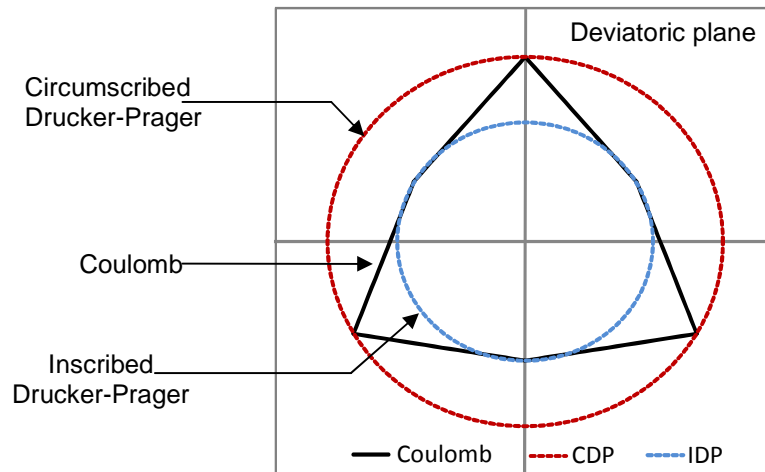


Figure 2.3 The cross section of (a) the Coulomb, (b) the circumscribed and (c) the inscribed Drucker-Prager on the deviatoric plane

### ***Modified Wiebols and Cook criterion***

Wiebols and Cook (1968) proposed a failure criterion based on the additional energy stored around Griffith cracks due to the sliding of crack surfaces over each other. They hypothesised that in a homogeneous specimen of rock that can be regarded as an elastic material there exists a large number of uniformly distributed and randomly oriented closed, plane cracks, the dimensions of which fall within a limited range. When subjected to stress, a volume of such material stores within itself strain energy, which can be divided into two parts. Firstly, there is the strain energy which would be stored in the same volume of material when subjected to the same stresses, in the absence of any cracks. Secondly, there is the additional strain energy due to the presence of cracks.

When all three principal stresses applied to the material are compressive, the surfaces of any closed crack can be subjected only to normal compressive stress,  $\sigma_n$  and shear stress,  $\tau$ . Let

the coefficient of sliding friction between the opposite surfaces of the cracks be a constant  $\mu$ . Sliding between the opposite surfaces of a crack under the influence of the applied stress occurs if  $|\tau| - \mu\sigma_n > 0$ . The quantity  $(|\tau| - \mu\sigma_n)$  is defined as the ‘effective shear stress’ and the strain energy per unit volume of the material stored around the cracks, as a result of the sliding produced by this stress, is defined as the ‘effective shear strain energy’. The effective shear stress on any crack depends on the magnitudes of the principal stresses and the orientation of the crack relative to the directions of these stresses.

The effective shear strain energy depends on the magnitudes of the effective shear stresses on each crack in a unit volume, the number of such cracks, and their size and shape. It is assumed that each crack contributes to failure when it slides, and that the strength of rock is determined by some maximum value of the effective shear strain energy. It then follows that the strength of rock is a function of its properties, and also a function of the magnitude of each of the principal stresses. The strain energy criterion proposed by Wiebols and Cook (1968) had a major drawback as the coefficient of friction between two crack surfaces ( $\mu$ ) could not be determined through a standard experimental procedure.

Zhou (1994) introduced a three-dimensional model for compressive rock failure, which was an extension of the Drucker-Prager criterion with similar features to the effective strain energy criterion proposed by Wiebols and Cook (1968). The three-dimensional criterion introduced by Zhou (1994) is also referred to as modified Wiebols and Cook. According to this criterion, yield is predicted to occur when:

$$J_2^{1/2} = A + BJ_1 + CJ_1^2 \quad (2.4.17)$$

Where  $J_1$  and  $J_2$  are given by Eqs. 2.4.13 and 2.4.14 and parameters  $A$ ,  $B$ , and  $C$  are determined such that Eq. 2.4.17 is constrained by rock strengths at both triaxial and biaxial compressions. In the triaxial stress state ( $\sigma_1 > \sigma_2 = \sigma_3$ ), rock strength is given by the Coulomb criterion, i.e.  $\sigma_1 = \sigma_c + q\sigma_3$ , and in the biaxial state of stress ( $\sigma_1 = \sigma_2 > \sigma_3$ ) rock strength is given by  $\sigma_1 = G + q\sigma_3$ , where  $G$  is the biaxial plane strength of the rock, (Wiebols and Cook, 1968), and is defined as:

$$G = \sigma_{ci}(1 + 0.6 \tan \varphi) \quad (2.4.18)$$

With respect to constraining conditions and by substituting the uniaxial rock strength ( $\sigma_1 = \sigma_c$ ,  $\sigma_2 = \sigma_3 = 0$ ) into Eq. 2.4.17 and introducing four intermediate parameters, such as  $U_1, U_2, U_3$  and  $U_4$  as follows:

$$\begin{aligned}
 U_1 &= G + \sigma_3(q-1) - \sigma_c \\
 U_2 &= 2G + \sigma_3(q-1) - \sigma_c \\
 U_3 &= 2G + \sigma_3(2q+1) - \sigma_c \\
 U_4 &= \sigma_3(q+1) + 2\sigma_c
 \end{aligned} \tag{2.4.19}$$

Parameters  $A$ ,  $B$  and  $C$  are defined as:

$$\begin{aligned}
 C &= \frac{\sqrt{27}}{U_2} \left[ \frac{U_1}{U_3} - \frac{q-1}{q+2} \right] \\
 B &= \frac{(q-1)\sqrt{3}}{q+2} - \frac{U_4 C}{3} \\
 A &= \frac{\sigma_c}{\sqrt{3}} - \frac{s\sigma_c}{3} - \frac{C\sigma_c^2}{9}
 \end{aligned} \tag{2.4.20}$$

### ***Modified Lade criterion***

A three-dimensional failure criterion in terms of stress invariants and three material parameters, was introduced by Kim and Lade (1984). However, the criterion was initially developed for soil and was later modified for concrete by Lade (1982). The material parameters can be determined from any type of strength test, including the simplest possible, such as the uniaxial compression or conventional triaxial compression tests. The Lade criterion is given as:

$$\left( \frac{I_1^3}{I_3} - 27 \right) \left( \frac{I_1}{P_a} \right)^m = \eta_1 \tag{2.4.21}$$

Where  $I_1 = \sigma_1 + \sigma_2 + \sigma_3$  and  $I_3 = (\sigma_1) \cdot (\sigma_2) \cdot (\sigma_3)$  and  $m$  is a rock mass constant. The value of  $I_1^3/I_3$  is 27 under the hydrostatic stress condition, i.e.  $\sigma_1 = \sigma_2 = \sigma_3$ . Furthermore, parameters  $\eta_1$  and  $m$  in the Lade criterion can be determined by plotting  $(I_1^3/I_3 - 27)$  vs.  $(P_a/I_1)$  at failure in a log-log diagram and locating the best fitting straight line. The intercept of this line with the vertical line  $(\frac{P_a}{I_1})=1$  is the value of  $\eta_1$ , and  $m$  is the slope of this line.

In order to apply Eq. 2.4.21 to rock material, Kim and Lade (1984) added a constant stress ( $a \cdot P_a$ ) to the principal stresses before substitution in Eq. 2.4.21 to incorporate the cohesion and the tension which can be sustained by rock material, as follows:

$$\bar{\sigma}_1 = \sigma_1 + a \cdot P_a$$

$$\bar{\sigma}_2 = \sigma_2 + a \cdot P_a$$

$$\bar{\sigma}_3 = \sigma_3 + a \cdot P_a \tag{2.4.22}$$

Where  $a$  is a dimensionless parameter and  $P_a$  is the atmospheric pressure and is in the same units as  $\sigma_1, \sigma_2$  and  $\sigma_3$ . According to Kim and Lade (1984), the parameter  $a$ , which plays a very important role in characterising the tensile strength of rock, can be determined through triaxial tests.

Ewy (1999) developed a modified version of the Lade criterion by introducing a shift constant with units of cohesion as  $S_1$  to shift the stress axes to the tensile region. In addition, he subtracted the pore pressure in order to handle effective stresses. The modified Lade criterion is expressed as follows:

$$\frac{(I'_1)^3}{I'_3} = 27 + \eta \tag{2.4.23}$$

Where

$$I'_1 = (\sigma_1 + S_1 - p_0) + (\sigma_2 + S_1 - p_0) + (\sigma_3 + S_1 - p_0)$$

$$I'_3 = (\sigma_1 + S_1 - p_0)(\sigma_2 + S_1 - p_0)(\sigma_3 + S_1 - p_0) \tag{2.4.24}$$

In Eqs. 2.4.24, the parameter  $p_0$  is pore pressure, which can be excluded from the formulation for non-porous rocks, and parameters  $S_1$  and  $\eta$  are material constant which can be directly derived from the Coulomb cohesion  $c$  and the angle of friction  $\varphi$  through the following expressions:

$$S_1 = \frac{c}{\tan \varphi}$$

$$\eta = \frac{2 \tan^2 \varphi (9 - 7 \sin \varphi)}{1 - \sin \varphi} \quad (2.4.25)$$

Under general stress conditions ( $\sigma_1 \neq \sigma_2 \neq \sigma_3$ ), the modified Lade criterion, as well as the original Lade criterion, predicts a strengthening effect due to increase of the intermediate principal stress. This is followed by a slight reduction in the rock strength once  $\sigma_2$  becomes ‘too high’.

### 2.4.3. Hoek-Brown based criteria

Despite its widespread acceptance and application, the Hoek-Brown criterion has some limitations. In the case of anisotropy, for instance, the Hoek-Brown Criterion should not be used unless allowance is made for this anisotropy. The strength anisotropy can be exemplified by a fault passing through a heavily jointed rock mass or a block of intact rock. The rock mass or the rock material may be treated as an isotropic medium to which the Hoek-Brown failure criterion is applicable, but the fault must be treated as an anisotropic weakness plane along which slip can occur at a much lower stress level than that which would cause failure in the rock mass or the rock material. Another important limitation is that the Hoek-Brown criterion was developed based on the assumption that only major and minor principal stresses contribute to rock failure and that intermediate principal stress does not have any influence.

In order to take into account the influence of the intermediate principal stress, significant efforts have been made to modify the Hoek-Brown criterion or to introduce a three-dimensional failure criterion based on the Hoek-Brown criterion. Input parameters of such a

three-dimensional criterion are the same as those of the Hoek-Brown model. The reason why such attention has been given to the Hoek-Brown criterion was outlined by Priest (2005) as:

- The Hoek-Brown criterion has been developed specifically for rock materials and rock masses.
- Input parameters for the Hoek-Brown criterion can be derived from uniaxial testing of the rock material, mineralogical examinations and measurements of the rock mass fracture characteristics.
- The Hoek-Brown criterion has been applied successfully to a wide range of intact and fractured rock types over the past decades (Hoek and Brown, 1997).

### ***Pan-Hudson criterion***

Pan and Hudson (1988) proposed a modified three-dimensional version of the Hoek-Brown criterion for predicting the strength of weak rock masses. Based on the assumption that intermediate principal stress influences rock failure, especially in the case of weak rocks, the Pan-Hudson criterion was developed and expressed in terms of invariants of the deviatoric stress tensor as follows:

$$\frac{3}{\sigma_c} J_2 + \frac{\sqrt{3}}{2} m_i \sqrt{J_2} - m_i \frac{I_1}{3} = s \sigma_c \quad (2.4.26)$$

If the major, intermediate and minor principal stresses are denoted as  $\sigma_1$ ,  $\sigma_2$  and  $\sigma_3$ , respectively, then  $I_1 = \sigma_1 + \sigma_2 + \sigma_3$  and  $J_2$  is the second invariant of the deviatoric stress tensor, or the mean shear stress at failure, and is given by Eq. 2.4.14. If the Pan-Hudson criterion is rearranged and is written in terms of  $\tau_{oct}$ , the octahedral shear stress at failure, it yields the following expression:

$$\frac{9}{2\sigma_c} \tau_{oct}^2 + \frac{3}{2\sqrt{2}} m_i \tau_{oct} - m_i \frac{I_1}{3} = s \sigma_c \quad (2.4.27)$$

Where  $\tau_{oct}$  is given by Eq. 2.4.9 and  $\frac{I_1}{3} = \frac{\sigma_1 + \sigma_2 + \sigma_3}{3}$ .

Priest (2010), through a comparative study, demonstrated that the Pan-Hudson criterion exhibits a substantially different pattern from that of other three-dimensional failure criteria, when predicting the failure of intact rock (Fig. 2.4).

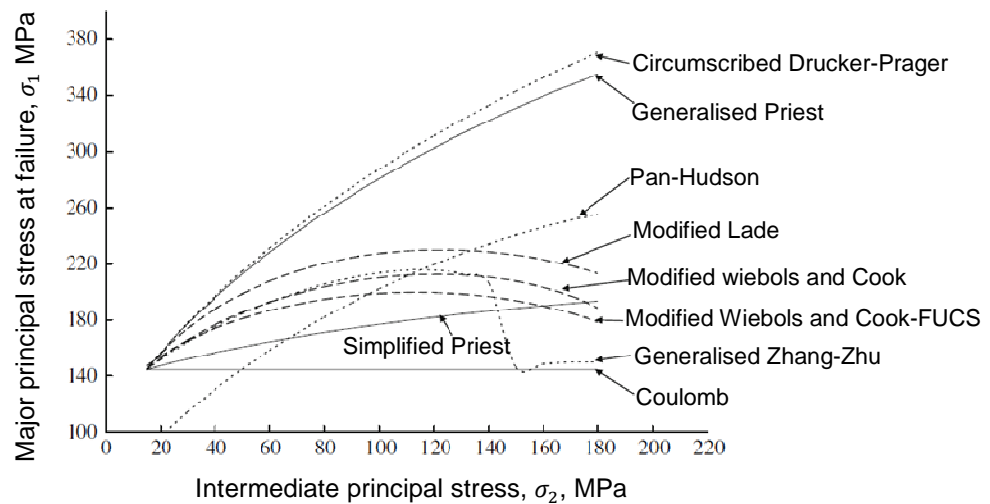


Figure 2.4 Relation between intermediate and major principal stresses at failure for eight different failure criteria for a rock mass subjected to a minor principal stress of 15 MPa, with a uniaxial compressive strength of 75 MPa,  $m_i = 19$  and  $GSI = 90$  (Priest (2010))

Furthermore, according to Zhang and Zhu (2007), for biaxial extension ( $\sigma_1 = \sigma_2 > \sigma_3$ ) or triaxial compression ( $\sigma_1 > \sigma_2 = \sigma_3$ ) stress states, the Pan-Hudson criterion does not reduce to the form of the original Hoek-Brown criterion. Furthermore, comparison with experimental data conducted on various rock types suggests that the Pan-Hudson criterion under-predicts the rock strength in triaxial compression, but over-predicts the strength in biaxial extension (Zhang, 2008, Zhang and Zhu, 2007). Reasons for the limitations of the Pan-Hudson criterion will be addressed in detail in Chapter 4.

### ***Generalised Priest criterion***

Priest (2005) developed a three-dimensional criterion by combining the two-dimensional Hoek-Brown criterion with the Drucker-Prager criterion. The Hoek-Brown criterion was adopted for its simplicity in acquiring input rock parameters and because it had already been widely used in the mining industry. The Drucker-Prager criterion was adopted for its common

application in borehole and wellbore stability in the petroleum industry. The generalised Priest criterion initially required a numerical iteration to calculate the effective maximum principal stress at failure. Melkounian et al. (2009) developed an explicit solution for the generalised Priest criterion. The term generalised implies that the parameter  $a$  and the dilation parameter  $m$  in the Hoek-Brown criterion are not taken simply as 0.5 and 1, respectively, and are calculated using either Eqs. 2.4.6 or Eqs. 2.4.7. An explicit expression for the generalised Priest criterion, as addressed by Melkounian et al. (2009), is given as follows:

$$\sigma_{1f} = 3\sigma_{3HB} + P - (\sigma_2 + \sigma_3) \quad (2.4.28)$$

Where  $\sigma_{1f}$  is the major principal stress at failure and  $\sigma_{3HB}$  and  $P$  are calculated as:

$$P = \sigma_c \left[ \left( \frac{m_b \sigma_{3HB}}{\sigma_c} \right) + s \right]^a \quad (2.4.29)$$

$$\sigma_{3HB} = \frac{\sigma_2 + \sigma_3}{2} + \frac{-E \mp \sqrt{E^2 - F(\sigma_2 - \sigma_3)^2}}{2F} \quad (2.4.30)$$

Parameters  $E$  and  $F$  are defined as:

$$F = 3 + m_i C^{a-1} \quad (2.4.31)$$

$$E = 2C^a \sigma_c$$

Where  $C$  is given by:

$$C = s + \frac{m_i (\sigma_2 + \sigma_3)}{2\sigma_c} \quad (2.4.32)$$

Further detail on the generalised Priest criterion and its application for prediction of intact rock strength will be addressed in Chapter 4.

### ***Simplified Priest criterion***

Priest (2005) proposed another three-dimensional version of the Hoek-Brown criterion by defining a weighting factor  $w$  ranging from 0 to 1.0. He then specified that when  $w$  is equal to

0, the intermediate principal stress,  $\sigma_2$  has no influence on failure and when  $w$  is equal to 1 the minor principal stress,  $\sigma_3$  has no influence. Priest (2005) suggested that the weighting factor  $w$  depends only on values of the minor principal stress,  $\sigma_3$ , and that it can be calculated by the following expression for a range of sedimentary and metamorphic rocks:

$$w \approx \alpha \sigma_3^\beta \quad (2.4.33)$$

Where  $\sigma_3$  is the minor principal stress and  $\alpha \approx \beta \approx 0.15$ , for the rock types examined. After defining the weighting factor  $w$ , the minor principal stress in the Hoek-Brown criterion can be defined as follows:

$$\sigma_{3HB} = w\sigma_2 + (1-w)\sigma_3 \quad (2.4.34)$$

The next step is to substitute the value for  $\sigma_{3HB}$  from Eq. 2.4.34 into the Hoek-Brown criterion, given by Eq. 2.4.5, to calculate  $\sigma_{1HB}$ . Therefore, the major principal stress calculated by the Hoek-Brown criterion is given by:

$$\sigma_{1HB} = \sigma_{3HB} + \sigma_c \left( m_b \frac{\sigma_3}{\sigma_c} + s \right)^a \quad (2.4.35)$$

Then the simplified Priest criterion is expressed as:

$$\sigma_{1f} = \sigma_{1HB} + 2\sigma_{3HB} - (\sigma_2 + \sigma_3) \quad (2.4.36)$$

The term  $\sigma_{1f}$  is the major principal stress at failure in the three-dimensional stress state, i.e. when  $\sigma_1 > \sigma_2 > \sigma_3$ . Further explanation on the simplified Priest criterion is given in Chapter4.

### ***Generalised Zhang-Zhu criterion***

Zhang and Zhu (2007) developed a three-dimensional version of the Hoek-Brown criterion based on the assumption made by Mogi (1971b) that a failure criterion can be expressed as:

$$\tau_{oct} = f(\sigma_1 + \sigma_3)$$

Where the function  $f$  is defined as a monotonically increasing function. Zhang and Zhu (2007), then proposed their criterion as:

$$\frac{9}{2\sigma_c} \tau_{oct}^2 + \frac{3}{2\sqrt{2}} m_b \tau_{oct} - m_b \sigma_{m,2} = s \sigma_c \quad (2.4.37)$$

Where the parameter  $\sigma_{m,2}$  is defined as  $\sigma_{m,2} = \frac{\sigma_1 + \sigma_3}{2}$ . Zhang (2008) highlighted that the Zhang-Zhu criterion could be simplified to the original form of the Hoek-Brown criterion for biaxial extension ( $\sigma_1 = \sigma_2 > \sigma_3$ ) and triaxial compression ( $\sigma_1 > \sigma_2 = \sigma_3$ ) states of stress. Furthermore, the only difference between the Zhang-Zhu and the Pan-Hudson criteria is the inclusion of the intermediate principal stress in the third term, in the right hand side of these two criteria, given by Eq. 2.4.27 and Eq. 2.4.37 (where both are written in terms of  $\tau_{oct}$ ).

In fact, the Zhang-Zhu criterion implies an assumption that the intermediate principal stress plays its strengthening role up to a certain point, after which the influence of  $\sigma_2$  on failure will be eliminated. This assumption accords with the experimental studies on rock performance under three-dimensional stress. Zhang (2008) modified the Zhang-Zhu (2007) criterion so that it could be applicable to all those rock masses to which the generalised Hoek-Brown criterion applies. The generalised Zhang-Zhu criterion is expressed as:

$$\frac{1}{\sigma_c^{(1/a-1)}} \left( \frac{3}{\sqrt{2}} \tau_{oct} \right)^{1/a} + \frac{m_b}{2} \left( \frac{3}{\sqrt{2}} \tau_{oct} \right) - m_b \sigma_{m,2} = s \sigma_c \quad (2.4.38)$$

## **CHAPTER 3**

### **Stress analysis around a borehole**

	<b>Page</b>
<b>3.1. Introduction</b>	<b>37</b>
<b>3.2. Stress analysis around a vertical borehole</b>	<b>40</b>
<b>3.3. Stress analysis around a deviated borehole</b>	<b>53</b>
<b>3.4. Numerical counterpart of the generalised Kirsch equations</b>	<b>60</b>
<b>3.5. A modification to the generalised Kirsch equations</b>	<b>70</b>

### 3.1. Introduction

When a borehole is introduced into an already stressed isotropic elastic rock, the pre-existing stress field in the vicinity of the borehole is redistributed. The primary driving factor that leads to borehole instability is the magnitude and deviatoric nature of the in situ rock stress that becomes concentrated in the rock adjacent to the borehole wall. Accurate knowledge of the new, induced stress field due to the introduction of the borehole is vital for drilling stable boreholes. The geological stresses can be measured by a variety of deformation measurement techniques including hydro fracturing, inelastic strain recovery and borehole breakout estimations. However, due to difficulties associated with in situ stress measurements, it is desirable for the induced stresses in the vicinity of the borehole to be estimated accurately by means of numerical or analytical models.

In two-dimensional analysis of axially symmetrical structures it is generally convenient to represent the state of stress and strain in terms of polar coordinates  $(r, \theta)$ . The angle  $\theta$  (0 to  $2\pi$ ) gives the anti-clockwise angle of rotation from a reference axis, such as the  $X$ -axis in Fig. 3.1. The distance  $r$  gives the radial distance from the centre of the axially symmetrical structure. In two dimensions the normal stress components are  $\sigma_{rr}$  (radial stress) and  $\sigma_{\theta\theta}$  (tangential or circumferential stress) with the associated shear stress  $\sigma_{r\theta}$ . Two-dimensional polar coordinates can be extended to three-dimensional cylindrical coordinates by defining the  $Z$ -axis to correspond to the axis of the axially symmetrical structure. In this case the additional normal stress component is  $\sigma_{zz}$  (axial stress) and the associated shear stresses are  $\sigma_{rz}$  and  $\sigma_{\theta z}$ . Two-dimensional and three-dimensional strains can be specified in the same way. It is important to remember that the actual orientations of the radial and tangential stress or strain components will vary with location around the axially-symmetrical structure. Polar and cylindrical coordinate systems are adopted because the stress and strain states around axially symmetrical structures generally vary directly as functions of the parameters  $r$  and  $\theta$ . The parameters  $r$  and  $\theta$  therefore not only serve to specify the orientation and location of the stress/strain components, but also appear in functions that define the values of the stress/strain components themselves at the specified location.

For an isotropic, linearly elastic and homogeneous material, Kirsch (1898) calculated stress components around a circular hole, when principal stresses were acting at infinity (Fig. 3.1).

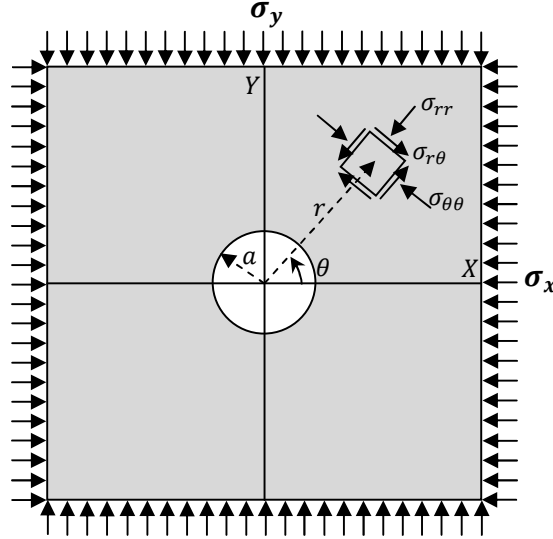


Figure 3.1 Stresses on an element at a radial distance  $r$  from the centre of a circular hole with radius  $a$ , in polar coordinates.

The radial, tangential and shear stresses at an anti-clockwise angle  $\theta$ , measured from the  $X$ -axis, and a radial distance  $r$  from the centre of the hole are given by the following equations:

$$\begin{aligned}\sigma_{rr} &= \frac{\sigma_x + \sigma_y}{2} \left(1 - \frac{a^2}{r^2}\right) + \frac{\sigma_x - \sigma_y}{2} \left(1 - 4\frac{a^2}{r^2} + 3\frac{a^4}{r^4}\right) \cos 2\theta \\ \sigma_{\theta\theta} &= \frac{\sigma_x + \sigma_y}{2} \left(1 + \frac{a^2}{r^2}\right) - \frac{\sigma_x - \sigma_y}{2} \left(1 + 3\frac{a^4}{r^4}\right) \cos 2\theta \\ \sigma_{r\theta} &= -\frac{\sigma_x - \sigma_y}{2} \left(1 + 2\frac{a^2}{r^2} - 3\frac{a^4}{r^4}\right) \sin 2\theta\end{aligned}\quad (3.1.1)$$

In order to apply Eqs. 3.1.1 for stress estimation around a borehole, the rock into which the borehole is drilled has to be assumed as continuous, homogeneous, isotropic and linearly elastic (CHILE) material. However, a rock with such properties rarely exists in nature. Furthermore, in borehole stability evaluation, especially in the presence of major discontinuities at the prospective location of the borehole, questions arise concerning the

validity of elastic stress analysis in the design process and the potential effect of the discontinuity on the stability of the borehole wall.

However, it should be noted that the elastic solution calculates the induced stresses based on the assumption that the pre-existing stress field has been redistributed due to the introduction of a hole into a CHILE material. Therefore, the elastic solution for estimating the induced stresses, coupled with a predictive model for rock strength (failure criterion) can be applied to model the rock behaviour adjacent to the borehole wall. If the intact rock does not fail under the induced stresses, then the possibility of slip along the major discontinuity should be investigated, considering the stress components acting on the faces of the discontinuity. On the other hand, if the induced stress around the borehole, calculated by means of the elastic solution, causes failure to initiate within the rock material, the extent to which the failure will progress needs to be determined and, if the failure appears to be too extensive, a suitable support system must be designed and implemented to resist the collapse of the borehole. Furthermore, the numerical techniques of stress estimation can also be given consideration as alternative approaches to analytical solutions, especially in cases of complicated constitutive relationships with respect to rock behaviour. Nevertheless, according to Brady and Brown (1993), in some cases, an elastic analysis presents a valid basis for design in a discontinuous rock mass and in others, provides a basis for judgement of the engineering significance of a discontinuity.

The three-dimensional version of Kirsch equations for stress estimation in the proximity of vertical and deviated boreholes was first derived by Fairhurst (1968) and has been widely applied in the mining and petroleum industries ever since. Generally, three-dimensional Kirsch equations are either applied to rock in situ stress measurements or to instability prediction of any underground structure with a circular cross section, such as tunnels, wellbores and boreholes. In rock in situ stress measurements, by means of borehole breakout or hydraulic fracturing methods, stresses around the borehole are measured and then subsequently substituted into the three-dimensional Kirsch equations to calculate the far field stresses. A detailed explanation of stress measurement methods is beyond the scope of this study and the reader is referred to Amadei and Stephansson (1997) for further explanation on rock stress and its measurement.

A detailed mathematical derivation of the 3D Kirsch equations was presented by Fairhurst (1968) and Jaeger et al. (2007). In addition, these equations have been applied as a closed form solution for calculating the induced stresses around a borehole by Amadei and Stephansson (1997), Zoback et al. (2003), Al-Ajmi (2006) and Fjær et al. (2008). However, apart from the mathematical derivation, there is no clear explanation of the boundary conditions on which these equations have been based. On the other hand, a thorough understanding of these boundary conditions is essential for this analytical solution to be confidently applied to stress analysis in the excavation proximity. In order to provide an unambiguous explanation of boundary conditions involved in the derivation of three-dimensional Kirsch equations, detailed investigations were conducted on the mathematical procedure and the simplifying assumptions adopted for deriving the three-dimensional equations from the original two-dimensional Kirsch equations.

A numerical counterpart of the three-dimensional Kirsch equations was also created to provide a further opportunity to validate and explain the boundary conditions and simplifying assumptions involved in the analytical model. Simplifying assumptions are usually made to facilitate the derivation of a closed form solution to a complicated problem. In some cases without these simplifying assumptions, deriving a closed form solution may be impossible. However, such assumptions, especially in the case of incompatibility with the physics of the real problem, may sacrifice the accuracy of the model. Therefore, a numerical model counterpart to the three-dimensional Kirsch equations enables one to further improve the accuracy of the model by eliminating some simplifying assumptions, without which the analytical solution would be impossible to be formulated.

## 3.2. Stress Analysis around a Vertical Borehole

### *Stresses before drilling the borehole*

Consider a block of rock, located at a great depth beneath the Earth's surface, to which far-field principal stresses  $\sigma_x$ ,  $\sigma_y$  and  $\sigma_z$  are acting in the Cartesian  $X$ ,  $Y$  and  $Z$  coordinate directions, respectively. Measuring the angle,  $\theta$ , counter-clockwise from the  $X$  direction, the initial values of radial ( $\sigma_{rr_0}$ ), tangential ( $\sigma_{\theta\theta_0}$ ) and vertical ( $\sigma_{zz_0}$ ) stress components, and also

the associated shear stress components ( $\sigma_{r\theta_0}$ ,  $\sigma_{rz_0}$  and  $\sigma_{\theta z_0}$ ), can be expressed in a cylindrical coordinate system as follows:

$$\begin{aligned} \sigma_{rr_0} &= \frac{\sigma_x + \sigma_y}{2} + \frac{\sigma_x - \sigma_y}{2} \cos 2\theta & \sigma_{zz_0} &= \sigma_z \\ \sigma_{\theta\theta_0} &= \frac{\sigma_x + \sigma_y}{2} - \frac{\sigma_x - \sigma_y}{2} \cos 2\theta & \sigma_{\theta z_0} &= \sigma_{rz_0} = 0 \\ \sigma_{r\theta_0} &= -\frac{\sigma_x - \sigma_y}{2} \sin 2\theta \end{aligned} \tag{3.2.1}$$

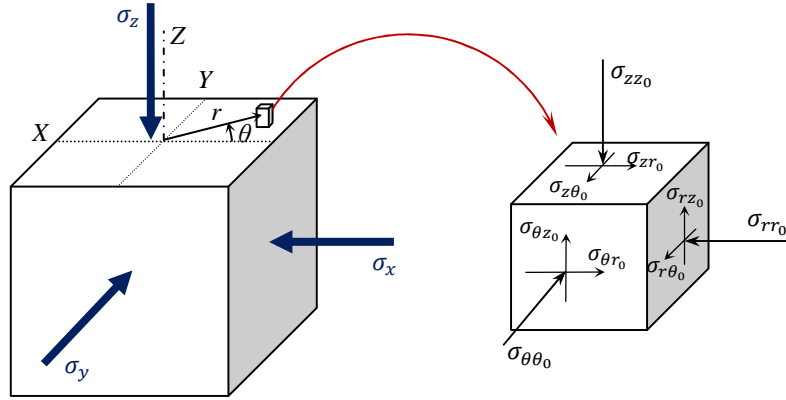


Figure 3.2 The model of the pre-stressed block of rock into which the borehole will be drilled

In order to model the pre-existing in situ stress field, a block of rock can be assumed to be removed from its position under the ground and to be loaded with the same in situ stress components from zero. Under such conditions the initial values of the stress components acting on an element located at an arbitrary point in the model, as illustrated in Fig. 3.2, can be expressed in a cylindrical coordinate system as follows:

$$\begin{aligned} \sigma_{rr_1} &= \frac{\sigma_x + \sigma_y}{2} + \frac{\sigma_x - \sigma_y}{2} \cos 2\theta & \sigma_{zz_1} &= \sigma_z - \nu(\sigma_x + \sigma_y) \\ \sigma_{\theta\theta_1} &= \frac{\sigma_x + \sigma_y}{2} - \frac{\sigma_x - \sigma_y}{2} \cos 2\theta & \sigma_{\theta z_1} &= \sigma_{rz_1} = 0 \end{aligned}$$

$$\sigma_{r\theta_1} = -\frac{\sigma_x - \sigma_y}{2} \sin 2\theta \quad (3.2.2)$$

In Eqs. 3.2.2 the vertical normal stress component,  $\sigma_{zz_0}$ , was calculated regarding the Poisson's effect and the Poisson's ratio,  $\nu$ .

### ***Stresses after drilling the borehole***

After a borehole of radius  $a$  has been drilled into an isotropic elastic rock block, which was loaded from zero by the same stress components as the pre-existing in situ, the radial,  $\sigma_{rr}$ , tangential,  $\sigma_{\theta\theta}$ , and in-plane shear,  $\sigma_{r\theta}$  stresses acting on an element of rock at a radial distance  $r$  from the borehole centre can be calculated by applying the well known Kirsch equations, given by Eqs. 3.1.1. However, it is important to remember that Eqs. 3.1.1 were originally developed for calculating stresses around a hole in a thin plane in two dimensions. On the other hand, since the axis of the borehole extends into the third dimension, i.e. the  $Z$ -axis of a Cartesian or cylindrical coordinate system, stress components along the borehole axis in the third dimension also need to be calculated.

In three-dimensional engineering problems, general stress states and the associated deformations are represented by means of second order tensors with six distinct components. However, in structures where one dimension is considerably greater than the other two dimensions, the strain components associated with the extended dimension are assumed to be constrained by nearby materials and are substantially smaller than the cross sectional strains. Considering the fact that the length of a borehole along its axis is substantially greater than the cross sectional dimensions on a plane perpendicular to the borehole axis, longitudinal deformations can be assumed to be negligible due to the constraint imposed by nearby geomaterials. Therefore, if the borehole axis is assumed to be coinciding with the  $Z$ -axis, all strain components along the  $Z$ -axis ( $\varepsilon_{zz}$ ,  $\varepsilon_{xz}$  and  $\varepsilon_{yz}$ ) are assumed to be zero and deformations are expected to occur only in planes perpendicular to the borehole axis, i.e. ( $X$ ,  $Y$ )-planes. Such simplifying assumption is referred to as plane strain conditions. Furthermore, the strain tensor which describes the plane strain conditions is expressed as:

$$[\boldsymbol{\varepsilon}] = \begin{bmatrix} \varepsilon_{xx} & \varepsilon_{xy} & 0 \\ \varepsilon_{yx} & \varepsilon_{yy} & 0 \\ 0 & 0 & 0 \end{bmatrix} \quad (3.2.3)$$

The stress state corresponding to the plane strain conditions is given by the following stress tensor:

$$[\boldsymbol{\sigma}] = \begin{bmatrix} \sigma_{xx} & \sigma_{xy} & 0 \\ \sigma_{yx} & \sigma_{yy} & 0 \\ 0 & 0 & \sigma_{zz} \end{bmatrix} \quad (3.2.4)$$

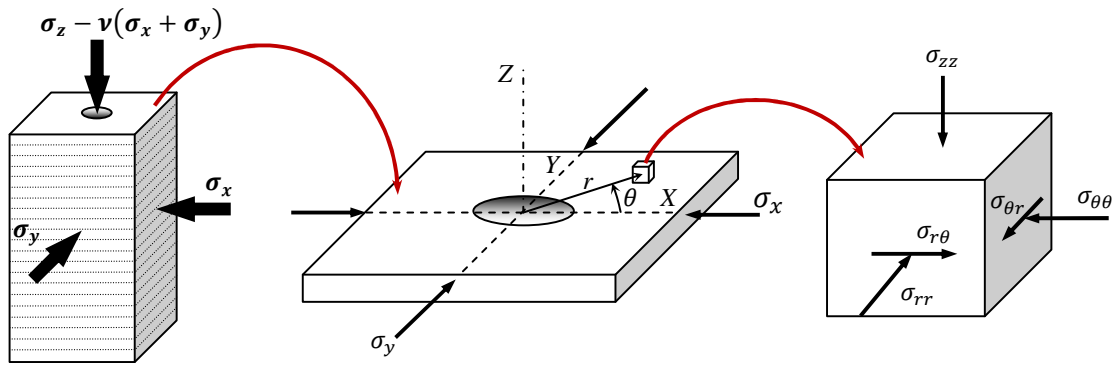


Figure 3.3 Demonstrating the conditions for applying plane strain assumption for calculating longitudinal stress components around a borehole

The component  $\sigma_{zz}$  can be temporarily removed from the analysis to effectively reduce the three-dimensional problem to a two-dimensional problem, dealing only with in-plane terms. The stress component  $\sigma_{zz}$  will then be determined in a manner to maintain the constraint of zero longitudinal strain, i.e.  $\varepsilon_{zz} = \varepsilon_{xz} = \varepsilon_{yz} = 0$ .

Therefore, when far-field in situ stresses are considered as principal stresses with respect to the borehole orientation (Fig. 3.3), considering Eqs. 3.2.2 and the assumption of plane strain the vertical stress component,  $\sigma_{zz}$ , and the associated out-of-plane shear stresses,  $\sigma_{rz}$  and  $\sigma_{\theta z}$ , can be calculated as follows:

$$\sigma_{zz} = \sigma_{zz_1} + \nu(\sigma_{rr} + \sigma_{\theta\theta}) = \sigma_z - 2\nu(\sigma_x - \sigma_y) \left( \frac{a^2}{r^2} \right) \cos 2\theta$$

$$\sigma_{rz} = \sigma_{\theta z} = 0 \quad (3.2.5)$$

### ***Changes in the initial stress state due to the introduction of the borehole***

The pre-existing in situ stress field is redistributed due to the introduction of the borehole. Changes in the initial stress state due to the stress redistribution can be manifested as the difference between the values of pristine stress components acting on a rock element before drilling the borehole, as illustrated in Fig. 3.2, and stress components on the same element after the completion of the drilling operations. Therefore, considering Eqs. 3.1.1, 3.2.1 and 3.2.5, changes in the pre-existing in situ stress field can be formulated as follows:

$$\Delta\sigma_{rr} = \sigma_{rr} - \sigma_{rr_0} = - \left[ \frac{\sigma_x + \sigma_y}{2} + \frac{\sigma_x - \sigma_y}{2} \left( 4 - 3 \frac{a^2}{r^2} \right) \cos 2\theta \right] \left( \frac{a^2}{r^2} \right)$$

$$\Delta\sigma_{\theta\theta} = \sigma_{\theta\theta} - \sigma_{\theta\theta_0} = \left[ \frac{\sigma_x + \sigma_y}{2} - \frac{\sigma_x - \sigma_y}{2} \left( 3 \frac{a^2}{r^2} \right) \cos 2\theta \right] \left( \frac{a^2}{r^2} \right)$$

$$\Delta\sigma_{r\theta} = \sigma_{r\theta} - \sigma_{r\theta_0} = \frac{\sigma_x + \sigma_y}{2} \left( 3 \frac{a^4}{r^4} - 2 \frac{a^2}{r^2} \right) \sin 2\theta$$

$$\Delta\sigma_{zz} = \sigma_{zz} - \sigma_{zz_0} = -2\nu(\sigma_x - \sigma_y) \left( \frac{a^2}{r^2} \right) \cos 2\theta$$

$$\Delta\sigma_{rz} = \Delta\sigma_{\theta z} = 0 \quad (3.2.6)$$

### ***Total induced in situ stresses***

Total induced in situ stress components acting on the rock material adjacent to the borehole wall can be calculated by adding the stress changes, given by Eqs. 3.2.6 to the initial in situ stress components given by Eqs. 3.2.1. Therefore, total induced stresses in the vicinity of a vertical borehole are given as follows:

$$\sigma_{rr(t)} = \sigma_{rr_0} + \Delta\sigma_{rr} = \frac{\sigma_x + \sigma_y}{2} \left(1 - \frac{a^2}{r^2}\right) + \frac{\sigma_x - \sigma_y}{2} \left(1 - 4\frac{a^2}{r^2} + 3\frac{a^4}{r^4}\right) \cos 2\theta$$

$$\sigma_{\theta\theta(t)} = \sigma_{\theta\theta_0} + \Delta\sigma_{\theta\theta} = \frac{\sigma_x + \sigma_y}{2} \left(1 + \frac{a^2}{r^2}\right) - \frac{\sigma_x - \sigma_y}{2} \left(1 + 3\frac{a^4}{r^4}\right) \cos 2\theta$$

$$\sigma_{r\theta(t)} = \sigma_{r\theta_0} + \Delta\sigma_{r\theta} = \frac{-(\sigma_x - \sigma_y)}{2} \left(1 + 2\frac{a^2}{r^2} - 3\frac{a^4}{r^4}\right) \sin 2\theta$$

$$\sigma_{zz(t)} = \sigma_{zz_0} + \Delta\sigma_{zz} = \sigma_z - 2\nu(\sigma_x - \sigma_y) \left(\frac{a^2}{r^2}\right) \cos 2\theta$$

$$\sigma_{rz(t)} = \sigma_{\theta z(t)} = 0 \tag{3.2.6}$$

After the completion of the drilling operations in a formation under pre-existing in situ stresses, total induced stresses acting on an element at a radial distance  $r$  from the borehole centre are given by Eqs. 3.2.6, provided that the far field in situ stresses are principal stresses with respect to the borehole orientation, as was the case for the vertical borehole illustrated in Fig. 3.3. Furthermore, Eqs. 3.2.6 show that  $\sigma_{rr}$  takes its smallest values and  $\sigma_{\theta\theta}$  takes its largest values, i.e.  $\sigma_{rr}$  and  $\sigma_{\theta\theta}$  are at their most deviatoric state, at  $r = a$ . This observation is important because rock failure will always be initiated at the point where the stresses are at their most deviatoric state, which is the case for rock material adjacent to the borehole wall. It is also important to note that Eqs. 3.2.6 have been derived based on the assumption that the hole has been drilled into a pre-stressed block of rock, as illustrated in Fig. 3.3, and the problem is entirely different from drilling a hole into a block and then loading the block from zero. It is of significant importance to take into account this boundary condition when developing a model for estimating the induced stresses around a borehole; nevertheless, it has always been neglected and has not been clearly explained in the existing literature.

In order to validate the assumed boundary conditions in the analytical model, a finite element analysis (FEA) was conducted using the commercial software package ABAQUS/6.9. This FEA was used to numerically calculate the induced stresses in the vicinity of the borehole with

exactly the same boundary conditions as those assumed for developing the analytical model. Some basic concepts of the finite element method applied in this analysis are presented in Appendix A.

### 3.2.1. Numerical model of a vertical borehole

Results of stress measurement in Australia indicate that the vertical stress  $\sigma_v$  increases linearly with depth at a rate of approximately 0.022 MPa/m, minor horizontal stress  $\sigma_h$  at a rate of approximately 0.015 MPa/m, major horizontal stress  $\sigma_H$  at a rate of between approximately 0.022 and 0.025 MPa/m, and pore fluid pressure at a rate of approximately 0.01 MPa/m (Hillis and Reynolds, 2000). Therefore, at a depth of 3000 m, the total principal stresses could typically be  $\sigma_v = 66$  MPa,  $\sigma_h = 45$  MPa and  $\sigma_H = 75$  MPa with a pore fluid pressure of 30 MPa in porous rocks.

Finite Element Analysis (FEA) was carried out, using the ABAQUS/6.9 software package, for estimating the induced stresses around a borehole at a depth of 3000 m. Here as well as for the analytical model, plane strain boundary conditions were assumed, i.e. assuming zero deformation along the axis of the vertical borehole. Furthermore, the borehole was assumed to be drilled in a rock with a Poisson's ratio of 0.35 and elastic moduli of 48 GPa. The borehole radius was taken as 0.08 m. Furthermore, it is of paramount importance to note that the borehole is assumed to be drilled in a block of rock which is already stressed. In order to incorporate this pre-stress field in the finite element model two alternative approaches can be adopted as follows:

- The model space can be created as a block without a hole on which a given set of far-field stresses are acting. The location of the prospective hole must be specified in the meshing step. The same as for the analytical model, all displacements along the Z-axis are supposed to be suppressed. After redistribution of the stress field in the model space and reaching the state of equilibrium, elements which have been ascribed to the location of the borehole will be removed from the model space and then the induced stresses due to the element removal will be measured. It should be noted that as a result of

suppressing the displacements along the Z-direction the term  $\nu(\sigma_{xx} + \sigma_{yy})$  will act in the opposite direction of the vertical stress,  $\sigma_z$ , due to the Poisson's effect and therefore, will be subtracted from the pristine value of  $\sigma_z$ .

- An alternative and more convenient approach for incorporating the pre-existing stress field is to create the model space as a block which contains the borehole under the given set of far-field stresses and define a constant nodal displacement in the Z-direction. The magnitude of this constant displacement is calculated as:

$$d = \frac{\nu(\sigma_{xx} + \sigma_{yy})}{E} \quad (3.2.7)$$

It merits noting that since the stiffness matrix is known (defined in the material property in ABAQUS/6.9), by introducing a nodal displacement, given by Eq. 3.2.7, the associated stress field is calculated and incorporated in subsequent steps of the finite element analysis.

The second approach has been adopted for conducting the finite element analysis (FEA) in the current study. The result of the numerical analysis was then compared to the existing analytical model (Eqs. 3.2.6). The zone of influence around the borehole was assumed to be a circle with a radius of 0.48 m which is six times greater than the borehole radius. Thus, the radial distance from the borehole wall and the border of the zone of influence was 0.4 m. This zone was discretised by 40 concentric circles and each one of these concentric circles was discretised into 120 elements. Therefore, the radial distance from the centre of the borehole to the centroid of each element can be calculated as:

$$r = a + \left( 5 \times 10^{-3} + 0.1m \right) \quad m = 0, 1, 2, \dots, 39 \quad (3.2.8)$$

Where  $a$  is the borehole radius and the parameter  $m$  is a counter for concentric circles, counting from 0 for the circle immediately adjacent to the borehole wall and 39 for the circle adjacent to the border of the zone of influence. Furthermore, the angle  $\theta$ , measured counter-clockwise from the X-axis, as illustrated in Fig. 3.4, indicates the angular location of the centroid of each element around the borehole and is given by:

$$\theta = \frac{3}{2} + 3(n-1) \quad n = 1, 2, \dots, 120 \quad (3.2.9)$$

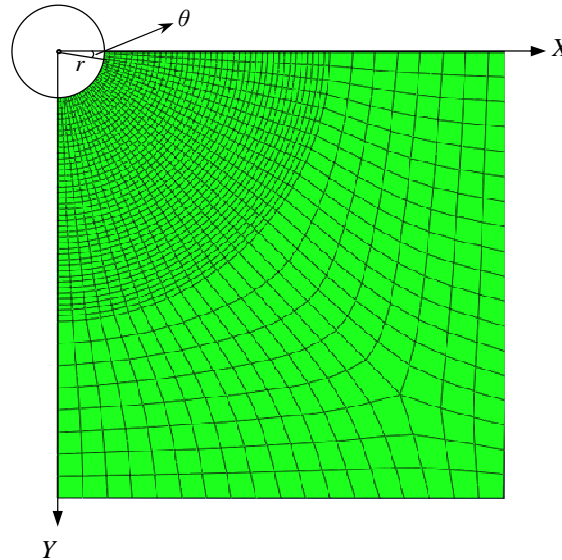


Figure 3.4 Radial distance from the borehole centre and angular position of a given element

The calculated values for  $r$  and  $\theta$  from Eqs. 3.2.8 and 3.2.9 were substituted into the analytical model (Eqs. 3.2.6) and then the corresponding stress components in analytical model and the numerical model were compared to one another. The results of the quantitative comparison between the numerical and analytical models are presented in Appendix B, Table B.1

According to Eqs. 3.2.6, induced stresses around the borehole not only vary as the radial distance from the borehole wall increases, for a constant  $\theta$ , but also alter with changing angular position around the borehole, for a constant  $r$ . Changes in the induced stresses in the finite element model as a function of angular position around the borehole have been illustrated in Figs. 3.5 and 3.6 and have been compared graphically with the analytical solution. Since errors in the numerical analysis in all cases are less than 2%, when compared with the analytical model, it can be inferred that the finite element analysis for estimating stresses around a borehole, which is drilled into an isotropic, homogeneous and linearly elastic rock, is valid and has been conducted accurately. Furthermore, since the finite element analysis clarifies the boundary conditions assumed for deriving the analytical model, for

which there exists no clear explanation in the literature, this study can also be considered as a cross-validation, as it sheds light on the procedure of formulating the analytical solution.

As can be observed in Figs. 3.5 and 3.6, stress concentration occurs at two opposite points at the borehole wall, i.e.  $\theta = 0^\circ$  and  $\theta = 180^\circ$ , and in the direction of the minimum horizontal stress,  $\sigma_h$ . Apart from the stress concentration, stresses are found to be highly deviatoric at these two angular positions (Figs. 3.5 and 3.6). Recalling that borehole instability occurs due to rock failure at the borehole wall, and knowing that a highly deviatoric stress state is an underlying factor which leads to rock failure, these angular positions, around the borehole, are of particular interest. However, since the induced stresses around the borehole also vary with radial distance from the borehole wall, it also merits investigating the changes in induced stresses along radial direction at  $\theta = 0^\circ$  or  $180^\circ$  to determine at what distance from the borehole wall the induced stresses are at their maximum deviatoric state.

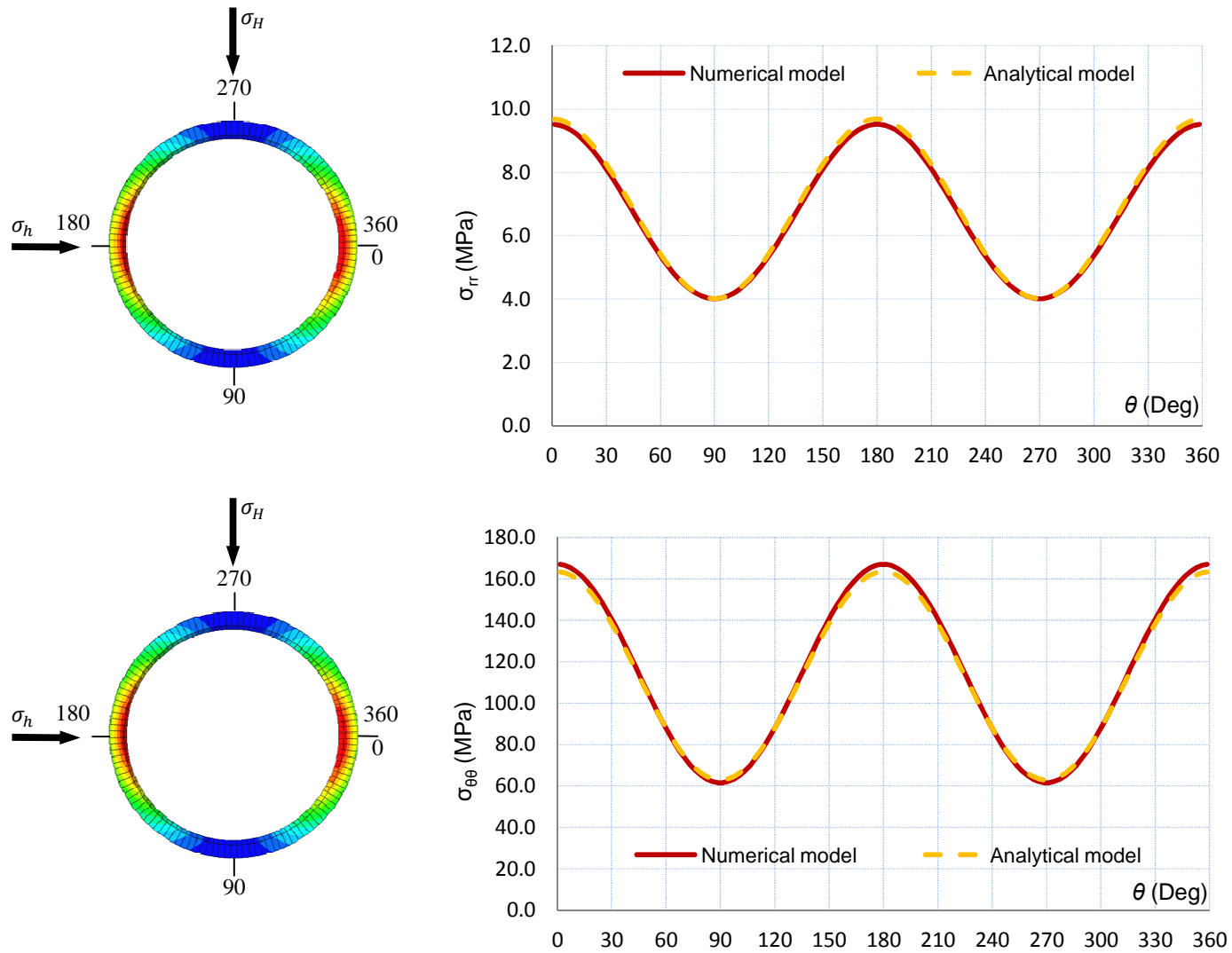


Figure 3.5 Comparison between numerical and analytical model for variation of induced radial ( $\sigma_{rr}$ ) and tangential ( $\sigma_{\theta\theta}$ ) stresses around the vertical borehole at  $r = 0.085$  m

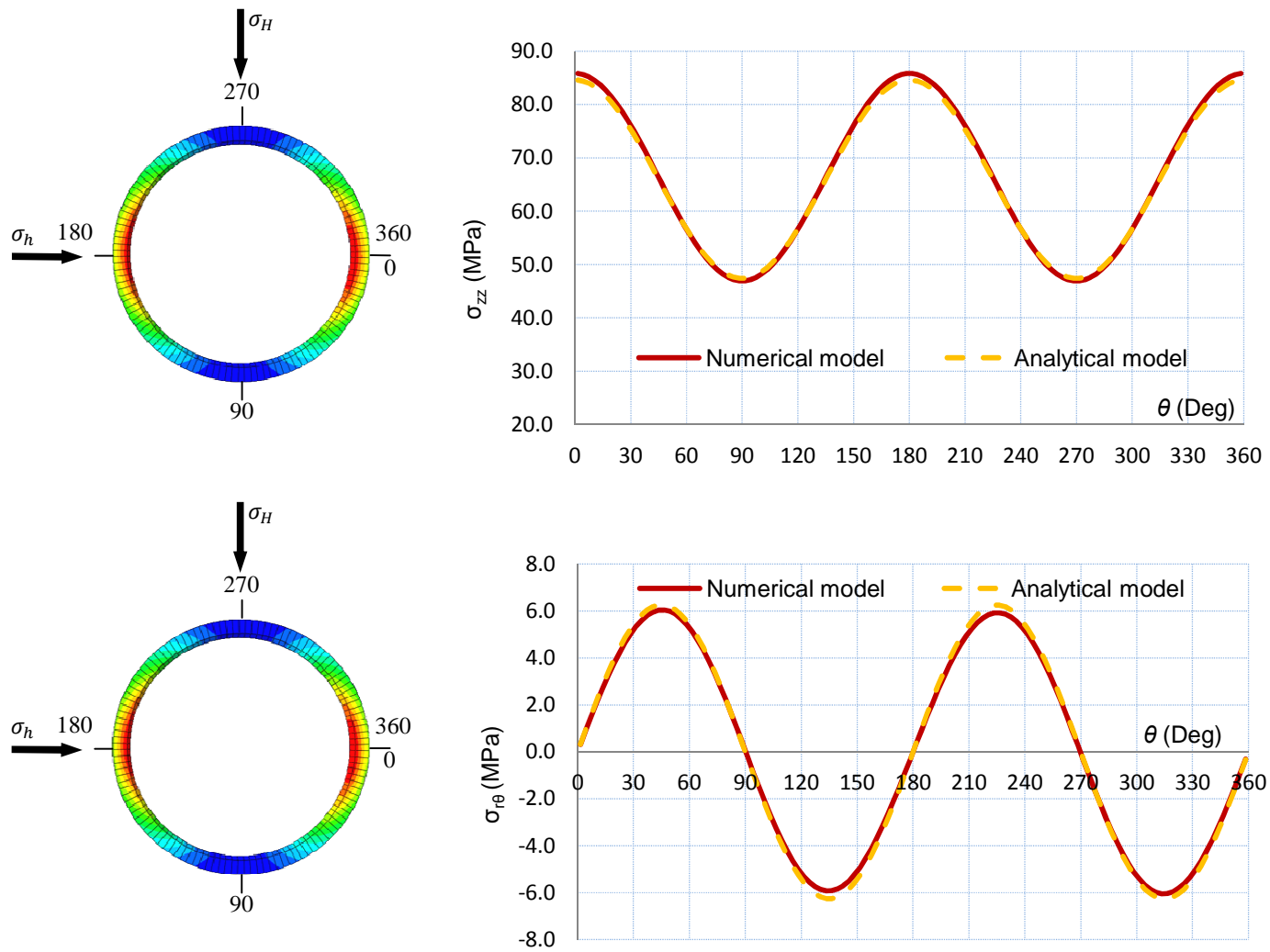


Figure 3.6 Comparison between numerical and analytical model for variation of induced vertical ( $\sigma_{zz}$ ) and in-plane shear ( $\sigma_{r\theta}$ ) stresses around the vertical borehole at  $r = 0.085$  m

Fig. 3.7 illustrates the changes in induced radial,  $\sigma_{rr}$ , tangential,  $\sigma_{\theta\theta}$ , and vertical,  $\sigma_{zz}$ , stresses along the radial direction,  $r$ . As is obvious from Fig. 3.7, the maximum values of induced stresses occur at the borehole wall, i.e. where  $r = 0.08$  m (borehole radius), and more importantly, the induced stress components are highly deviatoric at the borehole wall ( $r = 0.08$  m), compared to other points located at further distance from the borehole wall (Fig.3.7).

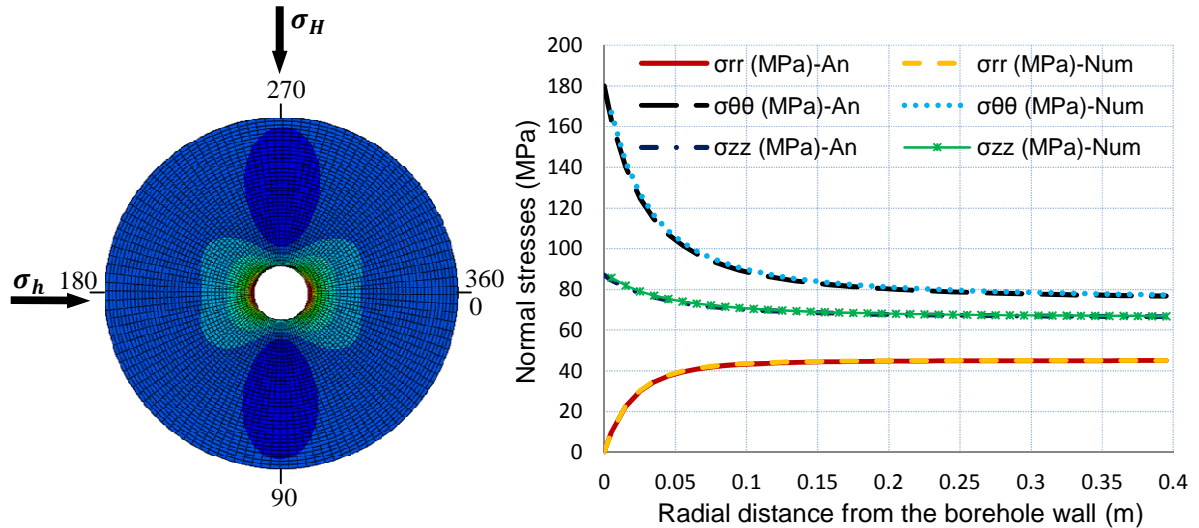


Figure 3.7 Comparison between numerical and analytical model for variation of induced stresses along the radial direction  $r$ , at  $\theta = 0$ , for the vertical borehole

Furthermore, the in-plane shear stress component,  $\sigma_{r\theta}$ , is zero at the borehole wall and, as illustrated in Fig. 3.8, it increases dramatically with increasing radial distance from the borehole wall until it reaches a maximum value at a distance close to the borehole wall, in this case at 0.05m, from the borehole wall. After reaching its peak value, at a small distance from the borehole wall, the in plane-shear stress,  $\sigma_{r\theta}$ , declines gradually until it reaches a plateau (in this case 0.8 MPa).

Accordingly, in the case of the elastic solution, rock failure is anticipated to initiate at two opposite points around the borehole, i.e.  $\theta = 0^\circ$  and  $\theta = 180^\circ$ , in the direction of the minimum horizontal stress,  $\sigma_h$ , and at the borehole wall due to the stress concentration and the deviatoric nature of the stress state. However, it should be noted that the occurrence of rock failure is highly dependent upon the strength of the rock material surrounding the borehole. Techniques for estimating the strength of rock material will be comprehensively investigated in Chapter 4.

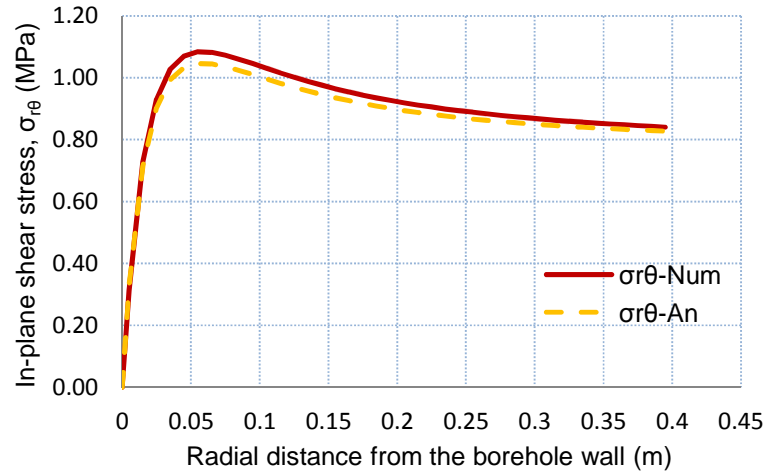


Figure 3.8 Comparison between numerical and analytical model for variation of induced in-plane shear stress along the radial direction  $r$ , at  $\theta = 0$ , for a vertical borehole

According to Eq. 3.2.6, and with respect to Figs. 3.7 and 3.8, the stress state at the two opposite points located on the borehole circumference, i.e.  $\theta = 0^\circ$  and  $\theta = 180^\circ$ , for a vertical borehole at the depth of 3000 m is given by the following stress tensor:

$$[\sigma_{ij}] = \begin{bmatrix} \sigma_{rr} & \sigma_{r\theta} & \sigma_{ra} \\ \sigma_{\theta r} & \sigma_{\theta\theta} & \sigma_{\theta a} \\ \sigma_{ar} & \sigma_{a\theta} & \sigma_{aa} \end{bmatrix} = \begin{bmatrix} 0 & 0 & 0 \\ 0 & 179.92 & 0 \\ 0 & 0 & 86.97 \end{bmatrix} \quad (3.2.10)$$

### 3.3. Stress Analysis around a Deviated Borehole

In cases where the far-field in situ stresses are not principal stresses with respect to the borehole orientation, for example, in the case of a deviated borehole, as illustrated in Fig. 3.9, a general stress state exists at the borehole proximity. Considering a block of rock, the upper and bottom faces of which are perpendicular to the borehole axis, all components of the associated stress tensor can be identified.

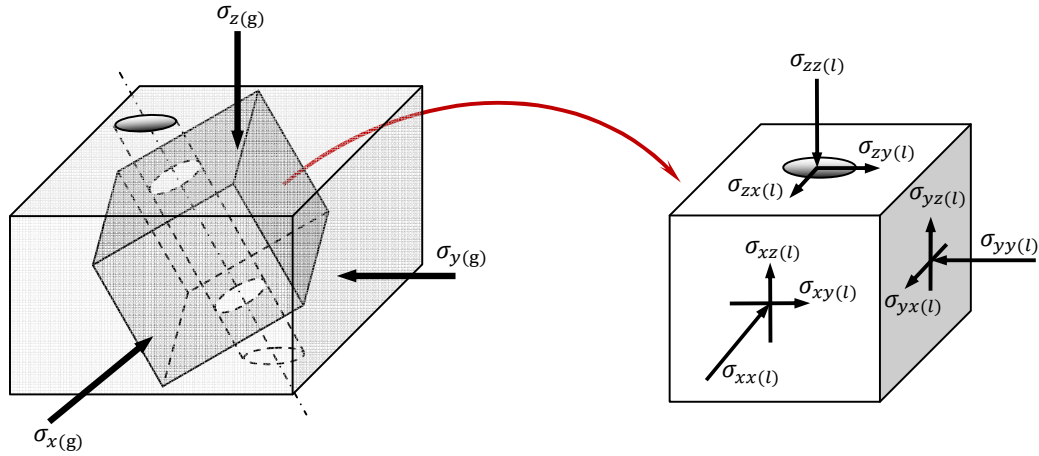


Figure 3.9 General stress state in the vicinity of an inclined borehole

Subscripts (g) and (l) in Fig. 3.9 represent the far-field stress components, measured with respect to the global and local coordinates, respectively. Since the following analyses were conducted considering a local coordinate system as a reference the Z-axis of which coincides with the axis of the borehole, the subscript *L* will be eliminated in any successive nomination of components of the general stress tensor. Therefore, the general stress tensor, which describes the stress state in the vicinity of a deviated borehole can be given as:

$$[\sigma_{ij}] = \begin{bmatrix} \sigma_{xx} & \sigma_{xy} & \sigma_{xz} \\ \sigma_{yx} & \sigma_{yy} & \sigma_{yz} \\ \sigma_{zx} & \sigma_{zy} & \sigma_{zz} \end{bmatrix} \quad (3.3.1)$$

Assuming the axis of the borehole to be the axis of elastic symmetry (isotropic case), induced stresses around a deviated borehole, for which far-field stresses are not principal stresses, were first analytically formulated by Hiramatsu and Oka (1962) and later explained in detail in a report by Fairhurst (1968). The strategy for deriving the analytical solution was to divide the general stress problem into two separate problems:

- a plane strain problem for calculating induced stresses around the deviated borehole due only to far-field normal stresses ( $\sigma_{xx}$ ,  $\sigma_{yy}$  and  $\sigma_{zz}$ ) and in-plane shear stress acting on a plane perpendicular to the borehole axis ( $\sigma_{xy} = \sigma_{yx}$ )

- an anti-plane strain problem for calculating induced stresses in the vicinity of the inclined borehole merely due to out of plane shear stresses ( $\sigma_{zx} = \sigma_{xz}$  and  $\sigma_{yz} = \sigma_{zy}$ )

Consequently, adopting the superposition method the general stress problem is assumed to be as the summation of the plane strain and anti-plane strain problems, as illustrated in Fig. 3.10.

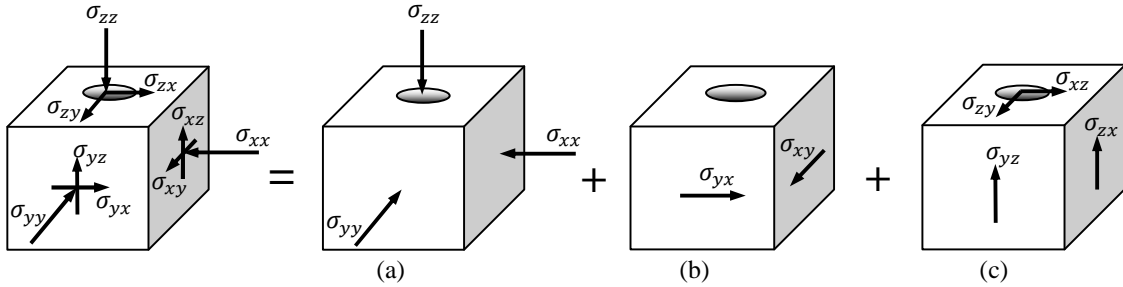


Figure 3.10 Corresponding stresses for (a) and (b) plain strain problem and (c) for anti-plane strain problem

Stress analysis for the case (a) in Fig. 3.10 is the same as for a vertical borehole, as explained in Section 3.2. In order to incorporate the effect of far-field in-plane shear stresses (Fig. 3.10 (b)), the induced stresses around the borehole due to the far-field normal stresses can be superposed by the induced stresses due to the pure far-field in-plane shear stresses. It merits noting that in both cases (a) and (b) in Fig. 3.10 stresses around the borehole are calculated based on the assumption of plane strain, i.e.  $\epsilon_{zz} = \epsilon_{zx} = \epsilon_{zy} = 0$ . The corresponding stress tensor, which describes the stress state in the cases (a) and (b) in Fig. 3.10, is also expressed by the plane strain stress tensor, given by Eq. 3.2.3.

### 3.3.1. Stresses at the borehole wall due to far-filed in-plane shear, $\sigma_{xy}$ and normal stresses, $\sigma_{xx}$ , $\sigma_{yy}$ and $\sigma_{zz}$

Consider a plane perpendicular to the borehole axis on which shear stresses  $\sigma_{xy} = \sigma_{yx}$  are acting (Fig. 3.11). If this plane is rotated to find the principal directions and the associated principal stresses, then Kirsch equations (Eqs. 3.1.1) can be applied to calculate the total stresses around the hole. The rotation matrix, for rotating a two-dimensional Cartesian coordinate system  $(X, Y)$ , is defined as follows:

$$R = \begin{bmatrix} \cos \beta & -\sin \beta \\ \sin \beta & \cos \beta \end{bmatrix} \quad (3.3.2)$$

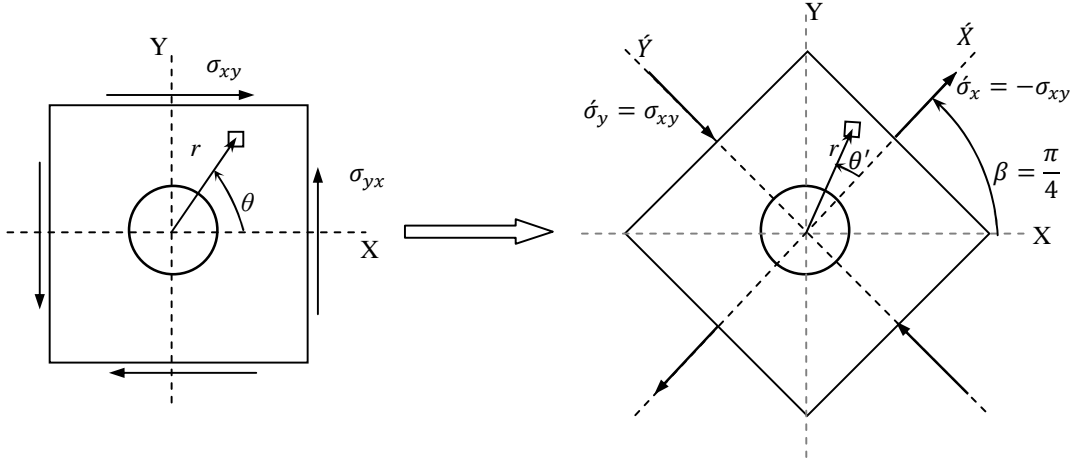


Figure 3.11 Demonstrating the method adopted for calculating induced stresses around a borehole due to pure far-field shear stresses, acting on a plane perpendicular to the borehole axis

The angle  $\beta$  by which the plane and the coordinates  $X$  and  $Y$  have to be rotated to put the plane in a position where it has its faces perpendicular to the principal directions  $X'$  and  $Y'$  (Fig. 3.11), can be calculated from the following relationship:

$$\begin{bmatrix} \cos \beta & -\sin \beta \\ \sin \beta & \cos \beta \end{bmatrix} \begin{bmatrix} 0 & \sigma_{xy} \\ \sigma_{yx} & 0 \end{bmatrix} \begin{bmatrix} \cos \beta & -\sin \beta \\ \sin \beta & \cos \beta \end{bmatrix}^T = \begin{bmatrix} \sigma_{xs} & 0 \\ 0 & \sigma_{ys} \end{bmatrix} \quad (3.3.3)$$

Subscript  $s$  for normal stress components in Eq. 3.3.3 indicates that the magnitude of the normal stresses  $\sigma_x$  and  $\sigma_y$  is equal to the magnitude of shear stresses  $\sigma_{xy} = \sigma_{yx}$ .

From Eq. 3.3.3 the angle  $\beta$  is calculated as  $\frac{\pi}{4}$  and  $\sigma_{ys} = -\sigma_{xs} = \sigma_{xy}$ , as illustrated in Fig. 3.11. Furthermore, stress components acting on an element at a radial distance  $r$  from the borehole centre and at an angular distance measured counter-clockwise from the  $X$ -axis can be calculated in a cylindrical coordinate system by substituting  $-\sigma_{xy}$  and  $\sigma_{xy}$  for  $\sigma_x$  and  $\sigma_y$ , respectively, and  $\theta' = \left(\theta - \frac{\pi}{4}\right)$  for  $\theta$  in Eqs. 3.1.1. Therefore, stress components around the borehole due only to far-field in-plane shear stresses are calculated as follows:

$$\sigma_{rr(FS)} = \sigma_{xy} \left( 1 - \frac{4a^2}{r^2} + \frac{3a^4}{r^4} \right) \sin 2\theta$$

$$\sigma_{\theta\theta(FS)} = -\sigma_{xy} \left( 1 + \frac{3a^4}{r^4} \right) \sin 2\theta$$

$$\sigma_{r\theta(FS)} = \sigma_{xy} \left( 1 + \frac{2a^2}{r^2} - \frac{3a^4}{r^4} \right) \cos 2\theta$$

$$\sigma_{rz(FS)} = \sigma_{\theta z(FS)} = 0 \quad (3.3.4)$$

Consequently, on the assumption of plane strain,  $\sigma_{aa(FS)}$  can be calculated as:

$$\sigma_{zz(FS)} = \nu \left( \sigma_{rr(FS)} + \sigma_{\theta\theta(FS)} \right) = -4\nu \sigma_{xy} \frac{a^2}{r^2} \sin 2\theta \quad (3.3.5)$$

The subscript *FS* in Eqs. 3.3.4 and 3.3.5 indicates that the stress components around the borehole have been calculated by merely considering the effect of far-field in-plane shear stresses on the induced stress field around the borehole. After superposing Eqs. 3.2.6 by Eqs. 3.3.4 and 3.3.5, components of induced stresses around the borehole due to the far-field normal and in-plane shear stresses are given as follows:

$$\sigma_{rr(NS)} = \frac{\sigma_x + \sigma_y}{2} \left( 1 - \frac{a^2}{r^2} \right) + \frac{\sigma_x - \sigma_y}{2} \left( 1 + \frac{3a^4}{r^4} - \frac{4a^2}{r^2} \right) \cos 2\theta + \sigma_{xy} \left( 1 + \frac{3a^4}{r^4} - \frac{4a^2}{r^2} \right) \sin 2\theta$$

$$\sigma_{\theta\theta(NS)} = \frac{\sigma_x + \sigma_y}{2} \left( 1 + \frac{a^2}{r^2} \right) - \frac{\sigma_x - \sigma_y}{2} \left( 1 + \frac{3a^4}{r^4} \right) \cos 2\theta - \sigma_{xy} \left( 1 + \frac{3a^4}{r^4} \right) \sin 2\theta$$

$$\sigma_{r\theta(NS)} = \left( -\frac{\sigma_x - \sigma_y}{2} \sin 2\theta + \sigma_{xy} \cos 2\theta \right) \left( 1 - \frac{3a^4}{r^4} + \frac{2a^2}{r^2} \right)$$

$$\sigma_{zz(NS)} = \sigma_z - 2\nu (\sigma_x - \sigma_y) \left( \frac{a^2}{r^2} \right) \cos 2\theta - 4\nu \sigma_{xy} \frac{a^2}{r^2} \sin 2\theta \quad (3.3.6)$$

The subscript *NS* in Eqs. 3.3.6 indicates that stresses at the borehole proximity have been calculated due only to the far-field normal and in-plane shear stresses.

### 3.3.2. Stresses at the borehole wall due to longitudinal shear stresses ( $\sigma_{xz} = \sigma_{zx}$ ) and ( $\sigma_{yz} = \sigma_{zy}$ )

The closed form solution for stress components around the borehole due to the far-field longitudinal shear stresses acting parallel to the borehole axis, i.e. the case (c) in Fig. 3.10, was derived by Fairhurst (1968) based on the assumption of anti-plane strain. As opposed to plane strain boundary conditions, which allow only for deformations in planes perpendicular to the borehole axis, in anti-plane strain deformations are assumed to take place only along the axis of the borehole and no deformation is allowed in planes containing the cross section of the borehole.

Considering a block of rock as illustrated in Fig. 3.10 (c), for infinitesimal displacements the strain tensor associated with out-of-plane shear stresses can be defined as follows:

$$[\varepsilon] = \begin{bmatrix} 0 & 0 & \frac{\partial u_x}{\partial z} + \frac{\partial u_z}{\partial x} \\ 0 & 0 & \frac{\partial u_y}{\partial z} + \frac{\partial u_z}{\partial y} \\ \frac{\partial u_z}{\partial x} + \frac{\partial u_x}{\partial z} & \frac{\partial u_z}{\partial y} + \frac{\partial u_y}{\partial z} & 0 \end{bmatrix} \quad (3.3.7)$$

However, under anti-plane strain conditions displacements along the *X* and *Y* directions are assumed to be zero. Considering rectangular Cartesian coordinates, the displacement field that leads to a state of anti-plane strain is given as follows:

$$\begin{aligned} u_x = u_y = 0 \\ u_z = u'_z(x, y) \end{aligned} \quad (3.3.8)$$

Where  $u_x$  and  $u_y$  are displacements along the  $X$  and  $Y$  directions respectively and  $U_z$  is the displacement in the  $Z$  direction which is defined as a function of  $x$  and  $y$ . Therefore, the strain tensor associated with anti-plane strain conditions is defined as:

$$\underset{\text{anti-plane strain}}{[\varepsilon]} = \begin{bmatrix} 0 & 0 & \frac{\partial u_z}{\partial x} \\ 0 & 0 & \frac{\partial u_z}{\partial y} \\ \frac{\partial u_z}{\partial x} & \frac{\partial u_z}{\partial y} & 0 \end{bmatrix} \quad (3.3.9)$$

According to Eqs. 3.3.8 and 3.3.9 anti-plane strain deformations can be visualised, considering an element of rock with dimensions of  $dx$ ,  $dy$  and  $dz$ , as illustrated in Fig. 3.12. Furthermore, for an isotropic and linear elastic material the stress tensor that results from a state of anti-plane strain can be expressed as:

$$\underset{\text{anti-plane strain}}{[\sigma]} = \begin{bmatrix} 0 & 0 & \sigma_{xz} \\ 0 & 0 & \sigma_{yz} \\ \sigma_{zx} & \sigma_{zy} & 0 \end{bmatrix} = \begin{bmatrix} 0 & 0 & G \frac{\partial u_z}{\partial x} \\ 0 & 0 & G \frac{\partial u_z}{\partial y} \\ G \frac{\partial u_z}{\partial x} & G \frac{\partial u_z}{\partial y} & 0 \end{bmatrix} \quad (3.3.10)$$

Where  $G$  is the shear modulus of the material.

Accordingly, induced stress components around the borehole when only far-field longitudinal stresses are involved and based on the assumption of anti-plane strain boundary conditions are given as follows:

$$\begin{aligned} \sigma_{rr(0s)} &= \sigma_{\theta\theta(0s)} = \sigma_{r\theta(0s)} = \sigma_{z\theta(0s)} = 0 \\ \sigma_{\theta z(0s)} &= (\sigma_{yz} \cos \theta - \sigma_{xz} \sin \theta) \left(1 + \frac{a^2}{r^2}\right) \\ \sigma_{rz(0s)} &= (\sigma_{yz} \sin \theta + \sigma_{xz} \cos \theta) \left(1 - \frac{a^2}{r^2}\right) \end{aligned} \quad (3.3.11)$$

The subscript *OS* in Eqs. 3.3.11 indicates that the stress components around the borehole have been calculated by considering the far-field out-of-plane shear stresses only.

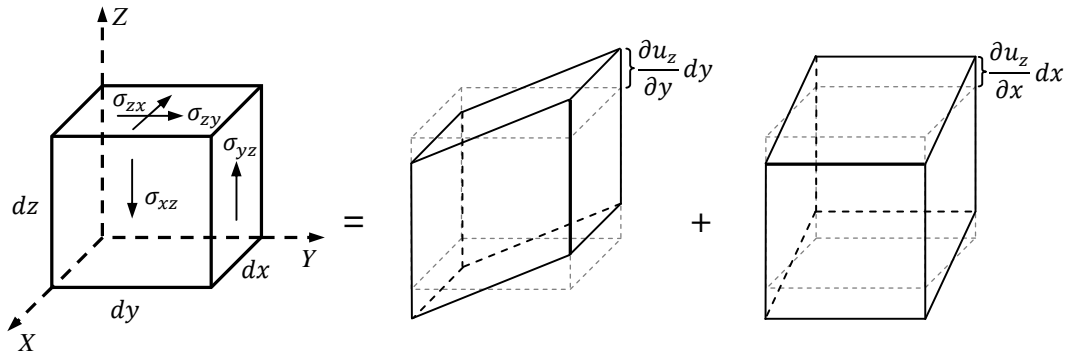


Figure 3.12 Deformations associated with anti-plane strain boundary conditions

Details of the mathematical procedure for deriving longitudinal stress components at the borehole wall,  $\sigma_{r\theta}$  and  $\sigma_{\theta a}$ , is beyond the scope of this research and the reader is referred to Fairhurst (1968) for further information. Eqs. 3.3.6 along with Eqs. 3.3.11 are referred to as the generalised Kirsch equations, which are being widely used for estimating stresses around boreholes, circular tunnels and any other underground structures with a circular cross section in the petroleum and mining industries.

In order to further clarify the boundary conditions assumed in deriving the generalised Kirsch equations, a finite element analysis (FEA) was conducted by assuming the same boundary conditions as those for the analytical model. The FEA for stress analysis around a deviated borehole was undertaken considering the stress conditions in the Earth’s crustal formations of Australia, as given in Section 3.2.1, at the depth of 3000 m. The results of the FEA were compared with the analytical model, namely the generalised Kirsch equations.

### 3.4. Numerical Counterpart of the Generalised Kirsch Equations

Assuming the far-field in situ stresses in the Earth’s crustal rocks in Australia at the depth of 3000 m as  $\sigma_h = 45$  MPa,  $\sigma_H = 75$  MPa and  $\sigma_z = 66$  MPa, the general stress state induced in the vicinity of a deviated borehole is expressed by the general stress tensor given by Eq. 3.3.1. It

was also assumed that the trajectory of the borehole was manifested by the trend/plunge system as 125/10. To specify the components of the general stress tensor necessitates transforming the stress tensor associated with the far-field in situ stresses from the global coordinate system into a local coordinate system, one coordinate of which coincides with the borehole axis. The rotation matrix for performing the transformation can be derived by calculating angles between the axes of the local coordinate system and their counterparts in the global coordinate system. Furthermore, the angle  $\theta_{uv}$  between two lines of trend/plunge  $\alpha_u/\beta_u$  and  $\alpha_v/\beta_v$  can be found from the following expression:

$$\cos \theta_{uv} = [\cos(\alpha_u - \alpha_v) \cos \beta_u \cos \beta_v] + [\sin \beta_u \sin \beta_v] \quad (3.4.1)$$

The trend and plunge of the axes of the global coordinate system ( $X, Y, Z$ ) are given as follows:

Global coordinate system		
Coordinates	Trend (Deg)	Plunge (Deg)
X-axis	0	0
Y-axis	90	0
Z-axis	0	90

On the other hand, the trend and plunge of the axes of a local coordinate system ( $L, M, N$ ) which has one of its axes coincide with the axis of the inclined borehole with trend and plunge of 125/10 are given as:

Local coordinate system		
Coordinates	Trend (Deg)	Plunge (Deg)
L-axis	125	-10
M-axis	215	0
N-axis	125	80

Therefore, with respect to Eq. 3.4.1 the rotation matrix is calculated as follows:

$$[R] = \begin{bmatrix} -0.5649 & 0.8067 & -0.1736 \\ -0.8192 & -0.5736 & 0.0000 \\ -0.0996 & 0.1422 & 0.9848 \end{bmatrix} \quad (3.4.2)$$

Furthermore, the stress state at the depth of 3000 m, in the Earth's crustal rock of Australia and with respect to the global coordinate system is given as a principal stress tensor as follows:

$$[\sigma_{ij}]_p = \begin{bmatrix} 45 & 0 & 0 \\ 0 & 75 & 0 \\ 0 & 0 & 66 \end{bmatrix} \quad (3.4.3)$$

Therefore, components of the general stress tensor, which describes the general stress state around the deviated borehole, are calculated by transforming the principal stress tensor, given by Eq. 3.4.3, and using the transformation matrix,  $[R]$ , given by Eq. 3.4.2, as follows:

$$[\sigma_{ij}]_g = [R][\sigma_{ij}]_p[R]^T = \begin{bmatrix} 65.1565 & -13.8812 & -0.1487 \\ -13.8812 & 54.8697 & -2.4476 \\ -0.1487 & -2.4476 & 65.9738 \end{bmatrix} \quad (3.4.5)$$

The finite element model was created for the deviated borehole using ABAQUS/ 6.9. The borehole radius was given as 0.08 m and the borehole was assumed to be drilled in an isotropic, homogeneous and linearly elastic material with elastic modulus of 48 GPa and Poisson's ratio of 0.35.

Boundary conditions assumed for performing the FEA to calculate induced stresses around the deviated borehole were the same as those assumed for deriving the generalised Kirsch equations. It merits noting that separating the general stress problem into two problems and assuming plane strain boundary condition for one and anti-plane strain boundary condition for the other are simplifying measures which make the derivation of analytical solution possible. However, in reality it is impossible for a block of rock to undergo deformations, on the one hand, on the assumption of plane strain conditions, which is manifested by zero out-of-plane deformations ( $\varepsilon_{zz} = \varepsilon_{zx} = \varepsilon_{zy} = 0$ ), and on the other hand, on the assumption of anti-plane strain conditions, which allows only for the out-of-plane deformations such that  $\varepsilon_{zx} \neq \varepsilon_{zy} \neq 0$  and  $\varepsilon_{zz} = 0$ . It is also impossible to perform these incompatible boundary conditions on a single finite element model and therefore, as for the analytical model, two separate models have been created; one for estimating the induced stresses due to the far-field normal and in

plane shear stresses and the other for modelling induced stresses around the deviated borehole due to the far-field out-of-plane shear stresses.

As is inferred from Eqs. 3.3.6 the radial stress,  $\sigma_{rr}$ , is at its smallest and the tangential stress,  $\sigma_{\theta\theta}$ , is at its largest values at  $r = a$ . Furthermore, as was explained in Section 3.2.1, in the case of a vertical borehole subjected to far-field normal stresses only, the tangential stress is at its maximum value at  $\theta = 0^\circ$  and  $\theta = 180^\circ$ , compared to any other angular positions around the borehole. Points located on these two opposite angular positions on the circumference of the vertical borehole lied in the direction of the minimum horizontal stress and were referred to as stress concentration points (Figs. 3.5 and 3.6). However, when a borehole is drilled into a block of rock which is subjected to far-field normal and in-plane shear stresses, the two opposite points of stress concentration do not lie in the direction of the minimum horizontal stress,  $\sigma_h$ , as they do in the case of a vertical borehole (Figs. 3.13 and 3.14).

An illustrative comparison between the results of the numerical stress analysis, i.e. FEA, and the results of the estimation of induced stresses around the deviated borehole by means of the analytical model, i.e. the generalised Kirsch equations, is presented in Figs. 3.13, 3.14 and 3.15. As can be observed, the results of the finite element analysis comply with the results of the analytical model, which is indicative of validity of the finite element model. Furthermore, the finite element model further clarifies the assumed boundary conditions and simplifying assumptions adopted for deriving the generalised Kirsch equations for calculation of induced stresses in the proximity of a deviated borehole. A quantitative comparison and the associated error analysis are given in Appendix B, Tables B.1-B.5

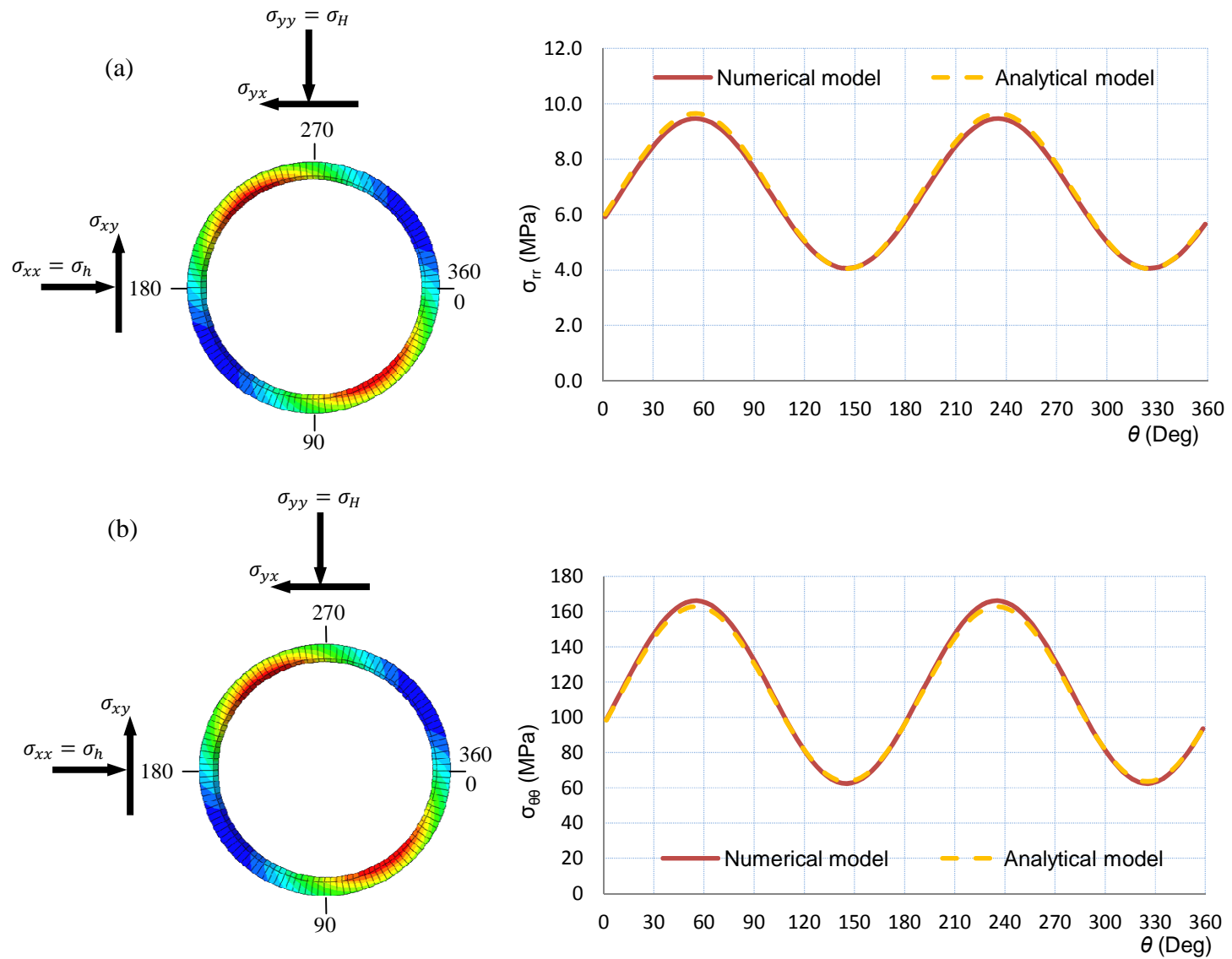


Figure 3.13 Comparison between numerical and analytical model for variation of induced radial ( $\sigma_{rr}$ ) and tangential ( $\sigma_{\theta\theta}$ ) stresses around the inclined

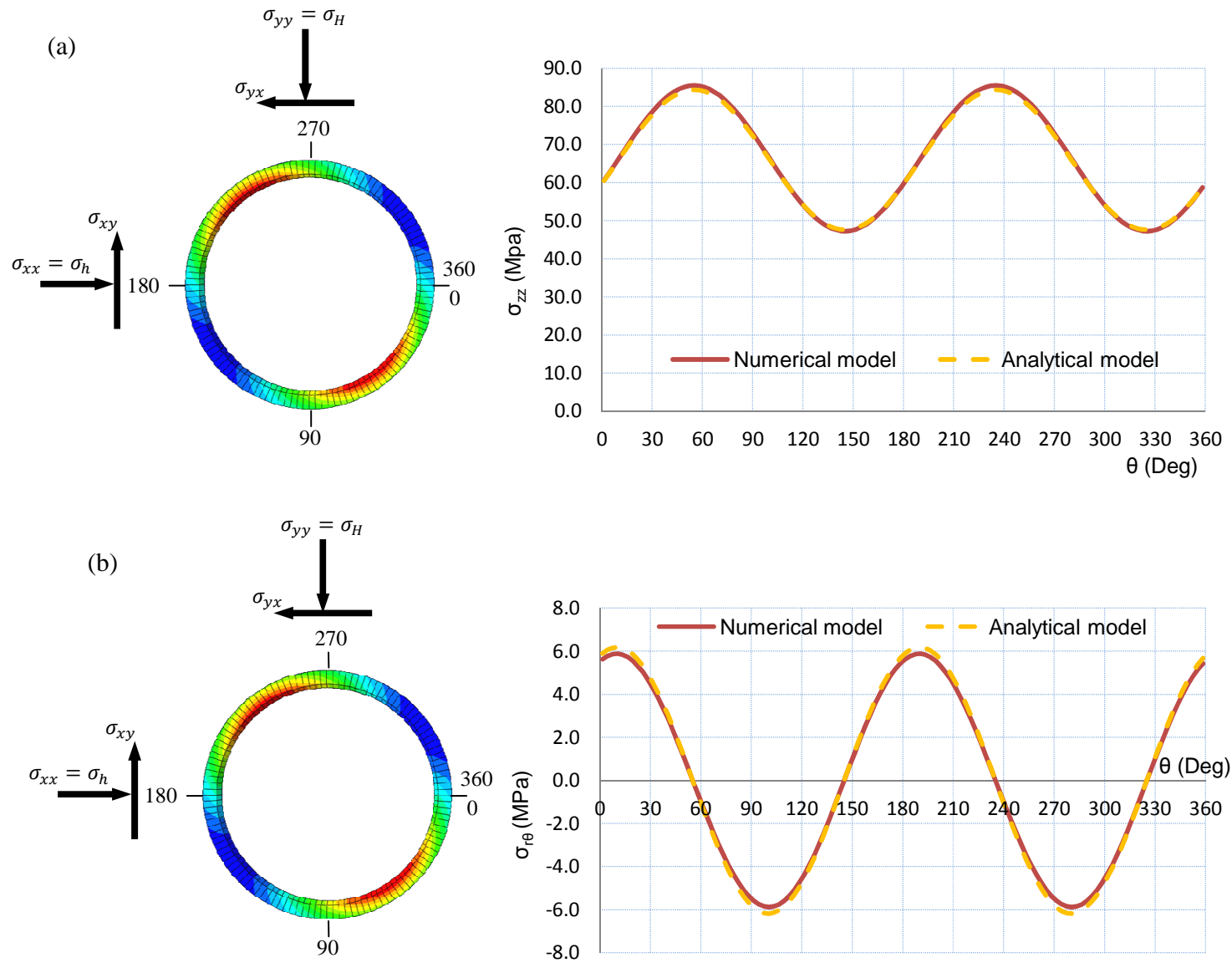


Figure 3.14 Comparison between numerical and analytical model for variation of induced vertical ( $\sigma_{zz}$ ) and in-plane shear ( $\sigma_{r\theta}$ ) stresses around the borehole at  $r = 0.085$  m

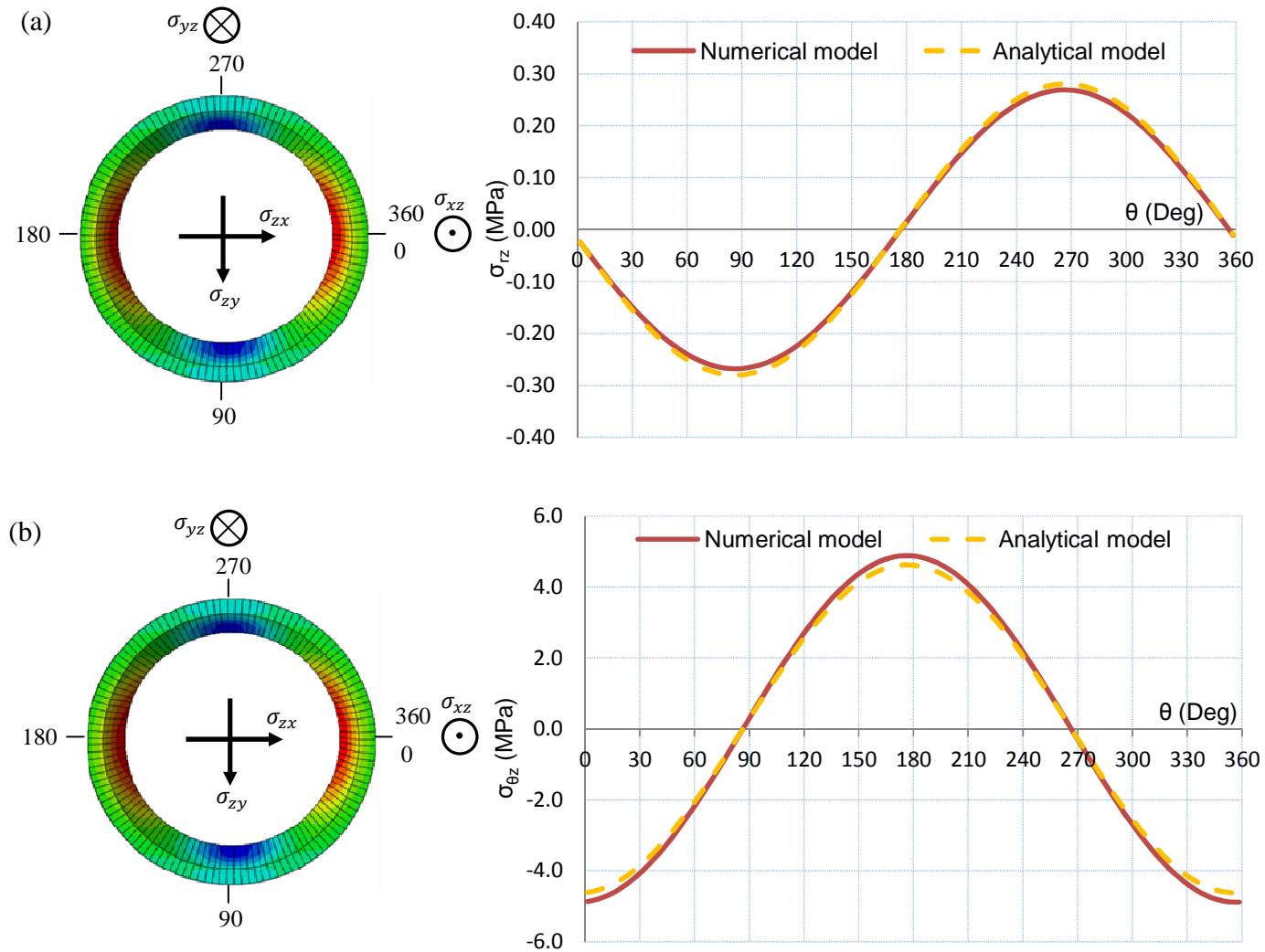


Figure 3.15 Comparison between numerical and analytical model for variation of induced longitudinal shear stresses  $\sigma_{rz}$  and  $\sigma_{\theta z}$ , around the inclined borehole at  $r = 0.085$  m

The region of stress concentration is represented in red in the contour model in Figs. 3.13 and 3.14. It merits mentioning that only two distinct points in these stress concentration region, at which  $\sigma_\theta$  is at its maximum value, are of particular interest. Furthermore, induced stresses around the borehole are at their most deviatoric state at these two opposite points of stress concentration. Therefore, it is of utmost importance to determine the angular position of the two opposite points of stress concentration. As illustrated in Fig. 3.13 (b), the graph, which represents changes in tangential stress  $\sigma_{\theta\theta}$  as a function of angular position  $\theta$  around the borehole, shows four optimum points where the slope of the tangent line to the graph is zero. Therefore, there are four angular positions around the borehole where the value of the tangential stress is either maximum or minimum.

To find these angular positions necessitates differentiating the function  $\sigma_{\theta\theta}$ , given by Eqs. 3.3.6, with respect to  $\theta$  and equating the derivative to zero as follows:

$$\frac{d\sigma_{\theta\theta}}{d\theta} = (\sigma_x - \sigma_y) \left( 1 + \frac{3a^4}{r^4} \right) \sin 2\theta - 2\sigma_{xy} \left( 1 + \frac{3a^4}{r^4} \right) \cos 2\theta = 0 \quad (3.4.6)$$

Therefore, the angular position where the tangential stress is at its minimum or maximum is given by:

$$\tan 2\theta = \frac{2\sigma_{xy}}{\sigma_x - \sigma_y} \quad (3.4.7)$$

Eq. 3.4.7 yields four values for the angle  $\theta$  all of which satisfy Eq. 3.4.6. Recalling that the periodicity of  $\tan 2\theta$  is  $\frac{\pi}{2}$ , four angular positions are determined as:  $\theta, \theta + \frac{\pi}{2}, \theta + \pi, \theta + \frac{3\pi}{2}$ . Substituting these values for  $\theta$  into the  $\sigma_{\theta\theta}$ -function (Eqs. 3.3.6), the maximum and minimum values of  $\sigma_{\theta\theta}$  and, more importantly, the angular positions associated with the maximum value of  $\sigma_{\theta\theta}$  can be identified.

In the case of the deviated borehole, which was considered as a case example for developing the finite element model, four angular positions at which the  $\sigma_{\theta\theta}$ -function is either at its maximum or minimum values are determined by applying Eq. 3.4.7, as is presented in Table 3.1.

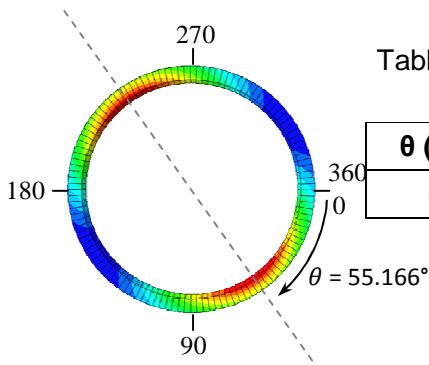


Table 3.1 Determining the angular position of the two points of stress concentration

$\theta$ (Deg)	55.166	145.166	235.166	325.166
$\sigma_{\theta\theta}$	max	min	max	min

Fig. 3.16 illustrates changes in induced stresses at the angular position  $\theta = 55.166^\circ$  as a function of radial distance from the borehole wall, for both numerical and analytical models. Induced stresses are at their most deviatoric state at the borehole wall, where the induced stresses are either at their maximum or minimum values at a given angular position. Therefore, the rock failure is envisaged to initiate at the borehole wall and at two opposite angular position where stress concentration occurs, in this case at  $\theta = 55.166^\circ$  and  $\theta = 235.66^\circ$ . In order to predict the rock failure at the borehole wall and at the two stress concentration points the common strategy is to determine the stress state at these two points at the borehole wall and then investigate whether the rock material is strong enough to sustain the induced stress state. With respect to Fig. 3.16 (and also error analysis Tables B.1-B.5 given in Appendix B), the induced stress state at the two stress concentration points, i.e.  $\theta = 55.166^\circ$  and  $\theta = 235.66^\circ$ , at the wall of the deviated borehole which has been studied as a case example can be identified by the following stress tensor:

$$[\sigma_{ij}] = \begin{bmatrix} \sigma_{rr} & \sigma_{r\theta} & \sigma_{rz} \\ \sigma_{\theta r} & \sigma_{\theta\theta} & \sigma_{\theta z} \\ \sigma_{zr} & \sigma_{z\theta} & \sigma_{zz} \end{bmatrix} = \begin{bmatrix} 0 & 0 & 0 \\ 0 & 179.24 & -3.02 \\ 0 & -3.02 & 86.70 \end{bmatrix} \quad (3.4.8)$$

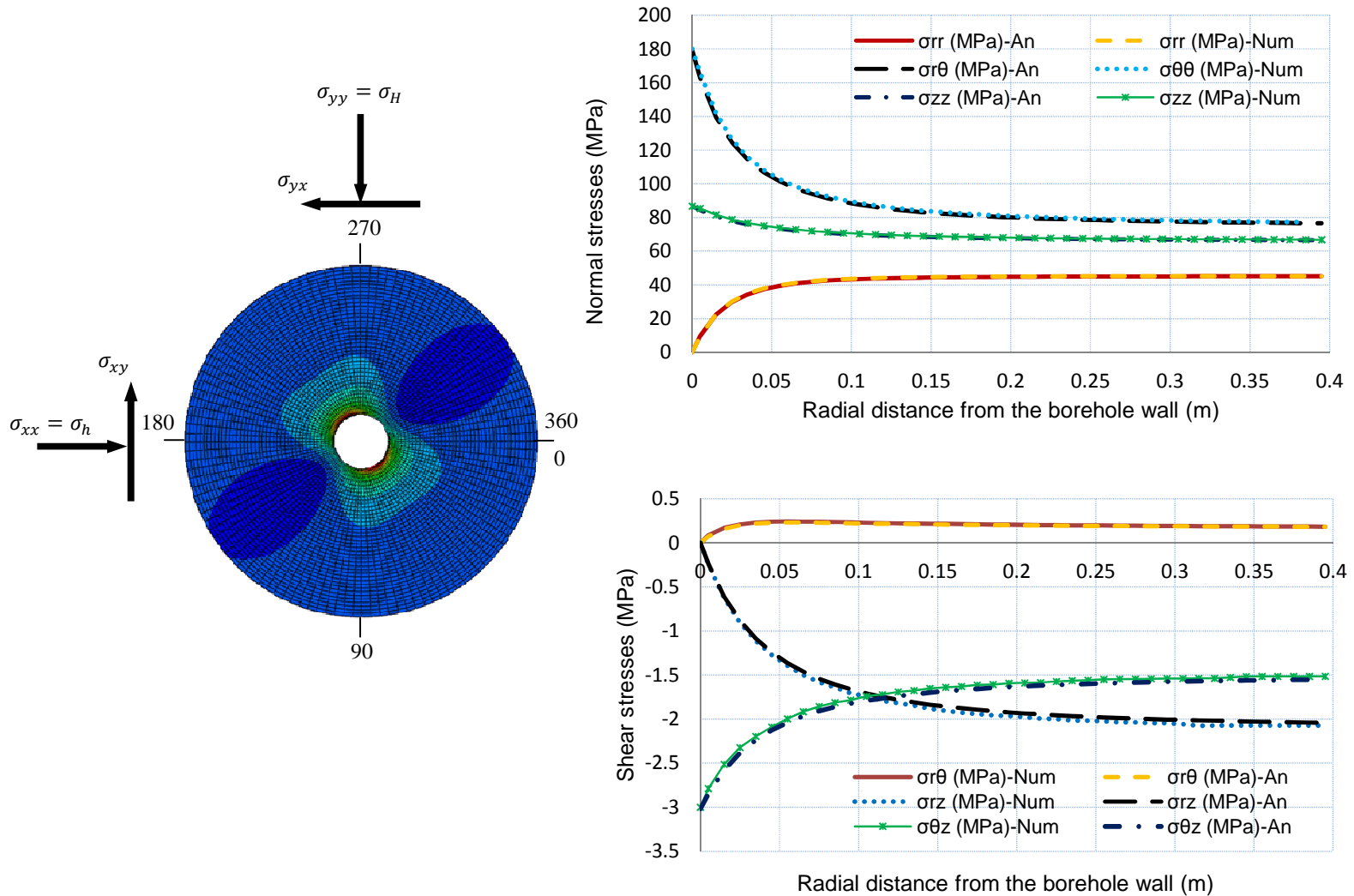


Figure 3.16 Comparison between numerical and analytical model for variation of induced stresses along the radial direction  $r$ , at  $\theta = 55.166^\circ$ , for the inclined borehole

### 3.5. A Modification to the Generalised Kirsch Equations

In the existing analytical model (generalised Kirsch), stresses around the borehole are estimated, on one hand, based on the assumption of plane strain in which no axial deformation is allowed and, on the other hand, based on the assumption of anti-plane strain in which no in-plane deformation is allowed and the only deformation is supposed to take place along the axis of the borehole. The plane strain boundary conditions were assumed in order to facilitate the calculation of the induced stresses around a borehole considering only the far-field in situ normal and in-plane shear stresses and the anti-plane strain boundary conditions were adopted to estimate the effect of the longitudinal, out-of-plane shear stresses on induced stresses around the borehole.

The underlying reason for separating the general stress problem to two problems; one on the assumption of plane strain and the other on the assumption of anti-plane strain was to reduce a three-dimensional problem to two two-dimensional problems for which deriving the analytical solution was feasible. The plane strain and anti-plane strain conditions are simplifying assumptions based on which analytical solutions can be derived as approximations to real general problems, where the mechanics of the three-dimensional problem allows for making such assumptions. Considering a block of rock at the depth of 3000 m, into which a borehole has been drilled, as illustrated in Fig. 3.17, the axial dimension is considerably greater than the cross sectional dimensions, so it can be assumed that the axial deformations are constrained by nearby geo-materials and, therefore, are negligible compared with cross sectional deformations. Hence, the physics of the problem allows for approximately calculating the induced stresses around the borehole due to a far-field general stress state on the assumption of plane strain. It should be noted that all out-of-plane deformations are assumed to be zero on the assumption of plane strain, i.e.  $\varepsilon_{zz} = \varepsilon_{xz} = \varepsilon_{yz} = 0$ . Furthermore, the corresponding out-of-plane shear stresses in the stress tensor associated with the plane strain conditions are also assumed to be zero, i.e.  $\sigma_{xz} = \sigma_{yz} = 0$ , and the vertical normal stress,  $\sigma_{zz}$ , is determined in a manner to restrain zero out-of-plane deformations. The strain and stress tensors associated with the plan stain conditions are given by Eqs. 3.2.2 and 3.2.3.

Therefore, the assumption of anti-plane strain conditions, in order to incorporate the effect of the far-field out-of-plane shear stresses on the induced stresses around the borehole, as explained in Section 3.3.2, is contradictory to the plane strain assumption. However, it was reasoned by Fairhurst (1968) that since out-of-plane shear stresses do not have any impact on the in-plane induced stresses around the borehole, i.e.  $\sigma_{rr}$ ,  $\sigma_{\theta\theta}$  and  $\sigma_{r\theta}$  (Eqs. 3.3.11), the induced out-of-plane stresses around the borehole can be calculated separately and on the assumption of anti-plane strain, which assumes a constant deformation along the borehole axis as a function of gradients of the axial displacement  $u_z$  in the  $X$  and  $Y$  directions as follows:

$$u_z = f\left(\frac{\partial u_z}{\partial x}, \frac{\partial u_z}{\partial y}\right) = \text{constant} \quad (3.5.1)$$

Nevertheless, it merits noting that although the longitudinal shear stresses do not affect the induced in-plane stresses around the borehole, the assumed boundary conditions can be highly influential on the calculated values for the out-of-plane stresses, namely  $\sigma_{zz}$ ,  $\sigma_{rz}$  and  $\sigma_{\theta z}$ .

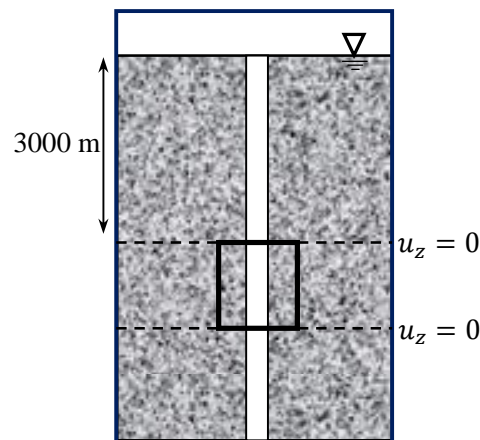


Figure 3.17 A section of a borehole at the depth of 3000 m

A more appropriate approach for estimating stresses around a borehole when a far-field general stress state is involved can be given by solving the three-dimensional problem and by assuming that deformations along the axis of the borehole is suppressed by nearby geomaterials as illustrated in Fig. 3.17. Although deriving an analytical solution to this three-dimensional problem may be difficult or even impossible, numerical methods such as FEA can be employed to solve the problem.

The general strain tensor for defining the three-dimensional deformations of a rock element with dimensions of  $dx$ ,  $dy$  and  $dz$ , in a Cartesian coordinate system can be expressed in terms of the infinitesimal displacements as:

$$[\varepsilon] = \begin{bmatrix} \frac{\partial u_x}{\partial x} & \frac{\partial u_x}{\partial y} + \frac{\partial u_y}{\partial x} & \frac{\partial u_x}{\partial z} + \frac{\partial u_z}{\partial x} \\ \frac{\partial u_x}{\partial y} + \frac{\partial u_y}{\partial x} & \frac{\partial u_y}{\partial y} & \frac{\partial u_y}{\partial z} + \frac{\partial u_z}{\partial y} \\ \frac{\partial u_x}{\partial z} + \frac{\partial u_z}{\partial x} & \frac{\partial u_y}{\partial z} + \frac{\partial u_z}{\partial y} & \frac{\partial u_z}{\partial z} \end{bmatrix} \quad (3.5.2)$$

However, since the assumption of zero deformation along the borehole axis is also indicative of zero displacement, i.e.  $u_z = 0$ , along the axis of the borehole, which is assumed to be coinciding with the  $Z$ -axis of the Cartesian coordinate system, the deformation of the rock element in the proximity of the borehole and at the depth of 3000 m is assumed to be manifested by the following strain tensor:

$$[\varepsilon] = \begin{bmatrix} \frac{\partial u_x}{\partial x} & \frac{\partial u_x}{\partial y} + \frac{\partial u_y}{\partial x} & \frac{\partial u_x}{\partial z} \\ \frac{\partial u_x}{\partial y} + \frac{\partial u_y}{\partial x} & \frac{\partial u_y}{\partial y} & \frac{\partial u_y}{\partial z} \\ \frac{\partial u_x}{\partial z} & \frac{\partial u_y}{\partial z} & 0 \end{bmatrix} \quad (3.5.3)$$

The stress tensor corresponding to this strain tensor can be given as follows:

$$[\sigma] = \begin{bmatrix} E\left(\frac{\partial u_x}{\partial x}\right) & G\left(\frac{\partial u_x}{\partial y} + \frac{\partial u_y}{\partial x}\right) & G\left(\frac{\partial u_x}{\partial z}\right) \\ G\left(\frac{\partial u_x}{\partial y} + \frac{\partial u_y}{\partial x}\right) & E\left(\frac{\partial u_y}{\partial y}\right) & G\left(\frac{\partial u_y}{\partial z}\right) \\ G\left(\frac{\partial u_x}{\partial z}\right) & G\left(\frac{\partial u_y}{\partial z}\right) & \sigma_{zz} \end{bmatrix} \quad (3.5.4)$$

Where  $E$  is the elastic modulus and  $G$  is the shear modulus of the rock material. In Eq. 3.5.4 the vertical normal stress,  $\sigma_{zz}$ , is supposed to be determined in order to satisfy the condition of zero displacement along the axis of the borehole. Therefore,  $\sigma_{zz}$  can be defined as a function of gradients of the longitudinal displacements in the  $X$ ,  $Y$  and  $Z$  directions as follows:

$$\sigma_{zz} = f\left(\frac{\partial u_z}{\partial x}, \frac{\partial u_z}{\partial y}, \frac{\partial u_z}{\partial z}\right) \tag{3.5.5}$$

Applying the proposed boundary conditions, given by the strain tensor in Eq. 3.5.3, the results of the finite element analysis indicate that the normal and in-plane shear components of the induced stress state around the deviated borehole remain unaltered, compared to their values calculated by means of the generalised Kirsch equations (Appendix B, Table B.5). Therefore, Eqs. 3.3.6 can be applied to calculate the stress components  $\sigma_{rr}$ ,  $\sigma_{\theta\theta}$ ,  $\sigma_{zz}$  and  $\sigma_{r\theta}$ . However, longitudinal shear stresses  $\sigma_{rz}$  and  $\sigma_{\theta z}$  substantially change under the proposed boundary conditions, as illustrated in Fig. 3.18.

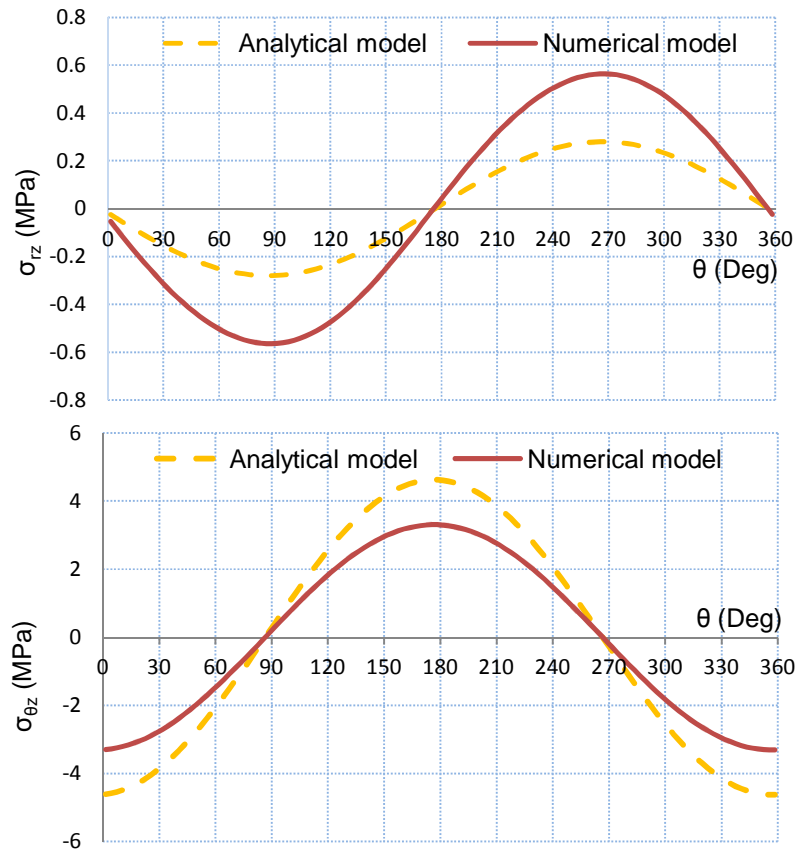


Figure 3.18 Changes in longitudinal shear stresses around the borehole under the proposed boundary conditions

Based on the results of the finite element analysis, the formulation of the out-of-plane shear stresses  $\sigma_{rz}$  and  $\sigma_{\theta z}$  can be modified as follows:

$$\sigma_{\theta z} = \frac{1}{\sqrt{2}}(\sigma_{yz} \cos \theta - \sigma_{xz} \sin \theta) \left(1 + \frac{a^2}{r^2}\right)$$

$$\sigma_{rz} = 2(\sigma_{yz} \sin \theta + \sigma_{xz} \cos \theta) \left(1 - \frac{a^2}{r^2}\right) \tag{3.5.6}$$

The angular position of the points with stress concentration around the borehole can be given by Eq. 3.4.7 as  $\theta = 55.166^\circ$ , which is also confirmed by the results of the finite element analysis for the deviated borehole considered as an example for finite element analysis in the current study. Furthermore, at  $\theta = 55.166^\circ$ , a row of elements in the radial direction can be selected (Fig. 3.19) in order to indicate changes of the longitudinal shear stresses as a function of radial distance from the borehole wall. Therefore according to Fig. 3.19 the induced stress components at the two points of stress concentration are given by the following stress tensor:

$$[\sigma_{ij}] = \begin{bmatrix} \sigma_{rr} & \sigma_{r\theta} & \sigma_{rz} \\ \sigma_{\theta r} & \sigma_{\theta\theta} & \sigma_{\theta z} \\ \sigma_{zr} & \sigma_{z\theta} & \sigma_{zz} \end{bmatrix} = \begin{bmatrix} 0 & 0 & 0 \\ 0 & 179.12 & -1.85 \\ 0 & -1.85 & 86.70 \end{bmatrix} \tag{3.5.7}$$

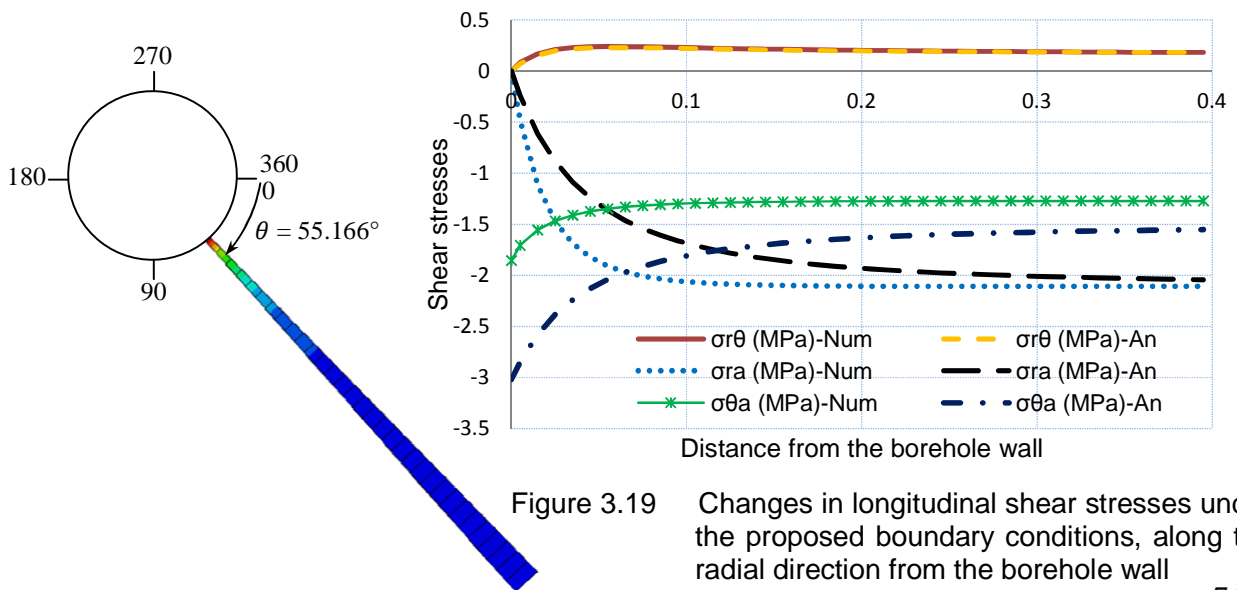


Figure 3.19 Changes in longitudinal shear stresses under the proposed boundary conditions, along the radial direction from the borehole wall

According to Eq.3.5.7 the only stress component at the borehole wall which changes compared to the analytical solution, i.e. the generalised Kirsch equations, is  $\sigma_{\theta z}$ . It also merits noting that although the values of the stress component  $\sigma_{rz}$  differ from the values calculated by means of the generalised Kirsch equations, at farther radial distances it takes the value of zero at the borehole wall.

## **CHAPTER 4**

### **Rock strength analysis in three-dimensional stress**

	<b>Page</b>
<b>4.1. Introduction</b>	<b>76</b>
<b>4.2. Definition of general, principal and deviatoric stress tensors</b>	<b>77</b>
<b>4.3. Failure function in principal stress space</b>	<b>80</b>
<b>4.4. Failure functions in deviatoric stress space</b>	<b>82</b>
<b>4.5. Failure criteria on deviatoric and meridian planes</b>	<b>87</b>
<b>4.6. Failure criteria especially developed for rock material</b>	<b>91</b>
<b>4.7. Experimental evaluation of rock behaviour under three-dimensional stress</b>	<b>109</b>
<b>4.8. True-triaxial experiments at The University of Adelaide</b>	<b>124</b>

## 4.1. Introduction

Apart from the evaluation of stress conditions in the borehole proximity, an accurate estimation of rock strength under a three-dimensional stress state is vital for predicting the borehole instability. In other words, when drilling through rock or when considering the stability of borehole in good quality, brittle rock, investigating the behaviour of intact rock in three-dimensional stress regime is a key parameter in designing and drilling stable boreholes. The strength evaluation of intact rock is even more important when considering stability of boreholes with smaller cross sectional dimensions compared to discontinuity spacing and at great depths.

According to Paterson and Wong (2005), the mechanical properties of intact rock material such as failure strength, fracture angle and ductility, are function of stress state, temperature and strain rate. Mechanical behaviour of rock under a given stress state which is induced and imposed on rock due to the introduction of an opening in the Earth's crustal formations is the focal point of interest of this chapter. The effect of stress state on rock strength has been comprehensively investigated under conventional triaxial compression ( $\sigma_1 > \sigma_2 = \sigma_3$ ) and extension ( $\sigma_1 = \sigma_2 > \sigma_3$ ) stress states. However, as pointed out by Mogi (2007), due to the complicated procedure of true-triaxial experiments rock behaviour in general stress state ( $\sigma_1 > \sigma_2 > \sigma_3$ ) has not been studied adequately. On the other hand, to confidently predict the borehole instability due to the rock failure at the borehole wall an accurate estimation of rock strength under the induced three-dimensional stress state in the borehole vicinity is required.

Rock strength can be interpreted as the ultimate loading capacity of rock material in a given stress state. The stress state at which failure occurs is often referred to as failure stress. Since most rocks fail with an abrupt failure and plastic deformation is barely observed before macroscopic disintegration, the failure stress in this study is considered as the stress state at which rock material is disintegrated, as defined by Priest and Hunt (2005). The strength of rock material surrounding an underground structure at the depth of interest can be determined by simulating the in situ stress conditions in experimental studies. However, due to difficulties with reproducing in situ conditions at great depth and complex experimental procedures of

three-dimensional rock testing, it is desirable to predict the rock failure stress by means of an accurate predictive model. Such a predictive model is usually presented as a failure criterion, which is either an empirical or analytical formulation.

A failure criterion for a rock is a mathematical expression that defines the stress state as a combination of stress components which leads to rock failure. Such a criterion is usually expressed in terms of the stress tensor and material properties of rock. It is important to remember that the term ‘failure’ implies that the rock has completely disintegrated. It is, however, possible for the rock to become unserviceable in an engineering sense, if substantial inelastic deformations develop. In this context the term ‘yield criterion’ is more appropriate to be adopted. Rock failure criteria can be developed fundamentally from the mechanical analysis of an assumed failure mechanism, or can be developed empirically by modelling the observed behaviour of rock during laboratory or site tests.

## 4.2. Definition of General, Principal and Deviatoric Stress Tensors

The general stress state which is imposed on a block of rock (Fig.4.1) can be expressed by means of a second order tensor which is often referred to as stress tensor  $\sigma_{ij}$ :

$$\sigma_{ij} = \begin{bmatrix} \sigma_{11} & \sigma_{12} & \sigma_{13} \\ \sigma_{21} & \sigma_{22} & \sigma_{23} \\ \sigma_{31} & \sigma_{32} & \sigma_{33} \end{bmatrix} \quad (4.2.1)$$

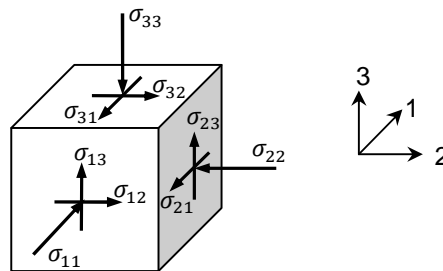


Figure 4.1 Compressive general stresses on a block of rock

If the rock block shown in Fig. 4.1 is rotated so that all shear stresses on all faces are eliminated (Fig. 4.2), then the normal stresses acting on each face are known as principal

stresses and the associated directions are referred to as principal directions. The stress tensor which describes this stress state is known as principal stress tensor,  $[\sigma_{ij}]_p$ , and can be written as:

$$[\sigma_{ij}]_p = \begin{bmatrix} \sigma_{11} & 0 & 0 \\ 0 & \sigma_{22} & 0 \\ 0 & 0 & \sigma_{33} \end{bmatrix} \quad (4.2.2)$$

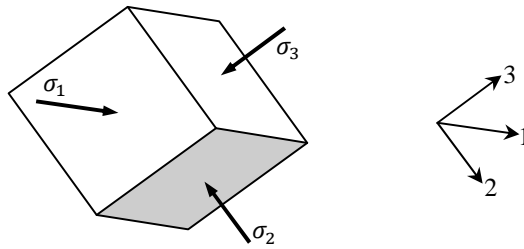


Figure 4.2 Principal stresses on a block of rock

It should be noted that although in Eq. 4.2.2 stress components in the general stress tensor (Eq. 4.2.1) have changed due to the rotation of the rock block and the coordinate system, the actual stress state remains unaltered. Furthermore, there are certain invariants associated with every tensor which are independent of the orientation of the coordinate system. For example, a vector is a simple first order tensor and it is represented by three components in a three-dimensional space. The magnitude of these components depend on the coordinate system chosen to represent the vector, but the length of the vector is a scalar and is independent of the orientation of the coordinate. Similarly, in association with every second order tensor, such as the stress tensor, there exist three independent invariant quantities. Accordingly, the first ( $I_1$ ), second ( $I_2$ ) and third ( $I_3$ ) invariants of the principal stress tensor are defined as follows:

$$I_1 = \sigma_1 + \sigma_2 + \sigma_3$$

$$I_2 = \sigma_1\sigma_2 + \sigma_2\sigma_3 + \sigma_3\sigma_1$$

$$I_3 = \sigma_1 \sigma_2 \sigma_3 \quad (4.2.3)$$

Furthermore, the hydrostatic stress tensor,  $[\sigma_{ij}]_H$ , associated with the principal stress tensor (Eq. 4.2.2) is defined as follows:

$$[\sigma_{ij}]_H = \frac{I_1}{3} \delta_{ij} \quad (4.2.4)$$

Where  $I_1$  is the first invariant of the principal stress tensor and the term  $\frac{I_1}{3}$  is referred to as the mean normal stress. The 3×3 matrix  $\delta_{ij}$  is known as the 'kronecker delta' and is defined as:

$$\delta_{ij} = \begin{cases} 1 & \text{if } i = j \text{ (No sum)} \\ 0 & \text{if } i \neq j \end{cases} = \begin{bmatrix} 1 & 0 & 0 \\ 0 & 1 & 0 \\ 0 & 0 & 1 \end{bmatrix} \quad (4.2.5)$$

When considering rock performance under a given stress state it is important to note that even rocks with no shear strength will not fail or disintegrate under hydrostatic stress state ( $\sigma_1 = \sigma_2 = \sigma_3$ ). Under high hydrostatic stress state, due to the closure of pre-existing voids and micro-fractures in the rock body, rock becomes rather compact and consequently stronger. Therefore, it can be inferred that, as opposed to metal materials, the failure stress of rock is dependent upon the mean normal stress. However, the main factor which causes the rock to fail is the deviation of stress state from the hydrostatic state of stress. Hence, to predict the rock failure it is necessary to evaluate the deviatoric nature of the stress state acting on the rock.

Considering the principal stress tensor in Eq. 4.2.2, the deviatoric stress tensor,  $[\sigma_{ij}]_d$ , can be written as:

$$[\sigma_{ij}]_d = \begin{bmatrix} S_{11} & 0 & 0 \\ 0 & S_{22} & 0 \\ 0 & 0 & S_{33} \end{bmatrix} \quad (4.2.6)$$

Where the diagonal components in Eq. 4.2.6 are defined as:

$$S_{ii} = \sigma_{jj} - \frac{I_1}{3} \delta_{ij} \quad (\text{No sum}) \quad (4.2.7)$$

Furthermore, the first ( $J_1$ ), second ( $J_2$ ) and third ( $J_3$ ) invariants of the principal deviatoric stress tensor are defined as follows: (for simplicity  $S_{11}$ ,  $S_{22}$  and  $S_{33}$  are written as  $S_1$ ,  $S_2$  and  $S_3$ )

$$J_1 = S_1 + S_2 + S_3 \quad (a)$$

$$J_2 = \frac{1}{6} \left[ (S_1 - S_2)^2 + (S_2 - S_3)^2 + (S_3 - S_1)^2 \right] \quad (b)$$

$$J_3 = S_1 S_2 S_3 \quad (c) \quad (4.2.8)$$

It is also noteworthy that:

$$S_{ii} - S_{jj} = \sigma_{ii} - \sigma_{jj} \quad \text{No sum} \quad (4.2.9)$$

### 4.3. Failure Function in Principal Stress Space

In general stress state ( $\sigma_1 > \sigma_2 > \sigma_3$ ) all possible combinations of the stress components, which cause the rock to fail can be represented by means of a mathematical formulation known as a failure criterion. For an isotropic and homogenous material in a uniform stress regime, the failure criterion can be expressed in terms of a stress tensor,  $[\sigma_{ij}]$ , which satisfies the following relationship:

$$F(\sigma_{ij}) = 0 \quad (4.3.1)$$

However, models for predicting the rock failure stress are commonly expressed in terms of principal stresses. Therefore, the function  $F$  in Eq. 4.3.1 can also be written in terms of principal stresses as:

$$f(\sigma_1, \sigma_2, \sigma_3) = 0 \quad (4.3.2)$$

The function  $f$  in Eq. 4.3.2, can be interpreted as a surface in the principal stress-space ( $\sigma_1, \sigma_2, \sigma_3$ ), as illustrated in Fig. 4.3. This surface is a geometrical representation of all failure

points in the stress space and is, accordingly, known as the failure surface. All stress points inside the failure surface are stress states at which the rock does not fail and any point located on the surface represents a failure stress point. Stress points outside of this surface are theoretically meaningless. However, when experimental data lies outside of a failure surface, it is inferred that the associated failure criterion underestimates the rock strength. On the other hand, observing experimental data inside the failure surface indicates that the rock strength has been overestimated. According to Mogi (2007), one of the most fundamental problems of rock mechanics is the study of the shape of the failure surface for various rock types.

It also merits noting that the analysis of induced stresses adjacent to an excavation will usually produce a general stress tensor (where the shear stresses are non-zero) expressed relative to a local set of axes. On the other hand, failure functions expressed in terms of principal stresses are applicable only when the stress state is manifested by the principal stress tensor. In order to apply such failure functions (Eq. 4.3.2) for estimating rock strength, it is necessary to transform the local general stress tensor into the principal stress tensor. However, recalling that the invariants of a second order tensor are independent of the orientation of the coordinate system, it is more convenient to express failure functions in terms of the invariants of the principal stress tensor or the deviatoric principal stress tensor to effectively eliminate the transformation operations of the stress tensor from the procedure of the rock strength analysis.

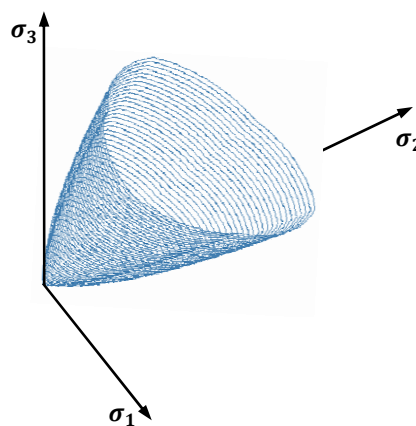


Figure 4.3 Failure surface in the principal stress space

#### 4.4. Failure functions in deviatoric stress space

The stress space can be defined using a Cartesian coordinate system, each axis of which represents one of the three principal stresses. Any arbitrary point  $P$  in the principal stress space is identified by three stress components and represents a unique stress state. Furthermore, the position of the point  $P$  in the stress space can be addressed by a stress vector  $\vec{\sigma} = (\sigma_1, \sigma_2, \sigma_3)$ , as illustrated in Fig. 4.4. The line  $\sigma_1 = \sigma_2 = \sigma_3$ , which makes equal angles with the three principal stress axes is called the ‘Stress-space diagonal’ or the ‘Hydrostatic axis’ (Fig. 4.4).

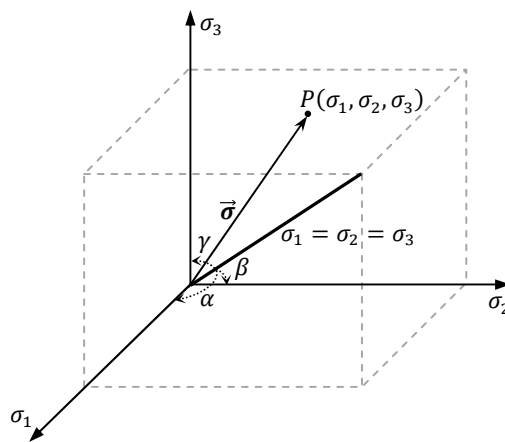
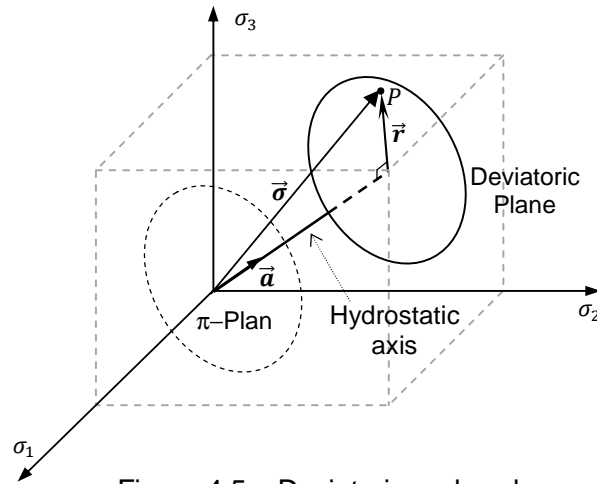


Figure 4.4 Hydrostatic axis and the stress vector  $\vec{\sigma}$  in the principal stress space

If  $\alpha$ ,  $\beta$  and  $\gamma$  are angles between the hydrostatic axis and axes  $\sigma_1$ ,  $\sigma_2$  and  $\sigma_3$ , respectively, the following relation holds between the direction cosines:

$$\cos \alpha = \cos \beta = \cos \gamma = \frac{1}{\sqrt{3}} \quad (4.4.1)$$

A plane perpendicular to the hydrostatic axis which also contains the point  $P$  is called the principal stress-deviator plane or simply the ‘deviatoric plane’. A deviatoric plane which contains the origin of the principal stress space is known as the  $\pi$ -Plane (Fig. 4.5).

Figure 4.5 Deviatoric and  $\pi$ -plane

Defining the unit vector  $\vec{a} = \frac{1}{\sqrt{3}}(1, 1, 1)$  along the hydrostatic axis, the magnitude of the projection of stress vector,  $\vec{\sigma}$ , on the stress-space diagonal (the line  $\sigma_1 = \sigma_2 = \sigma_3$ ), can be calculated as:

$$\vec{\sigma} \cdot \vec{a} = \frac{1}{\sqrt{3}} (\sigma_1 + \sigma_2 + \sigma_3) = \frac{\sqrt{3}}{3} I_1 = \sqrt{3} \sigma_{oct} \quad (4.4.2)$$

Where,  $I_1$  is the first invariant of the principal stress tensor and  $\sigma_{oct}$  is the octahedral mean normal stress. On a certain deviatoric plane, given by  $I_1 = \text{constant}$ , the distance between the point  $P$  and the hydrostatic axis which can be given as the magnitude of the vector  $\vec{r}$ , as illustrated in Fig. 4.6, can be calculated as:

$$|\vec{r}| = |\vec{\sigma}|^2 - (\vec{\sigma} \cdot \vec{a})^2 \quad (4.4.3)$$

Substitution of Eq. 4.4.2 into Eq. 4.4.3 yields the following relationship:

$$|\vec{r}| = \left( \frac{1}{3} \left[ (\sigma_1 - \sigma_2)^2 + (\sigma_2 - \sigma_3)^2 + (\sigma_3 - \sigma_1)^2 \right] \right)^{\frac{1}{2}} = \tau_{oct} = \sqrt{2J_2} \quad (4.4.4)$$

The magnitude of the vector  $\vec{r}$ , which originates from the hydrostatic axis and terminates at the point  $P$  on the deviatoric plane (Fig. 4.5), indicates a factor by which the given stress state deviates from the hydrostatic stress state. Furthermore, a given stress point in the principal

stress space, which is a Cartesian coordinate system, can be represented in a cylindrical coordinate system as well. Two coordinates of such a cylindrical coordinate system are the hydrostatic axis and the vector  $\vec{r}$  on the deviatoric plane. The third coordinate, which is the angle  $\theta$ , is measured counter-clockwise from one axis of a Cartesian coordinate system on the deviatoric plane.

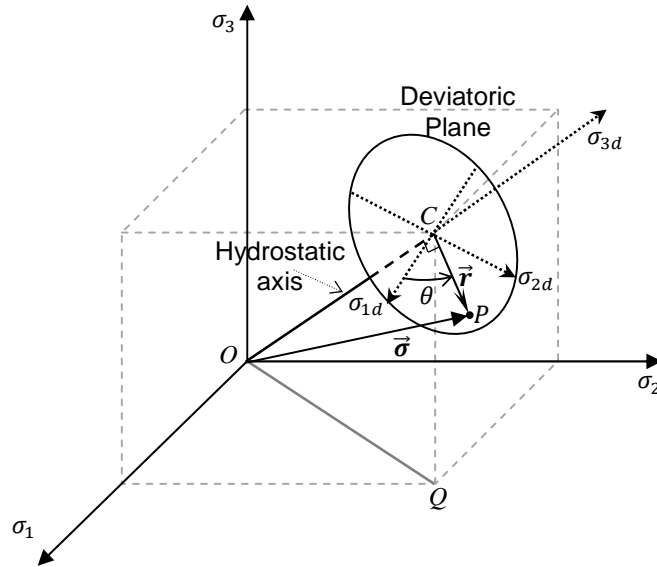


Figure 4.6 Cartesian coordinate system on the deviatoric plane

Such a Cartesian coordinate system on the deviatoric plane can be defined by transforming the principal stress coordinates  $(\sigma_1, \sigma_2, \sigma_3)$  so that the  $\sigma_3$ -axis coincides with the hydrostatic axis. The axes of the transformed Cartesian coordinate system are labelled as  $\sigma_{1d}, \sigma_{2d}$  and  $\sigma_{3d}$  in Fig. 4.6. Accordingly, any point in the  $(\sigma_1, \sigma_2, \sigma_3)$ -space can be transformed to the  $(\sigma_{1d}, \sigma_{2d}, \sigma_{3d})$ -space using a transformation matrix, through the following relationship:

$$\begin{bmatrix} \sigma_{1d} \\ \sigma_{2d} \\ \sigma_{3d} \end{bmatrix} = \begin{bmatrix} \frac{\sqrt{2}}{2} & 0 & -\frac{\sqrt{2}}{2} \\ -\frac{\sqrt{6}}{6} & \frac{2\sqrt{6}}{6} & -\frac{\sqrt{6}}{6} \\ \frac{\sqrt{3}}{3} & \frac{\sqrt{3}}{3} & \frac{\sqrt{3}}{3} \end{bmatrix} \begin{bmatrix} \sigma_1 \\ \sigma_2 \\ \sigma_3 \end{bmatrix} \quad (4.4.5)$$

After defining three orthogonal coordinates ( $\sigma_{1d}$ ,  $\sigma_{2d}$  and  $\sigma_{3d}$ ) on the deviatoric plane the angle  $\theta$  can be measured counter-clockwise from the  $\sigma_{1d}$ -axis. The relationship between the cylindrical,  $(r, \theta, \sigma_{3d})$  and Cartesian,  $(\sigma_1, \sigma_2, \sigma_3)$ , components of the point  $P$ , as illustrated in Fig. 4.6, can also be established. Considering the point  $P$  in the cylindrical coordinate system in Fig. 4.6, the length  $QC$  can be calculated from the following relationship:

$$|QC| = |OC| \cos \gamma = \left[ \frac{\sqrt{3}}{3} (\sigma_1 + \sigma_2 + \sigma_3) \right] \left( \frac{\sqrt{3}}{3} \right) = \frac{\sigma_1 + \sigma_2 + \sigma_3}{3} = \frac{I_1}{3} \quad (4.4.6)$$

Where  $\gamma$  is the angle between the hydrostatic axis ( $OC$  in Fig. 4.6) and the  $\sigma_3$ -axis, and  $I_1$  is the first invariant of the principal stress tensor. To calculate, for example, the third component of the point  $P$  in the principal stress space, i.e.  $\sigma_3$ , it is necessary to add the magnitude of the projection of the vector  $\vec{r}$  along the  $QC$ -direction to the length of the  $QC$ , given by Eq. 4.4.6. Components of the vector  $\vec{r}$  in  $\sigma_{1d}$  and  $\sigma_{2d}$  directions are  $r \cos \theta$  and  $r \sin \theta$ , respectively, as shown in Fig. 4.7. Therefore, considering Eq. 4.4.5 the magnitude of the projection of the vector  $\vec{r}$  in  $QC$  direction, parallel to the  $\sigma_3$ -axis, can be calculated as follows:

$$|\vec{r}_{QC}| = \left( -\frac{\sqrt{2}}{2} \right) r \cos \theta + \left( -\frac{\sqrt{6}}{6} \right) r \sin \theta \quad (4.4.7)$$

Substituting  $r = |\vec{r}|$  from Eq. 4.4.4 into Eq. 4.4.7 the third component of the stress point  $P$  in the principal stress space can be calculated as:

$$\sigma_3 = \frac{2\sqrt{J_2}}{\sqrt{3}} \sin \left( \theta + \frac{4\pi}{3} \right) + \frac{I_1}{3} \quad (4.4.8)$$

The first and the second components of the point  $P$  in the principal stress space ( $\sigma_1$  and  $\sigma_2$ ) can be calculated in the similar manner. Therefore, the relationship between the components of the stress point  $P$  in the cylindrical coordinate system  $(r, \theta, \sigma_{3d})$  and in the principal stress space  $(\sigma_1, \sigma_2, \sigma_3)$  can be established as follows:

$$\begin{Bmatrix} \sigma_1 \\ \sigma_2 \\ \sigma_3 \end{Bmatrix} = \frac{2\sqrt{J_2}}{\sqrt{3}} \begin{Bmatrix} \sin\left(\theta + \frac{2\pi}{3}\right) \\ \sin\theta \\ \sin\left(\theta + \frac{4\pi}{3}\right) \end{Bmatrix} + \frac{I_1}{3} \quad (4.4.9)$$

Since the component  $r$  of a stress point in the cylindrical system is indicative of deviation from the hydrostatic stress state, it can be concluded that the cylindrical coordinate system is more convenient for demonstrating the deviatoric nature of a stress point and can be, appropriately, referred to as the deviatoric stress space. Furthermore, in the deviatoric stress space, with respect to Eq. 4.4.2, any point on the  $\sigma_{3d}$ -axis, or the hydrostatic axis, can be addressed as  $\frac{\sqrt{3}}{3}I_1$  and considering Eq. 4.4.4 the magnitude of the  $r$  component for any stress point is given as  $\sqrt{2J_2}$ . Therefore, the coordinates of the deviatoric stress space can be identified also as  $(\sqrt{2J_2}, \theta, \frac{\sqrt{3}}{3}I_1)$ , in which  $I_1$  is the first invariant of the principal stress tensor and  $J_2$  is the second invariant of the deviatoric stress tensor. The angle  $\theta$ , known as the ‘lode angle’, according to Zienkiewicz et al. (1972) can be expressed in terms of second and third invariant of the stress deviator tensor,  $J_2$  and  $J_3$ , respectively.

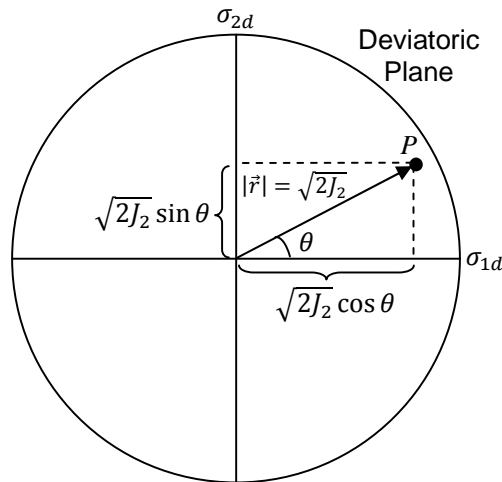


Figure 4.7 Polar components of point  $P$  on the deviatoric Plane

Considering Eq. 4.4.5, the term  $\sqrt{2J_2} \sin \theta$ , which represents the magnitude of the projection of the vector  $\vec{r}$  in the  $\sigma_{2d}$ -direction (Fig. 4.7) can also be written as:

$$\sqrt{2J_2} \sin \theta = \frac{\sqrt{6}}{6} (-\sigma_1 + 2\sigma_2 - \sigma_3) \quad (4.4.10)$$

Recalling Eq. 4.2.5 and rearranging Eq. 4.4.10,  $\sin \theta$  can be calculated as:

$$\sin \theta = \frac{\sqrt{3}S_2}{2\sqrt{J_2}} \quad (4.4.11)$$

According to Eqs. 4.2.7 (c), considering the trigonometric identity ( $\sin 3\theta = -4 \sin^3 \theta + 3 \sin \theta$ ) and knowing that  $S_2 = -(S_1 + S_3)$ , the lode angle  $\theta$  can be expressed in terms of the second ( $J_2$ ) and third ( $J_3$ ) invariants of the principal deviatoric stress tensor, as follows:

$$\sin 3\theta = \frac{-3\sqrt{3}J_3}{2J_2^{\frac{3}{2}}} \quad (4.4.12)$$

Since the failure stress of rock, as a brittle material, depends upon the effective mean normal stress ( $\frac{I_1}{3}$ ) and failure occurs only under highly deviatoric stress state, it is more convenient to express rock failure criteria as a function of the first invariant of principal stress tensor,  $I_1$ , and the second and third invariants of the principal deviatoric stress tensor ( $J_2$  and  $J_3$ ). Accordingly, the rock failure function in deviatoric stress space ( $\sqrt{2J_2}, \theta, \frac{\sqrt{3}}{3}I_1$ ) can be expressed as:

$$F(J_2, \sin 3\theta, I_1) = 0 \quad (4.4.13)$$

Where  $\sin 3\theta$  is given by Eq. 4.4.12. It also merits noting that by employing Eq. 4.4.9, any failure criteria in terms of principal stresses can be expressed in terms of invariants of the principal and principal deviatoric stress tensors.

## 4.5. Failure Criteria on Deviatoric and Meridian Planes

The failure function expressed by Eq. 4.4.13, represents a failure surface in the deviatoric stress space. Due to the presence of the term  $\sin 3\theta$  in Eq. 4.4.13, a number of general symmetry properties of the failure function can be addressed. The trace of this failure surface

on an arbitrary deviatoric plane is obtained for  $I_1 = \text{constant}$ . As the Sin-function is periodic with a period of  $360^\circ$  it is straightforward to conclude that the failure function in Eq. 4.4.13 is periodic with a period of  $120^\circ$  and therefore the trace of the failure surface on the deviatoric plane is repeated in every  $120^\circ$  and the distance  $R = |\vec{r}|$ , between hydrostatic axis and the trace of the failure surface on the deviatoric plane, is the same for  $\theta$  and for  $\theta + 120^\circ$  as well as for  $\theta + 240^\circ$  (see Fig. 4.8 (a)).

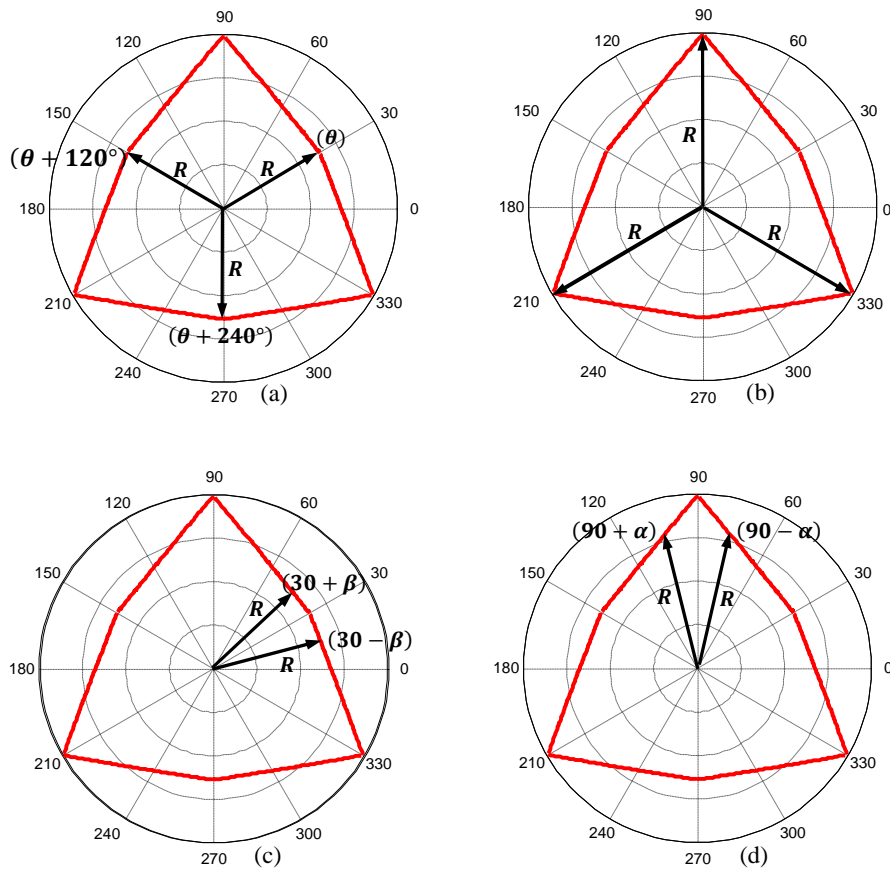


Figure 4.8 Symmetry properties of a failure criterion on the deviatoric plane

Due to the periodicity of  $120^\circ$  the cross sectional curve is also symmetric about  $\theta = 90^\circ$ ,  $\theta = 210^\circ$  and  $\theta = 330^\circ$ , as illustrated in Fig. 4.8 (b). Furthermore, setting  $\theta = 30^\circ \pm \beta$  yields  $\sin(90 - 3\beta) = \sin(90 + 3\beta)$  and accordingly, the magnitude of the vector  $\vec{r}$  is identical for  $\theta = 30^\circ + \beta$  and  $\theta = 30^\circ - \beta$ , which indicates that the trace of the failure surface on the deviatoric plane is also symmetric about  $\theta = 30^\circ$  and thereby also symmetric about  $\theta = 150^\circ$  and  $\theta = 270^\circ$ , (see Fig. 4.8 (c)). Similarly, for  $\theta = 90^\circ \pm \alpha$ , the magnitude

of the vector  $\vec{r}$  is the same and thereby the trace is symmetric about  $\theta = 90^\circ$ ,  $\theta = 210^\circ$  and  $\theta = 330^\circ$ , (see Fig. 4.8 (d)). The symmetry properties shown in Fig. 4.8 imply that the trace of the failure surface on the deviatoric plane is completely characterized by its form for  $-30^\circ < \theta < 30^\circ$  and that this form is repeated in other sectors of the deviatoric plane. Furthermore, if  $\sigma_1 > \sigma_2 > \sigma_3$  are principal stresses, the intermediate principal stress can be written as:

$$\sigma_2 = (1-\alpha)\sigma_1 + \alpha\sigma_3 \quad 0 \leq \alpha \leq 1 \quad (4.5.1)$$

Substituting Eq. 4.5.1 into Eq. 4.2.5 gives:

$$\begin{aligned} S_1 &= \frac{1}{3}(1+\alpha)(\sigma_1 - \sigma_3) \\ S_2 &= \frac{1}{3}(1-2\alpha)(\sigma_1 - \sigma_3) \\ S_3 &= -\frac{1}{3}(2-\alpha)(\sigma_1 - \sigma_3) \end{aligned} \quad (4.5.2)$$

Substituting  $S_2$  from Eq. 4.5.2 into Eq. 4.4.11 yields:

$$\sin \theta = \frac{1-2\alpha}{2\sqrt{\alpha^2 - \alpha + 1}} \quad (4.5.3)$$

Since the parameter  $\alpha$  ranges between 0 and 1 ( $0 < \alpha < 1$ ), it follows from Eq. 4.5.3 that the angle  $\theta$  ranges from  $-\frac{\pi}{6}$  and  $\frac{\pi}{6}$  ( $-\frac{\pi}{6} < \theta < \frac{\pi}{6}$ ). Therefore, with the ordering of the principal stresses such that  $\sigma_1 > \sigma_2 > \sigma_3$ , all stress states are covered by the angle  $\theta$  ranging between  $-\frac{\pi}{6}$  and  $\frac{\pi}{6}$ .

The ‘meridians’ of the failure surface are the curves where  $\theta = \text{constant}$  applies. In other words the ‘meridional’ curves are obtained by the intersection of the failure surface with a plane containing the hydrostatic axis.

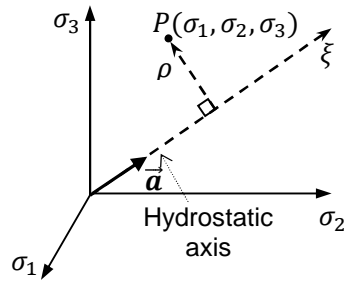


Figure 4.9 Meridional plane ( $\xi - \rho$  coordinates) [after Ottosen and Ristimna(2005)]

Accordingly, the meridians can be depicted in a  $(\xi, \rho)$  coordinate system, known as the ‘meridional plane’ (Fig. 4.9). With respect to Eqs. 4.4.2 and 4.4.4, coordinates  $\xi$  and  $\rho$  are defined as follows:

$$\xi = \frac{\sqrt{3}}{3}(\sigma_1 + \sigma_2 + \sigma_3) = \frac{\sqrt{3}}{3}I_1 \quad (4.5.4)$$

$$\rho = \sqrt{2J_2}$$

For rock materials two meridians are of particular interest. When  $\sigma_1 > \sigma_2 = \sigma_3$  applies, then in Eq. 4.5.1,  $\alpha = 1$  and from Eq. 4.5.2  $\theta = -\frac{\pi}{6}$ . This meridian is termed the ‘compressive meridian’, as the stress state  $\sigma_1 > \sigma_2 = \sigma_3$  corresponds to a hydrostatic stress state superposed by a compressive stress in the  $\sigma_1$ -direction. This stress state is often referred to as triaxial compression in rock mechanics experiments:

$$\sigma_1 > \sigma_2 = \sigma_3 \quad i.e. \quad \theta = -\frac{\pi}{6} \quad \text{compressive meridian}$$

Uniaxial compressive stress state is located on the compressive meridian, and so is the triaxial compressive stress state when the intermediate and the minor compressive principal stresses are equal. When  $\sigma_1 = \sigma_2 > \sigma_3$  holds then Eq. 4.5.1 postulates that  $\alpha = 0$  and Eq. 4.5.2 calculates the angle  $\theta$  as  $\frac{\pi}{6}$ . This meridian is termed the ‘tensile meridian’, as the stress state  $\sigma_1 = \sigma_2 > \sigma_3$  corresponds to a hydrostatic stress state superposed by a tensile stress in the  $\sigma_3$ -direction. This stress state is often referred to as triaxial extension in experimental studies of rock mechanics:

$$\sigma_1 = \sigma_2 > \sigma_3 \quad i.e. \quad \theta = \frac{\pi}{6} \quad \textit{tensile meridian}$$

The points where the tensile and compressive meridians intersect the deviatoric plane are illustrated in Fig. 4.10.

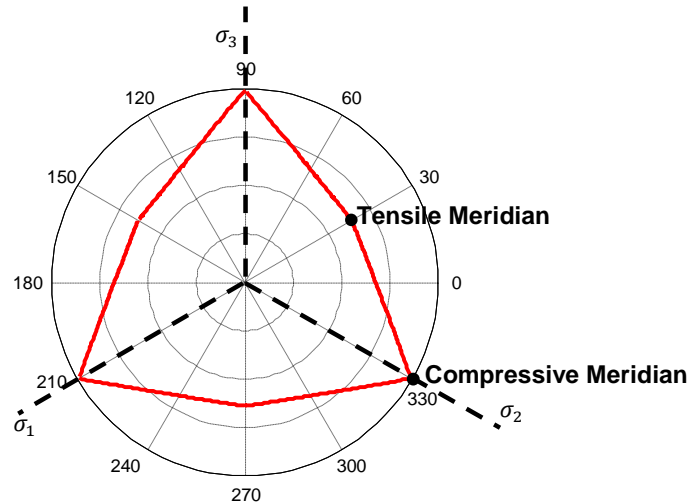


**Figure 4.10** Intersection of tensile and compressive meridians with the deviatoric plane

## 4.6. Failure Criteria Especially Developed For Rock Material

In this section a group of empirical three-dimensional rock failure criteria is studied in detail. Since the input parameters of these three-dimensional models are the same as those for the Hoek-Brown criterion, they can also be referred to as three-dimensional Hoek-Brown based criteria. The three-dimensional Hoek-Brown based criteria are first expressed in terms of the invariants of the deviatoric stress tensor using the method outlined in Section 4.4. Next the radial distance between the hydrostatic axis and the trace of the failure surface on the deviatoric plane is calculated in a unified way and by assuming  $I_1$ , the mean normal stress, as constant. The three-dimensional failure surface in the principal stress space is then plotted by reproducing the trace of the failure surface along the hydrostatic axis. For this purpose  $I_1$  needs to be defined as a variable.

### 4.6.1. The Hoek-Brown criterion

According to Hoek and Brown (1980), the Hoek-Brown criterion for estimating the failure stress of intact rock material can be expressed as a function of the major ( $\sigma_1$ ) and minor ( $\sigma_3$ ) principal stresses as:

$$F_{HB}(\sigma_1, \sigma_3) = \sigma_1 - \sigma_3 - \left( m_i \sigma_c \sigma_3 + s \sigma_c^2 \right)^{\frac{1}{2}} = 0 \quad (4.6.1)$$

Where the term  $m_i$  is the Hoek-Brown parameter  $m$  for intact rock and the parameter  $s$  for intact rock is 1. Substituting the relevant formulation for  $\sigma_1$  and  $\sigma_3$  from Eqs. 4.4.9 into Eq. 4.6.1, the Hoek-Brown criterion can be expressed in terms of invariants of the principal deviatoric stress tensor as follows:

$$F_{HB} = 2J_2^{\frac{1}{2}} \cos \theta - \left[ m_i \sigma_c \frac{J_2^{\frac{1}{2}}}{-\sqrt{3}} (\sin \theta + \sqrt{3} \cos \theta) + \frac{m_i \sigma_c I_1}{3} + s \sigma_c^2 \right] = 0 \quad (4.6.2)$$

$$\left( -\frac{\pi}{6} \leq \theta \leq \frac{\pi}{6} \right)$$

Rearranging Eq. 4.6.2, the Hoek-Brown criterion for intact rock can be written as a quadratic equation in terms of  $J_2$  in the following form:

$$F_{HB} = \left( 4 \cos^2 \theta \right) \frac{J_2}{\sigma_c^2} + \left( \frac{2 m_i \sin \left( \theta + \frac{\pi}{3} \right)}{\sqrt{3}} \right) \frac{\sqrt{J_2}}{\sigma_c} - \frac{m_i I_1}{3 \sigma_c} - s = 0 \quad (4.6.3)$$

According to Eqs. 4.4.4 and 4.6.3 and considering Fig. 4.5, the radial distance from the hydrostatic axis to any point on the trace of the Hoek-Brown failure surface on a certain deviatoric plane, given by  $I_1 = \text{constant}$ , can be calculated as follows:

$$r_{HB} = \sqrt{2J_{2HB}} = \frac{\sqrt{2}\sigma_c}{2\zeta} \left[ -\lambda_{HB} + \sqrt{\lambda_{HB}^2 + 4\zeta \left( \frac{m_i I_1}{3\sigma_c} + s \right)} \right] \quad (4.6.4)$$

Where parameters  $\zeta$  and  $\lambda$  are defined as follows:

$$\zeta = 4 \cos^2 \theta$$

$$\lambda_{HB} = \frac{2m_i \sin\left(\theta + \frac{\pi}{3}\right)}{\sqrt{3}} \quad -\frac{\pi}{6} \leq \theta \leq \frac{\pi}{6} \quad (4.6.5)$$

Furthermore, assuming  $I_1$  as constant, Eqs. 4.6.4 and 4.6.5 can be applied to plot the cross section of the Hoek-Brown failure surface on the deviatoric plane. As illustrated in Fig. 4.12, the cross section of the Hoek-Brown failure surface on the deviatoric plane is a hexagon. When  $\sigma_2 = \sigma_3$ , from Eqs. 4.5.1 and 4.5.3 it follows that  $\theta = -\frac{\pi}{6}$ . Substituting  $\theta$  as  $-\frac{\pi}{6}$  into Eq. 4.6.4, the distance between the hydrostatic axis and sharp corners of the hexagonal cross section of the Hoek-Brown criterion,  $r_{HB_s}$ , on the deviatoric plane, is calculated as follows:

$$r_{HB_s} = \sqrt{2J_{2HB_s}} = \frac{\sqrt{2}\sigma_c}{6} \left[ \frac{-2m_i}{\sqrt{3}} + \sqrt{\frac{4m_i^2}{3} + 12\left(\frac{m_i I_1}{3\sigma_c} + s\right)} \right] \quad (4.6.6)$$

Likewise,  $\sigma_1 = \sigma_2$  indicates that in Eq. 4.5.1  $\alpha = 0$  and from Eq. 4.5.3  $\theta$  is given as  $\frac{\pi}{6}$ . Therefore, the distance between the hydrostatic axis and blunt corners of the hexagonal cross section of the Hoek-Brown criterion ( $r_{HB_b}$ ), is calculated as follows (Fig. 4.11):

$$r_{HB_b} = \sqrt{2J_{2HB_b}} = \frac{\sqrt{2}\sigma_c}{6} \left[ \frac{-m_i}{\sqrt{3}} + \sqrt{\frac{m_i^2}{3} + 12\left(\frac{m_i I_1}{3\sigma_c} + s\right)} \right] \quad (4.6.7)$$

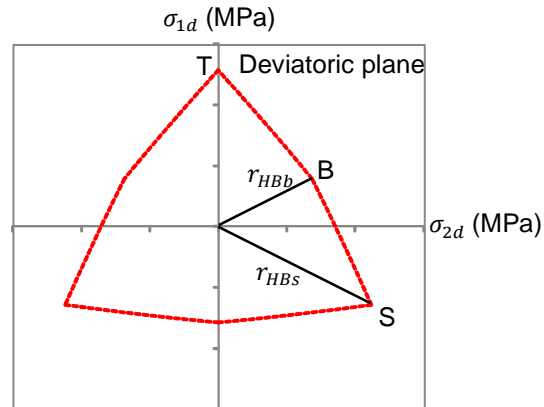


Figure 4. 11 The cross section of the Hoek-Brown failure surface on the deviatoric plane

Accordingly, sharp corners in the hexagonal cross section of the Hoek-Brown failure surface represent points where minor and intermediate stresses swap places, i.e.  $\sigma_2 = \sigma_3$ , and blunt corners are points where major and intermediate principal stresses become equal, i.e.  $\sigma_1 = \sigma_2$ . Furthermore, it also merits noting that Eq. 4.6.4, in which the angle  $\theta$  is constrained such that  $-\frac{\pi}{6} \leq \theta \leq \frac{\pi}{6}$ , gives only the section SB of the Hoek-Brown failure surface cross section in Fig. 4.11 and other sections of this hexagonal cross section can be plotted considering the symmetric properties of the failure criterion. The Hoek-Brown criterion is a periodic function with the period of  $\frac{\pi}{3}$ , and hence, its trace on the deviatoric plane is repeated every  $\frac{\pi}{3}$  radians. Consequently, to plot, for example, the section BT in Fig. 4.11 requires replacing the angle  $\theta$  in Eq. 4.4.9 with  $\theta + \frac{\pi}{3}$ , which results in the following relationship:

$$\begin{Bmatrix} \sigma_1 \\ \sigma_2 \\ \sigma_3 \end{Bmatrix} = \frac{2\sqrt{J_2}}{\sqrt{3}} \begin{Bmatrix} \sin\left(\theta + \frac{\pi}{3}\right) \\ \sin(\theta + \pi) \\ \sin\left(\theta + \frac{5\pi}{3}\right) \end{Bmatrix} + \frac{I_1}{3} \quad (4.6.8)$$

Substituting Eq. 4.6.8 into Eq. 4.6.1 results in formulating the Hoek-Brown criterion in terms of invariants of the principal deviatoric stress tensor, similar to Eq. 4.6.4 with defining the parameter  $\lambda_{HB}$  in Eq. 4.6.4, as follows:

$$\lambda_{HB \text{ (for BT)}} = \frac{2m_i \sin\left(\frac{\pi}{3} - \theta\right)}{\sqrt{3}} \quad -\frac{\pi}{6} \leq \theta \leq \frac{\pi}{6} \quad (4.6.9)$$

However, the parameter  $\zeta$  remains unaltered. Other sections of the graph can be plotted in the similar manner. Therefore, on the assumption of  $I_1 = \text{constant}$ , the trace of a given failure criterion can be plotted on a certain deviatoric plane. In order to reproduce the Hoek-Brown cross sections on different deviatoric planes along the hydrostatic axis to produce the relevant three-dimensional failure surface, as illustrated in Fig. 4.12, the parameter  $I_1$  is assumed to be a variable and is defined, considering Eq.4.6.4 for the Hoek-Brown criterion, as follows:

$$I_{1HB} = \frac{3 \left( \zeta J_{2HB} + \lambda_{HB} \sigma_c \sqrt{J_{2HB} - s \sigma_c^2} \right)}{m_i} \quad (4.6.10)$$

The components  $r$  and  $I_1$  of a failure stress point in the deviatoric stress space predicted by the Hoek-Brown criterion are given by Eqs. 4.6.4 and 4.6.10 for various values of the angle  $\theta$  ( $r_{HB}$  and  $I_{1HB}$ ). In order to calculate the corresponding components of the failure stress point in the principal stress space, the transformation matrix in Eq. 4.4.5 can be applied. After transformation from the deviatoric stress space into the principal stress space of all failure stress points predicted by the Hoek-Brown the three-dimensional failure surface associated with the Hoek-Brown criterion can be plotted in the principal stress space (see Fig. 4.12). The relevant MATLAB code for plotting the Hoek-Brown failure surface can be found in Appendix F.

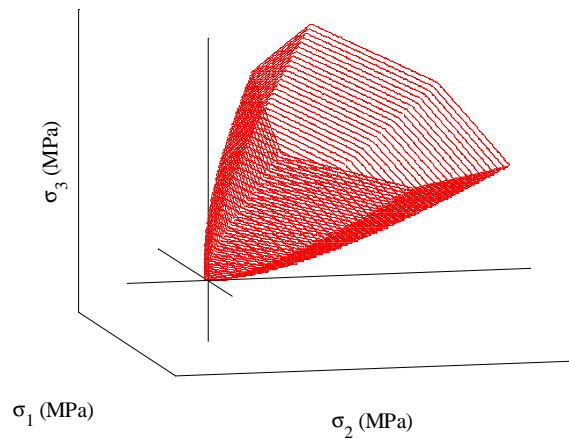


Figure 4.12 The Hoek-Brown criterion in the principal stress space

As is obvious from Eq. 4.6.1 the Hoek-Brown criterion incorporates only the minor principal stress in rock failure stress ( $\sigma_1$ ) formulation and neglects the influence of the intermediate principal stress on rock strength. In order to include the influence of the intermediate principal stress to estimate the rock strength in three-dimensional stress state more precisely, a number of three-dimensional failure criteria, based on the Hoek-Brown criterion have been introduced over the past few decades. The reasons why the Hoek-Brown criterion has been adopted as a

basis for developing new three-dimensional predictive models were outlined in Chapter 2, Section 2.4.3.

#### 4.6.2. The Pan-Hudson criterion

The strategy adopted by Pan and Hudson (1988), for developing a three-dimensional criterion based on the Hoek-Brown criterion was to approximate the Hoek-Brown failure surface with a conical surface the cross section of which on the deviatoric plane is a circle between the inscribed and circumscribed circles to the hexagonal cross section of the Hoek-Brown criterion (Fig. 4.13). According to Pan and Hudson (1988) for weak rock masses with small  $m$  and  $s$  the hexagonal cross section of the Hoek-Brown on the deviatoric plane can be approximated by a circle. Although this approximation produces a negligible error where parameters  $m$  and  $s$  are small, errors cannot be ignored in the case of strong rocks for which parameters  $m$  and  $s$  are relatively large. In other words, the Pan-Hudson criterion does not work properly for good quality rock masses or intact rock. Furthermore, the Pan-Hudson criterion does not reduce to the original form of the Hoek-Brown criterion where  $\sigma_2 = \sigma_3$ . Consequently, as pointed out by Priest (2010), under triaxial compression ( $\sigma_1 > \sigma_2 = \sigma_3$ ) the Pan-Hudson criterion does not predict the same value for the failure stress as the Hoek-Brown criterion and other three-dimensional criteria developed based on the Hoek-Brown criterion. Another drawback of the Pan-Hudson criterion is that the criterion does not calculate the uniaxial strength of rock ( $\sigma_c$ ) under uniaxial compression ( $\sigma_1 > \sigma_2 = \sigma_3 = 0$ ). The Pan-Hudson criterion can be re-derived through the following procedure:

When  $\sigma_1 = \sigma_2$ , which corresponds to  $\theta = \frac{\pi}{6}$  (Eq. 4.5.1), Eq. 4.6.2 reduces to:

$$F_{HBb} = 3J_2 - m_i \sigma_c \left( \frac{2\sqrt{J_2}}{-\sqrt{3}} + \frac{I_1}{3} \right) - s \sigma_c^2 = 0 \quad (4.6.11)$$

Where  $F_{HBb}$  is a function which represents the points exactly located on the blunt corners of the Hoek-Brown cross section on a certain deviatoric plane ( $I_1 = \text{constant}$ ). Therefore, the radius of the inscribed circle to the Hoek-Brown hexagonal cross section on the deviatoric

plane can be calculated by solving Eq. 4.6.11 for the term  $\sqrt{J_2}$ , which is given also by Eq. 4.6.7. Furthermore, substituting  $\theta = -\frac{\pi}{6}$  into Eq. 4.6.2 yields:

$$F_{HB_s} = 3J_2 - m_i \sigma_c \left( \frac{\sqrt{J_2}}{-\sqrt{3}} + \frac{I_1}{3} \right) - s \sigma_c^2 = 0 \quad (4.6.12)$$

Where  $F_{HB_s}$  represents the points on sharp corners of the Hoek-Brown cross section on a particular deviatoric plane and therefore, the radius of the circumscribed circle to the Hoek-Brown criterion on the same deviatoric plane can be calculated by applying Eq. 4.6.12, as is given also by Eq. 4.6.6. Accordingly, the function  $F_{PH}$  which represents a mean circle between the inscribed and the circumscribed circles to the Hoek-Brown cross section can be expressed as follows:

$$F_{PH} = \frac{F_{HB_s} - F_{HBb}}{2} + F_{HBb} \quad (4.6.13)$$

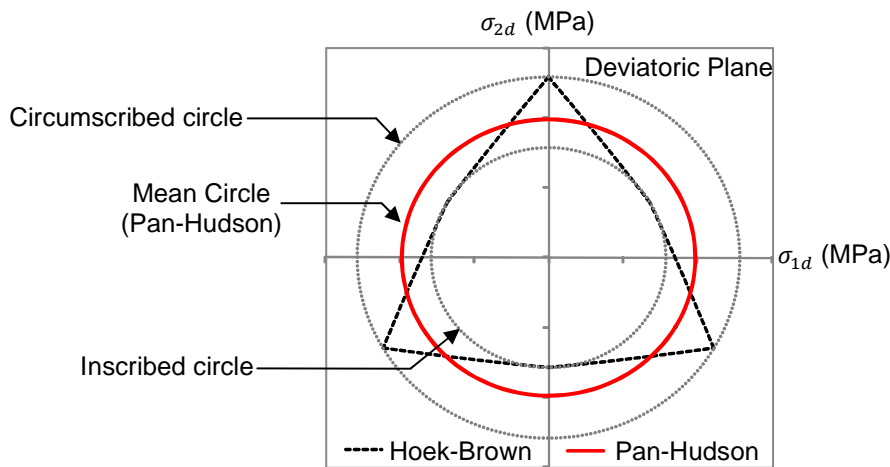


Figure 4.13 The cross section of the Hoek-Brown criterion on the deviatoric plane

Expanding and rearranging Eq. 4.6.13, the equation of the mean circle or the Pan-Hudson criterion, can be written as follows:

$$\frac{3}{\sigma_c} J_2 + \frac{\sqrt{3}}{2} m_i \sqrt{J_2} - m_i \frac{I_1}{3} = s \sigma_c \quad (4.6.14)$$

The radius of the mean circle or the distance between the hydrostatic axis and the trace of the Pan-Hudson criterion on the deviatoric plane is, therefore, given by:

$$r_{PH} = \sqrt{2J_{2PH}} = \frac{\sqrt{2}\sigma_c}{6} \left( -\lambda_{PH} + \sqrt{\lambda_{PH}^2 + 12 \left( \frac{m_i I_1}{3\sigma_c} + s \right)} \right) \quad (4.6.15)$$

Where  $m_i$ ,  $s$  and  $\sigma_c$  are the Hoek-Brown parameters and the parameter  $\lambda_{PH}$  is given as  $\frac{\sqrt{3}}{2}m_i$ .

As illustrated in Fig. 4.13, the Pan-Hudson circle has six intersections with the Hoek-Brown hexagonal cross section on the deviatoric plane. These intersections, however, do not coincide with the apices of the Hoek-Brown hexagonal cross section where  $\sigma_1 = \sigma_2$  or  $\sigma_3 = \sigma_2$ . This geometrical interpretation explains the reason why the Pan-Hudson criterion does not reduce to the original form of the Hoek-Brown criterion when the stress state is assumed as two-dimensional, i.e.  $\sigma_1 = \sigma_2$  or  $\sigma_3 = \sigma_2$ . Therefore, it is more appropriate to refer to the Pan-Hudson criterion as a three-dimensional failure criterion which sources its input parameters from the Hoek-Brown criterion, rather than a three-dimensional version of the Hoek-Brown.

The Pan-Hudson radius  $r_{PH}$  is given by Eq. 4.6.15 and therefore, the Pan-Hudson cross section on the deviatoric plane can be plotted for  $I_1 = \text{constant}$ . However, considering the parameter  $I_1$  as a variable the three-dimensional surface of the Pan-Hudson criterion can be plotted in the principal stress space (Fig. 4.14).

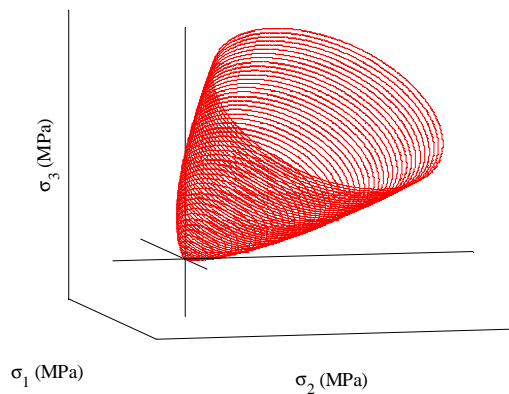


Figure 4.14 The Pan-Hudson criterion in the principal stress space

Considering Eq. 4.6.15 the parameter  $I_1$  for the Pan-Hudson criterion can be defined as:

$$I_{1PH} = \frac{9J_{2PH} + 3\sigma_c \sqrt{J_{2PH} - s\sigma_c^2}}{m_i \sigma_c} \quad (4.6.16)$$

The relevant MATLAB program, used for plotting the Pan-Hudson failure surface in the principal stress space can be found in Appendix F.

### 4.6.3. The Zhang-Zhu criterion

As pointed out by Zhang and Zhu (2007), it is desirable for a three-dimensional version of the Hoek-Brown criterion to be reduced to the original form of the Hoek-Brown criterion, when  $\sigma_2 = \sigma_3$  or  $\sigma_1 = \sigma_2$ . In triaxial compression ( $\sigma_1 > \sigma_2 = \sigma_3$ ) and extension ( $\sigma_1 = \sigma_2 > \sigma_3$ ) stress states, the second invariant of the deviatoric tensor,  $J_2$ , (Eqs. 4.2.7) reduces to:

$$J_2 = \frac{(\sigma_1 - \sigma_3)^2}{3} \quad (4.6.17)$$

Substituting Eq. 4.6.17 into Eq. 4.6.14, the Pan-Hudson criterion reduces to the following relationship:

$$(\sigma_1 - \sigma_3)^2 + \frac{m_i \sigma_c}{2} (\sigma_1 - \sigma_3) - m_i \sigma_c \sigma_m = s\sigma_c^2 \quad (4.6.18)$$

The parameter  $\sigma_m$  in Eq. 4.6.18 is the mean normal stress  $\left(\frac{I_1}{3}\right)$  and is assumed to be constant. Furthermore, rearranging Eq. 4.6.1, the Hoek-Brown criterion can also be written as:

$$(\sigma_1 - \sigma_3)^2 - m_i \sigma_c \sigma_3 = s\sigma_c^2 \quad (4.6.19)$$

Substituting Eq. 4.6.19 into Eq. 4.6.18, the constant parameter  $\sigma_m$  can be defined so that Eq. 4.6.18 reduces to the original form of the Hoek-Brown criterion under triaxial compression and extension states of stress. To satisfy this condition it is necessary to define the constant parameter  $\sigma_m$  as follows:

$$\sigma_m = \sigma_{m,2} = \frac{\sigma_1 + \sigma_3}{2} \quad (4.6.20)$$

Consequently, if the parameter  $\frac{I_1}{3}$  in the Pan-Hudson criterion is replaced with the parameter  $\sigma_{m,2} = \frac{\sigma_1 + \sigma_3}{2}$ , the resultant formulation predicts the same failure stress for intact rock material as the Hoek-Brown criterion where  $\sigma_2 = \sigma_3$  and  $\sigma_1 = \sigma_2$ . Replacing the parameter  $\frac{I_1}{3}$  in the Pan-Hudson criterion with  $\sigma_{m,2}$  yields a three dimensional version of the Hoek-Brown criterion, which was first proposed by Zhang and Zhu (2007). Accordingly, the Zhang-Zhu criterion for predicting the failure stress of intact rock in three-dimensional stress state is expressed as:

$$\frac{3}{\sigma_c} J_2 + \frac{\sqrt{3}}{2} m_i \sqrt{J_2} - m_i \sigma_{m,2} = s \sigma_c \quad (4.6.21)$$

Where the parameter  $\sigma_{m,2}$ , given by Eq. 4.6.20 can also be defined as follows:

$$\sigma_{m,2} = \frac{I_1}{3} - \frac{S_2}{2} \quad (4.6.22)$$

Furthermore, considering Eq. 4.4.11, the Eq. 4.6.22 can be written in the following form:

$$\sigma_{m,2} = \frac{I_1}{3} - \frac{\sqrt{3J_2}}{3} \sin \theta \quad (4.6.23)$$

Substituting Eq. 4.6.23 into Eq. 4.6.21, the Zhang-Zhu criterion can also be expressed as:

$$F_{ZZ} = \frac{3}{\sigma_c^2} J_2 + \frac{m_i}{2\sqrt{3}} (3 + 2 \sin \theta) \frac{\sqrt{J_2}}{\sigma_c} - \left( \frac{m_i I_1}{3 \sigma_c} + s \right) = 0 \quad (4.6.24)$$

Eq. 4.6.24 presents a more appropriate expression of the Zhang-Zhu criterion in the deviatoric stress space. Considering the function  $F_{ZZ}$  in Eq. 4.6.24, the radial distance between the hydrostatic axis and the trace of the Zhang-Zhu criterion on the deviatoric plane is calculated as follows:

$$r_{ZZ} = \sqrt{2J_{2ZZ}} = \frac{\sqrt{2} \sigma_c}{6} \left( -\lambda_{ZZ} + \sqrt{\lambda_{ZZ}^2 + 12 \left( \frac{m_i I_1}{3 \sigma_c} + s \right)} \right) \quad (4.6.25)$$

Where the parameter  $\lambda_{ZZ}$  for the Zhang-Zhu criterion is defined as:

$$\lambda_{ZZ} = \frac{m_i}{2\sqrt{3}} (3 + 2 \sin \theta) \quad (4.6.26)$$

The trace of the Zhang-Zhu failure surface on a deviatoric plane can be plotted by applying Eqs. 4.6.25 and 4.6.26 and assuming the term  $I_1$  as constant (Fig. 4.15).

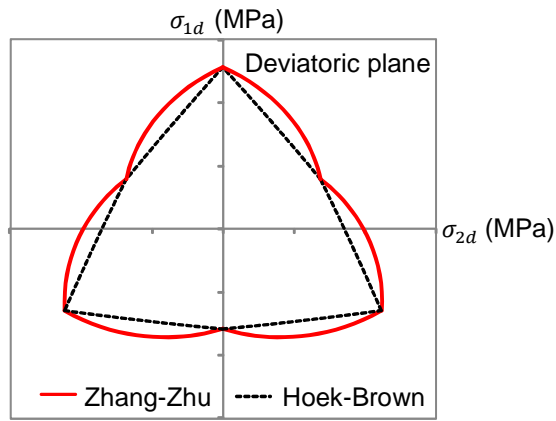


Figure 4.15 The cross section of the Zhang-Zhu criterion on the deviatoric plane

In order to reproduce the Zhang-Zhu cross sections on different deviatoric planes along the hydrostatic axis, to produce the associated three-dimensional failure surface, the Parameter  $I_1$  is assumed to be a variable and is defined, regarding to Eq. 4.6.25, for the Zhang-Zhu criterion, as follows:

$$I_{1ZZ} = 3 \left( \frac{2J_{2ZZ} + \lambda_{ZZ} \sigma_c \sqrt{J_{2ZZ} - s \sigma_c^2}}{m_i} \right) \quad (4.6.27)$$

Considering Eqs. 4.6.25, 4.6.26 and 4.6.27 and by applying an iteration loop, the three-dimensional failure surface corresponding to the Zhang-Zhu criterion can be plotted in the principal stress space (see Fig. 4.16). The relevant MATLAB code for plotting the Zhang-Zhu criterion can be found in Appendix F.

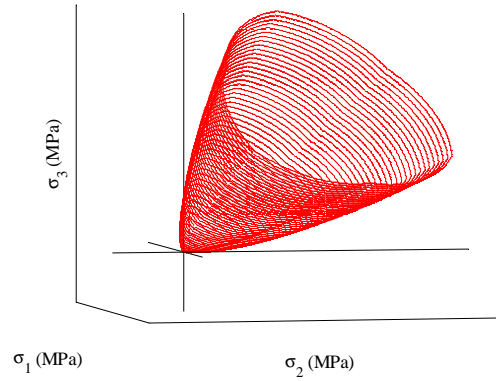


Figure 4.16 The Zhan-Zhu criterion in the principal stress space

#### 4.6.4. Generalised Priest criterion

Combining the Drucker-Prager and the Hoek-Brown criteria Priest (2005) developed a three-dimensional failure criterion. In the generalised Priest criterion the linkage between the Drucker-Prager and the Hoek-Brown criteria was based on the assumption that both criteria are supposed to give the uniaxial compressive strength of rock under uniaxial compression. The first invariant of the principal stress tensor ( $I_1$ ) and the second invariant of the principal deviatoric stress tensor ( $J_2$ ) reduce to the following expressions under uniaxial compression:

$$I_1 = \frac{\sigma_c}{3} \quad (4.6.28)$$

$$J_2 = \frac{\sigma_c^2}{3}$$

The Drucker-Prager criterion can be given as:

$$\sqrt{J_2} = A + \frac{BI_1}{3} \quad (4.6.29)$$

Substituting Eq. 4.6.28 into Eq. 4.6.29, parameters  $A$  and  $B$  can be given as follows:

$$A = \frac{\sigma_c(\sqrt{3}I_1 - 3\sqrt{J_2})}{3(I_1 - \sigma_c)} \quad (4.6.30)$$

$$B = \frac{3\sqrt{J_2} - \sigma_c\sqrt{3}}{I_1 - \sigma_c}$$

Priest (2005) pointed out that for the two criteria to be compatible the following relationship must be satisfied:

$$I_{1HB} = I_{1DP} = I_1 \quad (4.6.31)$$

Where

$$I_{1HB} = \frac{\sigma_{1HB} + 2\sigma_{3HB}}{3} \quad \text{and} \quad I_{1DP} = \frac{\sigma_{1f} + \sigma_2 + \sigma_3}{3} \quad (4.6.32)$$

In Eq. 4.6.32 the terms  $\sigma_{3hb}$  and  $\sigma_{1hb}$  are the minor principal stress at failure and the failure stress, calculated by means of the Hoek-Brown criterion through the following relationship:

$$\sigma_{1HB} = \sigma_{3HB} + \sigma_c \left( \frac{m\sigma_{3HB}}{\sigma_c} + s \right)^a \quad (4.6.33)$$

Furthermore, according to Priest (2005), the radial distance between the hydrostatic axis and the cross section of the failure surface on the deviatoric plane must be identical for both the Hoek-Brown and the Drucker-Prager criteria, that is:

$$r_{HB} = r_{DP} = r \quad (4.6.34)$$

Where

$$r_{HB} = \sqrt{\left(\sigma_{1HB} - \frac{I_1}{3}\right)^2 + 2\left(\sigma_{3HB} - \frac{I_1}{3}\right)^2} \quad (4.6.35)$$

$$r_{DP} = \sqrt{\left(\sigma_{1f} - \frac{I_1}{3}\right)^2 + \left(\sigma_2 - \frac{I_1}{3}\right)^2 + \left(\sigma_3 - \frac{I_1}{3}\right)^2}$$

The parameter  $\sigma_{1f}$  is the failure stress for the specified principal stresses  $\sigma_2$  and  $\sigma_3$ . Priest (2005) adopted a numerical iteration to solve Eqs. 4.6.29 to 4.6.35 for seven unknowns,

namely  $\sigma_{1HB}$ ,  $\sigma_{3HB}$ ,  $A$ ,  $B$ ,  $I_1$ ,  $J_2$  and  $\sigma_{1f}$ . Melkounian et al. (2009) developed an explicit solution for the Generalised Priest criterion. Considering the closed form solution of the generalised Priest criterion for intact rock material the major principal stress at failure is given as:

$$\sigma_1 = 3\sigma_{3HB} + P - (\sigma_2 + \sigma_3) \quad (4.6.36)$$

For intact rock parameter  $P$  is defined as:

$$P = \sigma_c \left[ \left( \frac{m_i \sigma_{3HB}}{\sigma_c} \right) + 1 \right]^{\frac{1}{2}} \quad (4.6.37)$$

Where

$$\sigma_{3HB} = \frac{\sigma_2 + \sigma_3}{2} + \frac{-E \mp \sqrt{E^2 - F(\sigma_2 - \sigma_3)^2}}{2F} \quad (4.6.38)$$

Parameters  $F$  and  $E$  are given as:

$$F = 3 + m_i C^{-\frac{1}{2}} \quad (4.6.39)$$

$$E = 2C^{\frac{1}{2}} \sigma_c$$

Where

$$C = 1 + \frac{m_i(\sigma_2 + \sigma_3)}{2\sigma_c} \quad (4.6.40)$$

Furthermore, under uniaxial compression the parameter  $J_{2HB}$ , given by Eq. 4.6.4, is supposed to be identical to  $J_2$ , given by Eqs. 4.6.28. Substituting Eq. 4.6.28 into Eq. 4.6.4 gives the following relationship:

$$\frac{4}{3} \cos^2 \theta + \frac{2m_i \sin\left(\frac{\pi}{3} - \theta\right)}{3} = \frac{1}{3} m_i + 1 \quad (4.6.41)$$

From Eq. 4.6.41 the angle  $\theta$  is calculated as  $\frac{\pi}{6}$ . Substituting this value for  $\theta$  into Eq. 4.6.4 the Priest criterion for intact rock can be expressed in terms of invariants of the deviatoric tensor as follows:

$$\frac{3}{\sigma_c} J_2 + \frac{\sqrt{3}}{3} m_i \sqrt{J_2} - \frac{m_i I_1}{3} = s \sigma_c \quad (4.6.42)$$

Furthermore, the radial distance from the hydrostatic axis to the trace of the generalised Priest criterion on a deviatoric plane, given by  $I_1 = \text{constant}$ , can be expressed as:

$$r_{GP} = \sqrt{2J_{2P}} = \frac{\sqrt{2}\sigma_c}{6} \left[ -\lambda_P + \sqrt{\lambda_P^2 + 12 \left( \frac{m_i I_1}{3\sigma_c} + s \right)} \right] \quad (4.6.43)$$

The parameter  $\lambda_P$  for the Priest criterion is defined as  $\frac{\sqrt{3}}{3} m_i$ . Considering Eq. 4.6.43 the cross section of the generalised Priest failure surface can be plotted on the deviatoric plane (see Fig. 4.17).

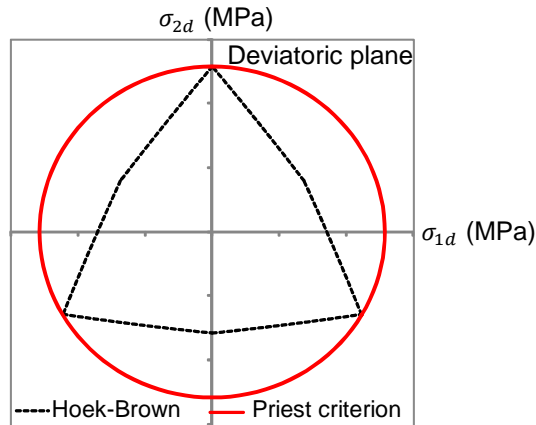


Figure 4.17 The cross section of the generalised Priest criterion on the deviatoric plane

In order to plot the corresponding three-dimensional failure surface of the Priest criterion (see Fig. 4.18) through the same approach as that adopted for other three-dimensional criteria (Appendix F), the Parameter  $I_1$  is assumed to be a variable.

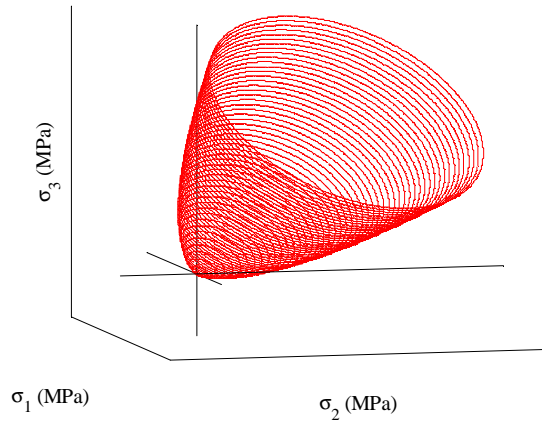


Figure 4.18 The generalised priest criterion in the principal stress space

From Eq. 4.6.43 the parameter  $I_1$  for the generalised Priest criterion is defined as:

$$I_{1GP} = \frac{9J_{2P} + m_i \sigma_c \sqrt{3J_{2P} - 3s\sigma_c^2}}{m_i \sigma_c} \quad (4.6.44)$$

#### 4.6.5. The Simplified Priest Criterion

In addition to the generalised Priest criterion, in order to incorporate the influence of the intermediate principal stress on the failure stress of rock, Priest (2005) proposed another three-dimensional failure criterion based on the Hoek-Brown criterion. He introduced a weighting factor  $w$  ranging from 0 to 1 and defined the minor principal stress ( $\sigma_{3HB}$ ) to be included in the Hoek-Brown criterion as follows:

$$\sigma_{3HB} = w\sigma_2 + (1-w)\sigma_3 \quad (4.6.45)$$

$$0 \leq w \leq 1$$

As is inferred from Eq. 4.6.45, when  $w$  is 0 the intermediate principal stress ( $\sigma_2$ ) has no influence and when  $w$  is 1 the minor principal stress ( $\sigma_3$ ) has no influence on rock strength. Substituting Eq. 4.6.45 into the Hoek-Brown criterion gives the following formulation:

$$\sigma_{1HB} = \sigma_{3HB} + \sigma_c \left( \frac{m\sigma_{3HB}}{\sigma_c} + s \right)^{\frac{1}{2}} \quad (4.6.46)$$

Considering Eqs. 4.6.31 and 4.6.32, the simplified Priest criterion for evaluation of the rock failure stress ( $\sigma_{1f}$ ) in three-dimensional stress is given by the following formulation:

$$\sigma_{1f} = \sigma_{1HB} + 2\sigma_{3HB} - (\sigma_2 + \sigma_3) \quad (4.6.47)$$

Substituting Eq. 4.4.9 into Eq. 4.6.47, the simplified Priest criterion can be written in terms of invariants of the deviatoric stress tensor as follows:

$$F_{SP} = \frac{J_2}{\sigma_c^2} \zeta_{SP} + \frac{\sqrt{J_2}}{\sigma_c} \lambda_{SP} - \left( \frac{m_i I_1}{3\sigma_c} + s \right) = 0 \quad (4.6.48)$$

Where parameters  $\zeta_{SP}$  and  $\lambda_{SP}$  are defined as follows:

$$\begin{aligned} \zeta_{SP} &= 36w^2 \sin^2 \left( \theta + \frac{\pi}{6} \right) - 6w \left( 3 + 2\sqrt{3} \sin 2\theta \right) + 12 \cos^2 \left( \theta - \frac{\pi}{6} \right) \\ \lambda_{SP} &= 2m_i \left( \frac{\sqrt{3}}{3} \sin \left( \theta + \frac{\pi}{3} \right) - w \sin \left( \theta + \frac{\pi}{6} \right) \right) \end{aligned} \quad (4.6.49)$$

Considering Eqs. 4.6.48 and 4.6.49, the radial distance from the hydrostatic axis and the trace of the simplified Priest criterion on the deviatoric plane can be expressed as:

$$r_{SP} = \sqrt{2J_{2SP}} = \frac{\sqrt{2}\sigma_c}{2\zeta_{SP}} \left[ -\lambda_{SP} + \sqrt{\lambda_{SP}^2 + 4\zeta_{SP} \left( \frac{m_i I_1}{3\sigma_c} + s \right)} \right] \quad (4.6.50)$$

Using Eqs. 4.6.49 and 4.6.50 the cross section of the simplified Priest criterion can be plotted on the deviatoric plane. However, it should be noted that since the parameter  $w$  appears in these equations, the shape of the cross section of the simplified Priest criterion changes with the changes of the parameter  $w$ . Priest (2005) proposed that for a range of sedimentary and metamorphic rocks the parameter  $w$  depends only on the minor principal stress ( $\sigma_3$ ) and could be calculated from the following relationship:

$$w \approx 0.15 \sigma_3^{0.15} \quad (4.6.51)$$

Therefore, if the minor principal stress ( $\sigma_3$ ) takes the values of, for example, 10 MPa and 100 MPa, the weighting factor  $w$  is calculated as 0.211 and 0.299, respectively. The cross sections of the simplified Priest criterion on the deviatoric plane are given in Fig. 4.19 (a) and (b), for cases when the least principal stress takes the values of 10 MPa and 100 MPa, respectively. As is obvious from Fig. 4.19, under biaxial extension ( $\sigma_1 = \sigma_2 > \sigma_3$ ), which is represented by blunt corners in the Hoek-Brown cross section, the simplified Priest criterion does not calculate the same value for the failure stress as the Hoek-Brown criterion. However, since the Hoek-Brown criterion itself was developed as an empirical criterion based on a series of conventional triaxial testes in which the stress condition is manifested by ( $\sigma_1 > \sigma_2 = \sigma_3$ ), there is no evidence proving that the Hoek-Brown criterion accurately calculates the failure stress under biaxial extension, i.e. when  $\sigma_1 = \sigma_2 > \sigma_3$  holds.

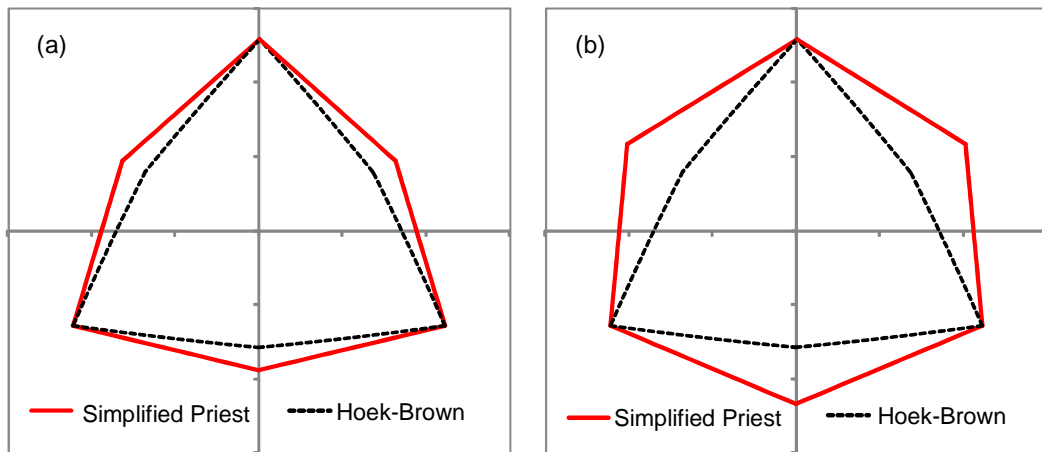


Figure 4.19 The cross section of the simplified Priest criterion on the deviatoric plane for (a)  $\sigma_3 = 10$  MPa, (b)  $\sigma_3 = 100$  MPa

The three-dimensional failure surface of the simplified Priest can also be plotted for a given value of  $\sigma_3$  and assuming the parameter  $I_1$  as a variable, which, considering Eq. 4.6.50, can be defined for the simplified Priest criterion as follows:

$$I_1 = \frac{3 \left( \zeta_{SP} J_{2SP} + \lambda_{SP} \sigma_c \sqrt{J_{2SP} - s \sigma_c^2} \right)}{m_i \sigma_c} \quad (4.6.52)$$

The relevant MATLAB code for plotting the three-dimensional failure surface, representing the simplified Priest criterion in the principal stress space can be found in Appendix F. The

effect of the weighting factor  $w$  (due to the change in the minor principal stress ( $\sigma_3$ ) values) on the shape of the simplified Priest failure surface is illustrated in Fig. 4.20 (a) and (b).

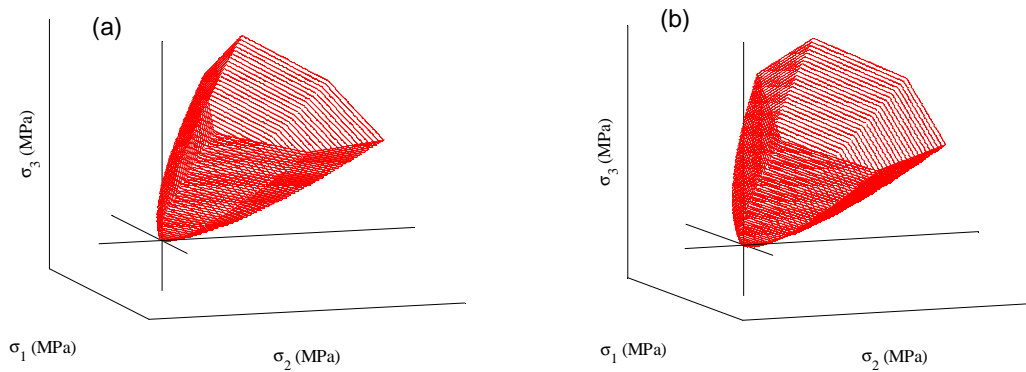


Figure 4.20 The Simplified Priest criterion in the principal stress space, for (a)  $\sigma_3 = 10$  MPa  $w = 0.211$  and (b)  $\sigma_3 = 100$  MPa,  $w = 2.99$

## 4.7. Experimental Evaluations of Rock Behaviour under Three-Dimensional Stress

Since the Hoek-Brown criterion is an empirical formulation which was developed and formulated by Hoek and Brown (1980), based on comprehensive experimental studies on the rock performance under conventional triaxial tests ( $\sigma_1 > \sigma_2 = \sigma_3$ ), it is also essential for three-dimensional failure criteria, which have been derived based on the Hoek-Brown criterion, to be validated against true-triaxial ( $\sigma_1 > \sigma_2 > \sigma_3$ ) experimental data. Colmenares and Zoback (2002) examined a number of selected failure criteria by comparing them with published true-triaxial experimental data for five different rock types, namely Dunham dolomite, Shirahama sandstone, Solnhofen limestone, Yuubari shale and KTB amphibolite. They first defined a correlation coefficient to investigate the extent of dependency of the failure stress of a particular rock type on the intermediate principal stress and then identified that the Modified Wiebols and Cook (Zhou, 1994) and the Modified Lade (Ewy, 1999) criteria are in reasonable agreement with experimental data, especially for those rocks with higher  $\sigma_2$ -dependency of failure stress. However, it should be noted that some three-dimensional Hoek-Brown based criteria which have been developed especially for rock material had not been

introduced at that time and therefore, were not included in the comparative study by Colmenares and Zoback (2002).

A statistical evaluation of the Hoek-Brown based three-dimensional failure criteria based on nine sets of published true-triaxial test data was carried out in this study. Data sets selected from true-triaxial experiments on nine different types of rocks, included three carbonates (Solnhofen limestone, Dunham Dolomite and Yamaguchi marble) and four silicates (Mizuho trachyte, Orikabe monzonite, Inada granite and Manazuru andesite) studied by Mogi (1971a), also presented by Mogi (2007), Westerly granite by Haimson and Chang (2000) and KTB amphibolite by Chang and Haimson (2000). All true-triaxial data were obtained from tests on prismatic rock specimens. The dimensions of the rock specimens in Mogi's experiments were 15×15×30 mm with the aspect ratio of 2, and for Westerly granite and KTB amphibolite the specimen's dimensions were 19×19×38 mm with the same aspect ratio of 2. Therefore, the true-triaxial data in which the intermediate principal stress is zero ( $\sigma_2 = 0$ ) can be applied for determining the Hoek-Brown parameter  $m_i$  and Coulomb parameters ( $c$  and  $\varphi$ ). Table 4.1 presents Coulomb input parameters ( $c$  and  $\varphi$ ), uniaxial compressive strength ( $\sigma_c$ ) and the input parameter  $m_i$  for the Hoek-Brown criterion for nine types of rocks discussed in this study. True-triaxial data sets are presented in Appendix C, tables C.1 to C.9.

Table 4.1 Hoek-Brown and Coulomb parameters of the rock types studied

Rock specimen	$\sigma_c$ (MPa)	$c$ (MPa)	$\varphi$ (Deg)	$m_i$
Westerly Granite	165	34	52.6	38.6
KTB Amphibolite	201	31.3	48.5	37.3
Dunham Dolomite	261	64.2	37.6	9.7
Solnhofen Limestone	310	90.4	29.5	4.6
Yamaguchi Marble	82	20	37.8	10.3
Mizuho Trachyte	100	25.9	35.3	10.9
Manazuru Andesite	140	27.2	47.5	33.7
Inada Granite	229	46.4	46	29.5
Orikabe Monzonite	234	50.8	43	20

#### 4.7.1. The influence of intermediate principal stress on failure stress

By plotting true-triaxial experimental data in  $\sigma_1 - \sigma_2$  domain, the  $\sigma_2$ -dependency of the fracture strength can be qualitatively illustrated (Fig. 4.21). In order to quantify the extent to

which the fracture strength ( $\sigma_1$ ) depends upon the change in  $\sigma_2$  values for a constant  $\sigma_3$ . Colmenares and Zobak (2002) calculated the correlation coefficient between  $\sigma_1$  and  $\sigma_2$  using linear Pearson's correlation as:

$$Corr[\sigma_1, \sigma_2] = \frac{Cov[\sigma_1, \sigma_2]}{S_{\sigma_1} S_{\sigma_2}} \quad (4.7.1)$$

Where  $S_{\sigma_1}$  and  $S_{\sigma_2}$  are the standard deviation of  $\sigma_1$  and  $\sigma_2$ , respectively. Pearson's correlation lies between -1 and 1. When the Pearson correlation is 1, it indicates that  $\sigma_1$  increases linearly with  $\sigma_2$  (perfect positive correlation) and when the Pearson correlation is -1, it means  $\sigma_1$  decreases linearly as  $\sigma_2$  increases (anti-correlation). If the two variables are absolutely independent, the Pearson correlation coefficient will be zero. However, the converse is not always true, i.e. a zero Pearson's correlation only postulates that there is no linear correlation between the two variables, yet the variables may be correlated non-linearly. On the other hand, as is obvious from Fig. 4.21, the relation between  $\sigma_1$  and  $\sigma_2$  is non-linear. Furthermore, if a second order polynomial (quadratic) function is fitted to data points in the  $\sigma_1 - \sigma_2$  domain for constant  $\sigma_3$  values, the coefficient of fitness to the quadratic function as a nonlinear correlation coefficient is calculated as:

$$r = \sqrt{1 - \frac{SSE}{SST}} \quad (4.7.2)$$

Where 'SSE' is the 'Sum of the Squared Errors' between the observed values of the fracture stress ( $\sigma_{1(obs)}$ ) and the fitted values of the fracture stress ( $\sigma_{1(fit)}$ ) given by:

$$SSE = \sum_{i=1}^N (\sigma_{1(obs)i} - \sigma_{1(fit)i})^2 \quad (4.7.3)$$

The parameter 'SST' in Eq. 4.7.2 is known as the 'Sum of the Squared Total' and is calculated as:

$$SST = \sum_{i=1}^N (\sigma_{1(obs)i} - \bar{\sigma}_{1(obs)i})^2 \quad (4.7.4)$$

The parameter  $\bar{\sigma}_{1(obs)}$  is the mean value of  $\sigma_{1(obs)i}$ . Therefore, since the experimental data do not demonstrate a linear relationship between the fracture stress ( $\sigma_1$ ) and the intermediate principal stress ( $\sigma_2$ ), calculation of the linear correlation coefficient between these two variables does not provide any information about the dependence of  $\sigma_1$  on  $\sigma_2$ . However, if it is assumed that the intermediate principal stress and the fracture stress are correlated through a quadratic relationship, this correlation can be quantified by applying Eq. 4.7.2. Furthermore, in order to visualise the extent of  $\sigma_2$ -dependency of the fracture stress at any given value for  $\sigma_3$ , calculated values for the non-linear correlation coefficient can be plotted versus the minor principal stress (Fig. 4.22).

The linear correlation coefficient between  $\sigma_1$  and  $\sigma_2$  calculated by the means of Pearson's linear correlation coefficient was also plotted versus the minor principal stress and is presented in Appendix C, Fig. C.1. As illustrated in Fig. 4.22, correlation of fitness to quadratic functions in almost all cases lies between 0.8-1, which indicates that the fracture stress closely correlates with the intermediate principal stress through a quadratic function. This close correlation suggests that the nature of dependency of the failure stress ( $\sigma_1$ ) on the intermediate principal stress ( $\sigma_2$ ) can be well simulated by a quadratic function.

Furthermore, all quadratic functions fitted to data points are concaved downward, i.e. the second derivatives of all quadratic functions are negative. Such quadratic functions grow to a maximum as the variable increases, thereafter the function declines with the increasing variable. Equating the first derivative of each one of these quadratic functions for a given value for  $\sigma_3$  to zero, the value of the intermediate principal stress after which increasing  $\sigma_2$  negatively affects the rock strength can be calculated. The application of the linear correlation coefficient can only be meaningful if two correlation functions are calculated; the first one from the point  $\sigma_2 = \sigma_3$  to the point  $\sigma_2 = \sigma$  at which the quadratic function is at its maximum, and the second one from the point  $\sigma_2 = \sigma$  down to the failure point, which is higher than the point  $\sigma_2 = \sigma_3$  (Fig. 4.21). It merits noting that the former yields a positive correlation and the latter gives an anti-correlation.

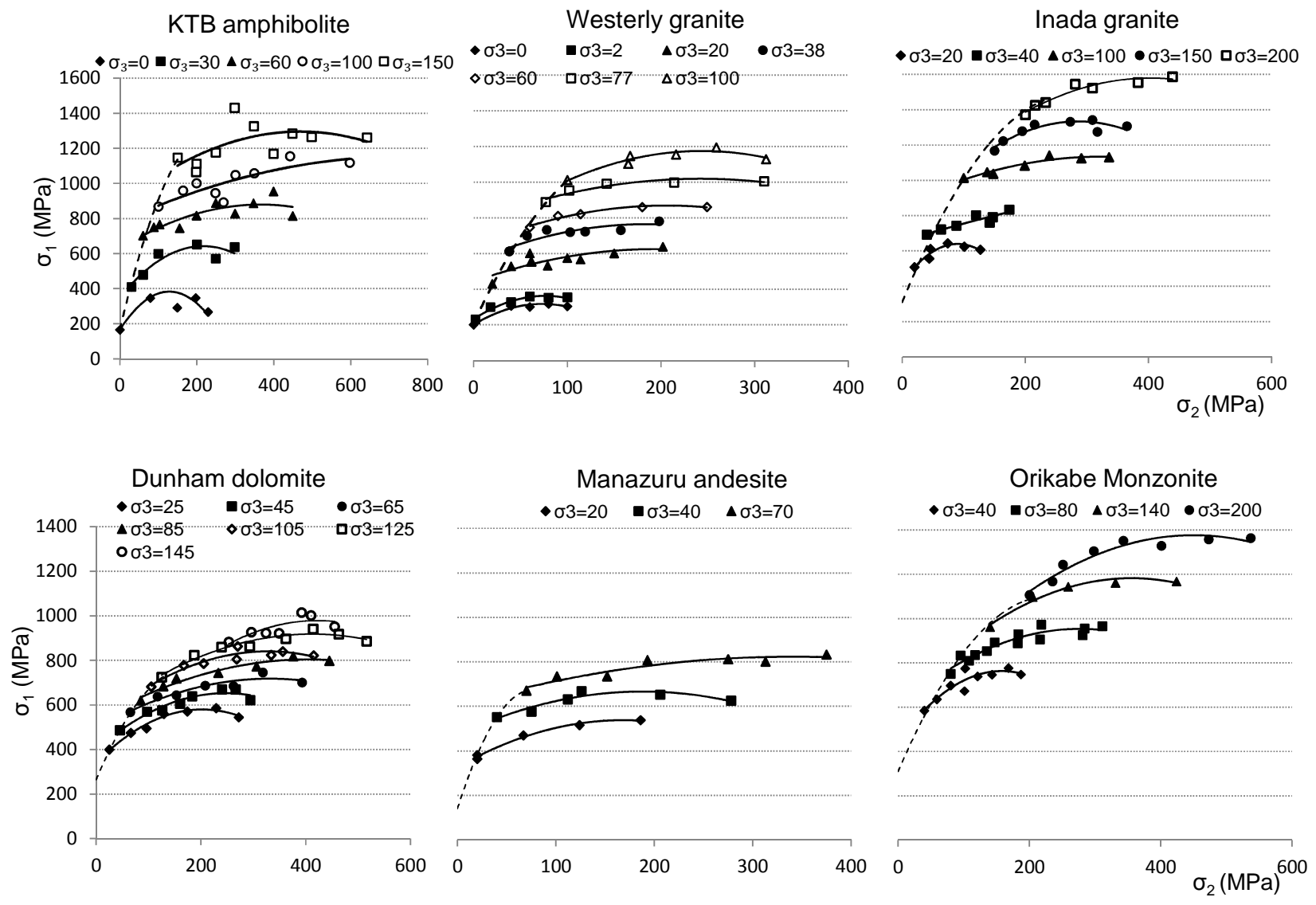
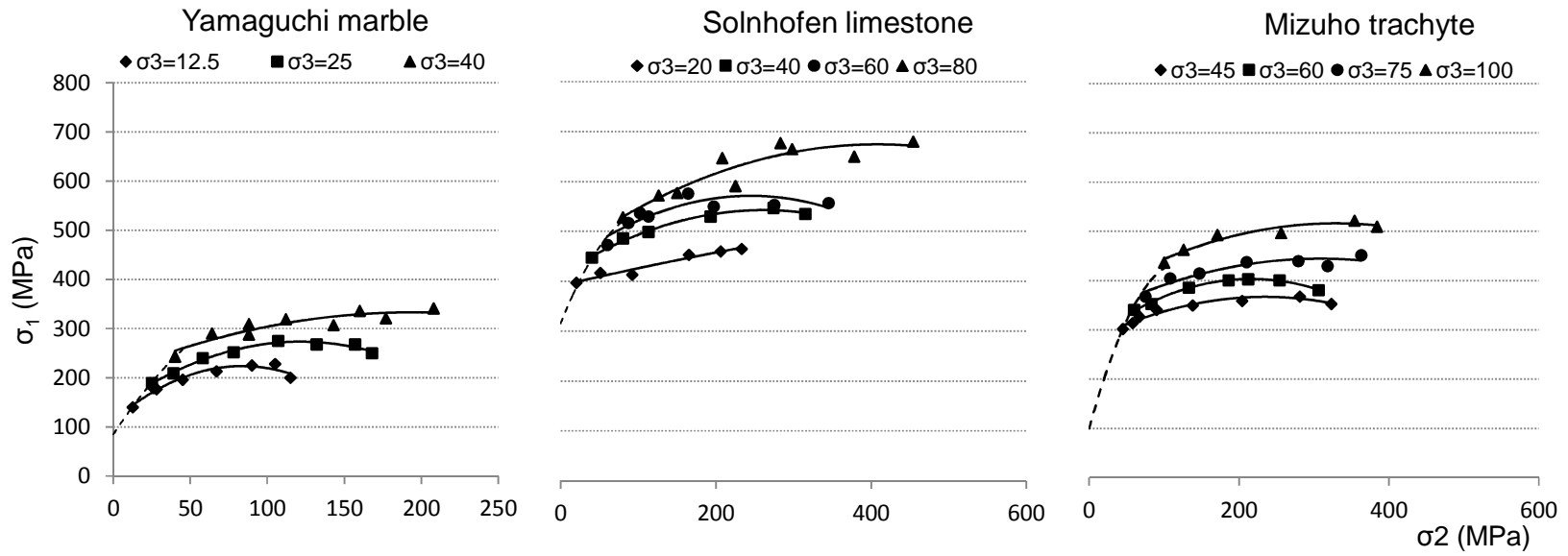


Figure 4.21 Fitting quadratic functions to true-triaxial experimental data in  $\sigma_1 - \sigma_2$  domain (continues)



Continued from Figure 4.21 Fitting quadratic functions to true-triaxial experimental data in  $\sigma_1 - \sigma_2$  domain

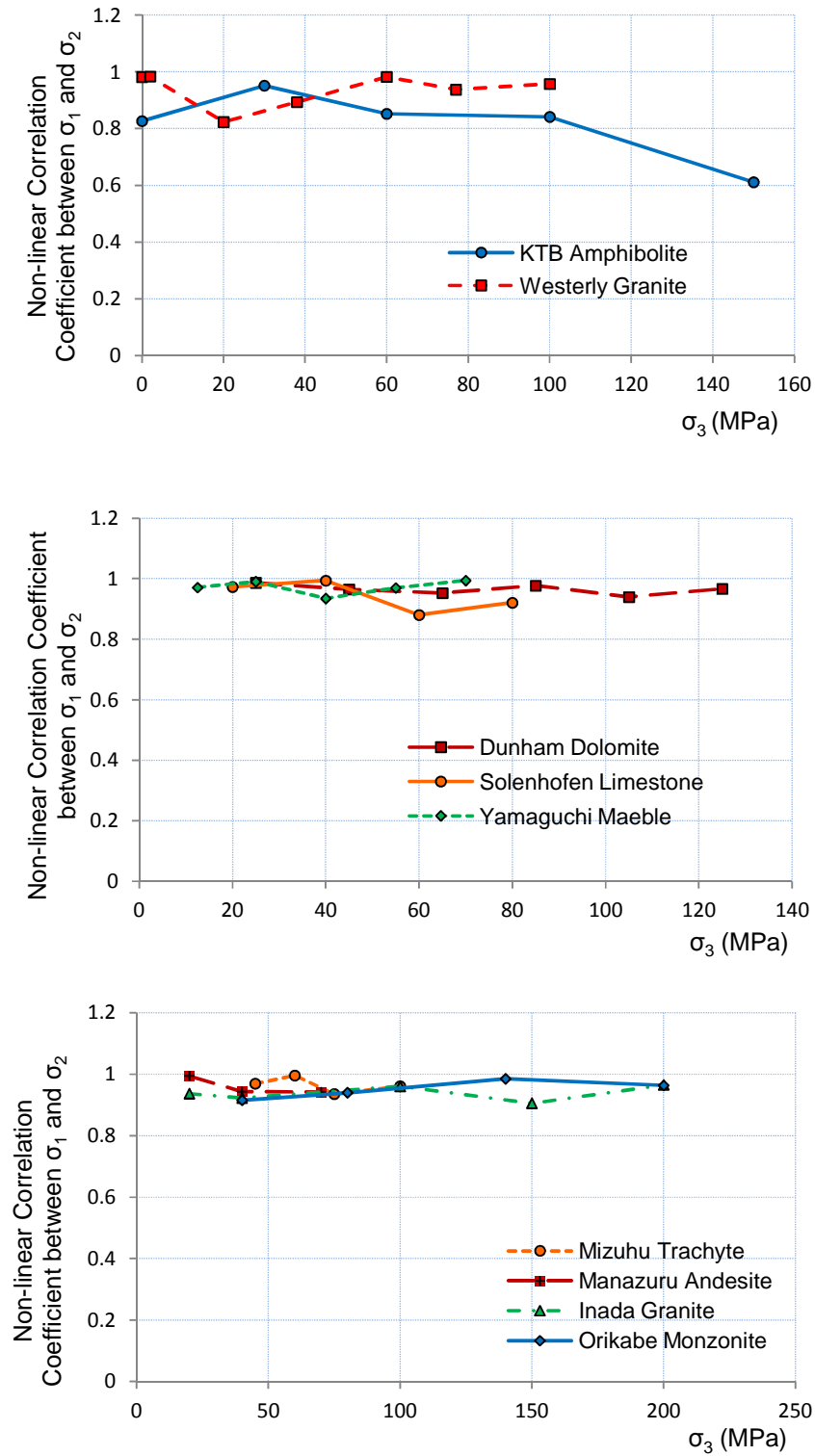


Figure 4.22 Non-linear correlation coefficient between the failure stress ( $\sigma_1$ ) and the intermediate principal stress ( $\sigma_2$ ) versus the least principal stress ( $\sigma_3$ )

### 4.7.2. A modification to the simplified Priest criterion

If the failure stress in the principal stress space is represented by a point  $P$ , as illustrated in Fig. 4.6, the length  $OC$  along the hydrostatic axis from the origin of the principal stress space perpendicular to a deviatoric plane containing the point  $P$  is calculated as:

$$OC_P = \frac{1}{\sqrt{3}}(\sigma_1 + \sigma_2 + \sigma_3) \quad (4.7.5)$$

Furthermore, the radial distance from the hydrostatic axis to the point  $P$  on the deviatoric plane can be given as follows:

$$r_P = \sqrt{2J_2} = \sqrt{\frac{1}{3}[(\sigma_1 - \sigma_2)^2 + (\sigma_2 - \sigma_3)^2 + (\sigma_3 - \sigma_1)^2]} \quad (4.7.6)$$

On the other hand, the Hoek-Brown criterion predicts a failure stress, which can also be represented by a point such as  $HB$  in the principal stress space. For such a stress point the length  $OC_{HB}$  along the hydrostatic axis and the radial distance  $r_{HB}$  from the hydrostatic axis can be given by the following expressions, recalling that the Hoek-Brown criterion assumes equal values for the intermediate and the minor principal stresses.

$$OC_{HB} = \frac{1}{\sqrt{3}}(\sigma_{1HB} + 2\sigma_{3HB}) \quad (a) \quad (4.7.7)$$

$$r_{HB} = \sqrt{2J_{2HB}} = \sqrt{\frac{2}{3}}(\sigma_{1HB} - \sigma_{3HB}) \quad (b)$$

In Eqs. 4.4.7,  $\sigma_{3HB}$  and  $\sigma_{1HB}$  are calculated from Eqs. 4.6.45 and 4.6.46, respectively. In order to develop a three-dimensional failure criterion based on the Hoek-Brown criterion, it is desired that the failure point  $HB$ , predicted by the Hoek-Brown criterion, coincides with the failure point  $P$  which occurs under the three-dimensional stress condition. Therefore, the stress vector  $\vec{\sigma}_P$  in Fig. 4.6, which indicates the position of the failure stress in the principal stress space, must be identical with the stress vector  $\vec{\sigma}_{HB}$  calculated by the means of the Hoek-Brown criterion:

$$\vec{\sigma}_P = \vec{\sigma}_{HB} \quad (4.7.8)$$

Therefore, considering Fig. 4.6 and recalling the Pythagoras theorem the Eq. 4.7.8 can be written as:

$$r_P^2 + OC_P^2 = r_{HB}^2 + OC_{HB}^2 \quad (4.7.9)$$

Rearranging Eq. 4.7.9, the failure stress  $\sigma_{1f}$  can be calculated as follows:

$$\sigma_{1f} = \left[ \sigma_{1HB}^2 + 2\sigma_{3HB}^2 - (\sigma_2^2 + \sigma_3^2) \right]^{\frac{1}{2}} \quad (4.7.10)$$

It should be noted that the prediction accuracy of the failure criterion given by Eq. 4.7.10 depends upon the weighting factor  $w$  which appears in the formulation of  $\sigma_{3HB}$  (Eq. 4.6.45) and consequently, in the formulation of  $\sigma_{1HB}$ . One strategy for formulating the weighting factor  $w$  is to substitute Eq. 4.6.45 into Eq. 4.6.38, which results in the following relationship:

$$w = \frac{1}{2} + \frac{-E \mp \sqrt{E^2 - F(\sigma_2 - \sigma_3)^2}}{2F(\sigma_2 - \sigma_3)} \quad (4.7.11)$$

Where parameters  $E$  and  $F$  are given by Eqs. 4.6.39. In a given stress state where  $\sigma_2$  and  $\sigma_3$  are known by substituting the weighting factor  $w$  from Eq. 4.7.11 into Eq. 4.7.10 the failure stress is calculated the same way as is done by the generalised Priest criterion. However, it merits noting that the generalised Priest criterion assumes, as does the Drucker-Prager criterion, a more profound strengthening effect for the intermediate principal stress than that which is observed in true-triaxial experiments and therefore, tends to overestimate the rock strength, especially at higher values of  $\sigma_2$ .

This overestimating tendency of the generalised Priest criterion can be addressed considering the circular cross section of this criterion on the deviatoric plane. This circular cross section indicates that the radial distance between the hydrostatic axis and the predicted failure point on the trace of the failure surface on the deviatoric plane is identical for all stress conditions. However, from Fig. 4.22 it can be observed that the failure stress decreases after the intermediate principal stress grows closer to the major principal stress. Therefore, the radial distance between the hydrostatic axis and the trace of the failure surface on the deviatoric

plane is supposed to be smaller when  $\sigma_1 = \sigma_2$ , i.e. at obtuse corners in the hexagonal cross section of the Hoek-Brown criterion on the deviatoric plane.

Accordingly, in order to incorporate the dual nature of  $\sigma_2$ -dependency of the failure stress, the weighting factor  $w$  can be determined so that the strengthening effect of the intermediate principal stress to be addressed in accordance with the true-triaxial test data. It should be noted that on a particular deviatoric plane the radial distance between the failure point  $P$  and the failure point predicted by the Hoek-Brown criterion are supposed to be identical, so according to Eqs. 4.7.6 and 4.7.7 (b) the following relationship holds:

$$(\sigma_1 - \sigma_2)^2 + (\sigma_2 - \sigma_3)^2 + (\sigma_3 - \sigma_1)^2 = 2(\sigma_{1HB} - \sigma_{3HB})^2 \quad (4.7.12)$$

On the other hand, considering Fig. 4.6, for a particular deviatoric plane the distance  $OC_P$  for the failure point  $P$  and the distance  $OC_{HB}$  for the point  $HB$  predicted by the Hoek-Brown criterion are equal and therefore, recalling Eqs. 4.7.5 and 4.7.7 (a) the major principal stress can be given as follows:

$$\sigma_1 = \sigma_{1HB} + 2\sigma_{3HB} - \sigma_2 - \sigma_3 \quad (4.7.13)$$

Substituting Eq. 4.7.13 into Eq. 4.7.12, and after series of expansion and rearrangement, the following relationship can be derived for calculating the weighting factor  $w$  for intact rock:

$$9w^4 - (18 + 4\eta)w^3 + (15 + 8\eta - 4\mu)w^2 - (6 + 5\eta - 4\mu)w + (1 + \eta - \mu) = 0 \quad (4.7.13)$$

Where parameters  $\eta$  and  $\mu$  are defined as follows:

$$\eta = \frac{m\sigma_c}{(\sigma_2 - \sigma_3)} \quad \text{and} \quad \mu = \frac{\sigma_c^2 + m\sigma_c\sigma_2}{(\sigma_2 - \sigma_3)^2} \quad \sigma_2 \neq \sigma_3 \quad (4.7.14)$$

However, substitution of the weighting factor  $w$ , given by Eqs. 4.7.13 and 4.7.14, into Eq. 4.7.10 again results in overestimation of the failure stress and the predicted values for the failure stress are quite similar to the predicted failure stress calculated by the generalised Priest criterion. It is also important to note that when  $\sigma_2 = \sigma_3$  Eq. 4.6.45 reduces to  $\sigma_{3HB} = \sigma_3$  and consequently the rock failure stress,  $\sigma_{1f}$  in Eq. 4.7.10 will be the same as the failure stress predicted by the original two-dimensional formulation of the Hoek-Brown criterion. An

alternative approach for determining the weighting factor  $w$  is to define this parameter so that to achieve minimum misfit with true-triaxial data. In order to achieve this goal, the parameter  $w$  was first defined to obtain exact match with experimental data for each case. On the other hand, the parameter  $w$  can be assumed to be proportional to parameters  $\eta$  and  $\mu$ , (which appear in Eq. 4.7.13 and are given by Eqs. 4.7.14), and to the minor principal stress ( $\sigma_3$ ) and the uniaxial strength ( $\sigma_c$ ) as follows:

$$w \propto \left( \frac{\mu}{\eta} - \frac{\sigma_3}{\sigma_c} \right) \quad (4.7.15)$$

The relationship between the weighting factor  $w$  and parameters  $\eta$ ,  $\mu$ ,  $\sigma_3$  and  $\sigma_c$  can be formulated as a power function by plotting the values of  $w$  for which Eq. 4.7.10 predicts the exact value of the failure stress versus the values of the term  $\left( \frac{\mu}{\eta} - \frac{\sigma_3}{\sigma_c} \right)$  for each stress state (Fig. 4.23) as follows:

$$w = 0.24 \left( \frac{\mu}{\eta} - \frac{\sigma_3}{\sigma_c} \right)^{0.5} \quad (4.7.16)$$

Substituting the parameter  $w$ , as is given by Eq. 4.7.16, into the proposed three-dimensional failure criterion given by Eq. 4.7.10, the dual nature of the  $\sigma_2$ -dependency of the failure stress is appropriately taken into account. A statistical comparison of three-dimensional failure criteria which source their input parameters from the Hoek-Brown criterion was carried out against nine sets of published true-triaxial experimental data and is presented in the subsequent section.

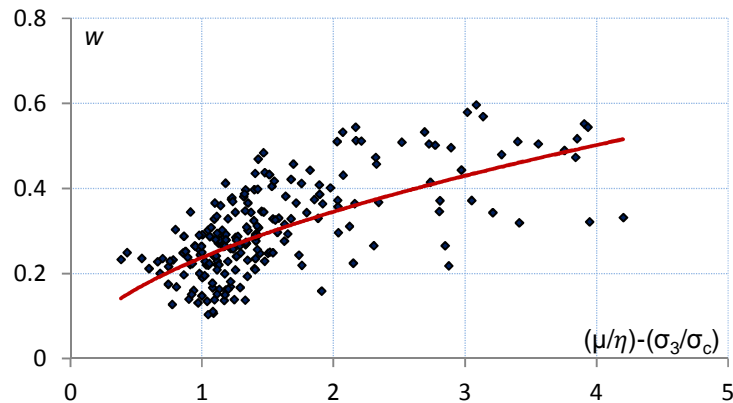


Figure 4.23 Actual values of the weighting factor  $w$  versus values of the term  $\frac{\mu}{\eta} - \frac{\sigma_3}{\sigma_c}$

### 4.7.3. Comparison of three-dimensional, Hoek-Brown based failure criteria

The common method used to compare the prediction accuracy of three-dimensional failure criteria to experimental data is to create a two-dimensional graph plotting  $\sigma_1$  versus  $\sigma_2$  for a constant  $\sigma_3$  (Appendix D,  $\sigma_1$  vs.  $\sigma_2$  graphs). A qualitative analysis is then undertaken to assess how well the various criteria fit the experimental data in  $\sigma_1$ - $\sigma_2$  domain. The key limitation of this method is that each analysis only takes into account a single slice of the three-dimensional stress space for a constant  $\sigma_3$ .

A more comprehensive error analysis can be conducted by giving consideration to three-dimensional failure surfaces of failure criteria in principal stress space. Any point on the failure surface represents a failure stress, which has been predicted by the associated failure function and can be addressed by a stress vector ( $\vec{\sigma}$ ). The stress vector from the origin of the principal stress space to the predicted stress point on the failure surface is depicted as  $\vec{\sigma}_{(model)}$  in Fig. 4.24. Similarly, an observed data point in the principal stress space can be represented by a stress vector as  $\vec{\sigma}_{(observed)}$ , as illustrated in Fig. 4.24.

The magnitude of the resulting vector,  $\vec{\sigma}_{(model)} - \vec{\sigma}_{(observed)}$ , quantifies the difference between the predicted and observed failure stresses and therefore, can be interpreted as a measure of prediction accuracy of the failure model. Furthermore, negative values of the subtraction resultant vector indicate that the relevant model underestimates the rock failure stress and positive values of this vector are interpreted as that the rock strength has been overestimated. Therefore, the prediction accuracy (PA) of a failure criterion, as a predictive model, can be defined as follows:

$$PA = \vec{\sigma}_{(model)} - \vec{\sigma}_{(observed)} \quad (4.7.5)$$

However, as the values of  $\sigma_2$  and  $\sigma_3$  are identical for both  $\vec{\sigma}_{(model)}$  and  $\vec{\sigma}_{(observed)}$ , the only distance relating to an error is in the  $\sigma_1$  direction. Therefore, Eq. 4.7.5 can be reduced to the following expression:

$$PA = \sigma_{1(model)} - \sigma_{1(observed)} \quad (4.7.6)$$

In addition, absolute percentage error can be defined as:

$$E = \left| \frac{\sigma_{1(model)} - \sigma_{1(observed)}}{\sigma_{1(observed)}} \right| \times 100 \quad (4.7.7)$$

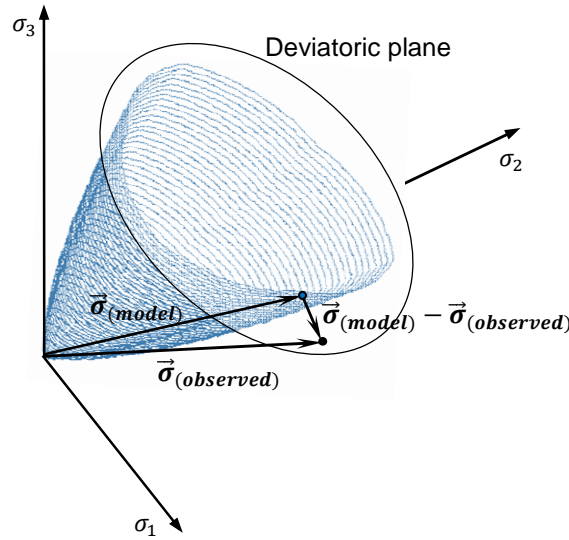


Figure 4.24 Difference between predicted and observed failure stresses

Comparing the calculated values of absolute percentage errors from Eq. 4.7.7 for each one of three-dimensional criteria incorporated in this study it was revealed that in all cases (with the exception for Yamaguchi Marble) the proposed criterion, given by Eq. 4.7.10, namely the modified simplified Priest, predicts the rock failure stress more accurately than other three-dimensional models. Results of this statistical comparison are presented in Table 4.2. After the proposed criterion the Zhang-Zhu criterion is in good agreement with the experimental data, and in the case of Yamaguchi marble is more accurate than other models, including the modified simplified Priest criterion. Furthermore, the relative likelihood of being zero for  $PA$ , which is a measure of difference between the experimental and predicted failure stress values and is given by Eq. 4.7.6, can be described using the probability density function (PDF) which is parameterised in terms of the ‘mean’ and ‘variance’ as follows:

$$f(PA | \mu, \sigma^2) = \frac{1}{\sigma\sqrt{2\pi}} e^{-\frac{(PA-\mu)^2}{2\sigma^2}} \quad (4.7.8)$$

Where  $\mu$  and  $\sigma$  are the mean and variance, respectively. The probability density functions, given by Eq. 4.7.8, were plotted versus  $PA$  for the nine data sets and six selected three-dimensional failure criteria which are presented in Appendix D. The values for mean and variance were also included in Figs. D.1 to D.9, in Appendix D.

Table 4.2 Comparison of 3D Hoek-Brown based criteria

<b>Manazuru Andesite</b>				
Criterion	Rank	$\sigma_{1(\text{model})} - \sigma_{1(\text{observed})}$ (MPa)	over/underestimation (average)	Average percentage error (%)
Modified Simplified Priest	1	4.15	overestimation	5.01
Simplified Priest	2	-16.11	underestimation	6.09
Zhang-Zhu	3	16.80	overestimation	6.79
Hoek-Brown	4	-100.04	underestimation	15.76
Generalised Priest	5	106.24	overestimation	17.83
Pan-Hudson	6	-170.01	underestimation	34.75
<b>Inada Granite</b>				
Criterion	Rank	$\sigma_{1(\text{model})} - \sigma_{1(\text{observed})}$ (MPa)	over/underestimation (average)	Average percentage error (%)
Modified Simplified Priest	1	-11.58	underestimation	3.73
Simplified Priest	2	-31.17	underestimation	4.34
Zhang-Zhu	3	-12.92	underestimation	4.67
Generalised Priest	5	59.83	overestimation	8.34
Hoek-Brown	4	-119.57	underestimation	12.99
Pan-Hudson	6	-336.48	underestimation	34.94
<b>Orikabe Monzonite</b>				
Criterion	Rank	$\sigma_{1(\text{model})} - \sigma_{1(\text{observed})}$ (MPa)	over/underestimation (average)	Average percentage error (%)
Modified Simplified Priest	1	-7.12	underestimation	5.64
Zhang-Zhu	3	-25.53	underestimation	6.41
Generalised Priest	5	45.28	overestimation	7.91
Simplified Priest	2	-54.12	underestimation	8.55
Hoek-Brown	4	-47.53	underestimation	9.76
Pan-Hudson	6	-251.34	underestimation	31.80
<b>Yamaguchi Marble</b>				
Criterion	Rank	$\sigma_{1(\text{model})} - \sigma_{1(\text{observed})}$ (MPa)	over/underestimation (average)	Average percentage error (%)
Zhang-Zhu	1	1.59	overestimation	3.88
Modified Simplified Priest	2	-3.33	underestimation	4.35
Simplified Priest	3	-23.35	underestimation	10.43
Generalised Priest	4	41.11	overestimation	15.87
Hoek-Brown	5	-42.64	underestimation	17.70
Pan-Hudson	6	-30.84	underestimation	18.74

Continues

<b>KTB Amphibolite</b>				
Criterion	Rank	$\sigma_{1(\text{model})} - \sigma_{1(\text{observed})}$ (MPa)	over/underestimation (average)	Average percentage error (%)
Modified Simplified Priest	1	33.68	overestimation	12.63
Zhang-Zhu	2	64.73	overestimation	13.65
Simplified Priest	3	-15.70	underestimation	15.91
Hoek-Brown	4	-132.07	underestimation	25.00
Pan-Hudson	5	-141.13	underestimation	25.33
Generalised Priest	6	216.71	overestimation	34.73
<b>Westerly Granite</b>				
Criterion	Rank	$\sigma_{1(\text{model})} - \sigma_{1(\text{observed})}$ (MPa)	over/underestimation (average)	Average percentage error (%)
Modified Simplified Priest	1	20.45	overestimation	9.32
Zhang-Zhu	2	19.56	overestimation	9.88
Simplified Priest	3	-38.89	underestimation	9.99
Hoek-Brown	4	-109.73	underestimation	17.97
Generalised Priest	5	112.70	overestimation	23.80
Pan-Hudson	6	-258.34	underestimation	40.95
<b>Dunham Dolomite</b>				
Criterion	Rank	$\sigma_{1(\text{model})} - \sigma_{1(\text{observed})}$ (MPa)	over/underestimation (average)	Average percentage error (%)
Modified Simplified Priest	1	-16.83	underestimation	3.19
Zhang-Zhu	2	-7.43	underestimation	4.29
Simplified Priest	3	-45.30	underestimation	7.02
Generalised Priest	5	83.56	overestimation	11.37
Hoek-Brown	4	-121.30	underestimation	16.69
Pan-Hudson	6	-102.99	underestimation	16.83
<b>Solnhofen Limestone</b>				
Criterion	Rank	$\sigma_{1(\text{model})} - \sigma_{1(\text{observed})}$ (MPa)	over/underestimation (average)	Average percentage error (%)
Modified Simplified Priest	1	8.72	overestimation	3.51
Zhang-Zhu	2	8.05	overestimation	3.71
Simplified Priest	3	-36.19	underestimation	7.09
Generalised Priest	5	63.52	overestimation	12.14
Hoek-Brown	4	-65.59	underestimation	12.21
Pan-Hudson	6	-47.75	underestimation	12.40
<b>Mizuho trachyte</b>				
Criterion	Rank	$\sigma_{1(\text{model})} - \sigma_{1(\text{observed})}$ (MPa)	over/underestimation (average)	Average percentage error (%)
Modified Simplified Priest	1	-14.26	underestimation	4.33
Zhang-Zhu	2	4.57	overestimation	4.65
Simplified Priest	3	-10.31	underestimation	4.49
Hoek-Brown	4	-43.98	underestimation	11.43
Pan-Hudson	5	-20.92	underestimation	16.20
Generalised Priest	6	65.40	overestimation	17.33

## 4.8. True-triaxial Experiments at the University of Adelaide

Although a number of true-triaxial experiments have been conducted over the past decades, as a major limitation in studying the rock performance under three-dimensional stress can still be mentioned the lack of adequate true-triaxial experimental data in order to validate the theoretical and empirical rock failure models. The main reasons for such limitation are the elaborate rock specimen preparation techniques and complicated testing procedures. According to Mogi (1971a) the major difficulty of the true-triaxial testing is ensuring the application of three orthogonal, independent yet homogeneous stresses to rock specimens. Nevertheless, there exists a serious need for further true-triaxial experiments to be conducted on rock material. Considering this serious demand a number of polyaxial tests were conducted at the University of Adelaide in collaboration with a group of four honours students. The main purposes of conducting true-triaxial experiments were to validate three-dimensional rock failure criteria developed based on the Hoek-Brown criterion, and to investigate the effect of the specimen size and shape on the apparent strength of the rock specimen.

### 4.8.1. Experimental setup

#### *True-triaxial apparatus*

The true-triaxial cell used for testing was designed and fabricated at the University of Adelaide by Prof. Stephen D. Priest and Dr. Nouné S. Melkounian in collaboration with Mr Adam Schwartzkopff et al. (2010) (Fig. 4.25). The design of the true-triaxial cell was adopted from and is similar to an existing design outlined by King et al. (1997) (Schwartzkopff et al., 2010). Lateral confining pressures are applied independently and orthogonally by two sets of hydraulic jacks mounted on a steel reaction ring by means of intermediate jack support units. Each opposing set of jacks is controlled by a hydraulic circuit, which is pressurised by a hand pump connected to an adjustable pressure relief valve. Each jack has a capacity of 718 KN, which corresponds to maximum pressures of 287, 200, 147 and 112 MPa on 50, 60, 70 and 80 mm sized cubic specimens, respectively. The hydraulic jacks control the extension of circular pistons on which intermediate platen base units are mounted using rare earth magnets. The platen base unit has an indentation into which the platen is inserted.

One important feature of the true-triaxial cell is that replaceable platens of various sizes render the cell capable of testing cubic specimens of different sizes, with dimensions of 50, 60, 70 and 80 mm. All different size platens were designed with the same dimensions at their base, to allow them to be slotted into the platen base unit and the platen dimensions change from the base to the contact surface to match the surface dimensions of the specimen. In order to avoid the grinding of the platens which could result in damaging the cell, the platens were designed with a 2% bevel around the edges to account for the deformation of the rock specimen during testing (Schwartzkopff et al., 2010).

Top and bottom platens were also fabricated for each specimen size and the contacting surfaces were designed to have the same chamfering as the lateral platens. Axial load is applied using a compression machine which has a maximum capacity of 5000 KN. Strains in the three principal stress directions are also monitored during testing by means of Linear Variable Differential Transducers (LVDTs). The loading system was thoroughly calibrated using a strain-gaged aluminium sample of known elastic properties. A detailed description of the design, fabrication and calibration procedures of the true-triaxial cell at the University of Adelaide is given in Schwartzkopff et al. (2010).

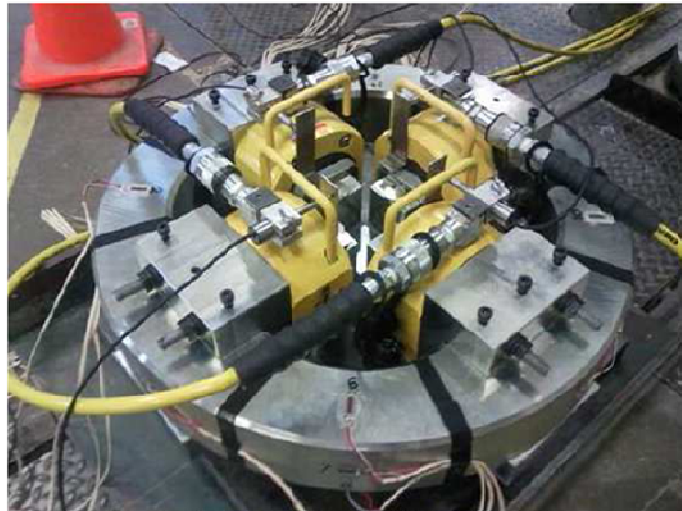


Figure 4.25 True-triaxial apparatus of the University of Adelaide [after Schwartzkopff et al.(2010)]

### *Specimen preparation*

Specimens were made from Kanmantoo bluestone, which is a hard fine-grained, medium to dark grey-blue meta-siltstone of early Cambrian age. The stone was sourced from the Kanmantoo Stone Quarry in the Adelaide Hills. The bluestone occurs within the Tapanappa formation within the larger Kanmantoo group within the Adelaide fold belt geological province. Kanmantoo bluestone was chosen because it is a relatively homogeneous rock. This homogeneity reduces the risk of inaccurate test results due to flaws in individual specimens.

To determine the uniaxial compressive strength,  $\sigma_c$ , and the parameter  $m_i$  for the Hoek-Brown criterion a number of cylindrical specimens with aspect ratio of 2.4 were prepared to be tested in the Hoek cell. Cores were drilled out from a block of Kanmantoo bluestone and were cut to make specimens of 100mm in length and 42mm in diameter. The top and bottom faces of the cores then were ground to minimise the parallelism offset.

To prepare cubic specimens of 60×60×60 mm dimensions to be tested in the true-triaxial apparatus, first, cores of 85mm diameter were drilled out of the Kanmantoo block. Once the cores were prepared, they were cut into rectangular prisms and then two cubes were cut out of each prism (Fig. 4.26). Cubic specimens (60×60×60 mm) were surface ground to obtain dimensions within 1mm from the prescribed size, with 0.05 mm of parallelism and orthogonality offsets. It was a requirement that the cubic specimens were slightly larger than their specified size to allow the cubes to be used in the true-triaxial cell without any contact between platens in the true-triaxial cell. Undersized or exact sized cubes may cause contact between platens.



Figure 4.26 Block of Kanmantoo Blue stone and preparation of cubic specimens [after Dong et al., (2011)]

***True-triaxial tests***

A total number of 10 true-triaxial tests were carried out on 60×60×60 mm cubic specimens of Kanmantoo blue stone. True-triaxial tests were conducted at the University of Adelaide and in collaboration with a group of four honour students. True-triaxial testing procedure consisted of simultaneously raising all three principal stresses at a constant rate until  $\sigma_3$  reached its prescribed value. Thereafter, the other two principal stresses ( $\sigma_1$  and  $\sigma_2$ ) were increased at the same rate until  $\sigma_2$  reached its predetermined magnitude. From this point  $\sigma_3$  and  $\sigma_2$  were kept constant and  $\sigma_1$  alone was raised until the specimen failed. Unloading was carried out after  $\sigma_1$  decreased approximately 5%-10% of its peak level. The results of true-triaxial tests are presented in Table 4.3.

Table 4.3 True-triaxial experimental data of Kanmantoo Bluestone, The University of Adelaide (2011)

Test No.	$\sigma_1$ (MPa)	$\sigma_2$ (MPa)	$\sigma_3$ (MPa)	$I_1$ (MPa)	$\sqrt{J_2}$ (MPa)
1	450.62	21.07	21.43	493.12	247.90
2	426.92	49.16	19.80	495.87	227.05
3	585.70	70.61	22.63	678.93	312.16
4	537.80	41.54	42.65	621.99	286.19
5	582.93	74.73	42.94	700.59	303.00
6	673.06	101.39	40.95	815.40	348.81
7	771.82	59.68	62.66	894.16	410.30
8	792.79	90.75	63.19	946.72	413.51
9	701.27	118.27	65.02	884.56	352.97
10	761.87	140.04	63.20	965.11	383.13

Different types of failure were observed from the true-triaxial tests. The most common failure mode from true-triaxial testing was a V-shaped crack (Fig. 4.27 (a)). This failure mode involved the formation of two distinct cracks running through the cubic specimen. Another failure mode observed from true-triaxial testing was an M-shaped crack (Fig. 4.27 (b)). It is important to mention that regardless of the mode of failure, failure planes were in the direction of the intermediate principal stress,  $\sigma_2$ , as was expected, and the specimens were separated out in the direction of the minimum principal stress,  $\sigma_3$ .

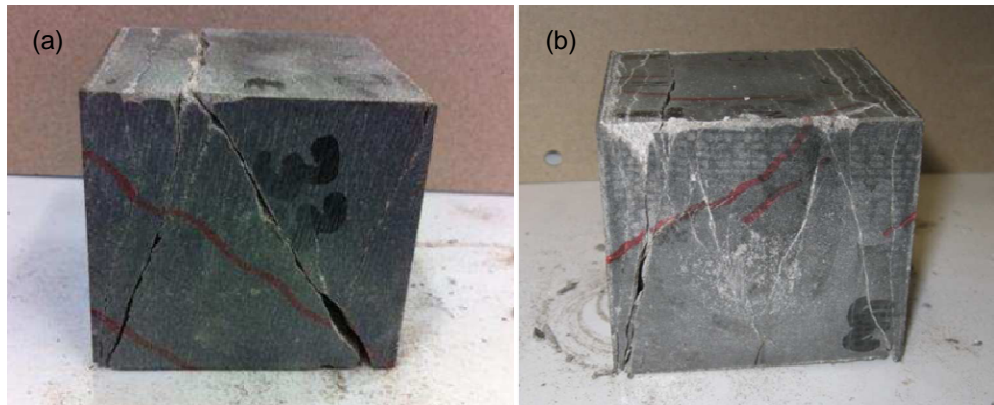


Figure 4.27 (a) The V-shaped failure mode and (b) the M-shaped failure mode [after Dong et al. (2011)]

### ***Comparison and validation of three-dimensional failure criteria against true-triaxial data***

Six rock failure criteria were selected and studied in this thesis. These criteria have been developed based on the Hoek-Brown failure criterion in the sense that their input parameters are the same as those for the Hoek-Brown criterion, namely the uniaxial compressive strength and the Hoek-Brown constant parameter  $m$ . In order to evaluate and validate the selected three-dimensional rock failure criteria against the true-triaxial experimental data, the uniaxial compressive strength and the Hoek-Brown constant parameter  $m$  for Kanmantoo bluestone had to be determined. Uniaxial tests were performed on cylindrical and cubic specimens of Kanmantoo bluestone. The aspect ratio (length/diameter) for cylindrical specimen was 2.4 and for the cubic specimen was 1 (Table 4.4).

Table 4.4 Uniaxial compressive strength of cylindrical and cubic specimens of Kanmantoo bluestone.

Rock specimen	Aspect Ratio (Length/Diameter)	UCS (MPa)	Average UCS (MPa)
cylinder	2.4	148.858	147.11343
cylinder	2.4	149.255	
cylinder	2.4	143.228	
cubic (60 × 60 mm)	1	190.278	190.27778
cubic (50 × 50 mm)	1	208.773	208.7727

It is important to remember that apparent strength in short specimens becomes higher due to the clamping effect at the two ends of the specimen. The underlying reason for this phenomenon is that the loading machine does not deform and expand as much as the rock does under the loading. The expansion of rock at machine-specimen interface exerts an additional confining pressure on the rock specimen. This confining pressure is the result of the frictional force acting on the interfacial area between the rock specimen and the loading machine and restricts the lateral expansion of the rock specimen at the two ends of the specimen. It is evident that with the increase of the length/diameter ratio, this effect should decrease gradually and disappear at some critical value. Above this critical value, the strength should remain constant and should represent the true strength under uniform compression. According to Mogi (2007), this critical value for length/diameter ratio is about 2.5. Therefore, considering Table 4.4, the uniaxial compressive strength of the Kanmantoo bluestone is determined as 147 MPa.

Conventional triaxial tests were also conducted on similar core samples, using the Hoek cell, to determine the empirical Hoek-Brown parameter  $m$  for the Kanmantoo bluestone. Confining pressure was applied at the same rate as the vertical load. Once the desired confining pressure was reached it was maintained constant by bleeding off excess pressure as necessary. Since the specimen tends to expand laterally as it is loaded vertically, confining pressure can become too high if it is not bled off. Vertical loading continued at a constant rate until the specimen failed. Hoek cell tests were performed under 5, 10 and 15 MPa confining pressures, as it is given in Table 4.5.

Table 4.5 Conventional triaxial tests for determining the Hoek-Brown constant parameter  $m$

Confining Pressure (MPa)	Failure Stress $\sigma_1$ (MPa)	$\sigma_3/\sigma_c$	$[(\sigma_1 - \sigma_3)/\sigma_c]^2$
5	212.556	0.034	1.994
10	232.051	0.068	2.282
15	241.533	0.102	2.375

The empirical parameter  $m$  can be determined by rearranging the Hoek-Brown criterion (Eq. 4.6.1) as follows:

$$\left(\frac{\sigma_1 - \sigma_3}{\sigma_c}\right)^2 = m \left(\frac{\sigma_3}{\sigma_c}\right) + 1 \quad (4.8.1)$$

By plotting  $[(\sigma_1 - \sigma_3)/\sigma_c]^2$  against  $(\sigma_3/\sigma_c)$ , for the experimental data (Table 4.5), the parameter  $m$  is determined as the slope of a best fit line, which intersects with the  $[(\sigma_1 - \sigma_3)/\sigma_c]^2$ -axis at 1, as illustrated in Fig. 4.28. Therefore, considering the Hoek cell tests the empirical parameter  $m$  is determined as equal to 16.131. However, the coefficient of determination,  $R^2$  value of -2.86 indicates that the line is not well fitting the data.

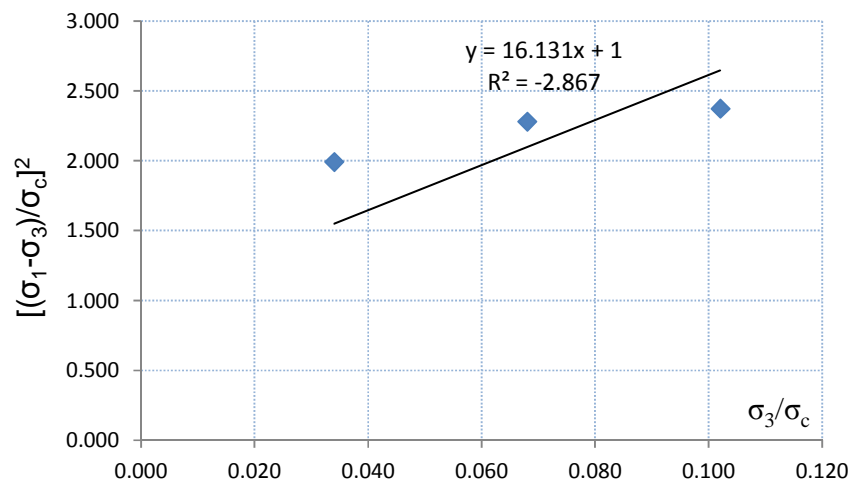


Figure 4.28 Best fit line to conventional triaxial data for determining the Hoek-Brown constant parameter  $m$

Inserting the uniaxial compressive strength,  $\sigma_c$ , as 147 MPa and the Hoek-Brown constant  $m$  as 16.131 into the selected three-dimensional rock failure criteria, the rock failure stress can be calculated by means of each failure criterion (Table 4.6). However, using these values for  $\sigma_c$  and  $m$  it was found out that all three-dimensional failure criteria underestimate the strength of the cubic rock specimen under three-dimensional stress, as illustrated in  $\sigma_1$ - $\sigma_2$  plots in Fig. 4.29.

Table 4.6 Predicted values of failure stress by the means of each selected failure criteria for  $m = 16.131$  and  $\sigma_c = 147$  MPa

$\sigma_2$	$\sigma_3$	$\sigma_1$ True-triaxial data	$\sigma_1$ Hoek-Brown	$\sigma_1$ Pan-Hudson	$\sigma_1$ Zhang-Zhu	$\sigma_1$ Generalised Priest	$\sigma_1$ Simplified Priest	$\sigma_1$ Modified Simplified Priest
0.00	0.00	147.00	147.00	48.64	147.00	147.00	147.00	147.00
21.07	21.43	450.62	290.64	156.87	290.06	289.66	290.37	291.45
49.16	19.80	426.92	281.73	210.52	324.41	353.85	302.60	333.63
70.61	22.63	585.70	297.08	254.76	360.98	405.29	329.43	369.71
41.54	42.65	537.80	393.14	245.11	391.65	390.71	392.38	395.45
74.73	42.94	582.93	394.41	305.79	433.59	458.52	415.01	448.16
101.39	40.95	673.06	385.64	343.49	455.52	501.63	423.40	466.79
59.68	62.66	771.82	475.38	317.15	471.73	469.58	473.47	479.48
90.75	63.19	792.79	477.43	370.80	508.94	527.78	494.47	528.73
118.27	65.02	701.27	484.47	415.62	541.77	576.70	516.38	558.67
140.04	63.20	761.87	477.47	442.21	556.64	606.53	522.54	570.16

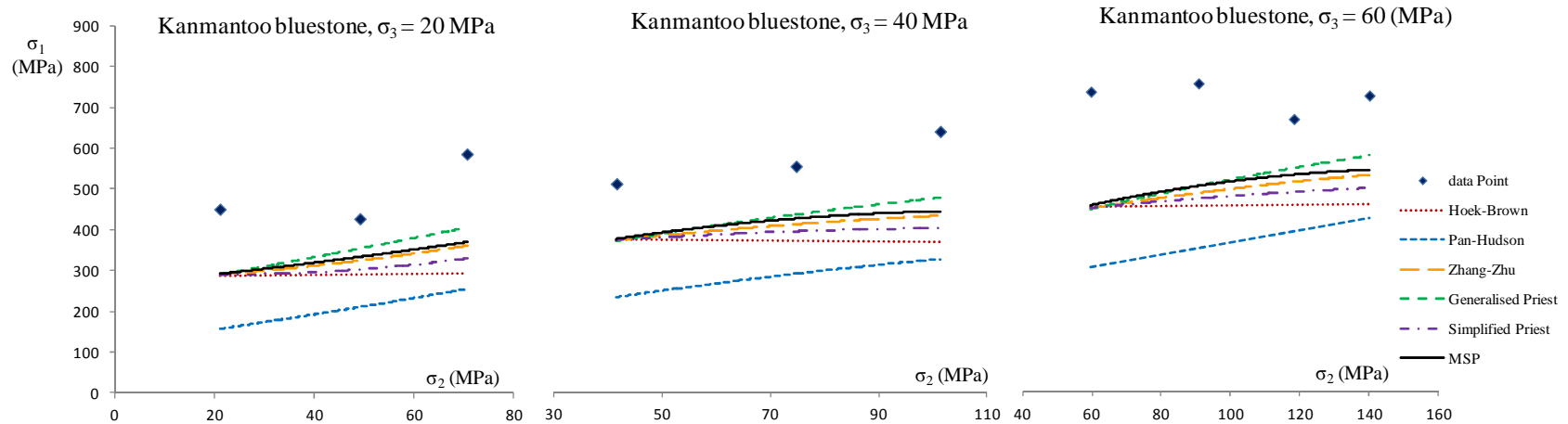


Figure 4.29  $\sigma_1$ - $\sigma_2$  plots, demonstrating that all 3D failure criteria underestimate the strength of the rock specimen

As is obvious from Table 4.6 and Fig. 4.29 the measured failure stress of cubic specimens of Kanmantoo bluestone is about 30% (in the case of the Pan-Hudson criterion 50%) higher than the predicted values of the failure stress of bluestone. One of the reasons for such discrepancies can be the clamping end effects caused by friction on the steel-rock interface. In order to eliminate the clamping end effect caused by friction on the steel-rock interface, thin layers of HDPE plastic were applied between the rock end surface and the steel platens. In this case, the failure mode can be described as two vertical cracks developed starting from the end surfaces of the rock sample and in the direction of the intermediate principal stress. The cubic specimen was separated out in the direction of the minimum principal stress and the failure stress was significantly low. This phenomenon seems to occur because of the intrusion of the plastic layer into the rock specimen (Fig. 4.30) and therefore this method is not recommended.

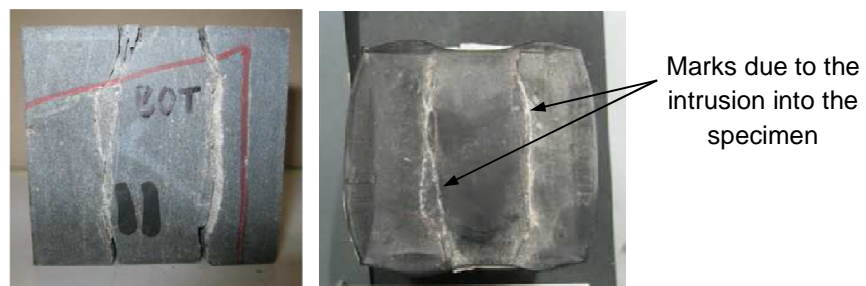


Figure 4.30 Intrusion of the HDPE plastic layer into the rock specimen [after Dong et al (2011)]

Another hypothesis can be described as the effect of the size and shape of the cubic rock specimens on the apparent strength of the rock, measured using the true-triaxial cell. The effect of the specimen's size and shape can be acknowledged by adjusting the input parameters of the three-dimensional failure criterion. As explained previously, the uniaxial compressive strength of the Kanmantoo bluestone measured by conducting uniaxial compression test on the 60×60×60 mm cubic specimen cannot be relied upon due to the pronounced clamping end effects. Therefore, it is recommended that the uniaxial compressive strength,  $\sigma_c$ , of the Kanmantoo blue stone be determined from the uniaxial compression tests on cylindrical specimens with aspect ratio of 2.4. On the other hand, the empirical parameter  $m$  can be determined for the cubic specimens of Kanmantoo bluestone tested in the true-

triaxial cell. For this purpose, true-triaxial tests in which  $\sigma_2 \approx \sigma_3$  can be adopted and the corresponding  $\sigma_1$  and  $\sigma_3$  values can be substituted into Eq. 4.81, as presented in Table 4.7.

Table 4.7 Triaxial test data on cubic rock specimens for determination the empirical parameter  $m$

Confining Pressure (MPa)	Failure Stress $\sigma_1$ (MPa)	$\sigma_3/\sigma_c$	$[(\sigma_1 - \sigma_3)/\sigma_c]^2$
21.07	450.62	0.11	5.10
41.54	537.80	0.22	6.80
59.68	771.82	0.31	14.00

It is also important to note that since the empirical parameter  $m$  is determined to account for the size and shape effects of the cubic specimens on the apparent rock strength measured in true-triaxial tests, the apparent uniaxial compressive strength of the 60×60×60 mm cube is substituted into Eq. 4.8.1 for determining the parameter  $m$ . It merits emphasising that the uniaxial compressive strength of the 60×60×60 mm cube must not be used as an input parameter for three-dimensional criteria, but only for determining the empirical parameter  $m$ . Plotting  $[(\sigma_1 - \sigma_3)/\sigma_c]^2$  against  $(\sigma_3/\sigma_c)$ , for the experimental data (Table 4.7), the parameter  $m$  is determined as the slope of the best fit line, which intersects with the  $[(\sigma_1 - \sigma_3)/\sigma_c]^2$ -axis at 1, as illustrated in Fig. 4.31.

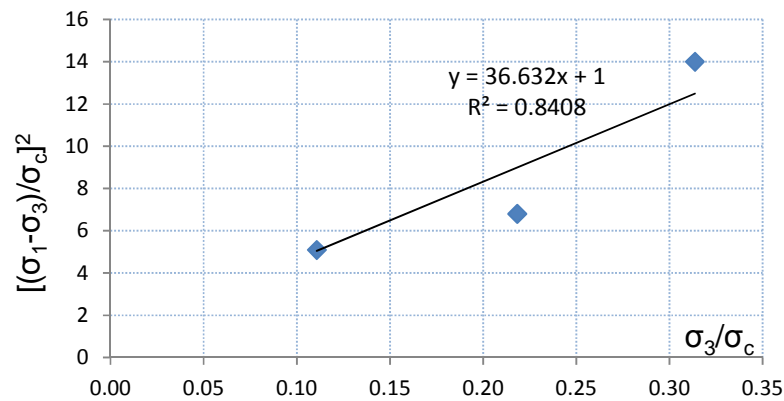


Figure 4.31 Best fit line to triaxial test data on cubic specimens for determining the empirical parameter  $m$

Inserting the uniaxial compressive strength,  $\sigma_c$ , as 147 MPa and the Hoek-Brown constant  $m$  as 36.6 into the selected three-dimensional rock failure criteria, the rock failure stress can be calculated by means of each failure criterion, as presented in Table 4.8 and illustrated in Fig. 4.32.

Table 4.8 Predicted values of failure stress by the means of each selected failure criteria for  $m = 36.6$  and  $\sigma_c = 190.3$  MPa

$\sigma_2$	$\sigma_3$	$\sigma_1$ True-triaxial data	$\sigma_1$ Hoek-Brown	$\sigma_1$ Pan-Hudson	$\sigma_1$ Zhang-Zhu	$\sigma_1$ Generalised Priest	$\sigma_1$ Simplified Priest	$\sigma_1$ Modified Simplified Priest/MSP
0.00	0.00	147.00	147.00	23.48	147.00	147.00	147.00	147.00
21.43	21.07	450.62	388.42	153.37	389.27	389.93	290.37	392.05
49.16	19.80	426.92	377.76	220.82	440.48	487.45	302.60	451.31
70.61	22.63	585.70	401.26	277.80	494.95	564.04	329.43	503.87
42.65	41.54	537.80	536.64	263.90	538.69	540.19	392.38	545.39
74.73	42.94	582.93	545.57	341.79	599.90	638.68	415.01	617.22
101.39	40.95	673.06	532.81	391.83	631.46	701.96	423.40	642.56
62.66	59.68	771.82	645.11	355.59	649.99	653.38	473.47	664.54
90.75	63.19	792.79	664.51	424.83	706.94	736.03	494.47	730.19
118.27	65.02	701.27	674.47	483.70	752.40	805.70	516.38	770.48
140.04	63.20	761.87	664.56	519.74	773.72	849.02	522.54	785.58

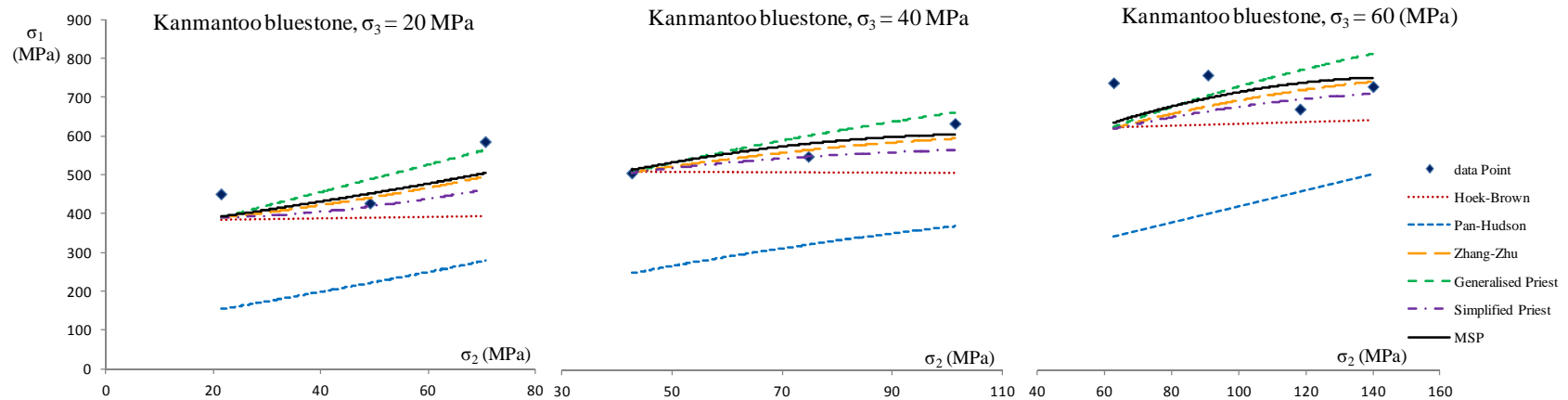


Figure 4.32  $\sigma_1$ - $\sigma_2$  plots, demonstrating the comparison of the selected three-dimensional failure criterion

As is obvious from Table 4.8 and Fig. 4.32, after adjusting the input parameter  $m$  to account for the higher apparent strength of the cubic rock specimens, the values for the failure stress predicted by means of three-dimensional rock failure criteria show reasonable agreement with the true-triaxial test data. Comparison of the selected rock failure criteria revealed that the modified simplified Priest and the Zhang-Zhu were the two criteria which predicted the rock strength more accurately than other three-dimensional failure models (Table 4.9).

Table 4.9 Error analysis and quantitative comparison of selected 3D failure criteria

Criterion	Rank	$\sigma_{1(\text{model})} - \sigma_{1(\text{observed})}$ (MPa)	over/underestimation (average)	Average percentage error (%)
Zhang-Zhu	1	-27.91	underestimation	7.00
Modified Simplified Priest	2	-16.51	underestimation	7.21
Simplified Priest	3	-44.01	underestimation	7.56
Generalised Priest	4	7.42	overestimation	8.59
Hoek-Brown	5	-77.60	underestimation	12.13
Pan-Hudson	6	-270.44	underestimation	49.82

## **CHAPTER 5**

### **A case study of prediction of borehole instability**

	<b>Page</b>
<b>5.1. Introduction</b>	<b>136</b>
<b>5.2. Prediction of borehole instability</b>	<b>137</b>
<b>5.3. Designing the drilling fluid</b>	<b>143</b>

## 5.1. Introduction

As outlined previously, a common strategy for borehole stability evaluation is to estimate the induced stresses at the borehole vicinity by means of analytical or numerical models, and then substitute the in situ stress components into a rock failure model to investigate whether or not the rock failure initiates. Stress analysis based on linear elasticity theory was carried out to estimate the induced stresses around a vertical and a deviated borehole in Chapter 3. The existing analytical model for stress estimation around a borehole is an elastic solution, which is a three-dimensional expansion of Kirsch equations and also is referred to as the generalised Kirsch equations. These equations have been widely applied in the petroleum and mining industries since they were introduced in 1962 by Hiramatsu and Oka. However, boundary conditions on which this elastic solution was based have been inadequately addressed in the existing literature.

Finite element analysis (FEA) was employed to first create the numerical counter part of the analytical solution in order to clarify the boundary conditions involved in the analytical solution. It appeared that in the case of a deviated borehole where the stress state around the borehole is a general stress state, some simplifying assumptions were made to facilitate the procedure of deriving the analytical solution. In other words, the three-dimensional problem was divided into two two-dimensional problems; one on the assumption of plane strain and the other on the assumption of anti-plane strain. It is assumed that under plane strain conditions there is no deformation along the borehole axis and all deformations take place in planes perpendicular to the axis of the borehole. On the other hand, under anti-plane strain conditions it is assumed that a constant deformation along the borehole axis is the only deformation that occurs. In order to eliminate this contradiction in the assumed boundary conditions in the analytical model, a finite element model was developed based on a new set of boundary conditions (Chapter 3, Section 3.5) which is in better compliance with the physics of the problem. A detailed explanation of the proposed boundary conditions is given in Section 3.5.

After estimating stresses around the borehole, the stability of the rock material at the borehole wall is required to be investigated. Under a given stress state, the maximum stress that can be

tolerated by rock is referred to as the failure stress. The stability of the rock material surrounding the borehole can be evaluated by comparing the rock failure stress with the maximum in situ stress at the borehole proximity. Failure stress for rock material can be estimated by means of mathematical formulations known as failure criteria. A number of common failure criteria were briefly explained in Chapter 2 and in Chapter 4 detailed discussions on failure criteria which were developed especially for rock material were presented. A new three-dimensional failure criterion was also introduced by improving the simplified Priest criterion developed by Priest (2005).

In this chapter first the stability of a deviated borehole is evaluated and then minimum and maximum mud weight for drilling the bore hole is calculated to demonstrate the practical application of the techniques developed in this thesis. Some equations and relations are repeated in the following sections for convenience.

## 5.2. Prediction of borehole instability

If the induced stresses around the borehole exceed the rock failure stress, failure of intact rock is expected to occur at the borehole wall. In order to demonstrate the procedure of predicting the borehole instability, a deviated borehole was considered in this section. The geometrical characteristics of the deviated borehole is the same as for the case example given for FEA in Chapter 3, i.e. a deviated borehole of radius 0.08 m with inclination of 125/10 (trend/plunge) is considered. The borehole is assumed to be drilled in the Australian crustal rocks with principal stresses being  $\sigma_h = 45$  MPa,  $\sigma_H = 75$  MPa and  $\sigma_z = 66$  MPa at the depth of 3000 m. In order to estimate the induced stresses around the deviated borehole the far-field principal stress components measured in the global Cartesian coordinate system must be transformed into a local Cartesian coordinate system which Z-axis coincides with the borehole axis (Fig. 3.10). Therefore, in this example the far-field stress state for the deviated bore hole can be given by the following general stress tensor:

$$[\sigma]_{ij} = \begin{bmatrix} 65.1565 & -13.8812 & -0.1487 \\ -13.8812 & 54.8697 & -2.4476 \\ -0.1487 & -2.4476 & 65.9738 \end{bmatrix} \quad (5.2.1)$$

The associated stress transformation procedure was outlined in Chapter 3. In the case of an unsupported deviated borehole in non-porous and isotropic material, the stresses at the borehole wall can be calculated according to the generalised Kirsch equations, as follows:

$$\begin{aligned}
 \sigma_{rr} &= 0 \\
 \sigma_{\theta\theta} &= (\sigma_x + \sigma_y) - 2(\sigma_x - \sigma_y)\cos 2\theta - 4\sigma_{xy}\sin 2\theta \\
 \sigma_{r\theta} &= 0 \\
 \sigma_{zz} &= \sigma_{z0} - 2\nu(\sigma_x - \sigma_y)\cos 2\theta - 4\nu\sigma_{xy}\sin 2\theta \\
 \sigma_{\theta z} &= (\sigma_{yz}\cos\theta - \sigma_{xz}\sin\theta) \\
 \sigma_{rz} &= 0
 \end{aligned} \tag{5.2.2}$$

Induced stresses are at their most deviatoric state at the borehole wall and stress concentration occurs at two opposite points on the circumference of the borehole. The angular position of these two points of stress concentration can be estimated by applying Eq. 3.4.7. In the case of this deviated borehole, the angular position of the two points of stress concentration are calculated as  $\theta = 55.166^\circ$  and  $\theta = 235.166^\circ$ . Therefore, induced stresses at two stress concentration points on the wall of the unsupported deviated borehole are given by the following stress tensor, as was calculated in Chapter 3:

$$\left[ \sigma_{ij} \right] = \begin{bmatrix} \sigma_{rr} & \sigma_{r\theta} & \sigma_{rz} \\ \sigma_{\theta r} & \sigma_{\theta\theta} & \sigma_{\theta z} \\ \sigma_{zr} & \sigma_{z\theta} & \sigma_{zz} \end{bmatrix} = \begin{bmatrix} 0 & 0 & 0 \\ 0 & 179.24 & -3.02 \\ 0 & -3.02 & 86.70 \end{bmatrix} \tag{5.2.3}$$

After calculating the induced stresses at two opposite points around the borehole the next step in borehole stability evaluation is to investigate whether or not the rock material at the borehole wall can sustain the induced stresses. It is important to remember that failure of a particular rock type occurs when the failure stress is exceeded by the applied stresses. Since the stress state at the borehole wall is three-dimensional, it is more suitable for the rock failure stress to be estimated by means of a three-dimensional failure criterion. In Chapter 4 a three-dimensional failure criterion based on the Hoek-Brown criterion was developed by modifying

the simplified Priest criterion. The criterion demonstrated significant accuracy in predicting rock failure stress in three-dimensional stress state when it was examined against the nine sets of published true-triaxial experimental data, and performed the best when compared to the other three-dimensional rock failure criteria. According to the proposed three-dimensional failure criterion, as also was outlined in Chapter 4, failure of intact rock occurs when:

$$\sigma_{1f} = \left[ \sigma_{1HB}^2 + 2\sigma_{3HB}^2 - (\sigma_2^2 + \sigma_3^2) \right]^{\frac{1}{2}} \quad (5.2.4)$$

The term  $\sigma_{1HB}$  in Eq. 5.2.4 is calculated, for intact rock material as follows:

$$\sigma_{1HB} = \sigma_{3HB} + \sigma_c \left( \frac{m\sigma_{3HB}}{\sigma_c} + 1 \right)^{\frac{1}{2}} \quad (5.2.5)$$

Also assuming a weighting factor  $w$  ranging from 0 to 1, the term  $\sigma_{3HB}$  is given by:

$$\begin{aligned} \sigma_{3HB} &= w\sigma_2 + (1-w)\sigma_3 \\ 0 &\leq w \leq 1 \end{aligned} \quad (5.2.6)$$

Where the weighting factor  $w$  is defined by the following expression:

$$w = 0.24 \left( \frac{\mu - \sigma_3}{\eta - \sigma_c} \right)^{0.5} \quad (5.2.7)$$

Where parameters  $\eta$  and  $\mu$  are defined as follows:

$$\begin{aligned} \eta &= \frac{m\sigma_c}{(\sigma_2 - \sigma_3)} \\ \mu &= \frac{\sigma_c^2 + m\sigma_c\sigma_2}{(\sigma_2 - \sigma_3)^2} \quad (\sigma_2 \neq \sigma_3) \end{aligned} \quad (5.2.8)$$

It is important to remember that when  $\sigma_2 = \sigma_3$  Eq. 5.2.6 reduces to  $\sigma_{3HB} = \sigma_3$  and consequently the rock failure stress,  $\sigma_{1f}$  in Eq. 5.2.4 will be the same as the failure stress predicted by the original two-dimensional formulation of the Hoek-Brown criterion.

If principal stresses acting on the borehole wall are in descending order such that  $\sigma_{\theta\theta} > \sigma_{zz} > \sigma_{rr}$ , then  $\sigma_{\theta\theta}$ ,  $\sigma_{zz}$  and  $\sigma_{rr}$  are corresponding to major ( $\sigma_1$ ), intermediate ( $\sigma_2$ ) and minor ( $\sigma_3$ ) principal stresses, respectively. It is important to note that stress components in Eq. 5.2.2 are not principal stresses. On the other hand, the proposed failure model for assessing rock stability has been formulated in terms of the principal stresses. Therefore, it is important to calculate the values and directions of the principal stresses associated with the general stress tensor in Eq. 5.2.2. The direction determined by the unit vector  $\lambda$  is said to be a principal direction of the stress tensor  $\sigma_{ij}$  if there exists a parameter  $\sigma_p$  such that:

$$(\sigma_{ij} - \sigma_p \delta_{ij})\lambda_j = 0 \quad (5.2.9)$$

Where  $\delta_{ij}$  is the Kronecker delta (Eq. 4.2.5). The expanded form of Eq. 5.2.9 is a set of three linear algebraic equations which can also be expressed in the following form:

$$\begin{bmatrix} (\sigma_{xx} - \sigma_p) & \sigma_{xy} & \sigma_{xz} \\ \sigma_{xy} & (\sigma_{yy} - \sigma_p) & \sigma_{yz} \\ \sigma_{xz} & \sigma_{yz} & (\sigma_{zz} - \sigma_p) \end{bmatrix} \begin{bmatrix} \lambda_1 \\ \lambda_2 \\ \lambda_3 \end{bmatrix} = 0 \quad (5.2.10)$$

In Eq. 5.2.10 the parameters  $\lambda_1$ ,  $\lambda_2$  and  $\lambda_3$  are direction cosines associated with the principal stress tensor. Furthermore, the three linear algebraic equations, given by Eq. 5.2.10, can be simultaneously solved by equating the determinant of the coefficient matrix to zero, as follows:

$$\begin{vmatrix} (\sigma_{xx} - \sigma_p) & \sigma_{xy} & \sigma_{xz} \\ \sigma_{xy} & (\sigma_{yy} - \sigma_p) & \sigma_{yz} \\ \sigma_{xz} & \sigma_{yz} & (\sigma_{zz} - \sigma_p) \end{vmatrix} = 0 \quad (5.2.11)$$

Evaluating the determinant in Eq. 5.2.11 gives the following characteristic equation:

$$\sigma_p^3 - I_1 \sigma_p^2 + I_2 \sigma_p - I_3 = 0 \quad (5.2.12)$$

Where  $I_1$ ,  $I_2$  and  $I_3$  are the first, second and third invariants of the general stress tensor and are given as follows:

$$I_1 = \sigma_{xx} + \sigma_{yy} + \sigma_{zz}$$

$$I_2 = \sigma_{xx}\sigma_{yy} + \sigma_{yy}\sigma_{zz} + \sigma_{zz}\sigma_{xx} - (\sigma_{xy}^2 + \sigma_{yz}^2 + \sigma_{xz}^2)$$

$$I_3 = \sigma_{xx}\sigma_{yy}\sigma_{zz} + 2\sigma_{xy}\sigma_{yz}\sigma_{xz} - (\sigma_{zz}\sigma_{xy}^2 + \sigma_{xx}\sigma_{yz}^2 + \sigma_{yy}\sigma_{xz}^2) \quad (5.2.13)$$

Eq. 5.2.12 is a cubic equation so there are three distinct values of  $\sigma_p$  that provide solutions. These roots of the cubic equation are the three principal stresses. Although the roots of the characteristic equation can be zero or negative, they are always real (i.e. never imaginary) in the mathematical sense. This special property means that a simple algorithm can be adopted for solving the equation. In order to solve the equation, five further intermediate parameters are needed to be defined as follows:

$$J_1 = I_1^2 - 3I_2$$

$$J_2 = \frac{2I_1^3 - 9I_1I_2 + 27I_3}{2}$$

$$J_3 = \sqrt{J_1^3 - J_2^2}$$

$$J_4 = \sqrt{J_1}$$

$$\theta = \frac{1}{3} \arctan\left(\frac{J_3}{J_2}\right) \quad (5.2.14)$$

The three principal stresses  $\sigma_1$ ,  $\sigma_2$  and  $\sigma_3$  are given by the following expressions: (it should be noted that  $\sigma_1 > \sigma_2 > \sigma_3$ ).

$$\sigma_1 = \frac{I_1 + 2J_4 \cos \theta}{3}$$

$$\sigma_2 = \frac{I_1 + 2J_4 \cos\left(\theta - \frac{2\pi}{3}\right)}{3}$$

$$\sigma_3 = \frac{I_1 + 2J_4 \cos\left(\theta - \frac{4\pi}{3}\right)}{3} \quad (5.2.15)$$

Therefore, principal stresses associated with the general stress tensor, given by Eq. 5.2.3 can be calculated as:

$$\begin{bmatrix} \sigma_{\theta\theta} & 0 & 0 \\ 0 & \sigma_{zz} & 0 \\ 0 & 0 & \sigma_{rr} \end{bmatrix} = \begin{bmatrix} \sigma_1 & 0 & 0 \\ 0 & \sigma_2 & 0 \\ 0 & 0 & \sigma_3 \end{bmatrix} = \begin{bmatrix} 179.338 & 0 & 0 \\ 0 & 86.6 & 0 \\ 0 & 0 & 0 \end{bmatrix} \quad (5.2.16)$$

Furthermore, according to the results of FEA based on the proposed boundary conditions which were outlined in Section 3.5, the induced stress state around the deviated borehole is given by the following stress tensor:

$$[\sigma_{ij}] = \begin{bmatrix} \sigma_{rr} & \sigma_{r\theta} & \sigma_{rz} \\ \sigma_{\theta r} & \sigma_{\theta\theta} & \sigma_{\theta z} \\ \sigma_{zr} & \sigma_{z\theta} & \sigma_{zz} \end{bmatrix} = \begin{bmatrix} 0 & 0 & 0 \\ 0 & 179.12 & -1.85 \\ 0 & -1.85 & 86.70 \end{bmatrix} \quad (5.2.17)$$

The corresponding principal stress tensor for the stress tensor in Eq. 5.2.10 is given as follows:

$$[\sigma_{ij}] = \begin{bmatrix} \sigma_1 & 0 & 0 \\ 0 & \sigma_2 & 0 \\ 0 & 0 & \sigma_3 \end{bmatrix} = \begin{bmatrix} 179.16 & 0 & 0 \\ 0 & 86.70 & 0 \\ 0 & 0 & 0 \end{bmatrix} \quad (5.2.18)$$

As is obvious there is no considerable difference between the calculated stresses by the means of the generalised Kirsch equations and the proposed numerical model. However, since the proposed boundary conditions are in relatively better agreement with the physics of the problem, as explained in Chapter 3, the borehole stability analysis in this section is continued by considering the induced stress tensor given by Eq. 5.2.11.

First it is assumed that the borehole has been drilled in a granite formation, which has the uniaxial compressive strength,  $\sigma_c$  of 229 MPa and the Hoek-Brown dilatancy parameter,  $m$ , of 29.5. Substituting the calculated values for the intermediate,  $\sigma_2 = \sigma_{zz}$ , and minor,  $\sigma_3 = \sigma_{rr}$ , principal stresses into Eqs. 5.2.4 to 5.2.7, the failure stress of the rock material at the borehole

wall is calculated as 460.73 MPa. Comparing this value of the rock failure stress to the major in situ principal stress,  $\sigma_1 = \sigma_{\theta\theta} = 179.16$  MPa, it is inferred that the rock material at the borehole wall does not fail in compression. However, if the borehole is drilled in a rock, for example marble, with uniaxial compressive strength of 82 MPa and the Hoek-Brown dilatancy parameter  $m$  of 12, the failure stress calculated by Eqs. 5.2.4 to 5.2.7, is 170.6 MPa which is smaller compared to the in situ major principal stress,  $\sigma_1 = 179.16$  MPa, and therefore failure is anticipated to initiate at the borehole wall. Table 5.1 summarises the associated calculation and procedure of the stability evaluation for the discussed example on the deviated borehole.

Table 5.1 Calculation of the failure stress for Granite and Marble

Rock	$\alpha$	$\beta$	w	$\sigma_{3HB}$	$\sigma_{1HB}$	Failure stress $\sigma_{1f}$ (MPa)	Occurrence of failure at the borehole wall
Granite	77.95	84.93	0.25	21.71	467.93	460.85 (>179.16)	No
Marble	11.35	12.25	0.25	21.60	188.88	170.58 (<179.16)	Yes

### 5.3. Designing the drilling fluid

In geotechnical engineering drilling fluid is used to aid the drilling of boreholes into the Earth. Liquid drilling fluid is often referred to as drilling mud. The three main categories of drilling fluids are water-based mud, non-aqueous mud, known as oil-based mud, and gaseous drilling fluid, in which a wide range of gases can be applied. The main functions of drilling fluids include providing hydrostatic pressure to prevent the borehole wall from failing, keeping the drill bit cool and cleaning the borehole during drilling by carrying out the drill cuttings. Drilling mud makes a column of fluid, which exerts a radial pressure on the borehole wall. The magnitude of this radial pressure at a depth of  $h$  is calculated as follows:

$$P_w = \rho gh \quad (5.3.1)$$

Where  $g$  is the gravitational acceleration and is usually assumed to be 9.81N/kg and  $\rho$  is the density of the drilling mud, which according to Eq. 5.3.1, is expressed in  $\text{kg/m}^3$ .

For an unsupported borehole the radial stress,  $\sigma_{rr}$ , at the borehole wall is zero and, as demonstrated in Section 5.2, the corresponding least principal stress acting on a rock element at the borehole wall is also zero. However, due to the column of the drilling fluid the radial pressure at the borehole wall increases to  $P_w$ . The radial and tangential induced stresses due to the hydrostatic pressure of the column of mud in the borehole are given as follows (Fig. 5.1):

$$\begin{aligned}\sigma_{rr} &= P_w \\ \sigma_{\theta\theta} &= -P_w\end{aligned}\quad (5.3.2)$$

If it is assumed that the drilling mud completely fills the borehole and the hydrostatic pressure,  $P_w$  is homogeneous around the circumference of the deviated borehole, then total stresses around a deviated borehole containing a column of drilling mud (Fig. 5.1) can be calculated by superimposing Eqs. 5.3.2 on the radial and tangential stress components ( $\sigma_{rr}$  and  $\sigma_{\theta\theta}$ ) in Eqs. 5.2.2 as follows:

$$\begin{aligned}\sigma_{rr} &= P_w \\ \sigma_{\theta\theta} &= (\sigma_x + \sigma_y) - 2(\sigma_x - \sigma_y) \cos 2\theta - 4\sigma_{xy} \sin 2\theta - P_w \\ \sigma_{r\theta} &= 0 \\ \sigma_{zz} &= \sigma_{z0} - 2\nu(\sigma_x - \sigma_y) \cos 2\theta - 4\nu\sigma_{xy} \sin 2\theta \\ \sigma_{\theta z} &= (\sigma_{yz} \cos \theta - \sigma_{xz} \sin \theta) \\ \sigma_{rz} &= 0\end{aligned}\quad (5.3.3)$$

The hydrostatic pressure imposed on the borehole wall due to the column of drilling mud, acts as a confining pressure and can dramatically increase the rock failure stress. In the case of drilling a deviated borehole in a Marble formation, where the rock failure in compression is expected to occur, it is desired to calculate the minimum hydrostatic pressure,  $P_{w(min)}$  to prevent the rock material at the borehole wall from failure.

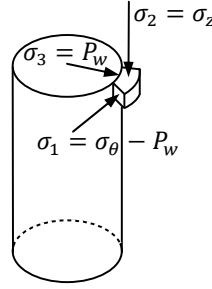


Figure 5.1 Principal in situ stresses acting on a rock element at the borehole wall, with drilling fluid

Superimposing Eq. 5.3.2 on the stress tensor calculated by the means of the finite element analysis, based on the proposed boundary conditions, the general stress state around the deviated borehole is given as:

$$[\sigma_{ij}] = \begin{bmatrix} \sigma_{rr} + P_w & \sigma_{r\theta} & \sigma_{rz} \\ \sigma_{\theta r} & \sigma_{\theta\theta} - P_w & \sigma_{\theta z} \\ \sigma_{zr} & \sigma_{z\theta} & \sigma_{zz} \end{bmatrix} = \begin{bmatrix} P_w & 0 & 0 \\ 0 & 179.12 - P_w & -1.85 \\ 0 & -1.85 & 86.70 \end{bmatrix} \quad (5.3.4)$$

The principal stress tensor associated with this general stress tensor can be calculated by applying Eqs. 5.2.13 to 5.2.15. Substituting the principal stresses into the proposed strength model given by Eqs. 5.2.4 to 5.2.7 and equating the calculated rock failure stress given by Eq.5.2.4 to the in situ major principal stress, i.e.  $\sigma_{1f} = \sigma_1 = 179.12 - P_w$ , the minimum hydrostatic pressure required for preventing the failure of the rock material at the borehole wall is calculated as  $P_{w(min)} = 176.9$  MPa. Therefore, according to Eq.5.3.1 the minimum density of the drilling mud for safely drilling the deviated borehole at the depth of 3000 m is calculated as:

$$\rho_{min} = \frac{176.9 \times 10^6 \text{ N/m}^2}{9.81 \text{ N/kg} \times 3000 \text{ m}} = 6010.873 \text{ Kg/m}^3$$

The upper limit or the maximum allowable hydrostatic pressure in the borehole  $P_{w(max)}$  is constrained by the hydraulic fracturing stress. Hydraulic fracture is a tensile fracture which is assumed to occur if any of stress components at the borehole wall becomes sufficiently tensile

to overcome the rock tensile strength,  $T_0$ . Since the most negative stress that can exist at the borehole wall at the two points of stress concentration around the borehole circumference, is the tangential stress, the condition for hydraulic fracturing is given as follows:

$$\sigma_{\theta\theta} - P_w = -T_0 \quad (5.3.5)$$

Where  $T_0$  is the rock tensile strength. Therefore the maximum allowable hydrostatic pressure in the borehole is calculated as follows:

$$P_{w(\max)} = \sigma_{\theta\theta} + T_0 \quad (5.3.6)$$

The tangential stress,  $\sigma_{\theta\theta}$  in Eq. 5.3.6 can be calculated for  $\theta=55.166^\circ$  using the generalised Kirsch equations. However, in this study the results of the FEA are applied for determining the tangential stress component around the deviated borehole.

Furthermore, Eqs. 5.2.4 to 5.2.7 can be applied to calculate the tensile strength of the rock,  $T_0$  through the following procedure:

- 1 - Equating  $\sigma_{1HB}$  to zero and calculate the parameter  $\sigma_{3HB}$  as follows:

$$\sigma_{3HB} = \frac{\sigma_c}{2} \left[ m - (m^2 + 4)^{\frac{1}{2}} \right] \quad (5.3.7)$$

- 2- Calculate parameters  $\alpha$  and  $\beta$ , by equating the intermediate principal stress to zero as follows:

$$\eta = \frac{m\sigma_c}{-\sigma_3} \quad \text{and} \quad \mu = \frac{\sigma_c^2}{\sigma_3^2} \quad (5.3.8)$$

- 3- Calculate the weighting factor  $w$  by substituting parameters  $\alpha$  and  $\beta$  from Eq. 5.3.8 into Eq. 5.2.7.

- 4- Setting  $\sigma_{1f}$  in Eq. 5.2.4 to zero, which yields the following equation:

$$2 \left[ 1 - 0.24 \left( \frac{\mu}{\eta} - \frac{\sigma_3}{\sigma_c} \right)^{\frac{1}{2}} \right] \sigma_3 - \sigma_3^2 = 0 \quad (5.3.9)$$

5- Solving Eq. 5.3.9 for  $\sigma_3$  and setting  $T_0 = -\sigma_3$

Following the five-step solution, the tensile strength of marble into which the deviated borehole has been drilled is calculated as  $T_0 = 4.77$  MPa. Therefore, considering Eq. 5.3.4 and Eq. 5.3.6 the maximum mud pressure is calculated as:

$$P_{w(\max)} = \sigma_{\theta\theta} + T_0 = 179.12 + 4.77 = 183.9 \text{ MPa}$$

Consequently, considering Eq. 5.3.1 the maximum allowable density of the drilling fluid is calculated as:

$$\rho_{\max} = \frac{183.9 \times 10^6 \text{ N/m}^2}{9.81 \text{ N/Kg} \times 3000 \text{ m}} = 6248.726 \text{ Kg/m}^3$$

# **CHAPTER 6**

## **Conclusion**

	<b>Page</b>
<b>6.1. Conclusion</b>	<b>147</b>
<b>6.2. Recommendations for future studies</b>	<b>148</b>

## 6.1. Summary and conclusions

Finite element analysis was carried out for calculating the induced stresses around a borehole in a continuum, homogeneous, isotropic and linearly elastic rock. Results from the FEA and the analytical models, i.e. the generalised Kirsch equations, were cross-evaluated for vertical and deviated boreholes to clarify the boundary conditions involved in deriving the existing analytical model. It appeared, however, that the boundary conditions assumed for deriving the generalised Kirsch equations are incompatible with the real life situation in the physical sense, i.e. in reality deformation of a continuum body cannot be assumed to be in plane strain and in anti-plane strain states simultaneously. The detailed explanation of the reason for this incompatibility is given in Chapter 3.

In order to address the contradictory boundary conditions assumed in the existing analytical model, a finite element analysis was carried out by applying a new set of boundary conditions. Assuming displacement as the unknown variable, the proposed boundary conditions can be given by the following strain tensor: (as is also given by Eq. 3.5.3 and is repeated here for convenience)

$$[\boldsymbol{\varepsilon}] = \begin{bmatrix} \frac{\partial u_x}{\partial x} & \frac{\partial u_x}{\partial y} + \frac{\partial u_y}{\partial x} & \frac{\partial u_x}{\partial z} \\ \frac{\partial u_x}{\partial y} + \frac{\partial u_y}{\partial x} & \frac{\partial u_y}{\partial y} & \frac{\partial u_y}{\partial z} \\ \frac{\partial u_x}{\partial z} & \frac{\partial u_y}{\partial z} & 0 \end{bmatrix} \quad (6.1.1)$$

The underlying assumption for proposing this set of boundary conditions is that displacements along the borehole axis are constrained by nearby geo-materials and are negligible, similar to the plane strain conditions in the physical sense. However, since the out-of-plane shear components appear in the corresponding stress tensor (Eq. 3.5.4), the problem cannot be considered as a plane strain problem.

Results from the FEA revealed that under the proposed boundary conditions, no significant changes occur in the values of radial,  $\sigma_{rr}$ , tangential,  $\sigma_{\theta\theta}$ , vertical,  $\sigma_{zz}$  and in-plane shear,  $\sigma_{r\theta}$ , stresses around the borehole when compared to the generalised Kirsch equations. However calculated values for out-of plane shear stresses,  $\sigma_{rz}$  and  $\sigma_{\theta z}$ , given by Eq. 3.3.11, demonstrated a dramatic change. Based on the results of the FEA the formulations of the out-of-plane shear stress components were modified, as was outlined in Chapter 3, Eqs. 3.5.6. These equations are also presented here for convenience:

$$\sigma_{\theta z} = \frac{1}{\sqrt{2}} (\sigma_{yz} \cos \theta - \sigma_{xz} \sin \theta) \left( 1 + \frac{a^2}{r^2} \right)$$

$$\sigma_{rz} = 2 (\sigma_{yz} \sin \theta + \sigma_{xz} \cos \theta) \left( 1 - \frac{a^2}{r^2} \right) \quad (6.1.2)$$

A comprehensive study was also conducted on three-dimensional rock failure criteria. A new three-dimensional failure criterion was developed by modifying the simplified Priest criterion as was outlined in Chapter 4, Section 4.7.2. True-triaxial experiments were conducted at the University of Adelaide and the results of the true-triaxial testing along with nine sets of published true-triaxial experimental data were applied to evaluate the proposed criterion versus other selected three-dimensional rock failure criteria which are more commonly applied in rock mechanics studies. Comparison of the selected three-dimensional rock failure criteria with the true-triaxial experimental data revealed that the proposed criterion, i.e. the modified simplified Priest criterion, can evaluate the rock strength under three-dimensional stress more accurately than other criteria in most cases. In some cases the Zhang-Zhu criterion provides more accurate prediction of the rock failure stress, however, even in such cases the Zhang-Zhu and the modified simplified Priest criteria are significantly close.

## 6.2. Recommendations for future studies

Although a numerical solution was presented in this study for implementing the proposed boundary conditions to calculate values of out-of-plane shear components ( $\sigma_{rz}$  and  $\sigma_{\theta z}$ ) around a deviated borehole, it merits developing an analytical solution for calculating the out-

of plane shears in order to analytically prove the formulation proposed for calculating the longitudinal stresses ( $\sigma_{rz}$  and  $\sigma_{\theta z}$ ) around a deviated borehole. Furthermore, this finite element model can be utilised as a platform for developing more sophisticated models for stress analysis around an opening excavated in geo-materials with more complicated constitutive behaviour and geological features.

The rock failure criterion for predicting the failure stress of intact rock developed in Chapter 4 can be generalised in order to evaluate the strength of rock masses when estimating the stability of underground excavations with larger cross sections than of a borehole.

Furthermore, a five-step solution for calculating the tensile strength of rock was outlined in this study by applying the proposed three-dimensional failure model. It would be worthwhile conducting a series of uniaxial tensile tests to evaluate the accuracy of the proposed method in predicting the tensile strength of rock.

## References

- AL-AJMI, A. 2006. *Wellbore stability analysis based on a new true-triaxial failure criterion*. PhD thesis, KTH Land and Water Resource Engineering.
- AMADEI, B. & STEPHANSSON, O. 1997. *Rock stress and its measurement*, Kluwer Academic Publishers.
- BÖKER, R. 1915. Die Mechanik der bleibenden Formänderung in kristallinisch aufgebauten Körpern. *Verhandl. Deut. Ingr. Mitt. Forsch.*, 175, 1-51.
- BOL, G., WONG, S. W., DAVIDSON, C. & WOODLAND, D. 1994. Borehole stability in shales. *SPE Drilling & Completion*, 9, 87-94.
- BRADLEY, W. B. 1979. Failure of Inclined Boreholes. *Journal of energy resources technology*, 101, 232-239.
- BRADY, B. & BROWN, E. 1993. *Rock mechanics for underground mining*, Chapman and Hall.
- BROWN, E. & HOEK, E. 1978. Trends in relationships between measured in-situ stresses and depth. *Int. J. Rock Mech. Min. Sci. & Geomech. Abstr*, 15, 78-85.
- CHANG, C. & HAIMSON, B. 2000. A new true triaxial cell for testing mechanical properties of rock, and its use to determine rock strength and deformability of Westerly granite. *International Journal of Rock Mechanics and Mining Sciences*, 37, 285-296.
- COLMENARES, L. B. & ZOBACK, M. D. 2002. A statistical evaluation of intact rock failure criteria constrained by polyaxial test data for five different rocks. *International Journal of Rock Mechanics and Mining Sciences*, 39, 695-729.
- CORNET, F. 1986. Stress determination from hydraulic tests on preexisting fractures—the HTPF method. 301-11.
- CRAWFORD, B. R., SMART, B. G. D., MAIN, I. G. & LIAKOPOULOU-MORRIS, F. 1995. Strength characteristics and shear acoustic anisotropy of rock core subjected to true triaxial compression. *International Journal of Rock Mechanics and Mining Sciences & Geomechanics Abstracts*, 32, 189-200.
- DONG, C., POLLIFRONE, A., WILLIAMS, M. & YANG, W. 2011. Experimental investigation of failure criteria related to borehole stability. Adelaide: The University of Adelaide.
- DRUCKER, D. C. & PRAGER, W. 1952. Soil mechanics and plastic analysis or limit design. *Quarterly of applied mathematics*, 10, 157-165.

- EWY, R. T. 1999. Wellbore-Stability Predictions by Use of a Modified Lade Criterion. *SPE Drilling & Completion*, 14, 85-91.
- FAIRHURST, C. 1964. Measurement of in-situ rock stresses. With particular reference to hydraulic fracturing. *Rock Mech.:(United States)*, 2.
- FAIRHURST, C. 1968. Methods of determining in-situ rock stresses at great depths *TRI-68*. Missouri river division, Corps of Engineers.
- FJÆR, E., HOLT, R. M., HORSRUD, P., RAAEN, A. M. & RISNES, R. 1992. Chapter 4 Stresses around boreholes. Borehole failure criteria. *Petroleum related rock mechanics*. Elsevier.
- FJÆR, E., HOLT, R. M., HORSRUD, P., RAAEN, A. M. & RISNES, R. 2008. Chapter 4 Stresses around boreholes. Borehole failure criteria. *In: E. FJÆR, R. M. H. P. H. A. M. R. & RISNES, R. (eds.) Developments in Petroleum Science*. Elsevier.
- GAZANIOL, D., FORSANS, T., BOISSON, M. & PLAU, J. 1994. Wellbore failure mechanisms in shale: Prediction and prevention. SPE paper 28851 presented at the European Petroleum Conference, held in London, UK. October.
- HAIMSON, B. 2006. True Triaxial Stresses and the Brittle Fracture of Rock *In: DRESEN, G., ZANG, A. & STEPHANSSON, O. (eds.) Rock Damage and Fluid Transport, Part I*. Birkhäuser Basel.
- HAIMSON, B. & CHANG, C. 2000. True triaxial strength and deformability of the German Continental Deep Drilling Program (KTB) deep hole amphibolite. *J. Geophys. Res.*, 105, 18999-19013.
- HAIMSON, B. & LEE, C. 1980. Hydrofracturing stress determinations at Darlington, Ontario. 42-50.
- HANDIN, J., HEARD, H. C. & MAGOUIRK, J. N. 1967. Effects of the Intermediate Principal Stress on the Failure of Limestone, Dolomite, and Glass at Different Temperatures and Strain Rates. *J. Geophys. Res.*, 72, 611-640.
- HEARD, H. C. 1960. Transition from brittle fracture to ductile flow in Solenhofen limestone as a function of temperature, confining pressure and interstitial fluid pressure. *Geol. Soc. Am. Mere.*, 79, 193-226.
- HILLIS, R. R. & REYNOLDS, S. D. 2000. The Australian Stress Map. *Journal of the Geological Society*, 157, 915-921.
- HIRAMATSU, Y. & OKA, Y. 1962. Stress around a shaft or level excavated in ground with a three-dimensional stress state. *Mem.Fac.Eng. Kyotu Univ.*, 24, 56-76.

- HIRAMATSU, Y. & OKA, Y. 1968. Determination of the stress in rock unaffected by boreholes or drifts, from measured strains or deformations. *International Journal of Rock Mechanics and Mining Sciences & Geomechanics Abstracts*, 5, 337-353.
- HOEK, E. 1983. Strength of jointed rock masses. *Rankine Lecture Géotechnique*, 33, 187-233.
- HOEK, E. & BROWN, E. T. 1980. Empirical strength criterion for rock masses. *Journal of the geotechnical engineering division*, 106, 1013-1035.
- HOEK, E. & BROWN, E. T. 1997. Practical estimates of rock mass strength. *International Journal of Rock Mechanics and Mining Sciences*, 34, 1165-1186.
- HOEK, E., CARRANZA-TORRES, C. T. & CORKUM, B. 2002. Hoek-Brown failure criterion-2002 edition. *Proceedings of the fifth North American rock mechanics symposium*. Toronto, Canada.
- HOSKINS, E. R. 1969. The failure of thick-walled hollow cylinders of isotropic rock. *International Journal of Rock Mechanics and Mining Sciences & Geomechanics Abstracts*, 6, 99-125.
- JAEGER, J. C., COOK, N. G. W. & ZIMMERMAN, R. W. 2007. *Fundamentals of rock mechanics*, Wiley-Blackwell.
- KÁRMÁN, T. V. 1911. Festigkeitsversuche unter allseitigem Druck. *Z. Verein Deut. Ingr.*, 55, 1749-1759.
- KIM, M. K. & LADE, P. V. 1984. Modelling rock strength in three dimensions. *International Journal of Rock Mechanics and Mining Sciences & Geomechanics Abstracts*, 21, 21-33.
- KIRSCH, E. G. 1898. Die Theorie der Elastizität und die Bedürfnisse der Festigkeitslehre. *Zeitschrift des Vereines deutscher Ingenieure*, 42, 797-807.
- LADE, P. V. 1982. Three-parameter failure criterion for concrete. *Journal of the Engineering Mechanics Division*, 108, 850-863.
- LIM, H. & LEE, C. 1995. Fifteen years experience on rock stress measurements in South Korea. 7-12.
- MELKOUMIAN, N., PRIEST, S. & HUNT, S. 2009. Further Development of the Three-Dimensional Hoek–Brown Yield Criterion. *Rock Mechanics and Rock Engineering*, 42, 835-847.
- MOGI, K. 1966. Some precise measurements of fracture strength of rocks under uniform compressive. *strength, Rock Mech. Engin. Geology*, 4, 51–55.
- MOGI, K. 1971a. Effect of the triaxial stress system on the failure of dolomite and limestone. *Tectonophysics*, 11, 111-127.

- MOGI, K. 1971b. Fracture and Flow of Rocks under High Triaxial Compression. *J. Geophys. Res.*, 76, 1255-1269.
- MOGI, K. 2007. *Experimental rock mechanics*, London. UK, Taylor & Francis/Balkema.
- NADAI, A. 1950. *Theory of Flow and Fracture of Solids*, New York, McGraw-Hill.
- OTTOSEN, N. S. & RISTINMAA, M. 2005. The mechanics of constitutive modelling. 145-202.
- PAN, X. D. & HUDSON, J. A. 1988. A simplified three dimensional Hoek-Brown yield criterion. In: M., R. (ed.) *Rock Mechanics and Power Plants, Proc. ISRM Symp.* Balkema, Rotterdam.
- PATERSON, M. S. & WONG, T. F. 2005. *Experimental rock deformation-the brittle field*, Springer Berlin Heidelberg New York.
- PESKA, P. & ZOBACK, M. D. 1995. Compressive and tensile failure of inclined well bores and determination of in situ stress and rock strength. *J. Geophys. Res.*, 100, 12791-12811.
- PRIEST, S. 2010. Comparisons Between Selected Three-Dimensional Yield Criteria Applied to Rock. *Rock Mechanics and Rock Engineering*, 43, 379-389.
- PRIEST, S. D. 2005. Determination of Shear Strength and Three-dimensional Yield Strength for the Hoek-Brown Criterion. *Rock Mechanics and Rock Engineering*, 38, 299-327.
- PRIEST, S. D. & HUNT, S. P. 2005. Application of a new three-dimensional yield criterion for argillaceous rocks. In: Proceedings of the 40th US Symposium on Rock Mechanics (USRMS): Rock Mechanics for Energy, Mineral and Infrastructure Development in the Northern Regions, Anchorage, Alaska 25–29. ARMA.
- SCHWARTZKOPFF, A., HARDEA, D., EGUDO, J. & CRICHTON, P. 2010. Design and fabrication of a true triaxial cell to compare 3D failure criteria for rock. Adelaide: The University of Adelaide.
- STEPHANSSON, O. 1983. Rock stress measurement by sleeve fracturing.
- WIEBOLS, G. A. & COOK, N. G. W. 1968. An energy criterion for the strength of rock in polyaxial compression. *International Journal of Rock Mechanics and Mining Sciences & Geomechanics Abstracts*, 5, 529-549.
- ZHANG, L. 2008. A generalized three-dimensional Hoek–Brown strength criterion. *Rock Mechanics and Rock Engineering*, 41, 893-915.
- ZHANG, L. & ZHU, H. 2007. Three-Dimensional Hoek-Brown Strength Criterion for Rocks. *Journal of Geotechnical and Geoenvironmental Engineering*, 133, 1128-1135.

- ZHOU, S. 1994. A program to model the initial shape and extent of borehole breakout. *Computers & Geosciences*, 20, 1143-1160.
- ZIENKIEWICZ, O. C., OWEN, D. R. J., PHILLIPS, D. V. & NAYAK, G. C. 1972. Finite element methods in the analysis of reactor vessels. *Nuclear Engineering and Design*, 20, 507-541.
- ZIENKIEWICZ, O. C. & TAYLOR, R. L. 1994. *The finite element method*, London, McGraw-Hill Book Company.
- ZIENKIEWICZ, O. C., TAYLOR, R. L. & ZHU, J. Z. 2005. *The finite element method. Its basis and fundamentals*, Butterworth-Heinmann.
- ZOBACK, M. D. 2007. *Reservoir Geomechanics*, New York.
- ZOBACK, M. D., BARTON, C. A., BRUDY, M., CASTILLO, D. A., FINKBEINER, T., GROLLMUND, B. R., MOOS, D. B., PESKA, P., WARD, C. D. & WIPRUT, D. J. 2003. Determination of stress orientation and magnitude in deep wells. *International Journal of Rock Mechanics and Mining Sciences*, 40, 1049-1076.
- ZOBACK, M. D. & HEALY, J. H. 1992. In situ stress measurements to 3.5 km depth in the Cajon Pass scientific research borehole: Implications for the mechanics of crustal faulting.
- ZOBACK, M. L. & ZOBACK, M. D. 1980. State of stress in the conterminous United States.

## **Appendix A**

### **The Finite Element Method**

## The Finite Element Method (FEM)

The finite element method (FEM) is a matrix algebraic method developed to solve partial differential equations (PDEs) in order to calculate linear or non-linear response of continuous physical systems to applied boundary conditions. The basic principle of the FEM is the division of this physical system into a number of simply shaped continuous sub-domains (finite elements) in order to find approximate solutions for the PDEs. This discretisation may facilitate the solution of a PDE system at discrete points in the model space in cases where an analytical solution is impossible to obtain. In order to provide a unique solution and convergence of the system of equations, appropriate boundary conditions have to be defined. The simple shape of each finite element is defined by its corner nodes which may be shared with adjacent elements, depending on their spatial position in the model space. All nodes and elements are uniquely defined in the model space by their identifier. The entirety of all entities defines the finite element mesh which is the discretised representation of the continuous problem space.

Once the model space is discretised, a set of linear equations of the unknown field variables is approximated for each element. The most common approach for problems in continuum mechanics is the displacement method in which the nodal displacement  $[\vec{u}(x)]$  is the unknown field variable. Solving the problem for the unknown field variable requires that the equilibrium of forces, internal continuity and a constitutive relationship with respect to the material behaviour be satisfied. Through these constitutive laws stresses are related to strains and hence to nodal displacements. The equilibrium equation can be derived from the equation of motion for small movements which can be written (in index notation) as:

$$\frac{\partial \sigma_{ij}}{\partial x_j} + \rho B_i = \rho a_i \quad (\text{A.1})$$

Where  $\rho$  is the density,  $B_i$  is the body force and  $a_i$  is the acceleration. For the elastic stress analysis around a borehole, acceleration can be assumed to be negligible since there exist no instantaneous displacements at the borehole wall and the equations of static equilibrium are applicable. In the absence of body forces, the resultant of all surface forces as well as the

resultant moment about any axis has to be vanished in the state of equilibrium. Therefore the equilibrium equation can be written as:

$$\frac{\partial \sigma_{ij}}{\partial x_j} = 0 \quad (\text{A.2})$$

For perfect linear elasticity, the strain tensor  $\epsilon_{kl}$  is proportional to the stress tensor  $\sigma_{ij}$ . This relationship is termed as Hook's law and can be expressed as:

$$\sigma_{ij} = C_{ijkl} \epsilon_{kl} \quad (\text{A.3})$$

The fourth-order tensor  $C_{ijkl}$ , which is a  $9 \times 9$  matrix, represents the elasticity tensor containing 81 components. However, the number of components reduces to 36 since both the stress tensor ( $\sigma_{ij}$ ) and the strain tensor ( $\epsilon_{kl}$ ) are symmetric, having only six distinct components. Substituting Eq. A.3 into Eq. A.2, the equilibrium equation of forces can be written as:

$$\frac{\partial}{\partial x_j} [C_{ijkl} \epsilon_{kl}] = \frac{\partial}{\partial x_j} \left[ \frac{1}{2} C_{ijkl} \left( \frac{\partial u_i}{\partial x_j} + \frac{\partial u_j}{\partial x_i} \right) \right] = 0 \quad (\text{A.4})$$

After each element has been approximated into a set of linear equations, the entirety of these approximation functions are assembled into a global equation of motion, which enables the solution of the numerical problem.

On the other hand, the matrix algebraic formulation of the fundamental equation of motion can be expressed as:

$$\bar{F} = \bar{M} \frac{\partial^2 \bar{u}}{\partial t^2} + \bar{C} \frac{\partial \bar{u}}{\partial t} + \bar{K} \bar{u} \quad (\text{A.5})$$

Where  $\bar{M}$  is the mass matrix,  $\bar{C}$  is the damping matrix and  $\bar{K}$  is the stiffness matrix. In this study, the finite element analysis (FEA) is restricted to static and Cauchy static problems, neglecting accelerations  $\left(\frac{\partial^2 \bar{u}}{\partial t^2}\right)$  and velocities  $\left(\frac{\partial \bar{u}}{\partial t}\right)$ . Therefore Eq. A.5 is reduced to the static equilibrium equation as follows:

$$\bar{F} = \bar{K}\bar{u} \quad (\text{A.6})$$

Since for isotropic materials the elasticity matrix,  $C$  in Eq. A.3, is the same as the stiffness matrix,  $K$  in Eq. A.6, the static equilibrium equation given by Eq. A.6 can be inverted to solve for the unknown displacements once the stiffness matrix is known. Subsequently, the stress and strain tensors can be derived.

Two basic principles, the Eulerian and the Lagrangian formulations can be followed to solve the constitutive equations within the finite element mesh. In the Eulerian approach, material properties or field variables migrate through the finite element mesh which is not deforming during the analysis. This prevents numerical instabilities due to excessive distortion of the finite element mesh. However, because the continuum is not explicitly defined, boundary conditions and boundary layers are difficult to trace or redefine. In the Lagrangian approach the material properties are explicitly defined for each element and the finite element mesh deforms during the analysis. The disadvantage of the Lagrangian approach is the explicit definition of the continuum, which leads to excessive distortion of the finite element mesh and to numerical instability when addressing large deformation problems. Since in the linear elastic solution deformations around a borehole are assumed to be infinitesimal, the ABAQUS/Standard implementation of the Lagrangian approach was adopted in this study.

The focus of this thesis is to apply the FEM for stress analysis around a borehole drilled in an isotropic, homogeneous and linearly elastic rock. To provide a description of the complete mathematical background of the FEM is beyond the scope of this study. Hence, only the fundamental concept and the basic equations have been outlined. For a complete mathematical description of the FEM the reader is referred to Zienkiewicz and Taylor (1994) and Zienkiewicz et al. (2005).

### ***Mesh resolution***

The accuracy of the FEA is directly dependent on the discretisation resolution. The behaviour of the discretised continuum, for example, the field variable  $\bar{u}(x)$  is described by a set of linear equations such as  $\bar{u}_\alpha = \alpha_0 + \alpha_1\bar{u}$ , in which  $\alpha$  indicates the approximation coefficients. Therefore, a finite discretisation is required in model regions where high gradients of  $\bar{u}(x)$

occur, for example, in the regions adjacent to the borehole wall. Fig. 3.4 demonstrates the impact of discretisation resolution on the accuracy of numerical approximation to a non-linear function.

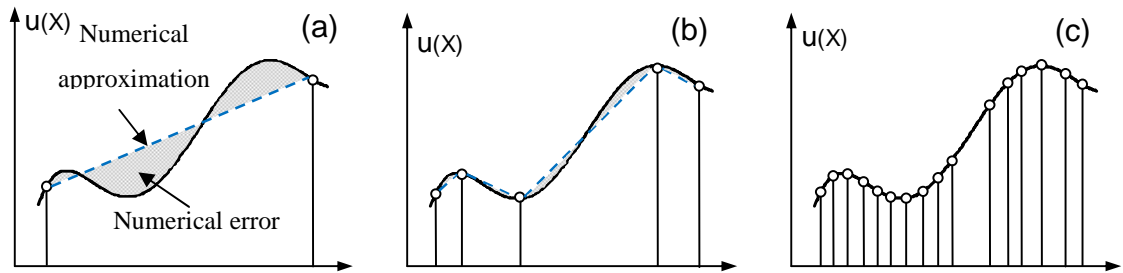


Figure A.1 The numerical error of the observed field variable (in this case  $\bar{u}(x)$ ) can be minimized by increasing the discretisation resolution stepwise from (a) to (c).

## **APPENDIX B**

**Quantitative comparison between analytical and numerical models**

Table B.1 Error analysis of the finite element model in comparison with the analytical solution, for calculating the induced stresses around the vertical borehole (for a quarter-model)

$\theta$ (deg)	Analytical solution						Numerical Analysis						Error calculation (%)					
	$\sigma_{rr}$	$\sigma_{\theta\theta}$	$\sigma_{aa}$	$\sigma_{r\theta}$	$\sigma_{ra}$	$\sigma_{\theta a}$	$\sigma_{rr}$	$\sigma_{\theta\theta}$	$\sigma_{aa}$	$\sigma_{r\theta}$	$\sigma_{ra}$	$\sigma_{\theta a}$	$\sigma_{rr}(e)$	$\sigma_{\theta\theta}(e)$	$\sigma_{aa}(e)$	$\sigma_{r\theta}(e)$	$\sigma_{ra}(e)$	$\sigma_{\theta a}(e)$
1.5	9.69	163.39	84.58	0.33	0.00	0.00	9.52	167.04	85.79	0.32	0.00	0.00	1.74	2.23	1.44	1.81	0.00	0.00
4.5	9.66	162.84	84.37	0.98	0.00	0.00	9.49	166.46	85.58	0.95	0.00	0.00	1.74	2.22	1.43	2.72	0.00	0.00
7.5	9.59	161.74	83.97	1.62	0.00	0.00	9.43	165.31	85.16	1.59	0.00	0.00	1.75	2.20	1.42	1.65	0.00	0.00
10.5	9.50	160.12	83.37	2.24	0.00	0.00	9.33	163.60	84.53	2.20	0.00	0.00	1.76	2.17	1.39	2.02	0.00	0.00
13.5	9.38	157.98	82.57	2.84	0.00	0.00	9.21	161.35	83.70	2.79	0.00	0.00	1.77	2.13	1.36	1.82	0.00	0.00
16.5	9.23	155.34	81.60	3.41	0.00	0.00	9.07	158.58	82.68	3.36	0.00	0.00	1.78	2.08	1.32	1.64	0.00	0.00
19.5	9.06	152.25	80.46	3.94	0.00	0.00	8.89	155.33	81.48	3.87	0.00	0.00	1.80	2.02	1.27	1.95	0.00	0.00
22.5	8.86	148.72	79.15	4.43	0.00	0.00	8.70	151.63	80.11	4.34	0.00	0.00	1.81	1.95	1.21	2.14	0.00	0.00
25.5	8.64	144.81	77.71	4.87	0.00	0.00	8.48	147.51	78.60	4.76	0.00	0.00	1.82	1.87	1.15	2.23	0.00	0.00
28.5	8.40	140.55	76.13	5.25	0.00	0.00	8.24	143.04	76.95	5.13	0.00	0.00	1.82	1.77	1.07	2.27	0.00	0.00
31.5	8.14	135.99	74.45	5.58	0.00	0.00	7.99	138.25	75.18	5.46	0.00	0.00	1.82	1.66	0.99	2.26	0.00	0.00
34.5	7.87	131.18	72.67	5.85	0.00	0.00	7.73	133.20	73.32	5.72	0.00	0.00	1.81	1.54	0.90	2.21	0.00	0.00
37.5	7.59	126.17	70.81	6.05	0.00	0.00	7.45	127.94	71.38	5.92	0.00	0.00	1.79	1.40	0.81	2.13	0.00	0.00
40.5	7.30	121.02	68.91	6.19	0.00	0.00	7.17	122.53	69.39	6.06	0.00	0.00	1.76	1.25	0.70	2.03	0.00	0.00
43.5	7.00	115.78	66.97	6.26	0.00	0.00	6.88	117.03	67.37	6.14	0.00	0.00	1.72	1.08	0.59	1.90	0.00	0.00
46.5	6.70	110.52	65.03	6.26	0.00	0.00	6.59	111.50	65.33	6.18	0.00	0.00	1.66	0.89	0.47	1.14	0.00	0.00
49.5	6.41	105.28	63.09	6.19	0.00	0.00	6.31	106.00	63.31	6.09	0.00	0.00	1.58	0.69	0.34	1.58	0.00	0.00
52.5	6.12	100.13	61.19	6.05	0.00	0.00	6.03	100.59	61.32	5.97	0.00	0.00	1.49	0.46	0.21	1.39	0.00	0.00
55.5	5.83	95.12	59.33	5.85	0.00	0.00	5.75	95.34	59.38	5.68	0.00	0.00	1.38	0.23	0.08	2.89	0.00	0.00
58.5	5.56	90.31	57.55	5.58	0.00	0.00	5.49	90.29	57.52	5.43	0.00	0.00	1.25	0.02	0.05	2.73	0.00	0.00
61.5	5.31	85.75	55.87	5.25	0.00	0.00	5.25	85.50	55.76	5.12	0.00	0.00	1.11	0.29	0.19	2.56	0.00	0.00
64.5	5.06	81.49	54.29	4.87	0.00	0.00	5.02	81.03	54.12	4.75	0.00	0.00	0.95	0.56	0.33	2.39	0.00	0.00
67.5	4.84	77.57	52.85	4.43	0.00	0.00	4.81	76.93	52.61	4.33	0.00	0.00	0.79	0.84	0.45	2.21	0.00	0.00
70.5	4.64	74.05	51.54	3.94	0.00	0.00	4.62	73.23	51.25	3.86	0.00	0.00	0.63	1.11	0.58	2.00	0.00	0.00
73.5	4.47	70.96	50.40	3.41	0.00	0.00	4.45	69.98	50.05	3.35	0.00	0.00	0.47	1.37	0.69	1.75	0.00	0.00
76.5	4.32	68.32	49.43	2.84	0.00	0.00	4.31	67.22	49.03	2.80	0.00	0.00	0.32	1.61	0.79	1.43	0.00	0.00
79.5	4.20	66.18	48.63	2.24	0.00	0.00	4.19	64.97	48.21	2.22	0.00	0.00	0.20	1.82	0.87	0.97	0.00	0.00
82.5	4.11	64.55	48.03	1.62	0.00	0.00	4.10	63.27	47.58	1.62	0.00	0.00	0.10	1.99	0.94	0.17	0.00	0.00
85.5	4.05	63.46	47.63	0.98	0.00	0.00	4.05	62.12	47.16	1.00	0.00	0.00	0.04	2.11	0.98	1.68	0.00	0.00
88.5	4.02	62.91	47.42	0.33	0.00	0.00	4.02	61.54	46.95	0.33	0.00	0.00	0.03	2.17	1.01	1.78	0.00	0.00

Table B.2 Error analysis of the finite element model in comparison with the analytical solution (the generalised Kirsch equations), for calculating the induced stresses around a deviated borehole (for a quarter-model)

$\theta$ (deg)	Analytical solution						Numerical Analysis						Error calculation (%)					
	$\sigma_{rr}$	$\sigma_{\theta\theta}$	$\sigma_{aa}$	$\sigma_{r\theta}$	$\sigma_{ra}$	$\sigma_{\theta a}$	$\sigma_{rr}$	$\sigma_{\theta\theta}$	$\sigma_{aa}$	$\sigma_{r\theta}$	$\sigma_{ra}$	$\sigma_{\theta a}$	$\sigma_{rr}$ (e)	$\sigma_{\theta\theta}$ (e)	$\sigma_{aa}$ (e)	$\sigma_{r\theta}$ (e)	$\sigma_{ra}$ (e)	$\sigma_{\theta a}$ (e)
1.5	6.02	98.38	60.51	5.90	-0.02	-4.61	5.92	98.71	60.59	5.63	-0.02	-4.77	1.60	0.34	0.14	4.54	1.26	3.49
4.5	6.30	103.42	62.37	6.06	-0.04	-4.58	6.19	103.97	62.52	5.78	-0.04	-4.74	1.71	0.53	0.25	4.64	0.79	3.47
7.5	6.59	108.56	64.27	6.16	-0.05	-4.54	6.47	109.34	64.50	5.86	-0.05	-4.70	1.80	0.72	0.36	4.74	1.74	3.46
10.5	6.89	113.75	66.19	6.18	-0.07	-4.49	6.76	114.77	66.50	5.88	-0.07	-4.64	1.88	0.89	0.47	4.85	2.30	3.43
13.5	7.18	118.94	68.11	6.14	-0.08	-4.42	7.04	120.19	68.49	5.84	-0.08	-4.57	1.93	1.05	0.57	4.96	2.67	3.40
16.5	7.47	124.06	70.00	6.03	-0.10	-4.35	7.32	125.55	70.47	5.83	-0.09	-4.49	1.97	1.19	0.67	3.41	2.94	3.36
19.5	7.75	129.07	71.85	5.86	-0.11	-4.26	7.59	130.78	72.40	5.65	-0.11	-4.40	2.00	1.33	0.76	3.46	3.15	3.31
22.5	8.02	133.90	73.64	5.62	-0.12	-4.16	7.86	135.84	74.26	5.42	-0.12	-4.29	2.01	1.45	0.85	3.49	3.31	3.26
25.5	8.28	138.50	75.34	5.32	-0.14	-4.05	8.12	140.66	76.03	5.13	-0.13	-4.18	2.01	1.56	0.92	3.49	3.44	3.19
28.5	8.53	142.82	76.94	4.96	-0.15	-3.92	8.35	145.19	77.70	4.79	-0.14	-4.05	2.00	1.65	1.00	3.44	3.56	3.12
31.5	8.75	146.82	78.42	4.55	-0.16	-3.79	8.58	149.38	79.25	4.39	-0.15	-3.90	1.99	1.74	1.06	3.34	3.66	3.03
34.5	8.96	150.46	79.76	4.08	-0.17	-3.65	8.78	153.19	80.65	3.95	-0.17	-3.75	1.98	1.82	1.12	3.16	3.75	2.93
37.5	9.14	153.68	80.95	3.58	-0.18	-3.49	8.96	156.57	81.90	3.47	-0.18	-3.59	1.96	1.88	1.17	2.86	3.83	2.81
40.5	9.30	156.46	81.98	3.03	-0.19	-3.33	9.11	159.49	82.97	2.96	-0.19	-3.42	1.94	1.93	1.22	2.39	3.89	2.67
43.5	9.43	158.76	82.83	2.45	-0.20	-3.16	9.24	161.91	83.87	2.37	-0.20	-3.23	1.93	1.98	1.25	3.25	3.96	2.51
46.5	9.53	160.57	83.50	1.84	-0.21	-2.97	9.35	163.81	84.57	1.77	-0.21	-3.04	1.91	2.02	1.28	4.03	4.01	2.32
49.5	9.60	161.86	83.97	1.21	-0.22	-2.78	9.42	165.16	85.07	1.16	-0.21	-2.84	1.90	2.04	1.30	4.70	4.06	2.09
52.5	9.64	162.61	84.25	0.57	-0.23	-2.59	9.46	165.96	85.36	0.56	-0.22	-2.65	1.89	2.06	1.31	3.26	4.11	2.59
55.5	9.65	162.82	84.33	-0.07	-0.24	-2.38	9.47	166.19	85.45	-0.07	-0.23	-2.46	1.88	2.07	1.32	4.51	4.15	3.17
58.5	9.64	162.49	84.21	-0.72	-0.25	-2.17	9.45	165.85	85.32	-0.69	-0.24	-2.26	1.88	2.07	1.32	4.19	4.19	3.84
61.5	9.59	161.62	83.89	-1.36	-0.25	-1.96	9.41	164.94	84.99	-1.30	-0.24	-2.02	1.88	2.06	1.31	4.15	4.22	3.13
64.5	9.51	160.21	83.37	-1.98	-0.26	-1.73	9.33	163.48	84.45	-1.88	-0.25	-1.79	1.88	2.04	1.30	4.75	4.25	3.38
67.5	9.40	158.29	82.66	-2.58	-0.26	-1.51	9.22	161.48	83.71	-2.49	-0.25	-1.56	1.89	2.01	1.27	3.43	4.28	3.70
70.5	9.26	155.88	81.76	-3.15	-0.27	-1.28	9.09	158.96	82.78	-3.00	-0.26	-1.31	1.90	1.97	1.24	4.87	4.30	2.56
73.5	9.10	153.00	80.70	-3.69	-0.27	-1.04	8.93	155.95	81.67	-3.54	-0.26	-1.08	1.91	1.93	1.20	4.05	4.32	3.78
76.5	8.91	149.68	79.47	-4.19	-0.28	-0.80	8.74	152.48	80.39	-3.99	-0.26	-0.83	1.91	1.87	1.16	4.89	4.33	3.21
79.5	8.70	145.96	78.10	-4.64	-0.28	-0.57	8.54	148.60	78.96	-4.48	-0.27	-0.58	1.92	1.80	1.10	3.58	4.35	3.05
82.5	8.47	141.89	76.59	-5.04	-0.28	-0.32	8.31	144.34	77.39	-4.86	-0.27	-0.33	1.92	1.73	1.04	3.64	4.36	2.63
85.5	8.23	137.50	74.97	-5.39	-0.28	-0.08	8.07	139.75	75.70	-5.19	-0.27	-0.08	1.91	1.64	0.98	3.65	4.36	3.37
88.5	7.96	132.84	73.24	-5.68	-0.28	0.16	7.81	134.88	73.91	-5.47	-0.27	0.17	1.90	1.54	0.90	3.62	4.37	3.75

Table B.3 Error analysis of the finite element analysis based on the proposed boundary conditions in comparison with the analytical solution (the generalised Kirsch's equations), for calculating the induced stresses around a deviated borehole (for a quarter-model)

$\theta$ (deg)	Numerical Analysis						Analytical solution						Error calculation (%)					
	$\sigma_{rr}$	$\sigma_{\theta\theta}$	$\sigma_{aa}$	$\sigma_{r\theta}$	$\sigma_{ra}$	$\sigma_{\theta a}$	$\sigma_{rr}$	$\sigma_{\theta\theta}$	$\sigma_{aa}$	$\sigma_{r\theta}$	$\sigma_{ra}$	$\sigma_{\theta a}$	$\sigma_{rr}(e)$	$\sigma_{\theta\theta}(e)$	$\sigma_{aa}(e)$	$\sigma_{r\theta}(e)$	$\sigma_{ra}(e)$	$\sigma_{\theta a}(e)$
1.5	5.92	98.68	60.31	-5.71	-0.05	-3.29	6.02	98.38	60.51	-5.90	-0.02	-4.61	1.64	0.30	0.33	3.32	0.30	0.33
4.5	6.19	103.91	62.07	-5.86	-0.08	-3.27	6.30	103.42	62.37	-6.06	-0.04	-4.58	1.84	0.48	0.48	3.39	0.48	0.48
7.5	6.46	109.26	63.88	-5.94	-0.11	-3.25	6.59	108.56	64.27	-6.16	-0.05	-4.54	2.02	0.65	0.61	3.45	0.65	0.61
10.5	6.74	114.67	65.71	-5.96	-0.14	-3.21	6.89	113.75	66.19	-6.18	-0.07	-4.49	2.16	0.80	0.72	3.51	0.80	0.72
13.5	7.02	120.07	67.54	-5.92	-0.17	-3.16	7.18	118.94	68.11	-6.14	-0.08	-4.42	2.29	0.95	0.83	3.55	0.95	0.83
16.5	7.29	125.41	69.35	-5.82	-0.20	-3.11	7.47	124.06	70.00	-6.03	-0.10	-4.35	2.39	1.08	0.93	3.57	1.08	0.93
19.5	7.56	130.62	71.12	-5.65	-0.22	-3.05	7.75	129.07	71.85	-5.86	-0.11	-4.26	2.48	1.21	1.02	3.58	1.21	1.02
22.5	7.82	135.66	72.83	-5.42	-0.25	-2.97	8.02	133.90	73.64	-5.62	-0.12	-4.16	2.55	1.32	1.10	3.56	1.32	1.10
25.5	8.07	140.46	74.45	-5.13	-0.28	-2.89	8.28	138.50	75.34	-5.32	-0.14	-4.05	2.60	1.42	1.18	3.50	1.42	1.18
28.5	8.31	144.97	75.97	-4.79	-0.30	-2.81	8.53	142.82	76.94	-4.96	-0.15	-3.92	2.65	1.50	1.26	3.39	1.50	1.26
31.5	8.52	149.15	77.37	-4.40	-0.33	-2.71	8.75	146.82	78.42	-4.55	-0.16	-3.79	2.68	1.58	1.33	3.23	1.58	1.33
34.5	8.72	152.94	78.64	-3.96	-0.35	-2.61	8.96	150.46	79.76	-4.08	-0.17	-3.65	2.71	1.65	1.41	2.97	1.65	1.41
37.5	8.89	156.30	79.75	-3.48	-0.37	-2.50	9.14	153.68	80.95	-3.58	-0.18	-3.49	2.74	1.71	1.48	2.60	1.71	1.48
40.5	9.05	159.21	80.70	-2.97	-0.39	-2.38	9.30	156.46	81.98	-3.03	-0.19	-3.33	2.76	1.75	1.56	2.02	1.75	1.56
43.5	9.17	161.61	81.47	-2.38	-0.41	-2.26	9.43	158.76	82.83	-2.45	-0.20	-3.16	2.78	1.79	1.64	2.73	1.79	1.64
46.5	9.27	163.50	82.06	-1.79	-0.43	-2.13	9.53	160.57	83.50	-1.84	-0.21	-2.97	2.80	1.82	1.73	2.74	1.82	1.73
49.5	9.34	164.84	82.45	-1.16	-0.45	-1.99	9.60	161.86	83.97	-1.21	-0.22	-2.78	2.82	1.84	1.81	4.31	1.84	1.81
52.5	9.37	165.63	82.64	-0.56	-0.47	-1.85	9.64	162.61	84.25	-0.57	-0.23	-2.59	2.85	1.85	1.91	2.29	1.85	1.91
55.5	9.38	165.85	82.64	0.07	-0.48	-1.71	9.65	162.82	84.33	0.07	-0.24	-2.38	2.88	1.86	2.01	4.30	1.86	2.01
58.5	9.36	165.50	82.43	0.69	-0.50	-1.55	9.64	162.49	84.21	0.72	-0.25	-2.17	2.91	1.85	2.11	3.52	1.85	2.11
61.5	9.31	164.58	82.02	1.30	-0.51	-1.40	9.59	161.62	83.89	1.36	-0.25	-1.96	2.95	1.84	2.23	3.81	1.84	2.23
64.5	9.23	163.12	81.41	1.90	-0.52	-1.24	9.51	160.21	83.37	1.98	-0.26	-1.73	2.99	1.81	2.35	4.04	1.81	2.35
67.5	9.12	161.11	80.61	2.49	-0.53	-1.08	9.40	158.29	82.66	2.58	-0.26	-1.51	3.03	1.78	2.47	3.65	1.78	2.47
70.5	8.99	158.59	79.63	3.00	-0.54	-0.91	9.26	155.88	81.76	3.15	-0.27	-1.28	3.07	1.74	2.61	4.94	1.74	2.61
73.5	8.83	155.58	78.48	3.56	-0.55	-0.74	9.10	153.00	80.70	3.69	-0.27	-1.04	3.11	1.68	2.75	3.64	1.68	2.75
76.5	8.64	152.11	77.17	3.99	-0.55	-0.57	8.91	149.68	79.47	4.19	-0.28	-0.80	3.16	1.62	2.89	4.76	1.62	2.89
79.5	8.43	148.23	75.72	4.46	-0.56	-0.40	8.70	145.96	78.10	4.64	-0.28	-0.57	3.19	1.55	3.05	3.89	1.55	3.05
82.5	8.21	143.97	74.13	4.85	-0.56	-0.23	8.47	141.89	76.59	5.04	-0.28	-0.32	3.23	1.47	3.21	3.91	1.47	3.21
85.5	7.97	139.38	72.44	5.18	-0.56	-0.06	8.23	137.50	74.97	5.39	-0.28	-0.08	3.26	1.37	3.38	3.90	1.37	3.38
88.5	7.71	134.52	70.65	5.46	-0.56	0.12	7.96	132.84	73.24	5.68	-0.28	0.16	3.27	1.27	3.55	3.86	1.27	3.55

Table B.4 Error analysis of the finite element model in comparison with the analytical solution (the generalised Kirsch's equations), for calculating the induced stresses along the radial distance  $r$  from the wall of a deviated borehole at  $\theta = 55.166^\circ$

r (m)	Numerical analysis						Analytical solution						Error calculation (%)					
	$\sigma_{rr}$	$\sigma_{\theta\theta}$	$\sigma_{aa}$	$\sigma_{r\theta}$	$\sigma_{ra}$	$\sigma_{a\theta}$	$\sigma_{rr}$	$\sigma_{\theta\theta}$	$\sigma_{aa}$	$\sigma_{r\theta}$	$\sigma_{ra}$	$\sigma_{a\theta}$	$\sigma_{rr}(e)$	$\sigma_{\theta\theta}(e)$	$\sigma_{aa}(e)$	$\sigma_{r\theta}(e)$	$\sigma_{ra}(e)$	$\sigma_{\theta a}(e)$
0.08	0.00	180.12	86.71	0.00	0.00	-3.00	0.00	179.24	86.70	0.00	0.00	-3.02	0.00	0.49	0.02	0.00	0.00	0.60
0.085	9.46	165.96	85.36	0.08	-0.25	-2.79	9.65	162.82	84.33	0.08	-0.24	-2.85	2.01	1.93	1.22	4.99	2.69	2.01
0.095	22.51	142.04	81.55	0.17	-0.63	-2.51	22.31	139.71	80.67	0.16	-0.61	-2.58	0.88	1.67	1.10	4.13	2.66	2.54
0.105	30.14	126.49	78.78	0.21	-0.91	-2.32	29.78	124.62	78.00	0.20	-0.88	-2.39	1.20	1.50	1.00	5.74	2.94	2.59
0.115	34.83	115.85	76.70	0.23	-1.11	-2.20	34.42	114.26	76.00	0.22	-1.08	-2.24	1.20	1.39	0.92	5.08	2.56	1.93
0.125	37.85	108.27	75.11	0.24	-1.27	-2.09	37.43	106.85	74.46	0.23	-1.24	-2.13	1.12	1.33	0.86	4.75	2.38	1.71
0.135	39.86	102.67	73.85	0.24	-1.40	-2.00	39.45	101.37	73.25	0.23	-1.36	-2.04	1.04	1.28	0.82	4.56	2.37	2.00
0.145	41.24	98.42	72.84	0.24	-1.50	-1.92	40.85	97.20	72.28	0.23	-1.46	-1.97	0.95	1.25	0.78	4.44	2.67	2.64
0.155	42.21	95.11	72.03	0.24	-1.58	-1.86	41.85	93.95	71.49	0.23	-1.54	-1.91	0.87	1.23	0.75	4.34	2.62	2.81
0.165	42.91	92.49	71.35	0.23	-1.64	-1.81	42.57	91.38	70.85	0.23	-1.61	-1.86	0.80	1.22	0.72	4.26	2.08	2.73
0.175	43.42	90.37	70.79	0.23	-1.71	-1.78	43.10	89.30	70.30	0.22	-1.66	-1.82	0.74	1.21	0.70	4.19	2.70	2.20
0.185	43.81	88.64	70.32	0.23	-1.74	-1.74	43.51	87.59	69.85	0.22	-1.71	-1.79	0.69	1.20	0.67	4.11	2.07	2.78
0.195	44.10	87.20	69.92	0.22	-1.79	-1.72	43.82	86.17	69.46	0.22	-1.75	-1.76	0.64	1.19	0.66	4.03	2.61	2.26
0.205	44.32	85.99	69.57	0.22	-1.82	-1.69	44.06	84.99	69.13	0.21	-1.78	-1.74	0.59	1.18	0.64	3.94	2.02	2.69
0.215	44.49	84.96	69.27	0.22	-1.85	-1.68	44.25	83.98	68.84	0.21	-1.81	-1.72	0.55	1.17	0.62	3.85	2.02	2.46
0.225	44.63	84.08	69.01	0.22	-1.88	-1.65	44.40	83.11	68.59	0.21	-1.84	-1.70	0.52	1.16	0.61	3.75	2.60	2.78
0.235	44.74	83.32	68.78	0.21	-1.91	-1.64	44.52	82.37	68.38	0.21	-1.86	-1.68	0.49	1.16	0.60	3.65	2.65	2.62
0.245	44.82	82.66	68.58	0.21	-1.93	-1.63	44.62	81.72	68.18	0.20	-1.88	-1.67	0.46	1.15	0.59	3.54	2.68	2.41
0.255	44.89	82.08	68.40	0.21	-1.94	-1.61	44.70	81.15	68.01	0.20	-1.89	-1.66	0.43	1.14	0.57	3.42	2.63	2.65
0.265	44.95	81.56	68.24	0.21	-1.96	-1.61	44.77	80.65	67.86	0.20	-1.91	-1.65	0.41	1.13	0.56	3.30	2.46	2.32
0.275	45.00	81.11	68.10	0.20	-1.96	-1.59	44.83	80.21	67.73	0.20	-1.92	-1.64	0.39	1.12	0.55	3.18	2.10	2.62
0.285	45.04	80.70	67.97	0.20	-1.98	-1.59	44.87	79.82	67.61	0.20	-1.94	-1.63	0.37	1.10	0.54	3.05	2.29	2.34
0.295	45.07	80.34	67.86	0.20	-2.00	-1.59	44.91	79.47	67.50	0.20	-1.95	-1.62	0.35	1.09	0.53	2.92	2.51	2.07
0.305	45.09	80.01	67.75	0.20	-2.00	-1.57	44.95	79.15	67.40	0.19	-1.96	-1.61	0.33	1.08	0.52	2.78	2.23	2.44
0.315	45.12	79.71	67.65	0.20	-2.02	-1.56	44.97	78.87	67.31	0.19	-1.97	-1.61	0.31	1.07	0.51	2.65	2.48	2.70
0.325	45.13	79.44	67.57	0.20	-2.02	-1.56	45.00	78.62	67.23	0.19	-1.97	-1.60	0.30	1.05	0.50	2.50	2.24	2.61
0.335	45.15	79.19	67.49	0.20	-2.03	-1.55	45.02	78.38	67.16	0.19	-1.98	-1.60	0.29	1.04	0.49	2.36	2.23	2.85
0.345	45.16	78.97	67.41	0.19	-2.04	-1.55	45.04	78.17	67.09	0.19	-1.99	-1.59	0.27	1.02	0.48	2.21	2.40	2.85
0.355	45.17	78.76	67.34	0.19	-2.04	-1.55	45.06	77.98	67.03	0.19	-2.00	-1.59	0.26	1.00	0.47	2.07	2.09	2.55
0.365	45.18	78.57	67.28	0.19	-2.05	-1.54	45.07	77.80	66.97	0.19	-2.00	-1.58	0.25	0.98	0.46	1.91	2.30	2.51

Table B.5 Error analysis of the finite element analysis based on the proposed boundary conditions in comparison with the analytical solution (the generalised Kirsch's equations), for calculating the induced stresses along the radial distance  $r$  from the wall of a deviated borehole at  $\theta = 55.166^\circ$

r (m)	Numerical						Analytical						Error calculation (%)					
	$\sigma_{rr}$	$\sigma_{\theta\theta}$	$\sigma_{aa}$	$\sigma_{r\theta}$	$\sigma_{ra}$	$\sigma_{a\theta}$	$\sigma_{rr}$	$\sigma_{\theta\theta}$	$\sigma_{aa}$	$\sigma_{r\theta}$	$\sigma_{ra}$	$\sigma_{a\theta}$	$\sigma_{rr}(e)$	$\sigma_{\theta\theta}(e)$	$\sigma_{aa}(e)$	$\sigma_{r\theta}(e)$	$\sigma_{ra}(e)$	$\sigma_{a\theta}(e)$
0.08	0.00	179.12	86.71	0.00	0.00	-1.85	0.00	179.24	86.70	0.00	0.00	-3.02	0.00	0.06	0.02	0.00	0.00	38.72
0.085	9.38	165.85	82.64	0.08	-0.10	-1.71	9.65	162.82	84.33	0.08	-0.24	-2.85	2.80	1.86	2.01	3.87	59.08	40.09
0.095	22.29	142.02	79.20	0.17	-1.11	-1.56	22.31	139.71	80.67	0.16	-0.61	-2.58	0.10	1.66	1.83	4.69	82.09	39.69
0.105	29.82	126.54	76.78	0.21	-1.47	-1.47	29.78	124.62	78.00	0.20	-0.88	-2.39	0.12	1.54	1.56	3.67	66.75	38.53
0.115	34.45	115.95	75.01	0.22	-1.68	-1.41	34.42	114.26	76.00	0.22	-1.08	-2.24	0.09	1.48	1.31	2.12	55.34	37.05
0.125	37.44	108.38	73.66	0.24	-1.82	-1.37	37.43	106.85	74.46	0.23	-1.24	-2.13	0.03	1.44	1.08	4.82	46.65	35.48
0.135	39.44	102.80	72.60	0.24	-1.91	-1.35	39.45	101.37	73.25	0.23	-1.36	-2.04	0.03	1.42	0.88	4.89	39.87	33.94
0.145	40.82	98.56	71.76	0.24	-1.97	-1.33	40.85	97.20	72.28	0.23	-1.46	-1.97	0.08	1.40	0.72	3.68	34.47	32.48
0.155	41.80	95.26	71.08	0.23	-2.01	-1.32	41.85	93.95	71.49	0.23	-1.54	-1.91	0.11	1.39	0.58	1.82	30.10	31.13
0.165	42.51	92.64	70.52	0.22	-2.03	-1.31	42.57	91.38	70.85	0.23	-1.61	-1.86	0.14	1.38	0.46	0.34	26.51	29.90
0.175	43.04	90.52	70.05	0.22	-2.05	-1.30	43.10	89.30	70.30	0.22	-1.66	-1.82	0.16	1.37	0.36	2.59	23.52	28.79
0.185	43.44	88.78	69.66	0.21	-2.07	-1.29	43.51	87.59	69.85	0.22	-1.71	-1.79	0.17	1.36	0.27	4.80	21.01	27.78
0.195	43.74	87.34	69.33	0.21	-2.08	-1.29	43.82	86.17	69.46	0.22	-1.75	-1.76	0.17	1.35	0.20	2.27	18.88	26.88
0.205	43.98	86.13	69.04	0.20	-2.09	-1.29	44.06	84.99	69.13	0.21	-1.78	-1.74	0.18	1.34	0.13	4.81	17.06	26.06
0.215	44.17	85.10	68.79	0.22	-2.09	-1.28	44.25	83.98	68.84	0.21	-1.81	-1.72	0.18	1.33	0.08	3.94	15.49	25.32
0.225	44.32	84.21	68.57	0.20	-2.10	-1.28	44.40	83.11	68.59	0.21	-1.84	-1.70	0.18	1.32	0.03	2.97	14.13	24.66
0.235	44.44	83.45	68.38	0.20	-2.10	-1.28	44.52	82.37	68.38	0.21	-1.86	-1.68	0.18	1.31	0.01	4.06	12.94	24.06
0.245	44.54	82.79	68.21	0.20	-2.10	-1.28	44.62	81.72	68.18	0.20	-1.88	-1.67	0.17	1.30	0.05	3.08	11.89	23.51
0.255	44.63	82.20	68.07	0.20	-2.10	-1.28	44.70	81.15	68.01	0.20	-1.89	-1.66	0.17	1.29	0.08	1.34	10.97	23.02
0.265	44.69	81.69	67.93	0.20	-2.10	-1.28	44.77	80.65	67.86	0.20	-1.91	-1.65	0.17	1.28	0.10	2.20	10.15	22.57
0.275	44.75	81.23	67.81	0.19	-2.11	-1.27	44.83	80.21	67.73	0.20	-1.92	-1.64	0.17	1.27	0.13	2.94	9.42	22.16
0.285	44.80	80.82	67.71	0.20	-2.11	-1.27	44.87	79.82	67.61	0.20	-1.94	-1.63	0.16	1.26	0.15	1.54	8.77	21.79
0.295	44.84	80.46	67.61	0.19	-2.11	-1.27	44.91	79.47	67.50	0.20	-1.95	-1.62	0.16	1.24	0.16	4.04	8.18	21.45
0.305	44.87	80.13	67.52	0.19	-2.11	-1.27	44.95	79.15	67.40	0.19	-1.96	-1.61	0.16	1.23	0.18	4.43	7.66	21.13
0.315	44.91	79.83	67.44	0.18	-2.11	-1.27	44.97	78.87	67.31	0.19	-1.97	-1.61	0.15	1.21	0.19	4.71	7.18	20.84
0.325	44.93	79.56	67.36	0.18	-2.11	-1.27	45.00	78.62	67.23	0.19	-1.97	-1.60	0.15	1.20	0.20	4.88	6.75	20.58
0.335	44.95	79.31	67.30	0.18	-2.11	-1.27	45.02	78.38	67.16	0.19	-1.98	-1.60	0.15	1.18	0.21	4.95	6.35	20.33
0.345	44.97	79.08	67.23	0.18	-2.11	-1.27	45.04	78.17	67.09	0.19	-1.99	-1.59	0.15	1.16	0.22	4.95	5.99	20.10
0.355	44.99	78.87	67.17	0.18	-2.11	-1.27	45.06	77.98	67.03	0.19	-2.00	-1.59	0.14	1.14	0.22	4.92	5.67	19.89
0.365	45.01	78.68	67.12	0.18	-2.11	-1.27	45.07	77.80	66.97	0.19	-2.00	-1.58	0.14	1.12	0.22	4.98	5.37	19.70

## **APPENDIX C**

### **True-triaxial data from the literature**

Table C.1 True-triaxial data of Solnhofen Limestone, Mogi (2007)

Tests No.	$\sigma_1$ (MPa)	$\sigma_2$ (MPa)	$\sigma_3$ (MPa)	$I_1$ (MPa)	$\sqrt{J_2}$ (MPa)
1	310	0	0	310	178.98
2	397	20	20	437	217.66
3	417	51	20	488	220.80
4	413	92	20	525	209.23
5	453	165	20	638	220.40
6	460	206	20	686	220.87
7	465	233	20	718	222.57
8	449	40	40	529	236.14
9	446	40	40	526	234.40
10	486	80	40	606	246.76
11	499	113	40	652	246.65
12	530	193	40	763	250.69
13	547	274	40	861	253.75
14	535	315	40	890	248.01
15	473	60	60	593	238.45
16	517	87	60	664	256.41
17	537	102	60	699	264.11
18	530	113	60	703	257.42
19	576	164	60	800	272.89
20	550	197	60	807	252.81
21	553	275	60	888	247.17
22	557	345	60	962	249.39
23	528	80	80	688	258.65
24	572	126	80	778	271.75
25	577	150	80	807	269.02
26	647	208	80	935	297.38
27	591	225	80	896	263.34
28	677	283	80	1040	303.55
29	665	298	80	1043	295.65
30	650	378	80	1108	285.10
31	680	454	80	1214	303.03

Table C.2 True-triaxial data on Dunham Dolomite, Mogi (2007)

Test NO.	$\sigma_1$ (MPa)	$\sigma_2$ (MPa)	$\sigma_3$ (MPa)	$I_1$ (MPa)	$\sqrt{J_2}$ (MPa)
1	265	0	0	265	153.00
2	258	0	0	258	148.96
3	400	25	25	450	216.51
4	475	66	25	566	248.82
5	495	96	25	616	253.36
6	560	129	25	714	283.67
7	571	174	25	770	282.23
8	586	229	25	840	283.96
9	545	272	25	842	260.11
10	487	45	45	577	255.19
11	570	97	45	712	289.27
12	576	126	45	747	286.07
13	606	160	45	811	296.33
14	639	183	45	867	310.86
15	670	240	45	955	319.78
16	670	266	45	981	316.93
17	622	294	45	961	289.40
18	540	60	60	660	277.13
19	568	65	65	698	290.41
20	638	117	65	820	316.88
21	644	153	65	862	312.00
22	687	208	65	960	325.77
23	685	262	65	1012	316.79
24	746	318	65	1129	344.23
25	701	393	65	1159	318.05
26	620	85	85	790	308.88
27	684	128	85	897	334.11
28	719	153	85	957	348.07
29	744	233	85	1062	345.76
30	773	306	85	1164	351.25
31	818	376	85	1279	369.08
32	798	445	85	1328	356.51
33	682	105	105	892	333.13
34	778	167	105	1050	371.95
35	786	205	105	1096	367.72
36	805	268	105	1178	366.27
37	863	270	105	1238	398.63
38	824	334	105	1263	367.31
39	840	356	105	1301	373.60
40	822	415	105	1342	359.59
41	725	125	125	975	346.41
42	824	187	125	1136	386.91
43	860	239	125	1224	395.57
44	863	293	125	1281	386.82
45	897	362	125	1384	395.47
46	941	414	125	1480	413.74
47	918	463	125	1506	397.94
48	886	516	125	1527	380.55
49	883	253	145	1281	398.58
50	927	296	145	1368	414.83
51	923	324	145	1392	407.46
52	922	349	145	1416	402.84
53	1015	392	145	1552	448.34
54	1002	410	145	1557	438.77

Table C.3 True-triaxial data on Yamaguchi Marble, Mogi (2007)

Test No.	$\sigma_1$ (MPa)	$\sigma_2$ (MPa)	$\sigma_3$ (MPa)	$I_1$ (MPa)	$\sqrt{J_2}$ (MPa)
1	82	0	0	82	47.34
2	118	6	6	130	64.66
3	140	12.5	12.5	165	73.61
4	179	26	12.5	217.5	92.48
5	177	28	12.5	217.5	90.83
6	196	45	12.5	253.5	97.92
7	213	67	12.5	292.5	103.67
8	225	90	12.5	327.5	107.54
9	228	105	12.5	345.5	108.11
10	200	115	12.5	327.5	93.89
11	189	25	25	239	94.69
12	209	39	25	273	102.43
13	240	58	25	323	115.79
14	252	78	25	355	118.75
15	275	107	25	407	127.44
16	268	132	25	425	121.79
17	268	157	25	450	121.65
18	250	168	25	443	113.87
19	243	40	40	323	117.20
20	290	64	40	394	137.93
21	288	88	40	416	131.53
22	309	88	40	437	143.47
23	319	112	40	471	144.84
24	307	143	40	490	134.66
25	336	160	40	536	148.88
26	321	177	40	538	140.51
27	341	208	40	589	150.84

Table C.4 True-triaxial test data on Mizuho Trachyte (Mogi, 2007)

Test No.	$\sigma_1$ (MPa)	$\sigma_2$ (MPa)	$\sigma_3$ (MPa)	$I_1$ (MPa)	$\sqrt{J_2}$ (MPa)
1	100	0	0	100	57.74
2	196	15	15	226	104.50
3	259	30	30	319	132.21
4	302	45	45	392	148.38
5	314	58	45	417	151.69
6	327	67	45	439	156.85
7	341	90	45	476	159.50
8	350	138	45	533	156.32
9	359	204	45	608	157.00
10	368	281	45	694	167.13
11	353	323	45	721	169.83
12	341	60	60	461	162.24
13	353	83	60	496	162.93
14	386	133	60	579	171.08
15	401	186	60	647	172.42
16	403	212	60	675	171.87
17	401	254	60	715	171.04
18	381	306	60	747	167.92
19	368	75	75	518	169.16
20	405	108	75	588	181.75
21	415	147	75	637	179.17
22	438	210	75	723	183.47
23	440	279	75	794	182.92
24	430	318	75	823	181.48
25	452	363	75	890	197.06
26	437	100	100	637	194.57
27	463	126	100	689	202.49
28	493	171	100	764	209.43
29	497	256	100	853	200.01
30	522	354	100	976	212.46
31	510	384	100	994	210.01

Table C.5 True-triaxial test data on Orikabe Monzonite (Mogi, 2007)

Test No.	$\sigma_1$ (MPa)	$\sigma_2$ (MPa)	$\sigma_3$ (MPa)	$I_1$ (MPa)	$\sqrt{J_2}$ (MPa)
1	234	0	0	234	135.10
2	339	5	5	349	192.83
3	504	20	20	544	279.44
4	584.7	40	40	664.7	314.48
5	636	59	40	735	338.75
6	698	80	40	818	368.89
7	673	101	40	814	349.19
8	775	102	40	917	407.64
9	739	121	40	900	382.34
10	747	143	40	930	381.94
11	777	168	40	985	393.79
12	748	187	40	975	373.63
13	751	80	80	911	387.40
14	834	95	80	1009	431.06
15	810	108	80	998	413.62
16	836	117	80	1033	426.20
17	854	135	80	1069	431.87
18	893	147	80	1120	451.29
19	889	182	80	1151	440.59
20	930	183	80	1193	463.88
21	906	216	80	1202	442.88
22	973	218	80	1271	480.71
23	926	281	80	1287	441.99
24	956	284	80	1320	458.36
25	966	311	80	1357	459.60
26	962	140	140	1242	474.58
27	1098	205	140	1443	535.33
28	1144	259	140	1543	548.54
29	1161	331	140	1632	542.80
30	1168	424	140	1732	530.88
31	1107	200	200	1507	523.66
32	1168	235	200	1603	549.05
33	1244	251	200	1695	588.58
34	1305	298	200	1803	611.65
35	1352	343	200	1895	627.91
36	1329	401	200	1930	602.25
37	1358	473	200	2031	605.35
38	1364	537	200	2101	598.94

Table C.6 True-triaxial test data on Inada Granite (Mogi, 2007)

Test No.	$\sigma_1$ (MPa)	$\sigma_2$ (MPa)	$\sigma_3$ (MPa)	$I_1$ (MPa)	$\sqrt{J_2}$ (MPa)
1	236	0	0	236	136.25
2	232	0	0	232	133.95
3	339	5	5	349	192.83
4	504	20	20	544	279.44
5	583	40	40	663	313.50
6	571	40	40	651	306.57
7	600	40	40	680	323.32
8	636	59	40	735	338.75
9	698	80	40	818	368.89
10	673	101	40	814	349.19
11	775	102	40	917	407.64
12	739	121	40	900	382.34
13	747	143	40	930	381.94
14	777	168	40	985	393.79
15	748	187	40	975	373.63
16	718	80	80	878	368.35
17	742	80	80	902	382.21
18	794	80	80	954	412.23
19	834	95	80	1009	431.06
20	810	108	80	998	413.62
21	836	117	80	1033	426.20
22	854	135	80	1069	431.87
23	893	147	80	1120	451.29
24	889	182	80	1151	440.59
25	930	183	80	1193	463.88
26	906	216	80	1202	442.88
27	973	218	80	1271	480.71
28	926	281	80	1287	441.99
29	956	284	80	1320	458.36
30	966	311	80	1357	459.60
31	943	140	140	1223	463.61
32	981	140	140	1261	485.55
33	1098	205	140	1443	535.33
34	1144	259	140	1543	548.54
35	1161	331	140	1632	542.80
36	1168	424	140	1732	530.88
37	1107	200	200	1507	523.66
38	1168	235	200	1603	549.05
39	1244	251	200	1695	588.58
40	1305	298	200	1803	611.65
41	1352	343	200	1895	627.91
42	1329	401	200	1930	602.25
43	1358	473	200	2031	605.35
44	1364	537	200	2101	598.94

Table C.7 True-triaxial test data on Manazuru Andesite (Mogi, 2007)

Test No.	$\sigma_1$ (MPa)	$\sigma_2$ (MPa)	$\sigma_3$ (MPa)	$I_1$ (MPa)	$\sqrt{J_2}$ (MPa)
1	140	0	0	140	80.83
2	349	16	16	381	192.26
3	364	20	20	404	198.61
4	381	20	20	421	208.42
5	470	67	20	557	247.36
6	516	124	20	660	261.56
7	538	186	20	744	264.51
8	552	40	40	632	295.60
9	577	75	40	692	300.44
10	632	112	40	784	323.02
11	669	126	40	835	341.05
12	653	206	40	899	317.05
13	626	278	40	944	294.72
14	671	70	70	811	346.99
15	735	101	70	906	375.31
16	735	152	70	957	362.59
17	808	193	70	1071	395.39
18	812	275	70	1157	383.18
19	801	313	70	1184	372.28
20	833	375	70	1278	384.05
21	806	100	100	1006	407.61
22	875	110	110	1095	441.67
23	881	130	130	1141	433.59

Table C.8 True-triaxial test data on KTB Amphibolite (Chang and Haimson, 2000)

Test No.	$\sigma_1$ (MPa)	$\sigma_2$ (MPa)	$\sigma_3$ (MPa)	$I_1$ (MPa)	$\sqrt{J_2}$ (MPa)
1	165	0	0	165	95.26
2	346	79	0	425	181.31
3	291	149	0	440	145.51
4	347	197	0	544	174.03
5	267	229	0	496	144.44
6	410	30	30	470	219.39
7	479	60	30	569	251.02
8	599	100	30	729	310.29
9	652	200	30	882	321.48
10	571	249	30	850	272.13
11	637	298	30	965	304.19
12	702	60	60	822	370.66
13	750	88	60	898	390.54
14	766	103	60	929	395.78
15	745	155	60	960	371.11
16	816	199	60	1075	402.40
17	888	249	60	1197	433.90
18	828	299	60	1187	393.02
19	887	347	60	1294	419.90
20	954	399	60	1413	451.33
21	815	449	60	1324	377.56
22	868	100	100	1068	443.41
23	959	164	100	1223	478.54
24	1001	199	100	1300	494.10
25	945	248	100	1293	451.25
26	892	269	100	1261	417.12
27	1048	300	100	1448	499.70
28	1058	349	100	1507	497.07
29	1155	442	100	1697	538.26
30	1118	597	100	1815	509.05
31	1147	150	150	1447	575.62
32	1065	198	150	1413	514.98
33	1112	199	150	1461	541.82
34	1176	249	150	1575	565.95
35	1431	298	150	1879	700.78
36	1326	348	150	1824	629.64
37	1169	399	150	1718	531.23
38	1284	448	150	1882	587.89
39	1265	498	150	1913	570.47
40	1262	642	150	2054	557.23

Table C.9 True-triaxial test data on Westerly Granite (Haimson and Chang, 2000)

Test No.	$\sigma_1$ (MPa)	$\sigma_2$ (MPa)	$\sigma_3$ (MPa)	$I_1$ (MPa)	$\sqrt{J_2}$ (MPa)
1	201	0	0	201	116.05
2	306	40	0	346	166.33
3	301	60	0	361	159.31
4	317	80	0	397	164.85
5	304	100	0	404	154.94
6	231	2	2	235	132.21
7	300	18	2	320	167.62
8	328	40	2	370	178.26
9	359	60	2	421	191.58
10	353	80	2	435	184.31
11	355	100	2	457	182.23
12	430	20	20	470	236.71
13	529	40	20	589	288.27
14	602	60	20	682	325.09
15	554	62	20	636	296.92
16	553	61	20	634	296.60
17	532	79	20	631	280.13
18	575	100	20	695	300.01
19	567	114	20	701	292.48
20	601	150	20	771	304.92
21	638	202	20	860	317.58
22	605	38	38	681	327.36
23	620	38	38	696	336.02
24	700	57	38	795	376.84
25	733	78	38	849	390.22
26	720	103	38	861	376.39
27	723	119	38	880	374.30
28	731	157	38	926	370.56
29	781	198	38	1017	391.05
30	747	60	60	867	396.64
31	811	90	60	961	425.19
32	821	114	60	995	424.63
33	860	180	60	1100	431.43
34	861	249	60	1170	418.70
35	889	77	77	1043	468.81
36	954	102	77	1133	499.28
37	992	142	77	1211	510.55
38	998	214	77	1289	496.93
39	1005	310	77	1392	482.79
40	1012	100	100	1212	526.54
41	1103	165	100	1368	561.26
42	1147	167	100	1414	586.10
43	1155	216	100	1471	578.53
44	1195	259	100	1554	591.66
45	1129	312	100	1541	543.33

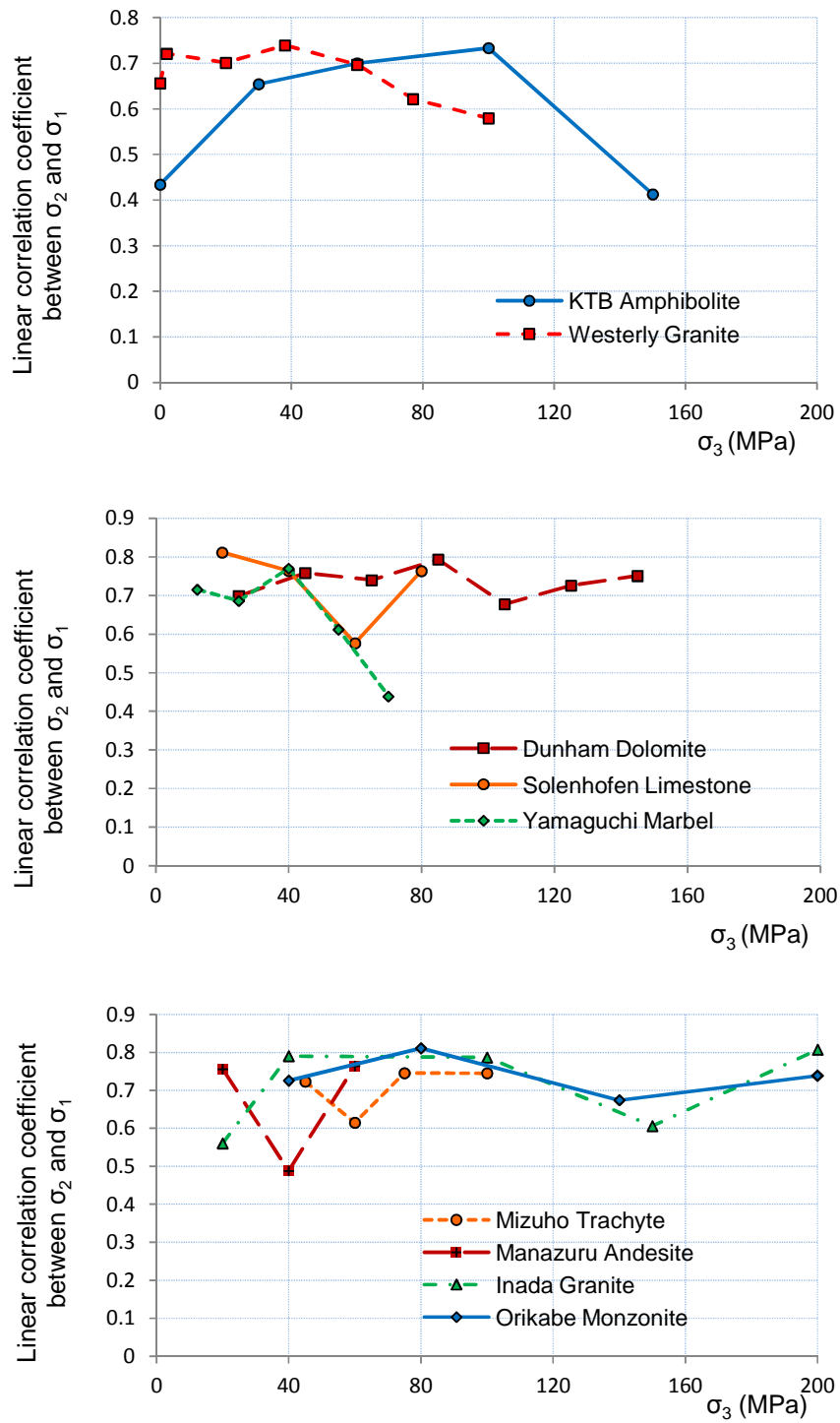
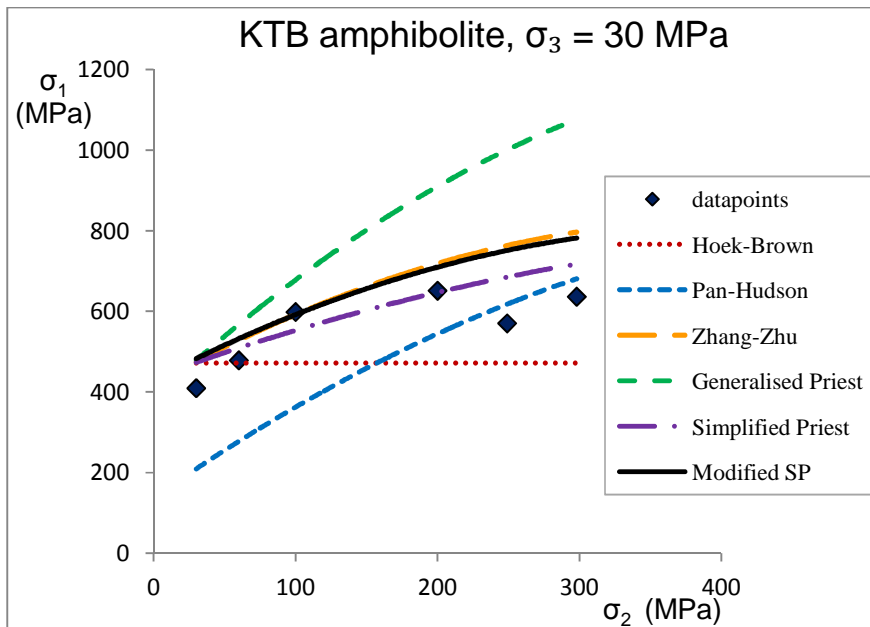
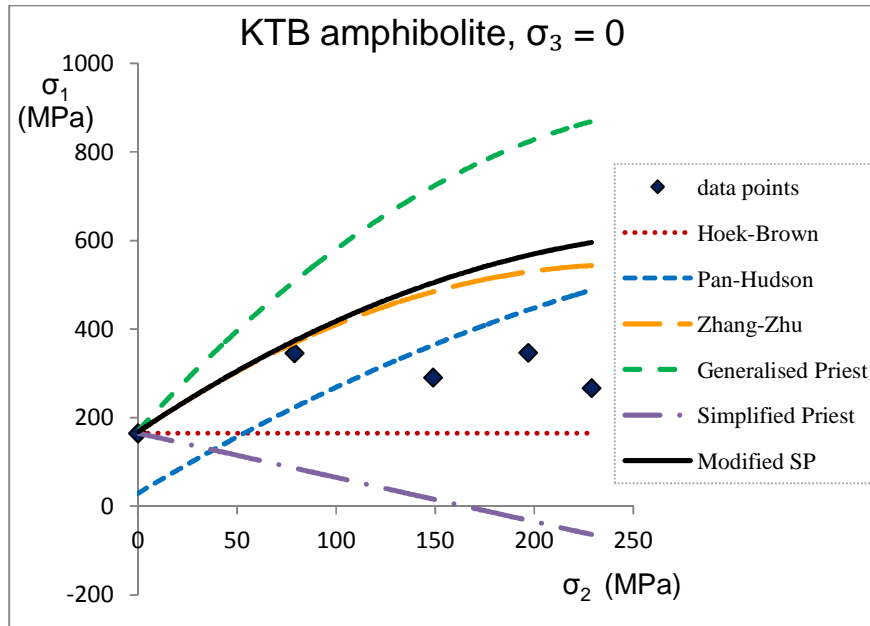


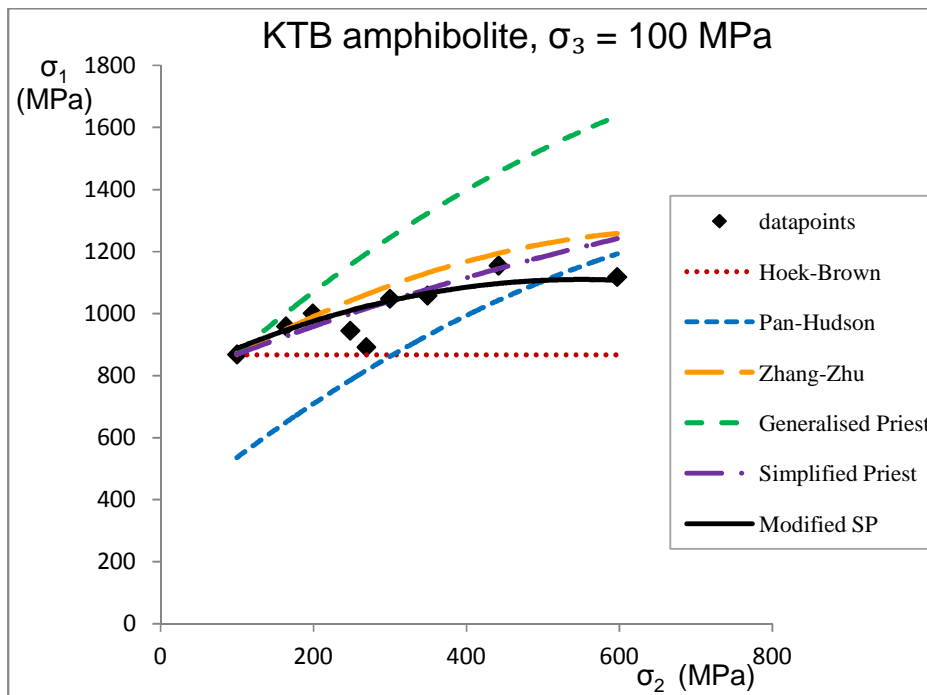
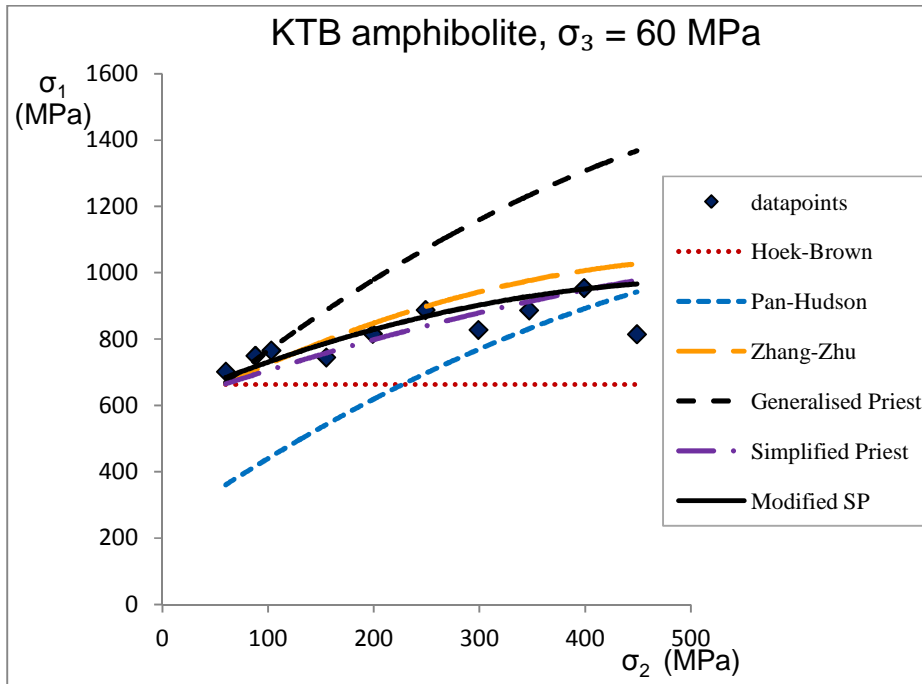
Figure C.1 Linear correlation coefficient calculated by the means of Pearson linear correlation coefficient for the nine sets of true-triaxial data

## **APPENDIX D**

**$\sigma_1$ - $\sigma_2$  plots for the selected rock types from the literature**

Figure D.1  $\sigma_1$  vs.  $\sigma_2$  Plots for KTB Amphibolite for different constant values of  $\sigma_3$





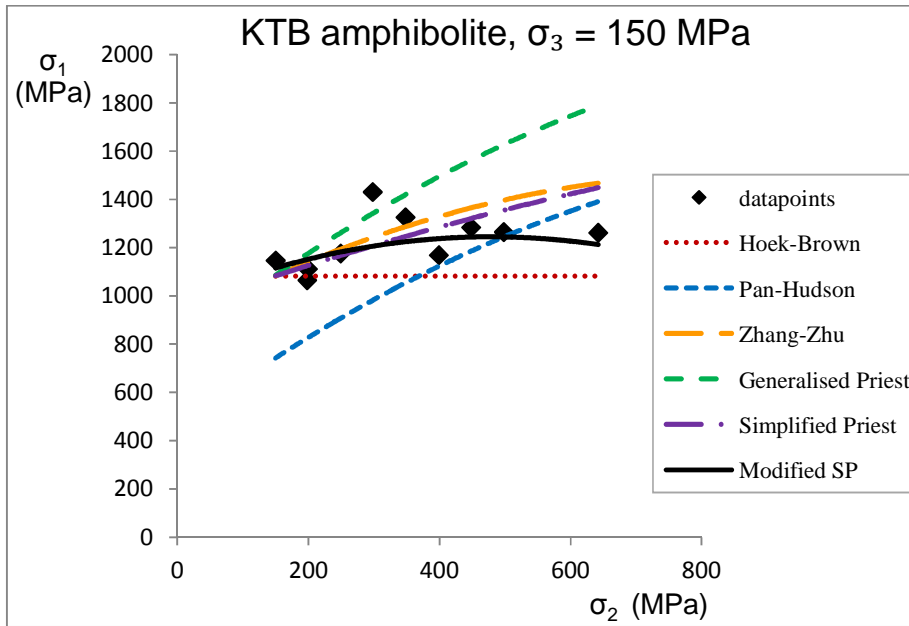
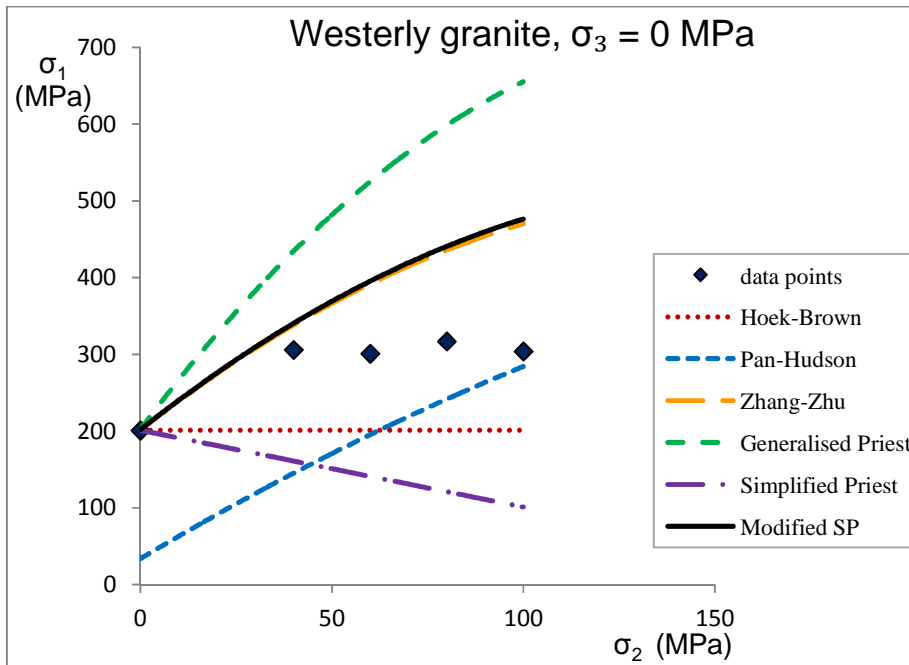
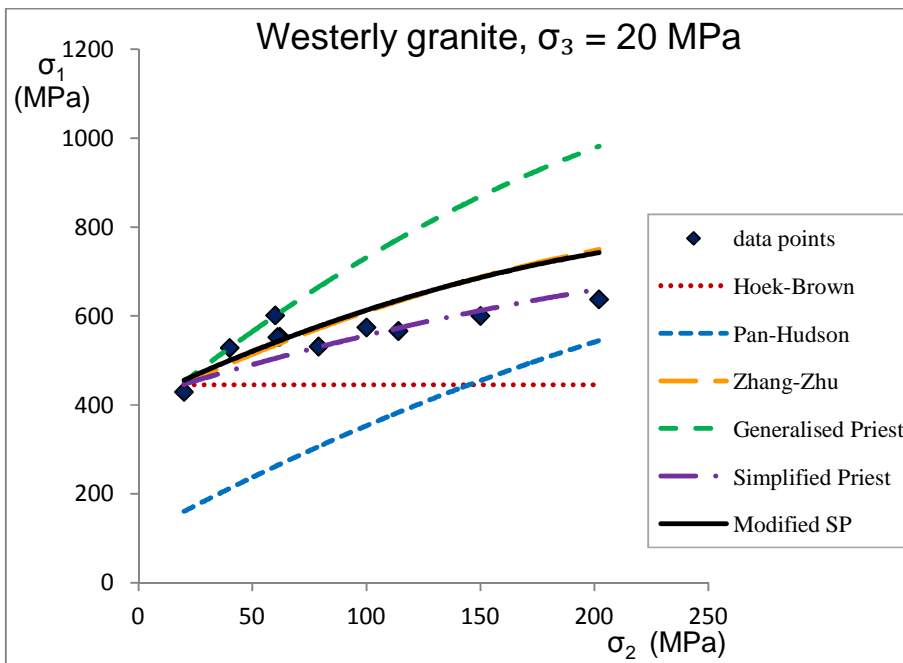
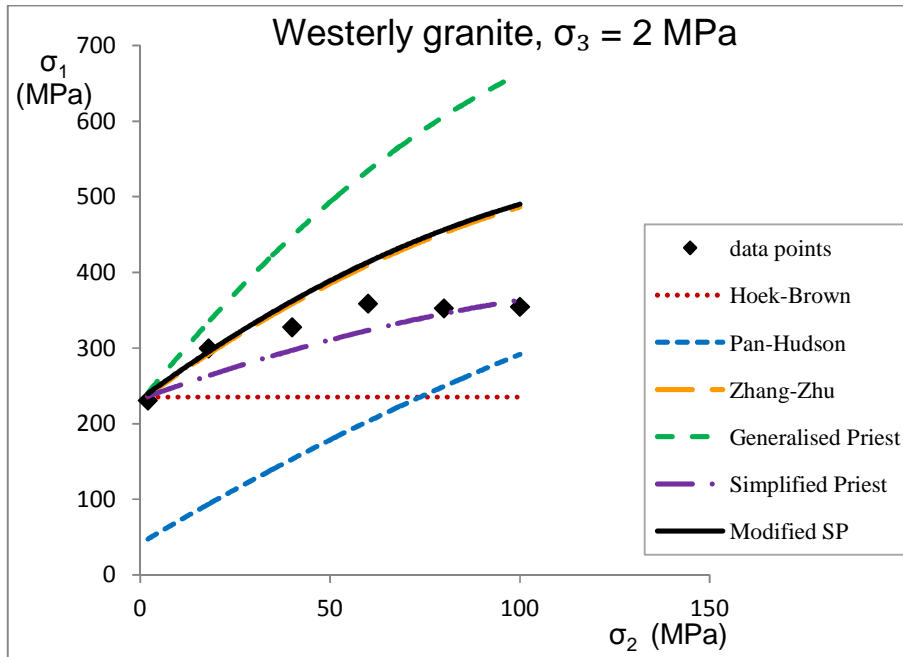
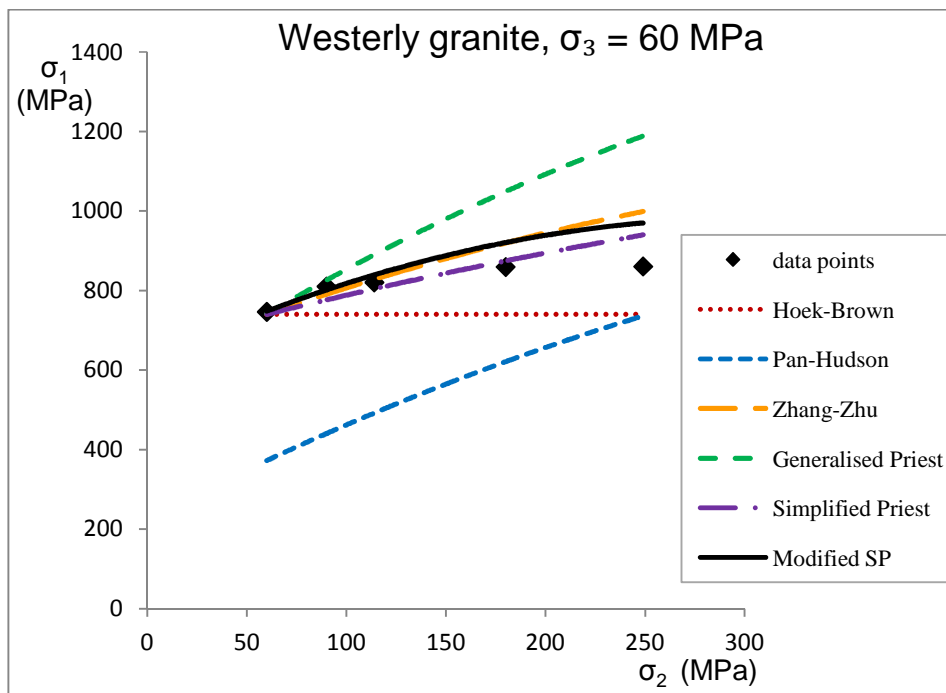
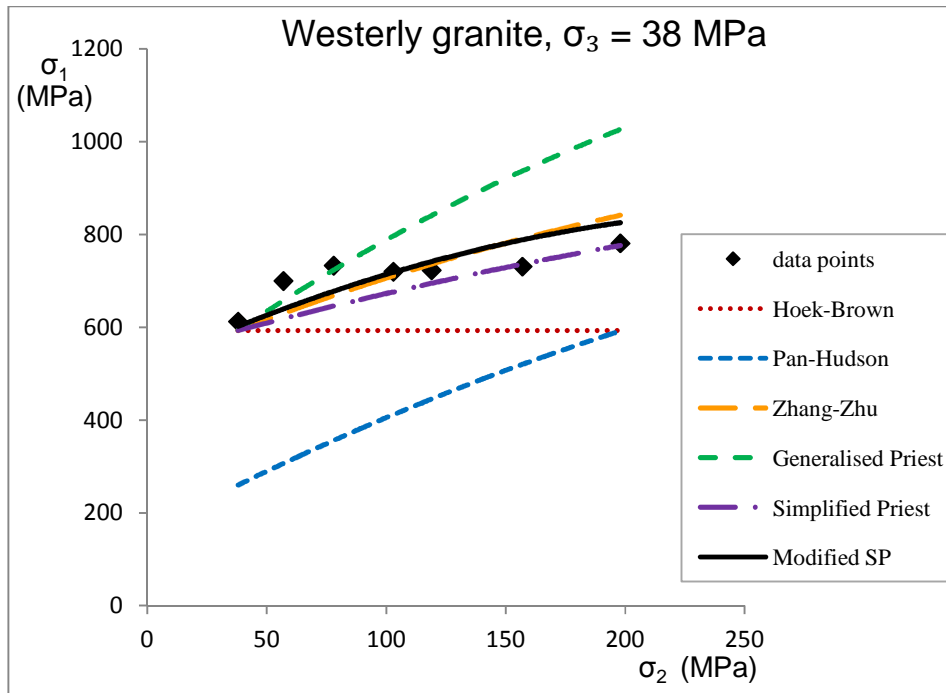


Figure D.2  $\sigma_1$  vs.  $\sigma_2$  Plots for Westerly Granite for different constant values of  $\sigma_3$







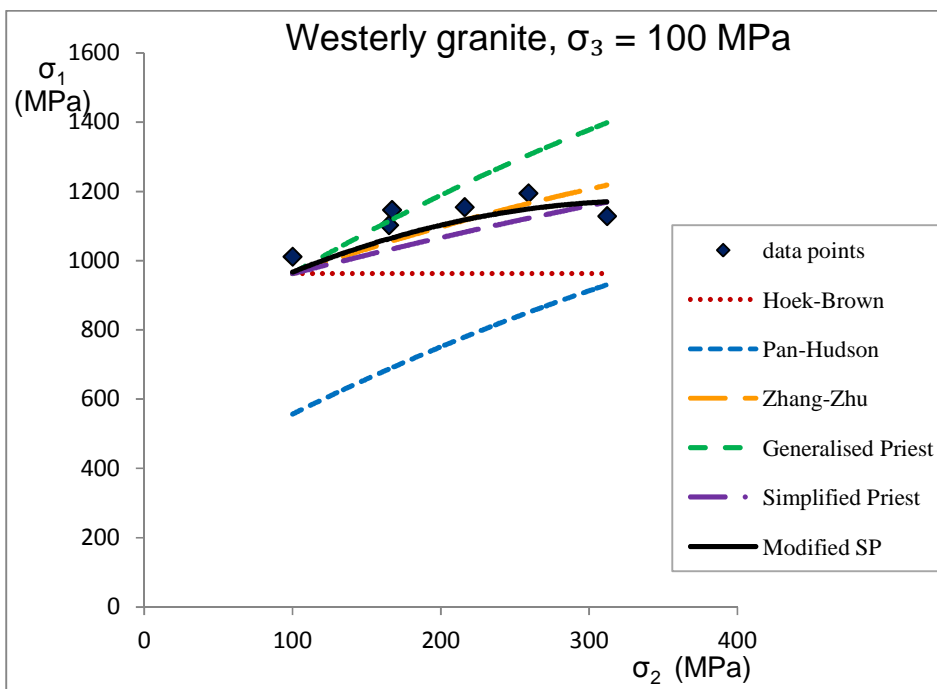
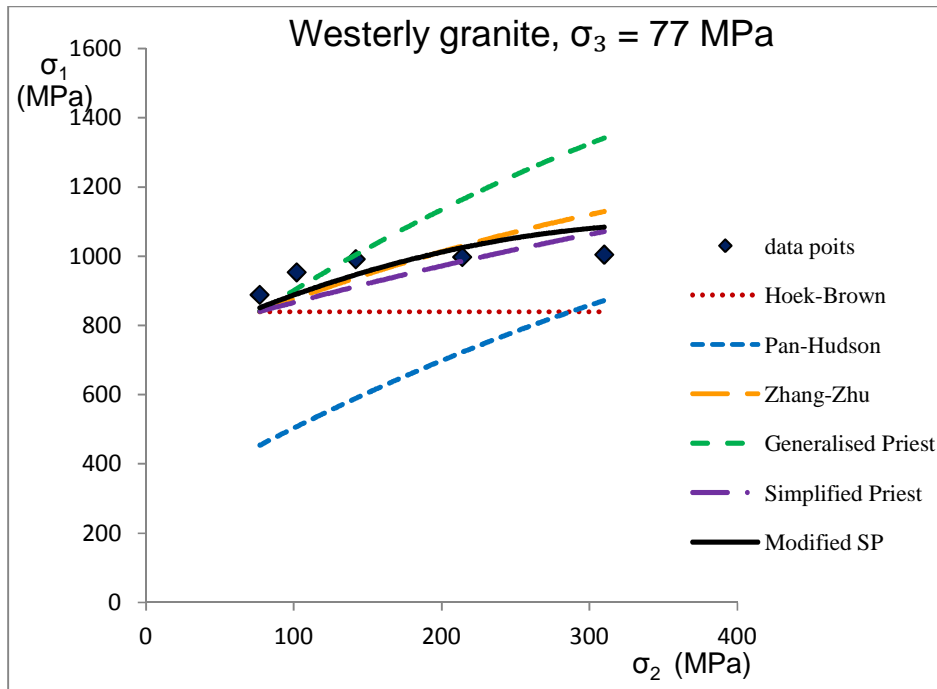
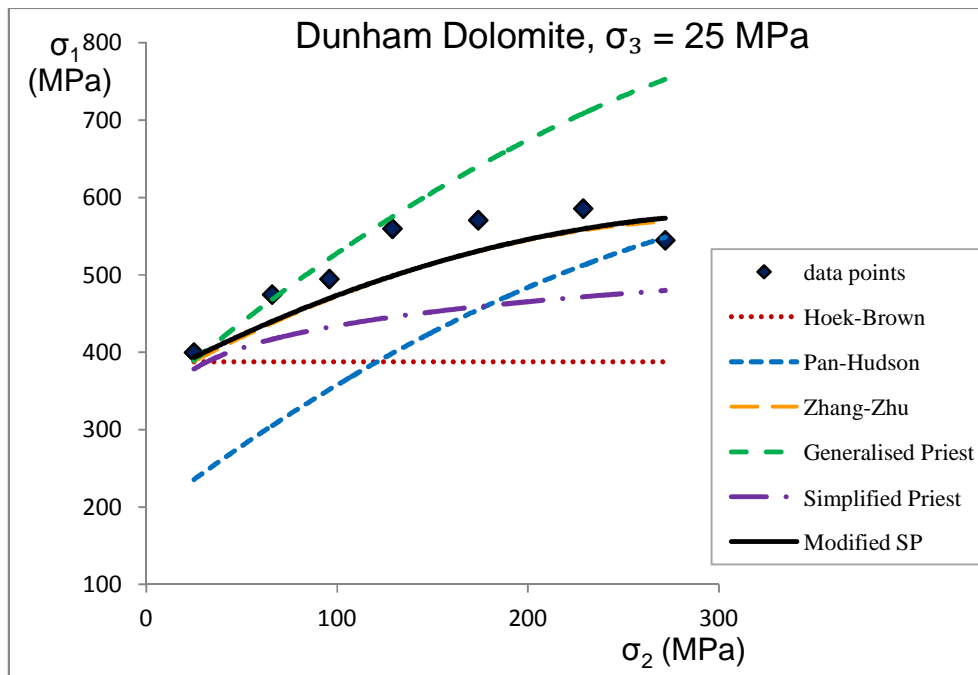
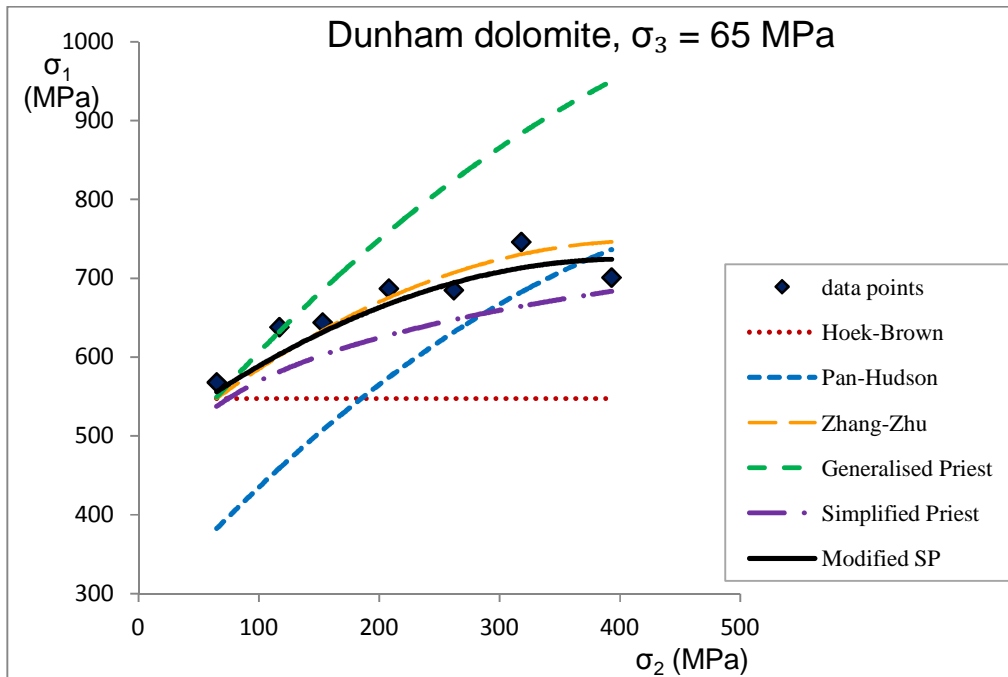
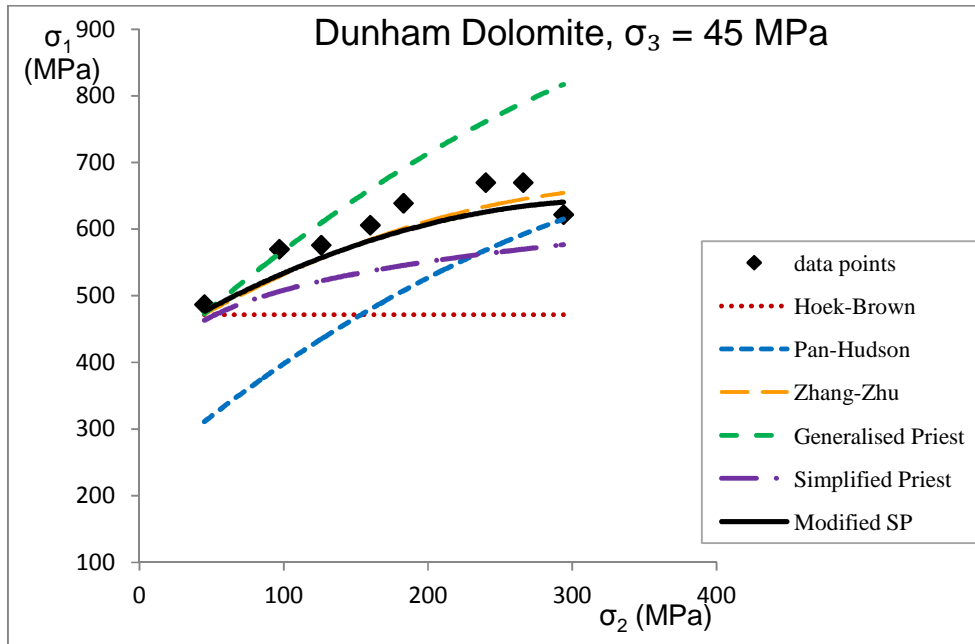
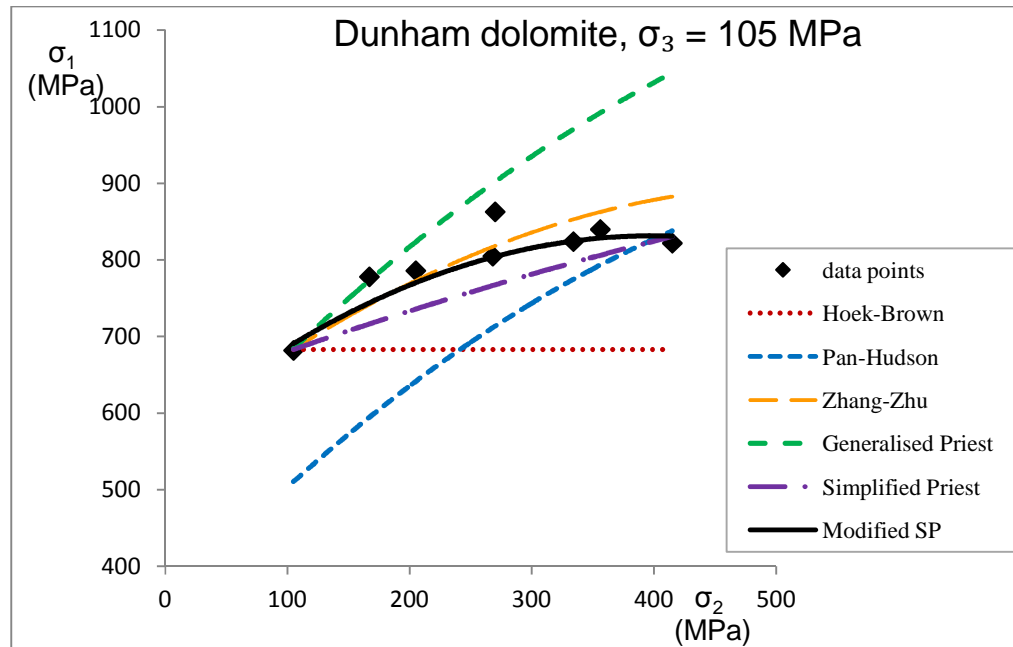
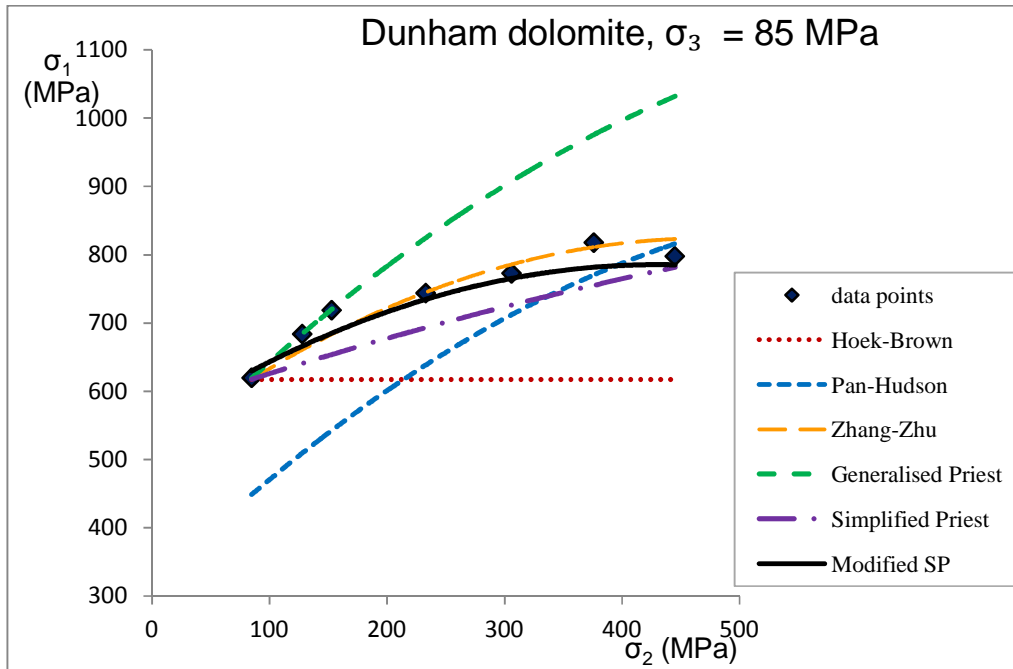


Figure D.3  $\sigma_1$  vs.  $\sigma_2$  Plots for Dunham Dolomite for different constant values of  $\sigma_3$







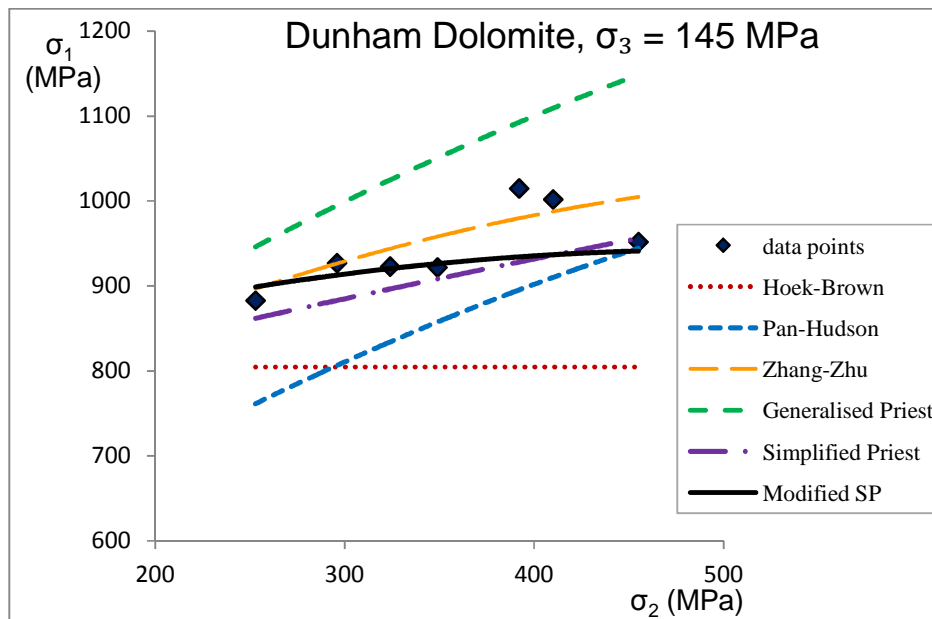
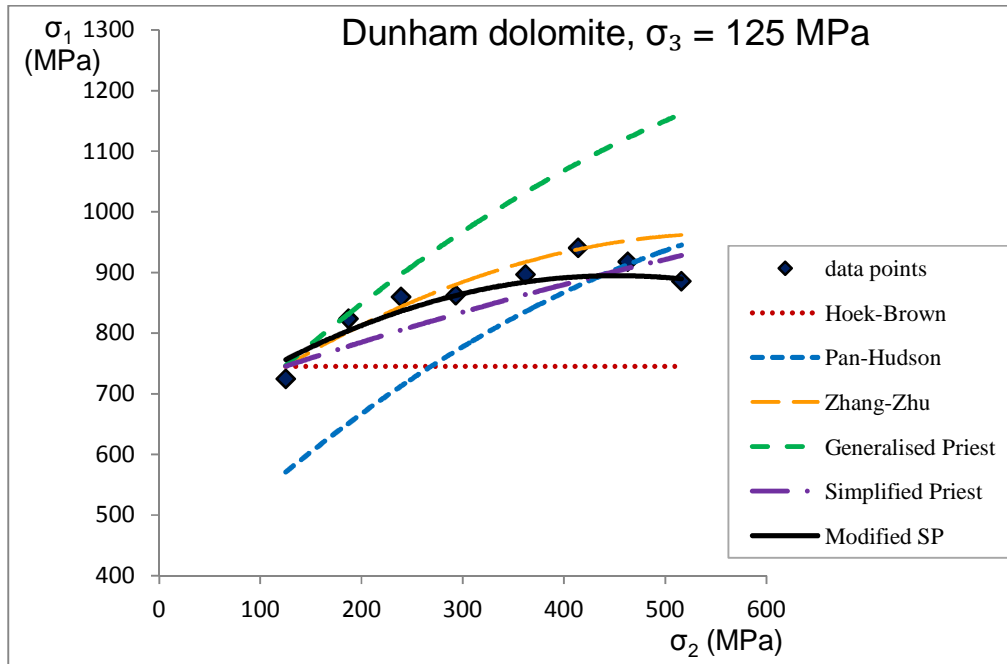
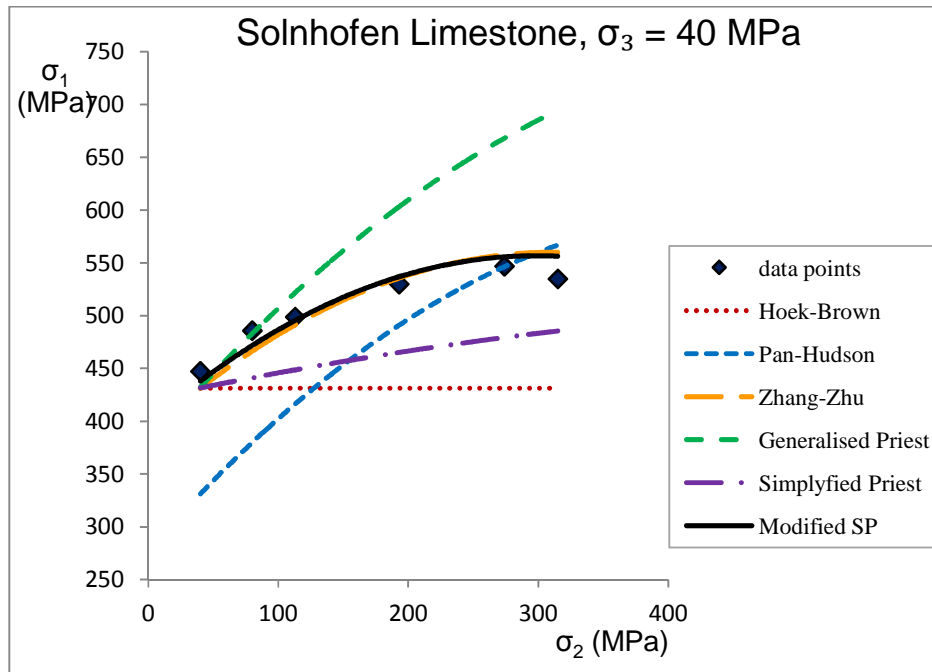
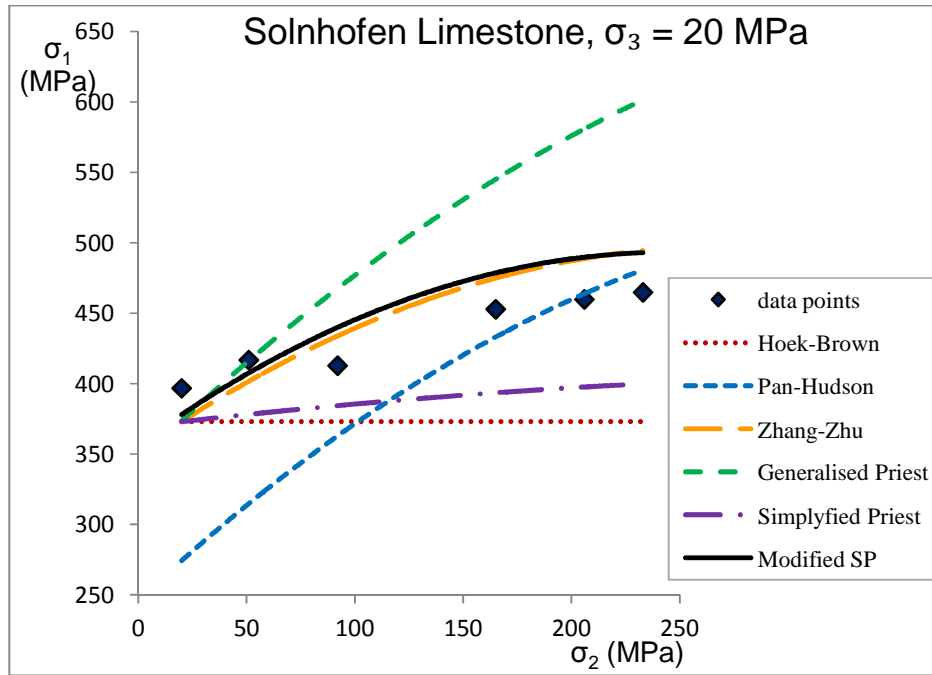


Figure D.4  $\sigma_1$  vs.  $\sigma_2$  Plots for Solnhofen Limestone for different constant values of  $\sigma_3$



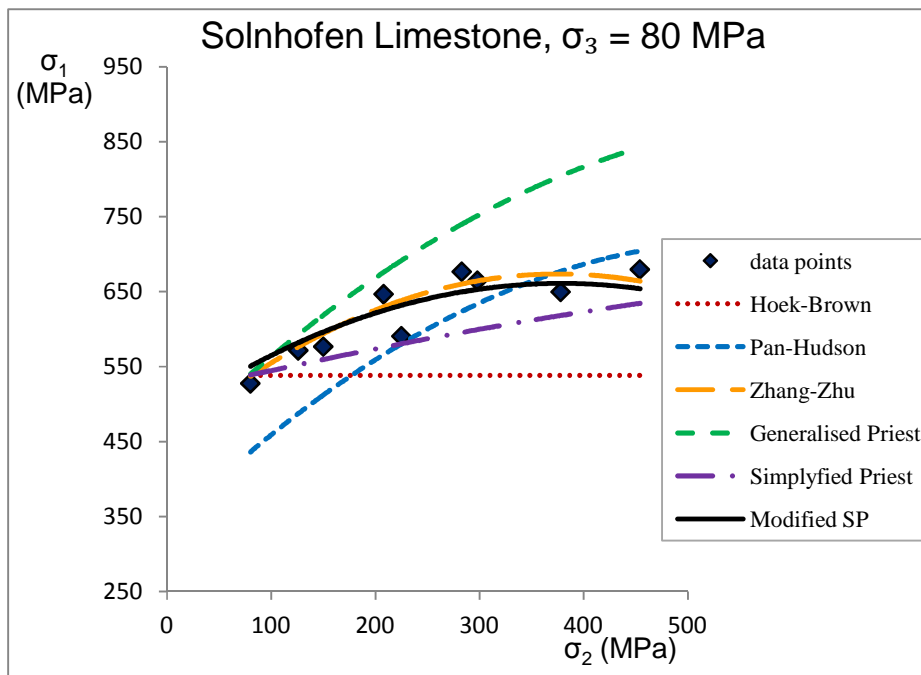
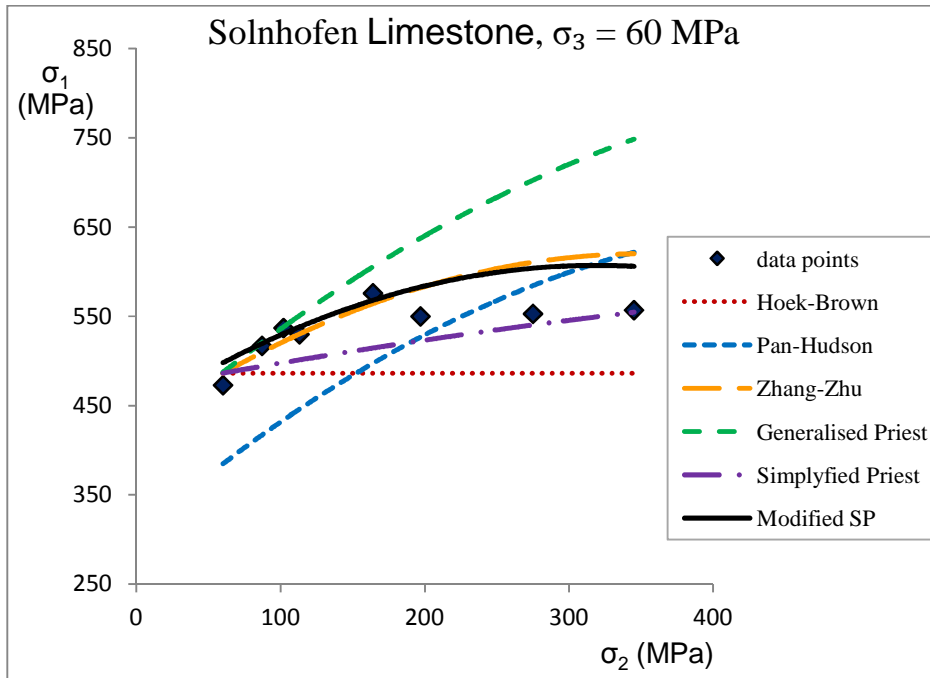
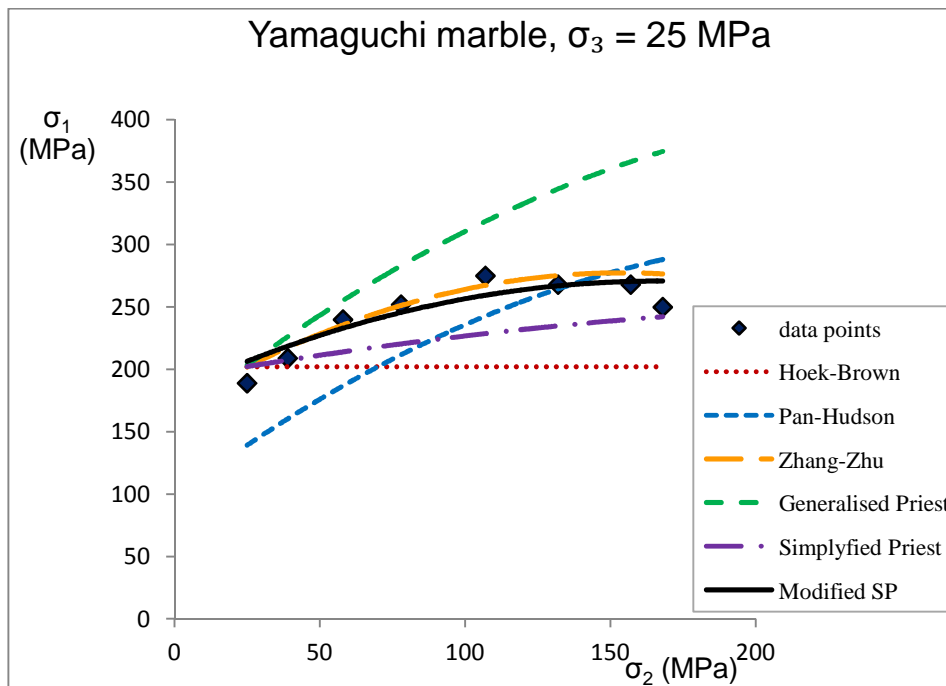
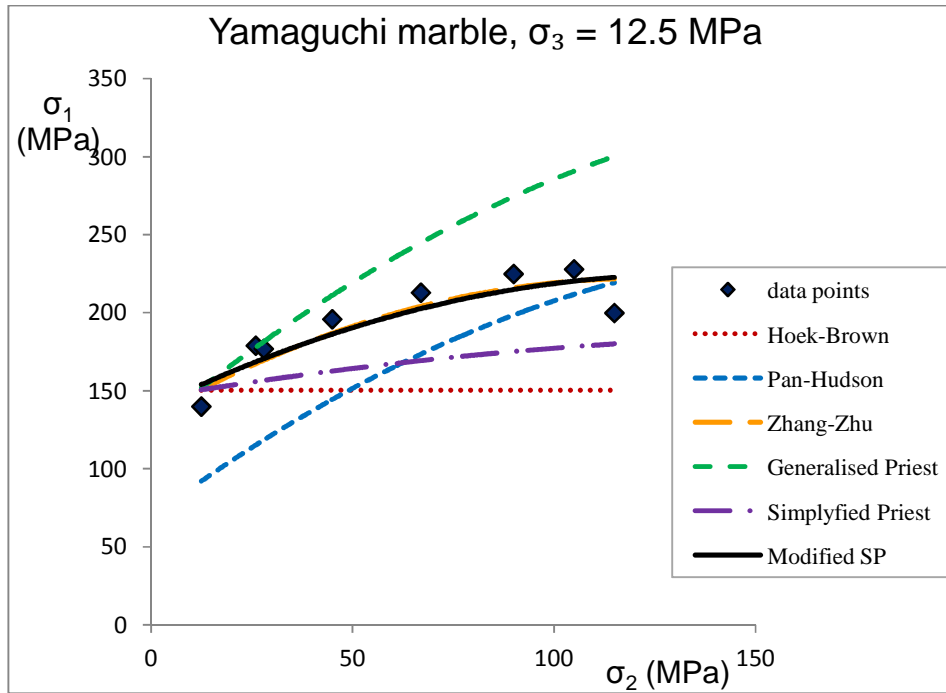


Figure D.5  $\sigma_1$  vs.  $\sigma_2$  Plots for Yamaguchi Marble for different constant values of



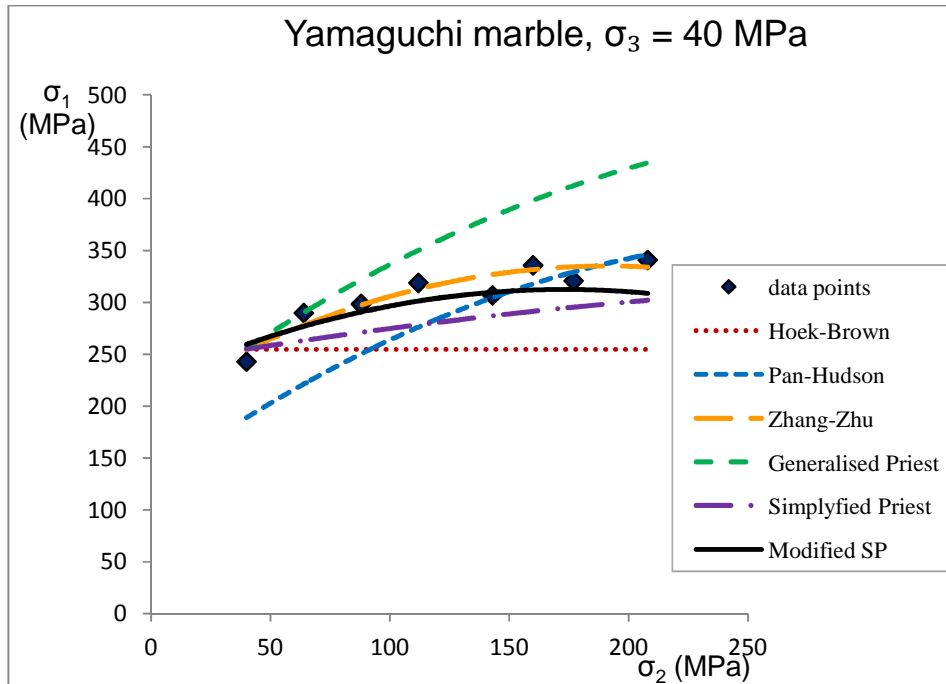
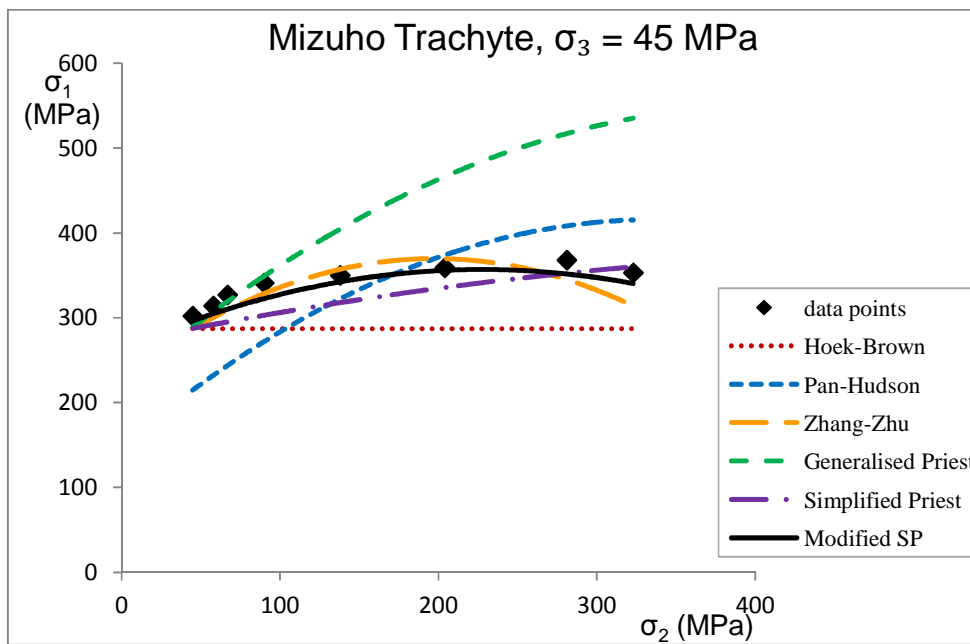
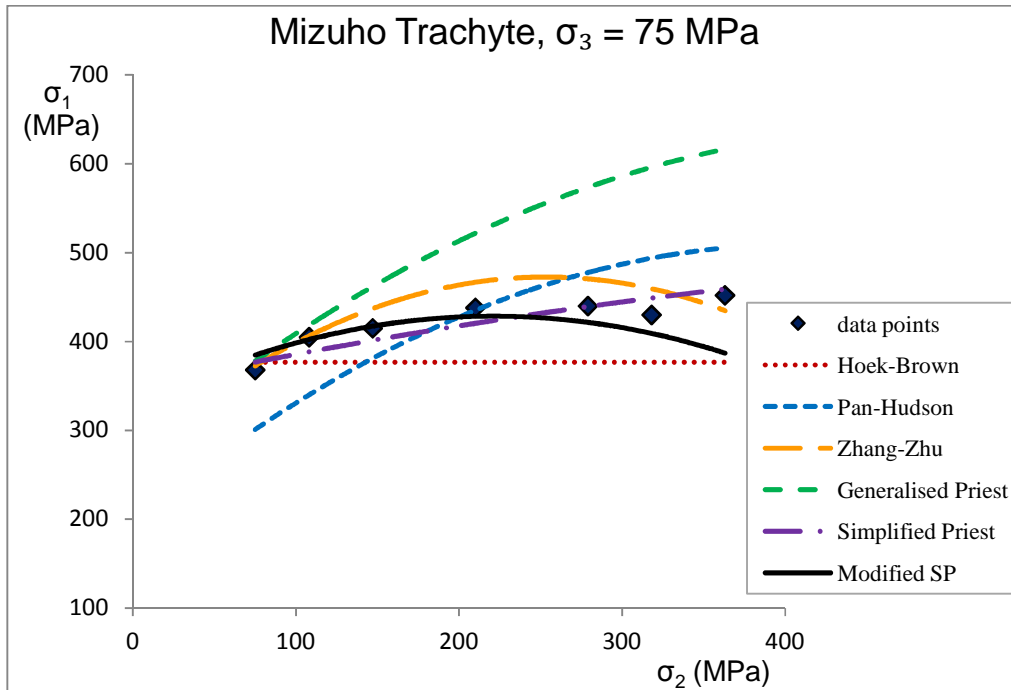
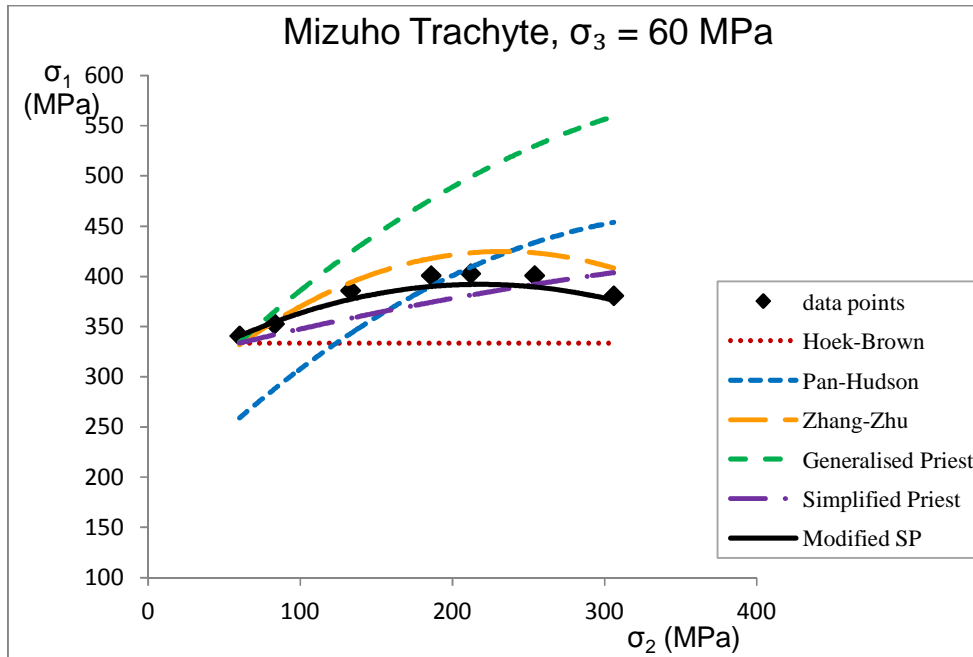


Figure D.6  $\sigma_1$  vs.  $\sigma_2$  Plots for Mizuho Trachyte for different constant values of  $\sigma_3$





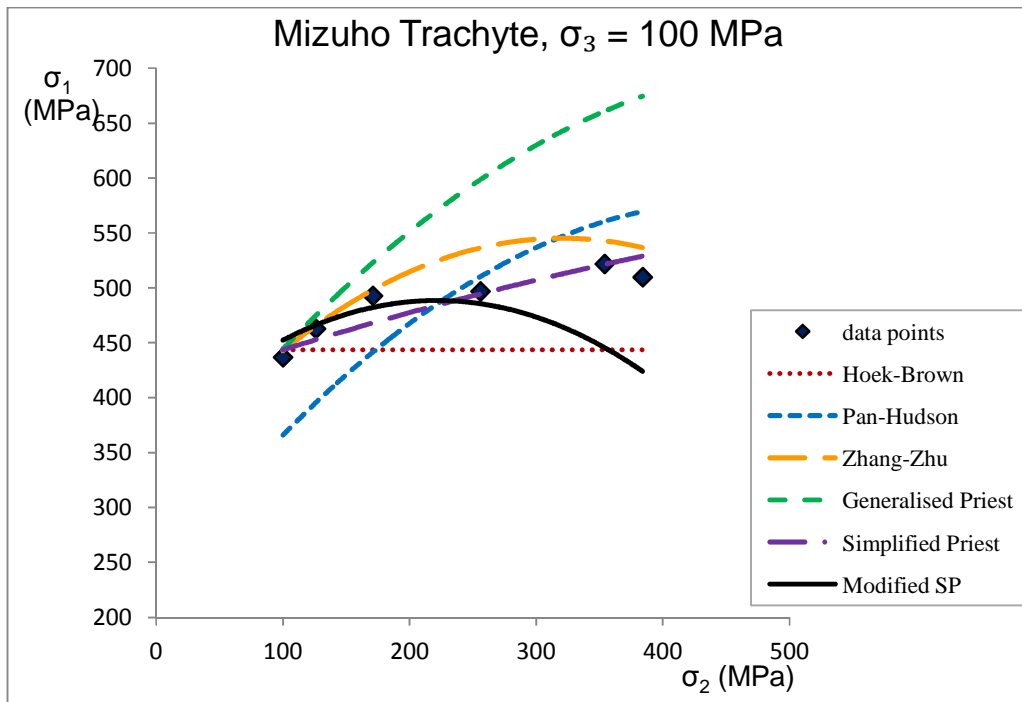
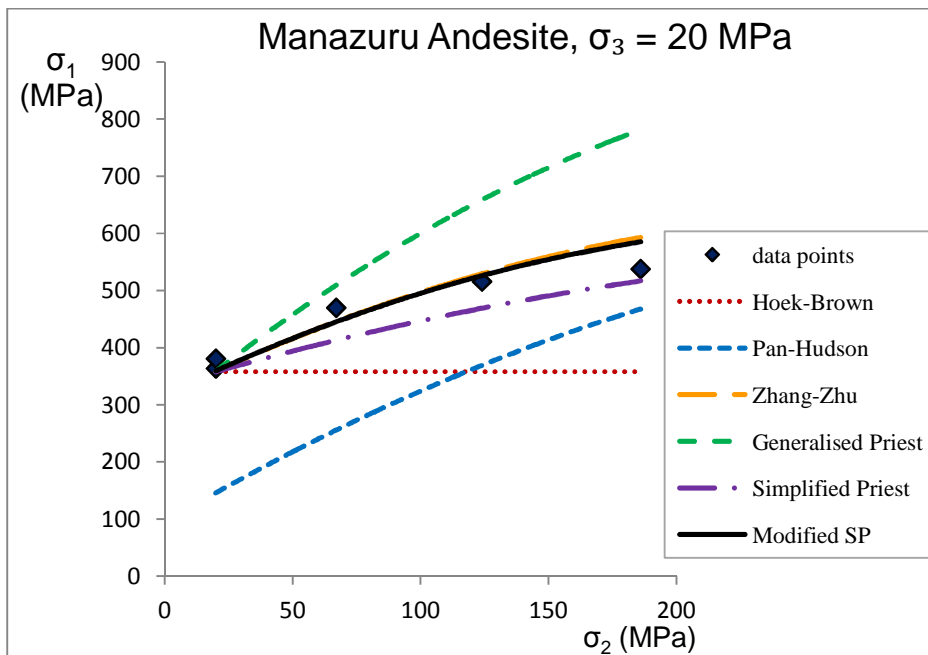


Figure D.7  $\sigma_1$  vs.  $\sigma_2$  Plots for Manazuru Andesite for different constant values of  $\sigma_3$



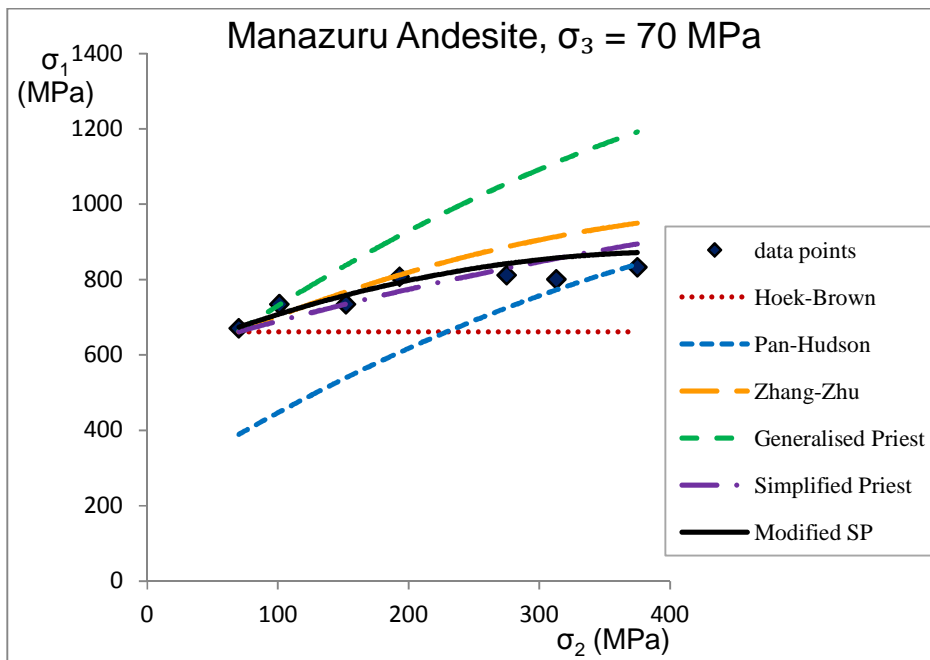
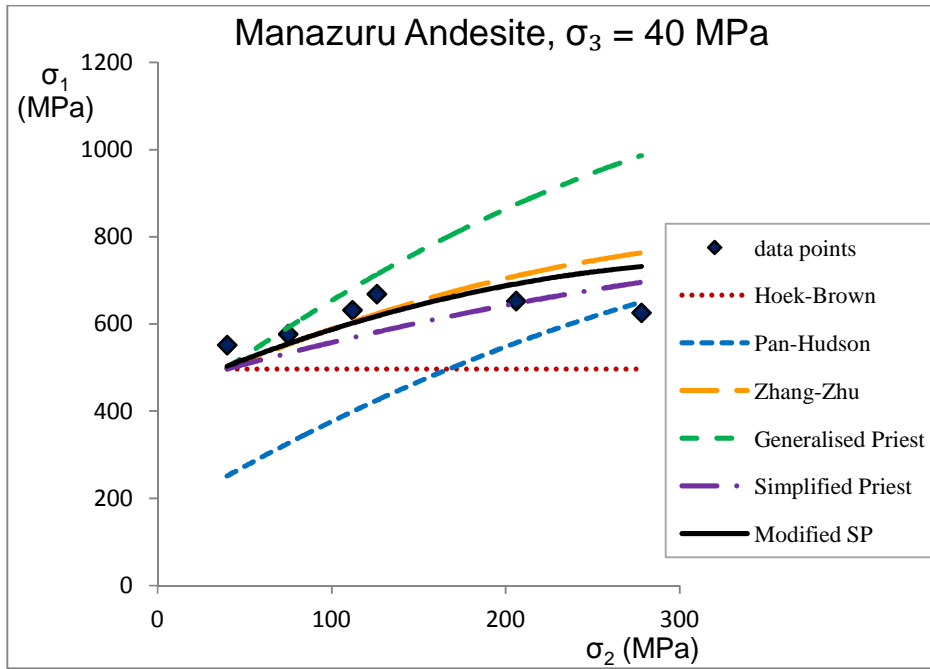
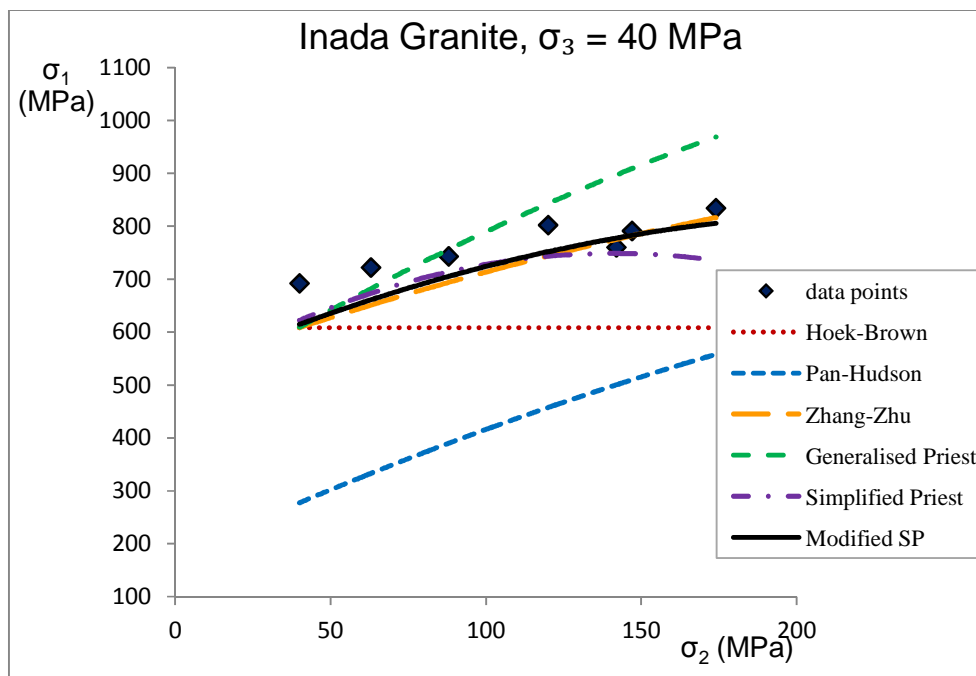
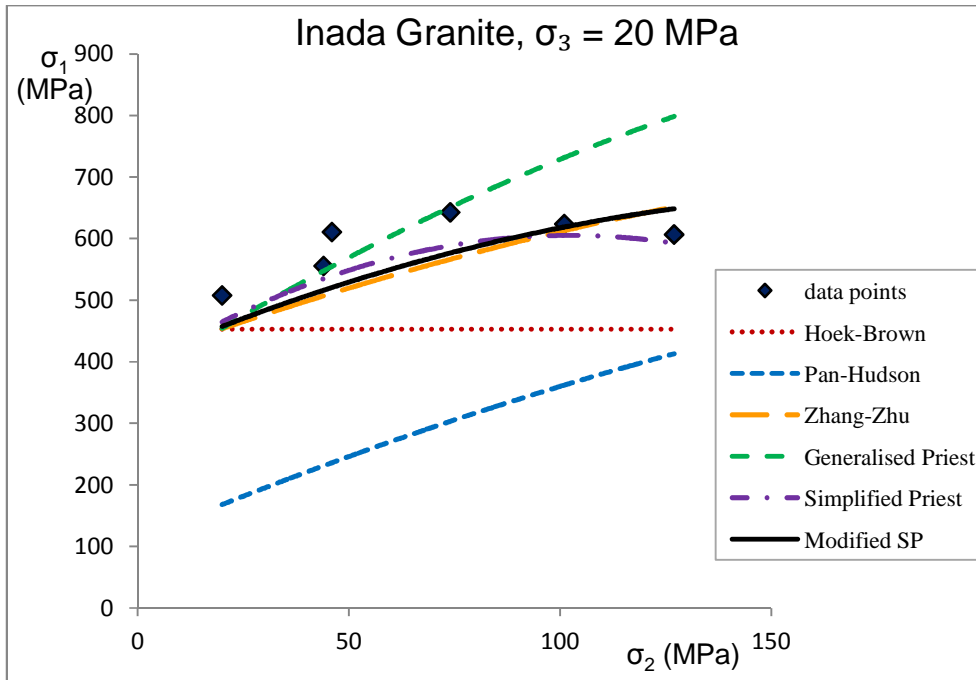
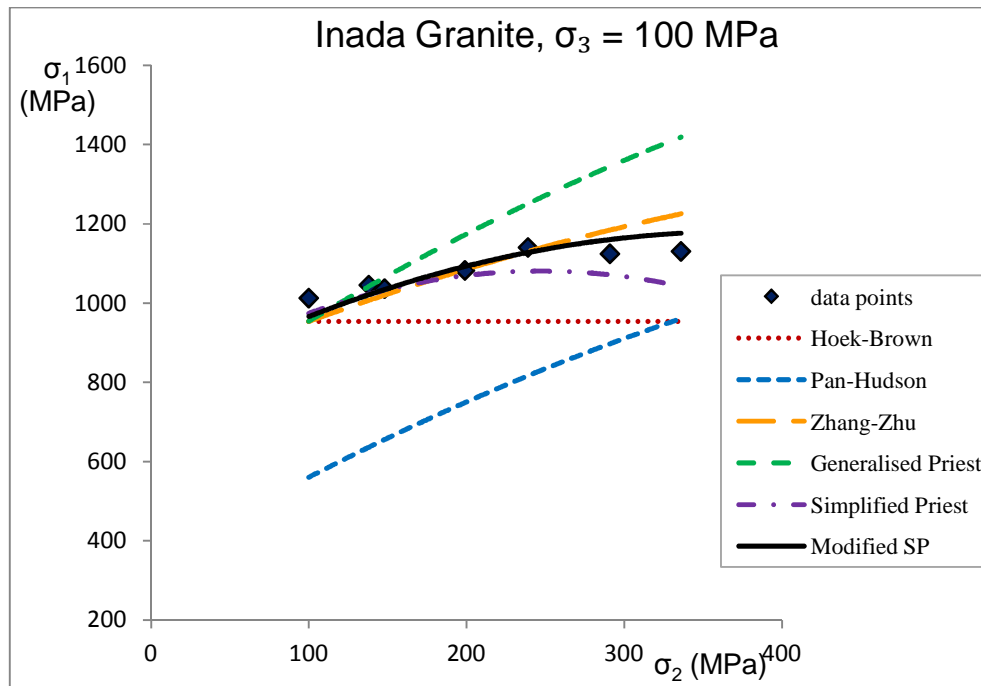


Figure D.8  $\sigma_1$  vs.  $\sigma_2$  Plots for Inada Granite for different constant values of  $\sigma_3$





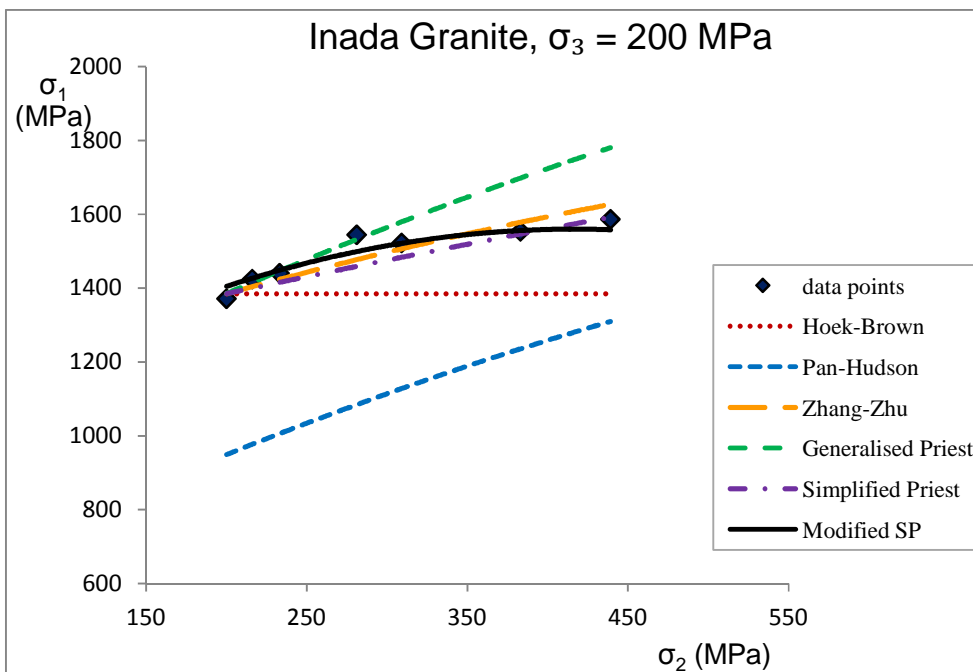
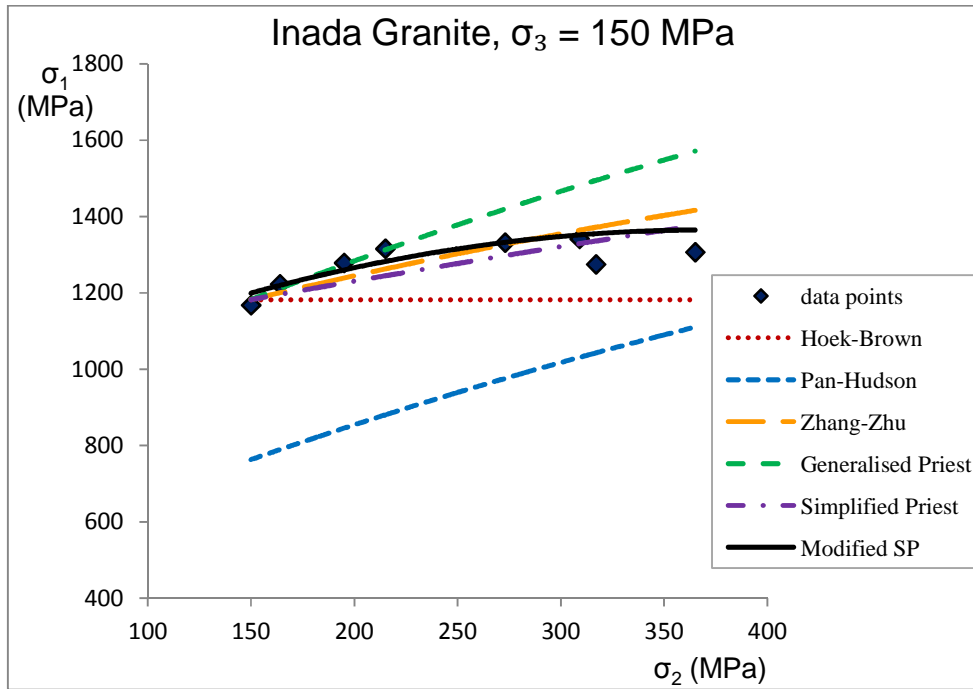
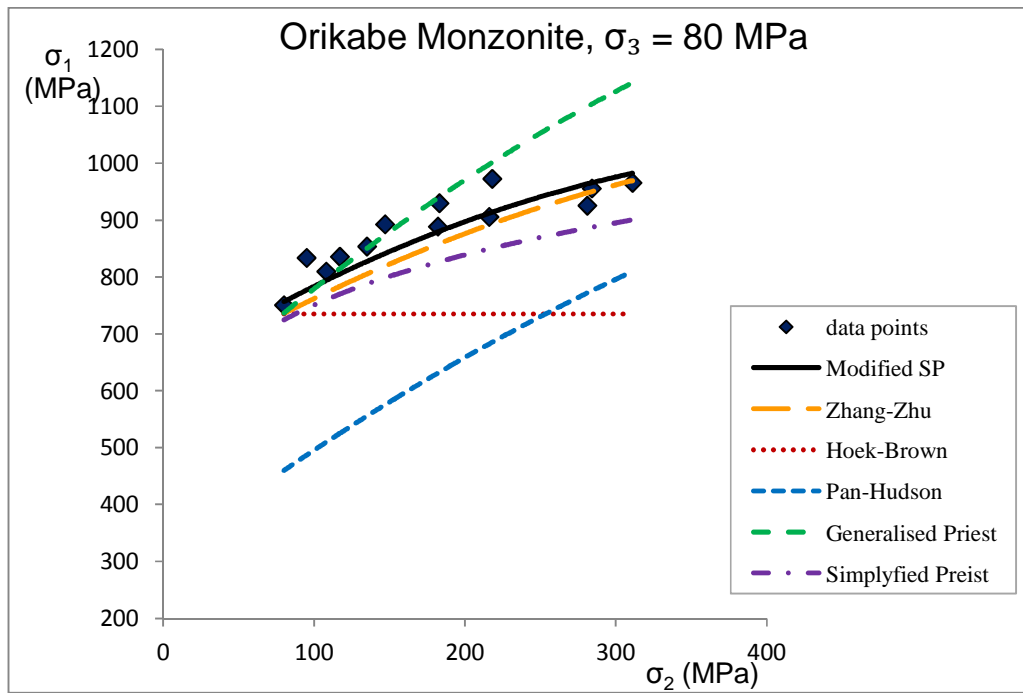
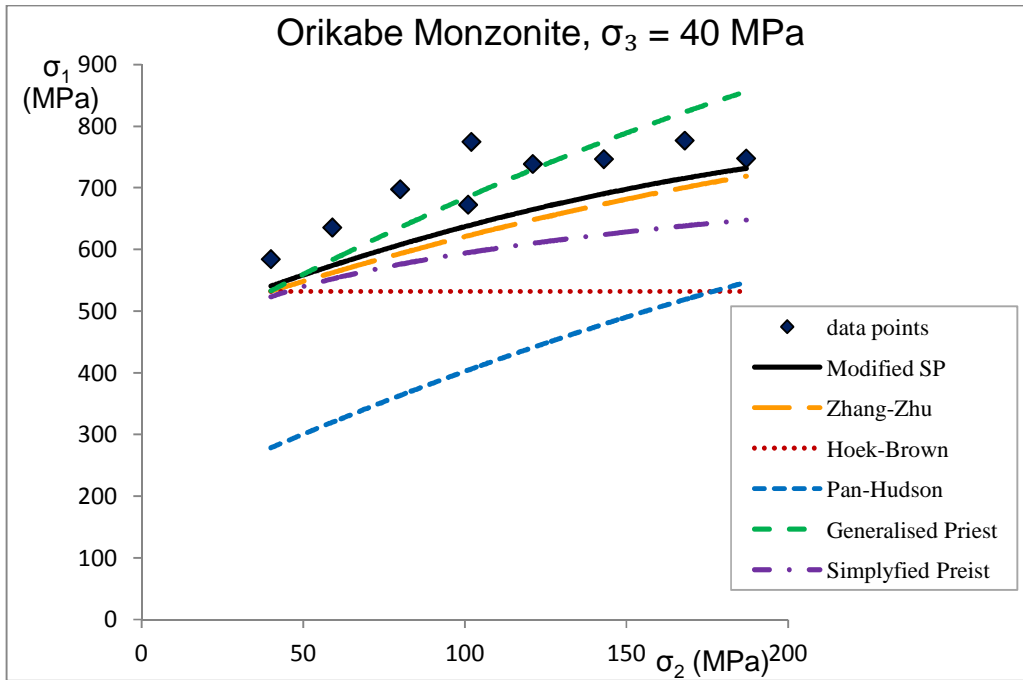
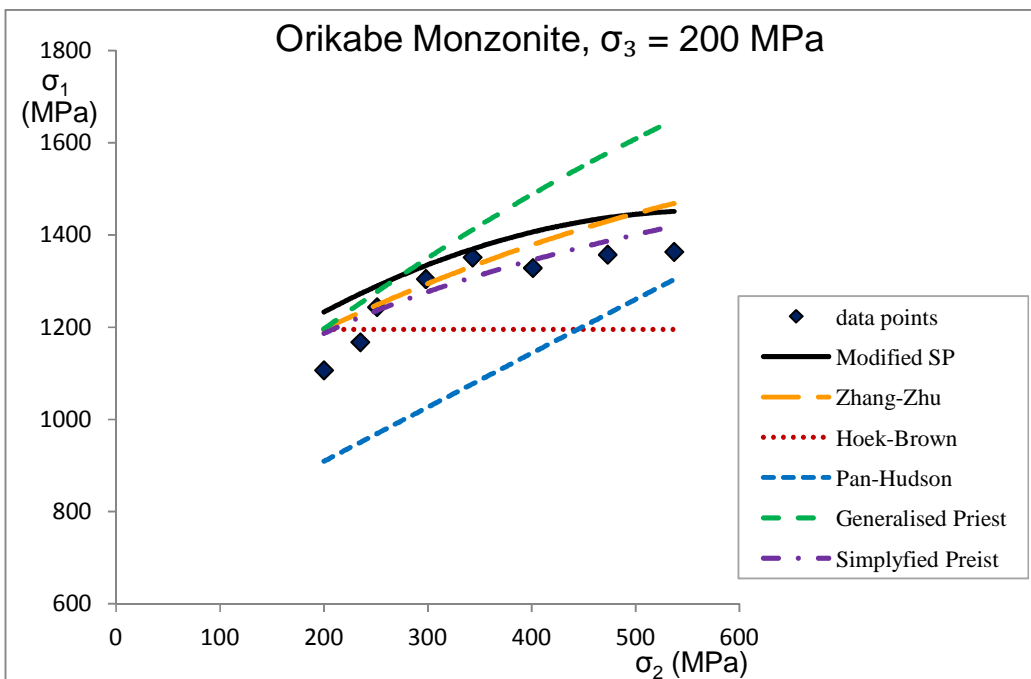
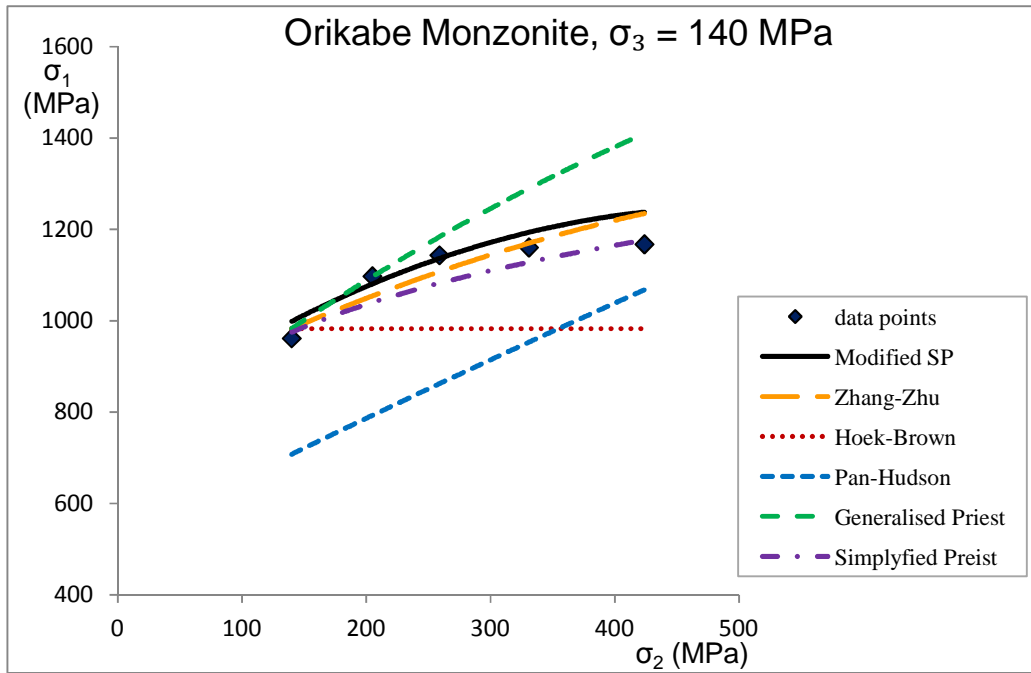


Figure D.9  $\sigma_1$  vs.  $\sigma_2$  Plots for Orikabe Monzonite for different constant values of





## **APPENDIX E**

### **Error analysis diagrams**

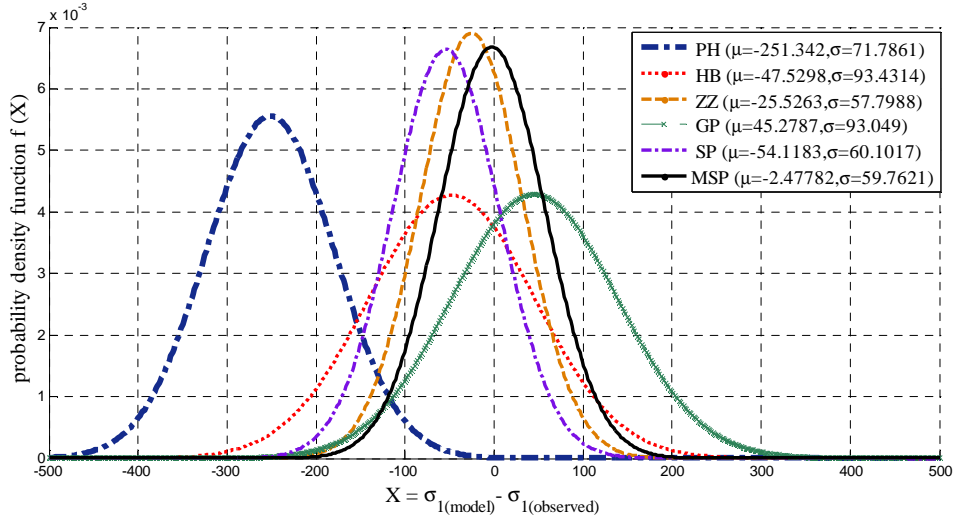


Figure E.1 Normal distribution of failure prediction accuracy of selected failure criteria for Orikabe Monzonite

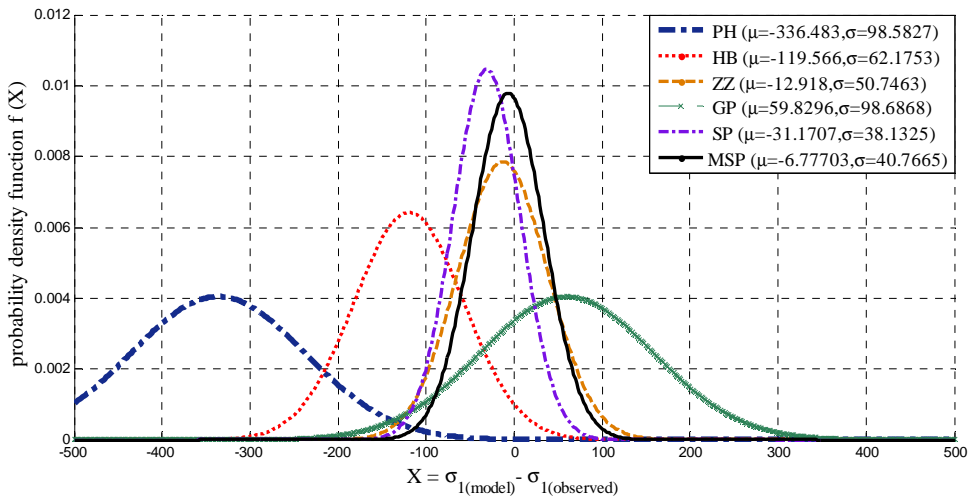


Figure E.2 Normal distribution of failure prediction accuracy of selected failure criteria for Inada Granite

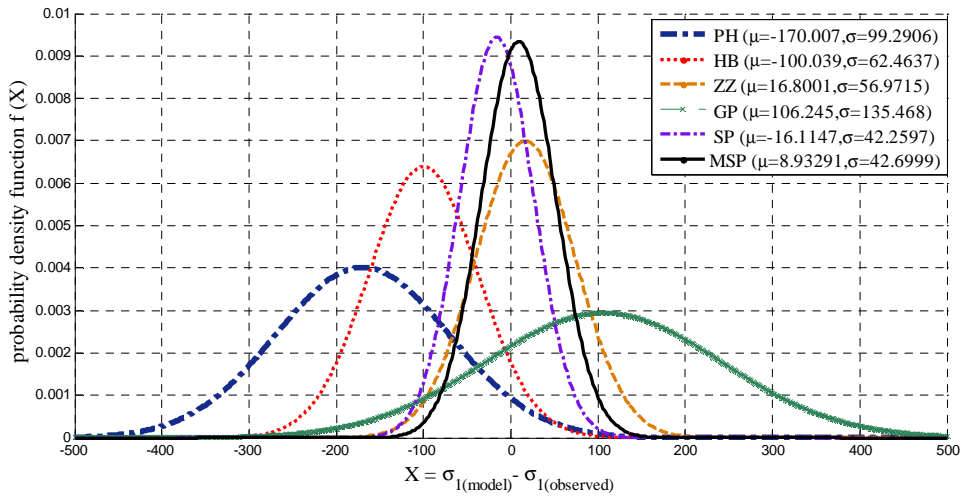


Figure E.3 Normal distribution of failure prediction accuracy of selected failure criteria for Manazuru Andesite

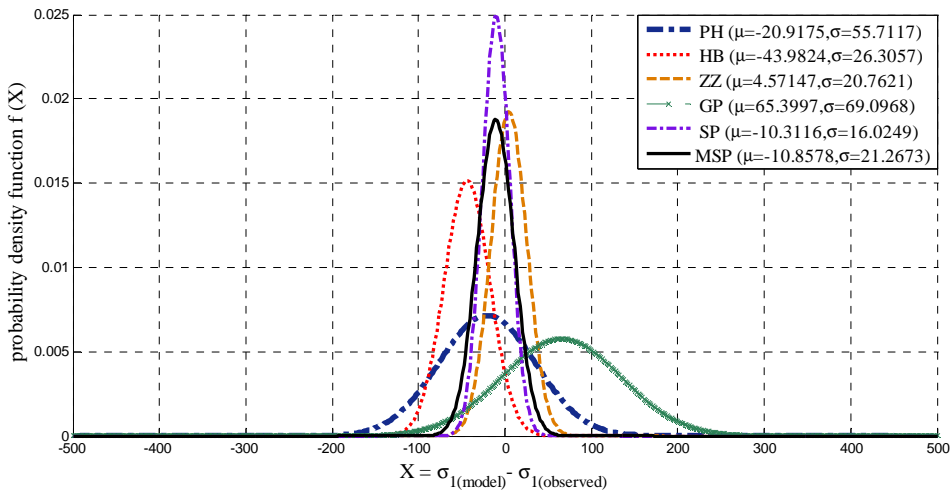


Figure E.4 Normal distribution of failure prediction accuracy of selected failure criteria for Mizuho Trachyte

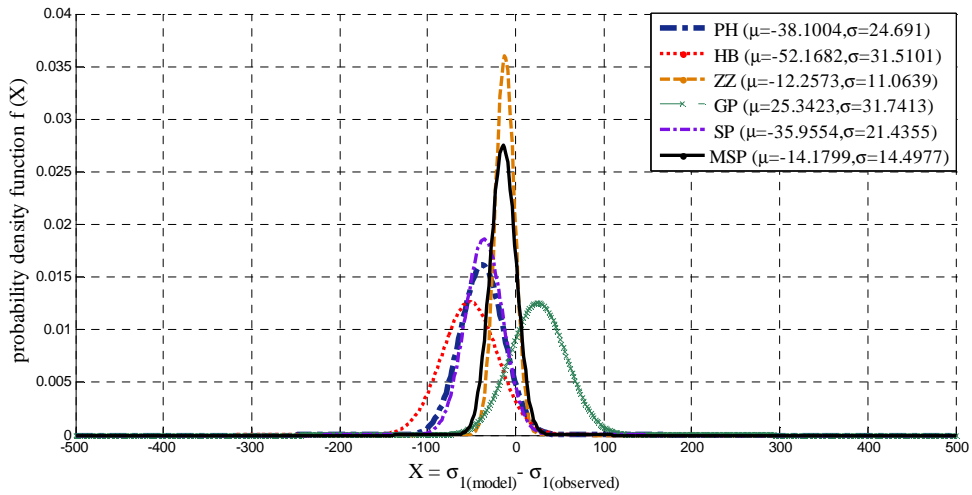


Figure E.5 Normal distribution of failure prediction accuracy of selected failure criteria for Yamaguchi Marble

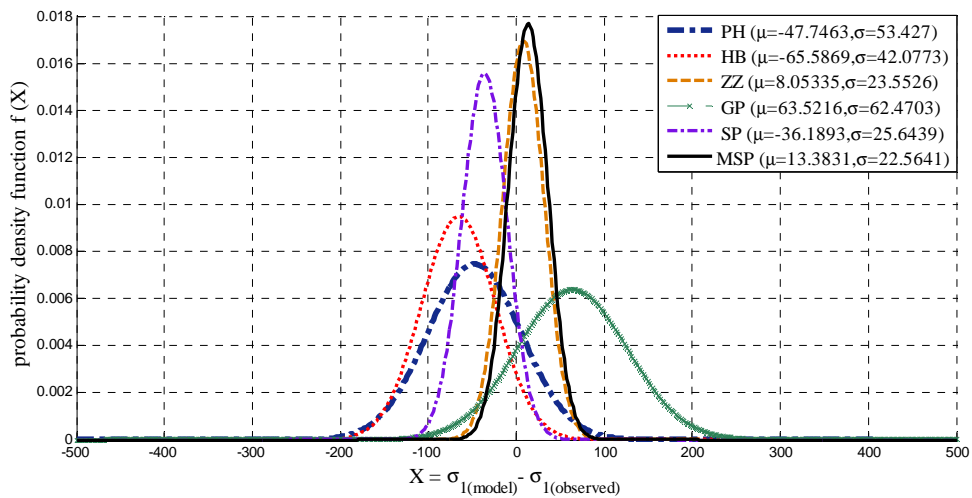


Figure E.6 Normal distribution of failure prediction accuracy of selected failure criteria for Solnhofen Limestone

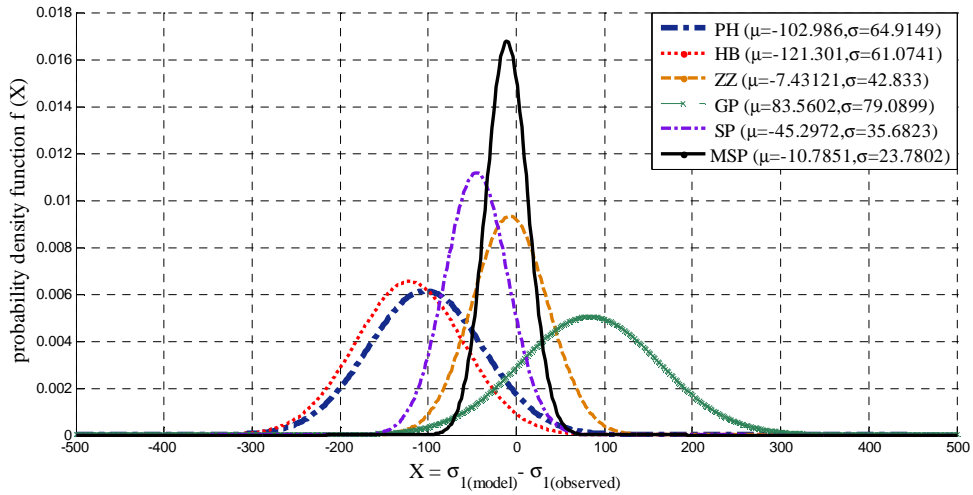


Figure E.7 Normal distribution of failure prediction accuracy of selected failure criteria for Dunham Dolomite

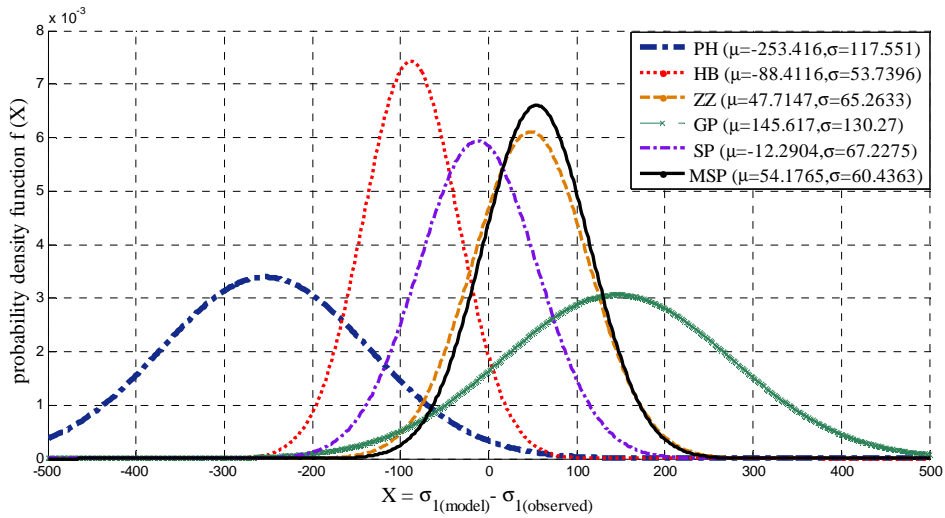


Figure E.8 Normal distribution of failure prediction accuracy of selected failure criteria for Westerly Granite

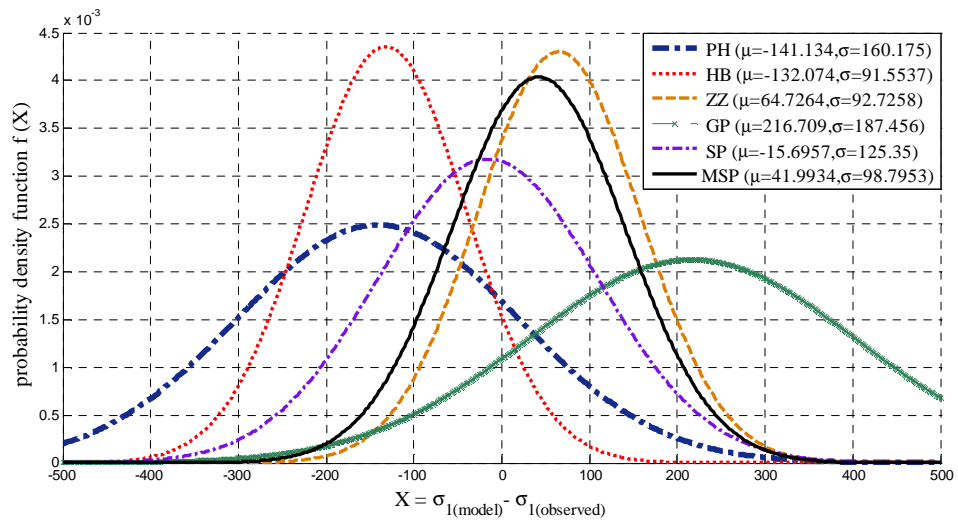


Figure E.9 Normal distribution of failure prediction accuracy of selected failure criteria for KTB Amphibolite

## **APPENDIX F**

**MATLAB programs for plotting three dimensional failure surfaces in the principal stress space**

## Hoek-Brown Criterion

```

%=====Hoek Brown Criterion=====
% Input parameters:
% I1= First invariant of stress tensor.
% mb= Parameter m for the Hoek-Brown Criterion.
% sigmac= Uniaxial strength of rock material.
% parameter S for the Hoek-Brown Criterion.
% Output:
% Failure surface for the Hoek-Brown criterion in three-dimensional stress
space.
%=====
I1=linspace(0,3500,50);
mb=20;
sigmac=100;
S=1;
%====Calculation of the Hoek-Brown radius on the deviatoric plane=====
%---[-pi/6,pi/6]-----
theta=(-pi/6:.01:pi/6);
lamda1=2*mb*sin(theta+pi/3)./sqrt(3);
A=4*(cos(theta)).^2;
for j=1:length(I1)
    for i=1:length(A)
        r1(i,j)=(sigmac./(2*A(i))).*(-
lamda1(i)+sqrt(lamda1(i).^2+4*A(i).*(mb*I1(j)/(3*sigmac))+S));
    end
end
%---[pi/6,pi/2]-----
theta1=(-(pi/6):0.01:pi/6);
lamda2=2*mb*sin(-theta1+pi/3)./sqrt(3);
A=4*(cos(theta1)).^2;
for j=1:length(I1)
    for i=1:length(A)
        r2(i,j)=(sigmac./(2*A(i))).*(-
lamda2(i)+sqrt(lamda2(i).^2+4*A(i).*(mb*I1(j)/(3*sigmac))+S));
    end
end
%---[pi/2,2*pi/3]-----
theta2=(-(pi/6):0.01:pi/6);
lamda1=2*mb*sin(theta2+pi/3)./sqrt(3);
for j=1:length(I1)
    for i=1:length(A)
        r3(i,j)=(sigmac./(2*A(i))).*(-
lamda1(i)+sqrt(lamda1(i).^2+4*A(i).*(mb*I1(j)/(3*sigmac))+S));
    end
end
%---[5*pi/6,7*pi/6]-----
theta3=(-(pi/6):0.01:pi/6);
lamda2=2*mb*sin(-theta3+pi/3)./sqrt(3);
for j=1:length(I1)
    for i=1:length(A)
        r4(i,j)=(sigmac./(2*A(i))).*(-
lamda2(i)+sqrt(lamda2(i).^2+4*A(i).*(mb*I1(j)/(3*sigmac))+S));
    end
end
%---[7pi/6,3pi/2]-----

```

```

theta4=(-pi/6):0.01:pi/6);
lamda1=2*mb*sin(theta+pi/3)./sqrt(3);
for j=1:length(I1)
    for i=1:length(A)
        r5(i,j)=(sigmac./(2*A(i))).*(-
lamda1(i)+sqrt(lamda1(i).^2+4*A(i).*(mb*I1(j)/(3*sigmac))+S));
    end
end
%---[3pi/2,-pi/6]-----
theta5=(-pi/6:0.01:pi/6);
lamda2=2*mb*sin(pi/3-theta)./sqrt(3);
for j=1:length(I1)
    for i=1:length(A)
        r6(i,j)=(sigmac./(2*A(i))).*(-
lamda2(i)+sqrt(lamda2(i).^2+4*A(i).*(mb*I1(j)/(3*sigmac))+S));
    end
end
%-----
figure(1)% 2-D Hoek-Brown trace on the deviatoric plane.
for h=1:length(I1)
    [X,Y] = pol2cart(theta,r1(:,h)');
    plot(X,Y)
    hold on
    [X1,Y1] = pol2cart(theta1+pi/3,r2(:,h)');
    plot(X1,Y1)
    hold on
    [X2,Y2] = pol2cart(theta2+2*pi/3,r3(:,h)');
    plot(X2,Y2)
    hold on
    [X3,Y3] = pol2cart(theta3+pi,r4(:,h)');
    plot(X3,Y3)
    hold on
    [X4,Y4] = pol2cart(theta4+4*pi/3,r5(:,h)');
    plot(X4,Y4)
    hold on
    [X5,Y5] = pol2cart(theta5+5*pi/3,r6(:,h)');
    plot(X5,Y5)
end
xlabel('\sigma_2d (MPa)','fontname','times new roman','fontsize',14)
ylabel('\sigma_1d (Mpa)','fontname','times new roman','fontsize',14)
R1=[1/sqrt(2) 0 -1/sqrt(2);-1/sqrt(6) 2/sqrt(6) -1/sqrt(6);1/sqrt(3)
1/sqrt(3) 1/sqrt(3)];
R=inv(R1);

figure(2)% 3-D Hoek-Brown surface in stress space.
for h=1:length(I1)
    [X,Y] = pol2cart(theta,sqrt(2).*r1(:,h)');
    I16((((2*A.*r1(:,h)'/sigmac)+lamda1).^2-lamda1.^2)./(4*A))-
S)*3*sigmac/mb;
    z1=I16;
    A1=R*[X;Y;z1/sqrt(3)];
    plot3(A1(1,:),A1(2,:),A1(3,:), 'r')
    hold on
    [X1,Y1] = pol2cart(theta1+pi/3,sqrt(2).*r2(:,h)');
    I16((((2*A.*r2(:,h)'/sigmac)+lamda2).^2-lamda2.^2)./(4*A))-
S)*3*sigmac/mb;
    z2=I16;

```

```

    B=R*[X1;Y1;z2/sqrt(3)];
    plot3(B(1,:),B(2,:),B(3,),'r')
    hold on
    [X2,Y2] = pol2cart(theta2+2*pi/3,sqrt(2).*r3(:,h)');
    I16=((((2*A.*r3(:,h)'/sigmac)+lamda1).^2-lamda1.^2)./(4*A))-
S)*3*sigmac/mb;
    z3=I16;
    C=R*[X2;Y2;z3/sqrt(3)];
    plot3(C(1,:),C(2,:),C(3,),'r')
    hold on
    [X3,Y3] = pol2cart(theta3+pi,sqrt(2).*r4(:,h)');
    I16=((((2*A.*r4(:,h)'/sigmac)+lamda2).^2-lamda2.^2)./(4*A))-
S)*3*sigmac/mb;
    z4=I16;
    D=R*[X3;Y3;z4/sqrt(3)];
    plot3(D(1,:),D(2,:),D(3,),'r')
    hold on
    [X4,Y4] = pol2cart(theta4+4*pi/3,sqrt(2).*r5(:,h)');
    I16=((((2*A.*r5(:,h)'/sigmac)+lamda1).^2-lamda1.^2)./(4*A))-
S)*3*sigmac/mb;
    z5=I16;
    E=R*[X4;Y4;z5/sqrt(3)];
    plot3(E(1,:),E(2,:),E(3,),'r')
    hold on
    [X5,Y5] = pol2cart(theta5+5*pi/3,sqrt(2).*r6(:,h)');
    I16=((((2*A.*r6(:,h)'/sigmac)+lamda2).^2-lamda2.^2)./(4*A))-
S)*3*sigmac/mb;
    z6=I16;
    F=R*[X5;Y5;z6/sqrt(3)];
    plot3(F(1,:),F(2,:),F(3,),'r')
end

% Moving axes to the origin of coordinate system.
plot3(get(gca,'XLim'),[0 0],[0 0],'k');
plot3([0 0],[0 0],get(gca,'ZLim'),'k');
plot3([0 0],get(gca,'YLim'),[0 0],'k');

% REMOVE TICKS
set(gca,'Xtick',[]);
set(gca,'Ytick',[]);
set(gca,'Ztick',[]);

% GET OFFSETS
Xoff=diff(get(gca,'XLim'))./30;
Yoff=diff(get(gca,'YLim'))./30;
Zoff=diff(get(gca,'ZLim'))./30;
xlabel('\sigma_2 (MPa)','fontname','times new roman','fontsize',14)
ylabel('\sigma_1 (MPa)','fontname','times new roman','fontsize',14)
zlabel('\sigma_3 (MPa)','fontname','times new roman','fontsize',14)

```

## ***Pan-Hudson Criterion***

```
%=====Pan-Hudson Criterion=====
% Input parameters:
% I1= First invariant of stress tensor.
% mb= Parameter m for the Hoek-Brown Criterion.
% sigmac= Uniaxial strength of rock material.
% parameter S for the Hoek-Brown Criterion.
% Output:
% Failure surface for the Hoek-Brown criterion in three-dimensional stress
space.
%=====
clear all
close all
I1=linspace(0,3500,50);
mb=20;
sigmac=100;
S=1;
e=0.00;
%%====Calculation of the Pan-Hudson radius on the deviatoric plane=====
%==[-pi/6,pi/6]=====
theta=(-pi/6:.01:pi/6);
A=3*ones(1,length(theta));
lamda=(sqrt(3)/2)*mb*ones(1,length(theta));
for j=1:length(I1)
    for i=1:length(lamda)
        r1(i,j)=(sigmac./6).*(-
lamda(i)+sqrt(lamda(i).^2+12.*(mb*I1(j)/(3*sigmac))+S));
    end
end
%==[pi/6,pi/2]=====
theta1=(-(pi/6)+e:0.01:pi/6);
for j=1:length(I1)
    for i=1:length(lamda)
        r2(i,j)=(sigmac./6).*(-
lamda(i)+sqrt(lamda(i).^2+12.*(mb*I1(j)/(3*sigmac))+S));
    end
end
%=====[pi/2,2pi/3]=====
theta2=(-(pi/6)-e:0.01:pi/6);
for j=1:length(I1)
    for i=1:length(lamda)
        r3(i,j)=(sigmac./6).*(-
lamda(i)+sqrt(lamda(i).^2+12.*(mb*I1(j)/(3*sigmac))+S));
    end
end
%=====[5pi/6,7pi/6]=====
theta3=(-(pi/6)-e:0.01:pi/6);
for j=1:length(I1)
    for i=1:length(lamda)
        r4(i,j)=(sigmac./6).*(-
lamda(i)+sqrt(lamda(i).^2+12.*(mb*I1(j)/(3*sigmac))+S));
    end
end
%=====[7pi/6,3pi/2]=====
theta4=(-(pi/6)-e:0.01:pi/6);
```

```

for j=1:length(I1)
    for i=1:length(lamda)
        r5(i,j)=(sigmac./6).*(-
lamda(i)+sqrt(lamda(i).^2+12.*(mb*I1(j)/(3*sigmac))+S));
    end
end
%===== [3pi/2,-pi/6] =====
theta5=(-pi/6:0.01:pi/6);
for j=1:length(I1)
    for i=1:length(lamda)
        r6(i,j)=(sigmac./6).*(-
lamda(i)+sqrt(lamda(i).^2+12.*(mb*I1(j)/(3*sigmac))+S));
    end
end
%-----
figure(1)% 2-D Pan-Hudson trace on the deviatoric plane.
for h=1:length(I1)
    [X,Y] = pol2cart(theta,r1(:,h)');
    plot(X,Y)
    hold on
    [X1,Y1] = pol2cart(theta1+pi/3,r2(:,h)');
    plot(X1,Y1)
    hold on
    [X2,Y2] = pol2cart(theta2+2*pi/3,r3(:,h)');
    plot(X2,Y2)
    hold on
    [X3,Y3] = pol2cart(theta3+pi,r4(:,h)');
    plot(X3,Y3)
    hold on
    [X4,Y4] = pol2cart(theta4+4*pi/3,r5(:,h)');
    plot(X4,Y4)
    hold on
    [X5,Y5] = pol2cart(theta5+5*pi/3,r6(:,h)');
    plot(X5,Y5)
end
xlabel('\sigma_2d (MPa)','fontname','times new roman','fontsize',14)
ylabel('\sigma_1d (Mpa)','fontname','times new roman','fontsize',14)
R1=[1/sqrt(2) 0 -1/sqrt(2);-1/sqrt(6) 2/sqrt(6) -1/sqrt(6);1/sqrt(3)
1/sqrt(3) 1/sqrt(3)];
R=inv(R1);
R1=[1/sqrt(2) 0 -1/sqrt(2);-1/sqrt(6) 2/sqrt(6) -1/sqrt(6);1/sqrt(3)
1/sqrt(3) 1/sqrt(3)];
R=inv(R1);
figure(2)% 3-D Pan-Hudson surface in stress space.
for h=1:length(I1)
    [X,Y] = pol2cart(theta,sqrt(2).*r1(:,h)');
    I16((((6*r1(:,h)'/sigmac)+lamda).^2-lamda.^2)./(12))-S)*3*sigmac/mb;
    z1=I16;
    A1=R*[X;Y;z1/sqrt(3)];
    plot3(A1(1,:),A1(2,:),A1(3:,:), 'r')
    hold on
    [X1,Y1] = pol2cart(theta1+pi/3,sqrt(2).*r2(:,h)');
    I16((((6*r2(:,h)'/sigmac)+lamda).^2-lamda.^2)./(12))-S)*3*sigmac/mb;
    z2=I16;
    B=R*[X1;Y1;z2/sqrt(3)];
    plot3(B(1,:),B(2,:),B(3:,:), 'r')
    hold on

```

```

[X2,Y2] = pol2cart(theta2+2*pi/3,sqrt(2).*r3(:,h)');
I16=((((6*r3(:,h)'/sigmac)+lamda).^2-lamda.^2)./(12))-S)*3*sigmac/mb;
z3=I16;
C=R*[X2;Y2;z3/sqrt(3)];
plot3(C(1,:),C(2,:),C(3,:), 'r')
hold on
[X3,Y3] = pol2cart(theta3+pi,sqrt(2).*r4(:,h)');
I16=((((6*r4(:,h)'/sigmac)+lamda).^2-lamda.^2)./(12))-S)*3*sigmac/mb;
z4=I16;
D=R*[X3;Y3;z4/sqrt(3)];
plot3(D(1,:),D(2,:),D(3,:), 'r')
hold on
[X4,Y4] = pol2cart(theta4+4*pi/3,sqrt(2).*r5(:,h)');
I16=((((6*r5(:,h)'/sigmac)+lamda).^2-lamda.^2)./(12))-S)*3*sigmac/mb;
z5=I16;
E=R*[X4;Y4;z5/sqrt(3)];
plot3(E(1,:),E(2,:),E(3,:), 'r')
hold on
[X5,Y5] = pol2cart(theta5+5*pi/3,sqrt(2).*r6(:,h)');
I16=((((6*r6(:,h)'/sigmac)+lamda).^2-lamda.^2)./(12))-S)*3*sigmac/mb;
z6=I16;
F=R*[X5;Y5;z6/sqrt(3)];
plot3(F(1,:),F(2,:),F(3,:), 'r')
end
% Moving axes to the origin of coordinate system.
plot3(get(gca, 'XLim'),[0 0],[0 0], 'k');
plot3([0 0],[0 0],get(gca, 'ZLim'), 'k');
plot3([0 0],get(gca, 'YLim'),[0 0], 'k');
X=get(gca, 'Xtick');
Y=get(gca, 'Ytick');
Z=get(gca, 'Ztick');
XL=get(gca, 'XtickLabel');
YL=get(gca, 'YtickLabel');
ZL=get(gca, 'ZtickLabel');

% REMOVE TICKS
set(gca, 'Xtick', []);
set(gca, 'Ytick', []);
set(gca, 'Ztick', []);

% GET OFFSETS
Xoff=diff(get(gca, 'XLim'))./30;
Yoff=diff(get(gca, 'YLim'))./30;
Zoff=diff(get(gca, 'ZLim'))./30;
xlabel('\sigma_2 (MPa)', 'fontname', 'times new roman', 'fontsize', 14)
ylabel('\sigma_1 (MPa)', 'fontname', 'times new roman', 'fontsize', 14)
zlabel('\sigma_3 (MPa)', 'fontname', 'times new roman', 'fontsize', 14)

```

## Zhang-Zhu Criterion

```
%=====Zhang-Zhu Criterion=====
% Input parameters:
% I1= First invariant of stress tensor.
% mb= Parameter m for the Hoek-Brown Criterion.
% sigmac= Uniaxial strength of rock material.
% parameter S for the Hoek-Brown Criterion.
% Output:
% Failure surface for the Hoek-Brown criterion in three-dimensional stress
space.
%=====
I1=linspace(0,3500,50);
mb=20;
sigmac=100;
S=1;
e=0.00;
%====Calculation of the Zhang-Zhu radius on the deviatoric plane=====
%==[-pi/6,pi/6]=====
theta=(-pi/6:.01:pi/6);
lamda1=(sqrt(3)/2)*mb+(sqrt(3)/3)*mb*sin(theta);
%A=4*(cos(theta)).^2;
for j=1:length(I1)
    for i=1:length(lamda1)
        r1(i,j)=(sigmac./6).*(-
lamda1(i)+sqrt(lamda1(i).^2+12.*(mb*I1(j)/(3*sigmac))+S));
    end
end
%==[pi/6,pi/2]=====
theta1=(-(pi/6)+e:0.01:pi/6);
lamda2=(sqrt(3)/2)*mb-(sqrt(3)/3)*mb*sin(theta);
%A=4*(cos(theta)).^2;
for j=1:length(I1)
    for i=1:length(lamda2)
        r2(i,j)=(sigmac./6).*(-
lamda2(i)+sqrt(lamda2(i).^2+12.*(mb*I1(j)/(3*sigmac))+S));
    end
end
%=====[pi/2,2pi/3]=====
theta2=(-(pi/6)-e:0.01:pi/6);
lamda1=(sqrt(3)/2)*mb+(sqrt(3)/3)*mb*sin(theta);
for j=1:length(I1)
    for i=1:length(lamda1)
        r3(i,j)=(sigmac./6).*(-
lamda1(i)+sqrt(lamda1(i).^2+12.*(mb*I1(j)/(3*sigmac))+S));
    end
end
%=====[5pi/6,7pi/6]=====
theta3=(-(pi/6)-e:0.01:pi/6);
lamda2=(sqrt(3)/2)*mb-(sqrt(3)/3)*mb*sin(theta);
for j=1:length(I1)
    for i=1:length(lamda2)
        r4(i,j)=(sigmac./6).*(-
lamda2(i)+sqrt(lamda2(i).^2+12.*(mb*I1(j)/(3*sigmac))+S));
    end
end
```

```

%=====[7pi/6,3pi/2]====
theta4=(-pi/6-e:0.01:pi/6);
lamda1=(sqrt(3)/2)*mb+(sqrt(3)/3)*mb*sin(theta);
for j=1:length(I1)
    for i=1:length(lamda1)
        r5(i,j)=(sigmac./6).*(-
lamda1(i)+sqrt(lamda1(i).^2+12.*(mb*I1(j)/(3*sigmac))+S));
    end
end
%=====[3pi/2,-pi/6]====
theta5=(-pi/6:0.01:pi/6);
lamda2=(sqrt(3)/2)*mb-(sqrt(3)/3)*mb*sin(theta);
for j=1:length(I1)
    for i=1:length(lamda2)
        r6(i,j)=(sigmac./6).*(-
lamda2(i)+sqrt(lamda2(i).^2+12.*(mb*I1(j)/(3*sigmac))+S));
    end
end
%-----
figure(1)% 2-D Hoek-Brown trace on the deviatoric plane.
for h=1:length(I1)
    [X,Y] = pol2cart(theta,r1(:,h)');
    plot(X,Y)
    hold on
    [X1,Y1] = pol2cart(theta1+pi/3,r2(:,h)');
    plot(X1,Y1)
    hold on
    [X2,Y2] = pol2cart(theta2+2*pi/3,r3(:,h)');
    plot(X2,Y2)
    hold on
    [X3,Y3] = pol2cart(theta3+pi,r4(:,h)');
    plot(X3,Y3)
    hold on
    [X4,Y4] = pol2cart(theta4+4*pi/3,r5(:,h)');
    plot(X4,Y4)
    hold on
    [X5,Y5] = pol2cart(theta5+5*pi/3,r6(:,h)');
    plot(X5,Y5)
end
xlabel('\sigma_2d (MPa)','fontname','times new roman','fontsize',14)
ylabel('\sigma_1d (MPa)','fontname','times new roman','fontsize',14)
R1=[1/sqrt(2) 0 -1/sqrt(2);-1/sqrt(6) 2/sqrt(6) -1/sqrt(6);1/sqrt(3)
1/sqrt(3) 1/sqrt(3)];
R=inv(R1);
R1=[1/sqrt(2) 0 -1/sqrt(2);-1/sqrt(6) 2/sqrt(6) -1/sqrt(6);1/sqrt(3)
1/sqrt(3) 1/sqrt(3)];
R=inv(R1);
figure(2)% 3-D Hoek-Brown surface in stress space.
for h=1:length(I1)
    [X,Y] = pol2cart(theta,sqrt(2).*r1(:,h)');
    I16((((6*r1(:,h)'/sigmac)+lamda1).^2-lamda1.^2)./(12))-
S)*3*sigmac/mb;
    z1=I16;
    A1=R*[X;Y;z1/sqrt(3)];
    plot3(A1(1,:),A1(2,:),A1(3,:), 'r')
    hold on
    [X1,Y1] = pol2cart(theta1+pi/3,sqrt(2).*r2(:,h)');

```

```

I16=((((6*r2(:,h)'/sigmac)+lamda2).^2-lamda2.^2)./(12))-
S)*3*sigmac/mb;
z2=I16;
B=R*[X1;Y1;z2/sqrt(3)];
plot3(B(1,:),B(2,:),B(3,:), 'r')
hold on
[X2,Y2] = pol2cart(theta2+2*pi/3,sqrt(2).*r3(:,h)');
I16=((((6*r3(:,h)'/sigmac)+lamda1).^2-lamda1.^2)./(12))-
S)*3*sigmac/mb;
z3=I16;
C=R*[X2;Y2;z3/sqrt(3)];
plot3(C(1,:),C(2,:),C(3,:), 'r')
hold on
[X3,Y3] = pol2cart(theta3+pi,sqrt(2).*r4(:,h)');
I16=((((6*r4(:,h)'/sigmac)+lamda2).^2-lamda2.^2)./(12))-
S)*3*sigmac/mb;
z4=I16;
D=R*[X3;Y3;z4/sqrt(3)];
plot3(D(1,:),D(2,:),D(3,:), 'r')
hold on
[X4,Y4] = pol2cart(theta4+4*pi/3,sqrt(2).*r5(:,h)');
I16=((((6*r5(:,h)'/sigmac)+lamda1).^2-lamda1.^2)./(12))-
S)*3*sigmac/mb;
z5=I16;
E=R*[X4;Y4;z5/sqrt(3)];
plot3(E(1,:),E(2,:),E(3,:), 'r')
hold on
[X5,Y5] = pol2cart(theta5+5*pi/3,sqrt(2).*r6(:,h)');
I16=((((6*r6(:,h)'/sigmac)+lamda2).^2-lamda2.^2)./(12))-
S)*3*sigmac/mb;
z6=I16;
F=R*[X5;Y5;z6/sqrt(3)];
plot3(F(1,:),F(2,:),F(3,:), 'r')
end
% Moving axes to the origin of coordinate system.
plot3(get(gca,'XLim'),[0 0],[0 0],'k');
plot3([0 0],[0 0],get(gca,'ZLim'),'k');
plot3([0 0],get(gca,'YLim'),[0 0],'k');
X=get(gca,'Xtick');
Y=get(gca,'Ytick');
Z=get(gca,'Ztick');
XL=get(gca,'XtickLabel');
YL=get(gca,'YtickLabel');
ZL=get(gca,'ZtickLabel');

% REMOVE TICKS
set(gca,'Xtick',[]);
set(gca,'Ytick',[]);
set(gca,'Ztick',[]);

% GET OFFSETS
Xoff=diff(get(gca,'XLim'))./30;
Yoff=diff(get(gca,'YLim'))./30;
Zoff=diff(get(gca,'ZLim'))./30;
xlabel('\sigma_2 (MPa)','fontname','times new roman','fontsize',14)
ylabel('\sigma_1 (MPa)','fontname','times new roman','fontsize',14)

```

```
zlabel('\sigma_3 (MPa)', 'fontname', 'times new roman', 'fontsize', 14)
```

## ***Simplified Priest Criterion***

```
%=====Simplified-Priest
Criterion=====
% Input parameters:
% I1= First invariant of stress tensor.
% mb= Parameter m for the Hoek-Brown Criterion.
% sigmac= Uniaxial strength of rock material.
% parameter S for the Hoek-Brown Criterion.
% Output:
% Failure surface for the Hoek-Brown criterion in three-dimensional stress
space.
%=====
I1=linspace(0,3500,50);
mb=20;
sigmac=80;
S=1;
w=0.299289347;
e=0.00;
%====Calculation of the Simplified Priest radius on the deviatoric
plane=====
%==[-pi/6,pi/6]=====
theta=(-pi/6:.01:pi/6);
lamda1=2*mb.*((sqrt(3)/3)*sin(theta+pi/3)-w*sin(theta+pi/6));
A1=9*w^2*(sqrt(3)*sin(theta)+cos(theta)).^2-
6*w*(3+4*sqrt(3)*sin(theta).*cos(theta))+3*(sin(theta)+sqrt(3)*cos(theta)).
^2;
for j=1:length(I1)
    for i=1:length(lamda1)
        r1(i,j)=(sigmac./(2*A1(i)).*(-
        lamda1(i)+sqrt(lamda1(i).^2+4*A1(i).*(mb*I1(j)/(3*sigmac))+S));
    end
end
%==[pi/6,pi/2]=====
theta1=(-(pi/6)+e:0.01:pi/6);
lamda2=2*mb.*(-(sqrt(3)/3)*sin(theta-pi/3)+w*sin(theta-pi/6));
A2=9*w^2*(sqrt(3)*sin(theta)-cos(theta)).^2-6*w*(3-
4*sqrt(3)*sin(theta).*cos(theta))+3*(sin(theta)-sqrt(3)*cos(theta)).^2;;
for j=1:length(I1)
    for i=1:length(lamda2)
        r2(i,j)=(sigmac./(2*A2(i)).*(-
        lamda2(i)+sqrt(lamda2(i).^2+4*A2(i).*(mb*I1(j)/(3*sigmac))+S));
    end
end
%=====[pi/2,2pi/3]=====
theta2=(-(pi/6)-e:0.01:pi/6);
lamda1=2*mb.*((sqrt(3)/3)*sin(theta+pi/3)-w*sin(theta+pi/6));
for j=1:length(I1)
```



```

R=inv(R1);
R1=[1/sqrt(2)    0   -1/sqrt(2);-1/sqrt(6)    2/sqrt(6)   -1/sqrt(6);1/sqrt(3)
1/sqrt(3) 1/sqrt(3)];
R=inv(R1);
figure(2)% 3-D Simplified-Priest surface in stress space.
for h=1:length(I1)
    [X,Y] = pol2cart(theta,sqrt(2).*r1(:,h)');
    I16=((3*sigmac).*(((r1(:,h)'/sigmac).*(2*A1)+lamda1).^2-
lamda1.^2)./(4.*A1))-S))./mb;
    z1=I16;
    T1=R*[X;Y;z1/sqrt(3)];
    plot3(T1(1,:),T1(2,:),T1(3,:), 'r')
    hold on
    [X1,Y1] = pol2cart(theta1+pi/3,sqrt(2).*r2(:,h)');
    I16=((3*sigmac).*(((r2(:,h)'/sigmac).*(2*A2)+lamda2).^2-
lamda2.^2)./(4.*A2))-S))./mb;
    z2=I16;
    B=R*[X1;Y1;z2/sqrt(3)];
    plot3(B(1,:),B(2,:),B(3,:), 'r')
    hold on
    [X2,Y2] = pol2cart(theta2+2*pi/3,sqrt(2).*r3(:,h)');
    I16=((3*sigmac).*(((r3(:,h)'/sigmac).*(2*A1)+lamda1).^2-
lamda1.^2)./(4.*A1))-S))./mb;
    z3=I16;
    C=R*[X2;Y2;z3/sqrt(3)];
    plot3(C(1,:),C(2,:),C(3,:), 'r')
    hold on
    [X3,Y3] = pol2cart(theta3+pi,sqrt(2).*r4(:,h)');
    I16=((3*sigmac).*(((r4(:,h)'/sigmac).*(2*A2)+lamda2).^2-
lamda2.^2)./(4.*A2))-S))./mb;
    z4=I16;
    D=R*[X3;Y3;z4/sqrt(3)];
    plot3(D(1,:),D(2,:),D(3,:), 'r')
    hold on
    [X4,Y4] = pol2cart(theta4+4*pi/3,sqrt(2).*r5(:,h)');
    I16=((3*sigmac).*(((r5(:,h)'/sigmac).*(2*A1)+lamda1).^2-
lamda1.^2)./(4.*A1))-S))./mb;
    z5=I16;
    E=R*[X4;Y4;z5/sqrt(3)];
    plot3(E(1,:),E(2,:),E(3,:), 'r')
    hold on
    [X5,Y5] = pol2cart(theta5+5*pi/3,sqrt(2).*r6(:,h)');
    I16=((3*sigmac).*(((r6(:,h)'/sigmac).*(2*A2)+lamda2).^2-
lamda2.^2)./(4.*A2))-S))./mb;
    z6=I16;
    F=R*[X5;Y5;z6/sqrt(3)];
    plot3(F(1,:),F(2,:),F(3,:), 'r')
end
% Moving axes to the origin of coordinate system.
plot3(get(gca, 'XLim'),[0 0],[0 0], 'k');
plot3([0 0],[0 0],get(gca, 'ZLim'), 'k');
plot3([0 0],get(gca, 'YLim'),[0 0], 'k');
X=get(gca, 'Xtick');
Y=get(gca, 'Ytick');
Z=get(gca, 'Ztick');
XL=get(gca, 'XtickLabel');
YL=get(gca, 'YtickLabel');

```

```

ZL=get(gca,'ZtickLabel');

% REMOVE TICKS
set(gca,'Xtick',[]);
set(gca,'Ytick',[]);
set(gca,'Ztick',[]);

% GET OFFSETS
Xoff=diff(get(gca,'XLim'))./30;
Yoff=diff(get(gca,'YLim'))./30;
Zoff=diff(get(gca,'ZLim'))./30;
xlabel('\sigma_2 (MPa)','fontname','times new roman','fontsize',14)
ylabel('\sigma_1 (MPa)','fontname','times new roman','fontsize',14)
zlabel('\sigma_3 (MPa)','fontname','times new roman','fontsize',14)

```

## ***Generalised Priest Criterion***

```

%====Generalised-Priest
Criterion=====
% Input parameters:
% I1= First invariant of stress tensor.
% mb= Parameter m for the Hoek-Brown Criterion.
% sigmac= Uniaxial strength of rock material.
% parameter S for the Hoek-Brown Criterion.
% Output:
% Failure surface for the Hoek-Brown criterion in three-dimensional stress
space.
%=====
clear all
close all
I1=linspace(0,3500,50);
mb=20;
sigmac=100;
S=1;
e=0.00;
%%====Calculation of the Generalised Priest radius on the deviatoric
plane=====
%==[-pi/6,pi/6]=====
theta=(-pi/6:.01:pi/6);
A=3*ones(1,length(theta));
lamda=(sqrt(3)/3)*mb*ones(1,length(theta));
for j=1:length(I1)
    for i=1:length(lamda)
        r1(i,j)=(sigmac./6).*(-
lamda(i)+sqrt(lamda(i).^2+12.*(mb*I1(j)/(3*sigmac))+S));
    end
end
%==[pi/6,pi/2]=====
thetal=(-(pi/6)+e:0.01:pi/6);
for j=1:length(I1)
    for i=1:length(lamda)

```

```

        r2(i,j)=(sigmac./6).*(-
lamda(i)+sqrt(lamda(i).^2+12.*(mb*I1(j)/(3*sigmac))+S));
    end
end
%===== [pi/2,2pi/3] =====
theta2=(-(pi/6)-e:0.01:pi/6);
for j=1:length(I1)
    for i=1:length(lamda)
        r3(i,j)=(sigmac./6).*(-
lamda(i)+sqrt(lamda(i).^2+12.*(mb*I1(j)/(3*sigmac))+S));
    end
end
%===== [5pi/6,7pi/6] =====
theta3=(-pi/6)-e:0.01:pi/6);
for j=1:length(I1)
    for i=1:length(lamda)
        r4(i,j)=(sigmac./6).*(-
lamda(i)+sqrt(lamda(i).^2+12.*(mb*I1(j)/(3*sigmac))+S));
    end
end
%===== [7pi/6,3pi/2] =====
theta4=(-pi/6)-e:0.01:pi/6);
for j=1:length(I1)
    for i=1:length(lamda)
        r5(i,j)=(sigmac./6).*(-
lamda(i)+sqrt(lamda(i).^2+12.*(mb*I1(j)/(3*sigmac))+S));
    end
end
%===== [3pi/2,-pi/6] =====
theta5=(-pi/6:0.01:pi/6);
for j=1:length(I1)
    for i=1:length(lamda)
        r6(i,j)=(sigmac./6).*(-
lamda(i)+sqrt(lamda(i).^2+12.*(mb*I1(j)/(3*sigmac))+S));
    end
end
end
%-----
figure(1)% 2-D Generalised Priest trace on the deviatoric plane.
for h=1:length(I1)
    [X,Y] = pol2cart(theta,r1(:,h)');
    plot(X,Y)
    hold on
    [X1,Y1] = pol2cart(theta1+pi/3,r2(:,h)');
    plot(X1,Y1)
    hold on
    [X2,Y2] = pol2cart(theta2+2*pi/3,r3(:,h)');
    plot(X2,Y2)
    hold on
    [X3,Y3] = pol2cart(theta3+pi,r4(:,h)');
    plot(X3,Y3)
    hold on
    [X4,Y4] = pol2cart(theta4+4*pi/3,r5(:,h)');
    plot(X4,Y4)
    hold on
    [X5,Y5] = pol2cart(theta5+5*pi/3,r6(:,h)');
    plot(X5,Y5)
end

```

```

xlabel('\sigma_2d (MPa)', 'fontname', 'times new roman', 'fontsize', 14)
ylabel('\sigma_1d (Mpa)', 'fontname', 'times new roman', 'fontsize', 14)
R1=[1/sqrt(2) 0 -1/sqrt(2);-1/sqrt(6) 2/sqrt(6) -1/sqrt(6);1/sqrt(3)
1/sqrt(3) 1/sqrt(3)];
R=inv(R1);

R1=[1/sqrt(2) 0 -1/sqrt(2);-1/sqrt(6) 2/sqrt(6) -1/sqrt(6);1/sqrt(3)
1/sqrt(3) 1/sqrt(3)];
R=inv(R1);
figure(2)% 3-D Generalised Priest surface in stress space.
for h=1:length(I1)
[X,Y] = pol2cart(theta,sqrt(2)*r1(:,h)');
I16((((6*r1(:,h)'/sigmac)+lamda).^2-lamda.^2)./(12))-S)*3*sigmac/mb;
z1=I16;
A1=R*[X;Y;z1/sqrt(3)];
P1=plot3(A1(1,:),A1(2,:),A1(3,:), 'r')
%set(P1,'color',[1,0.7344,0]);
hold on
[X1,Y1] = pol2cart(theta1+pi/3,sqrt(2)*r2(:,h)');
I16((((6*r2(:,h)'/sigmac)+lamda).^2-lamda.^2)./(12))-S)*3*sigmac/mb;
z2=I16;
B=R*[X1;Y1;z2/sqrt(3)];
P2=plot3(B(1,:),B(2,:),B(3,:), 'r')
%set(P2,'color',[1,0.7344,0]);
hold on
[X2,Y2] = pol2cart(theta2+2*pi/3,sqrt(2)*r3(:,h)');
I16((((6*r3(:,h)'/sigmac)+lamda).^2-lamda.^2)./(12))-S)*3*sigmac/mb;
z3=I16;
C=R*[X2;Y2;z3/sqrt(3)];
P3=plot3(C(1,:),C(2,:),C(3,:), 'r')
%set(P3,'color',[1,0.7344,0]);
hold on
[X3,Y3] = pol2cart(theta3+pi,sqrt(2)*r4(:,h)');
I16((((6*r4(:,h)'/sigmac)+lamda).^2-lamda.^2)./(12))-S)*3*sigmac/mb;
z4=I16;
D=R*[X3;Y3;z4/sqrt(3)];
P4=plot3(D(1,:),D(2,:),D(3,:), 'r')
%set(P4,'color',[1,0.7344,0]);
hold on
[X4,Y4] = pol2cart(theta4+4*pi/3,sqrt(2)*r5(:,h)');
I16((((6*r5(:,h)'/sigmac)+lamda).^2-lamda.^2)./(12))-S)*3*sigmac/mb;
z5=I16;
E=R*[X4;Y4;z5/sqrt(3)];
P5=plot3(E(1,:),E(2,:),E(3,:), 'r')
%set(P5,'color',[1,0.7344,0]);
hold on
[X5,Y5] = pol2cart(theta5+5*pi/3,sqrt(2)*r6(:,h)');
I16((((6*r6(:,h)'/sigmac)+lamda).^2-lamda.^2)./(12))-S)*3*sigmac/mb;
z6=I16;
F=R*[X5;Y5;z6/sqrt(3)];
P6=plot3(F(1,:),F(2,:),F(3,:), 'r')
%set(P6,'color',[1,0.7344,0]);
end
% Moving axes to the origin of coordinate system.
plot3(get(gca,'XLim'),[0 0],[0 0], 'k');
plot3([0 0],[0 0],get(gca,'ZLim'),'k');
plot3([0 0],get(gca,'YLim'),[0 0], 'k');

```

```

X=get(gca,'Xtick');
Y=get(gca,'Ytick');
Z=get(gca,'Ztick');
XL=get(gca,'XtickLabel');
YL=get(gca,'YtickLabel');
ZL=get(gca,'ZtickLabel');

% REMOVE TICKS
set(gca,'Xtick',[]);
set(gca,'Ytick',[]);
set(gca,'Ztick',[]);

% GET OFFSETS
Xoff=diff(get(gca,'XLim'))./30;
Yoff=diff(get(gca,'YLim'))./30;
Zoff=diff(get(gca,'ZLim'))./30;
xlabel('\sigma_2 (MPa)','fontname','times new roman','fontsize',14)
ylabel('\sigma_1 (MPa)','fontname','times new roman','fontsize',14)
zlabel('\sigma_3 (MPa)','fontname','times new roman','fontsize',14)

```